UNIVERSITY OF CALIFORNIA
RIVERSIDE

Explaining Slow Earthquake Phenomena with a Frictional-Viscous Faulting Model

A Dissertation submitted in partial satisfaction
of the requirements for the degree of

Doctor of Philosophy

in

Geological Sciences

by

Baoning Wu

December 2021

Dissertation Committee:

Dr. David D. Oglesby, Chairperson
Dr. Gareth Funning
Dr. Abhijit Ghosh

The Dissertation of Baoning Wu is approved:

Committee Chairperson

University of California, Riverside

Acknowledgments

I couldn't imagine that this dissertation and my PhD can be finished without the love, support, and help from many people. I want to thank my PhD advisor David Oglesby. David brought me to his group at UC Riverside after I got my undergrad. I remember myself as a Chinese kid who was certainly enthusiastic but also very naive and irritable. David is very skillful in training me. He is good at encouraging me to wildly explore my interests, suggesting to me good materials to read and work on, while at the same time keeping me on the right track. David is very patient. He thinks carefully about what is good for his students, but he never imposes things on them, and he understands that it may take time for the students to appreciate his approaches and good intentions. During my five years of PhD, I have been through high and low. David has been always monitoring my progress, making sure I don't get over-complacent for good results and compliments, and not getting over-desperate for failures and criticisms. David leads by example. He is kind, honest, and generous, and he is always ready to help people around him to succeed and achieve their goals. I guess that's why David is always a passionate scientist, a proud dad, and a happy man. I appreciate everything David has taught me, and I owe this dissertation to him.

I wish to thank my PhD committee members: Gareth Funning and Abhi Ghosh. Gareth has always been the source of information and guidance for me and is always available as a friend and mentor. Abhi has helped me initiate the slow earthquake project, and has been my collaborator and a major source of slow earthquake discussion ever since. Both Gareth and Abhi provided me opportunities to join the 2019 Ridgecrest earthquake

response team. As an earthquake modeler, those field trips experiences of doing campaign GPS surveys and deploying seismic stations help me appreciate more about the data collecting process. I also want to thank my candidacy committee members, Jim Dieterich and Guanshui Xu. Jim taught me the background of slow earthquakes and helped me form a basic understanding of slow earthquake modeling. Although being a giant in the field, Jim is very modest and is always cautious about his understanding of earthquake models. Jim is always willing to rethink the existing theory with new observations, even those of his own that are widely accepted. His spirit deeply influences me and gives me confidence when my ideas challenge some of the traditional concepts. Guanshui, as a mechanical engineer with rich experience in the industry, taught me a lot about how to look at earthquake models from an engineering perspective, and help me appreciate the significance of my research.

I want to give a special thanks to my friend and colleague Christos Kyriakopoulos. Christos is not on my committee, but he is like my second advisor. Christos and I shared the same office for the first three years of my PhD, until he left for a faculty position at the University of Memphis. When he left, Christos left me a year of funding to support my research. Although the funding is not dedicated to my dissertation, it did provide me some additional time to focus and think more carefully about my dissertation. Christos is always willing to give me advice as a senior colleague to help me become a better student and a better scientist, for everything in my life from how to make dynamic rupture models to how to make a proper jump shot. Christos is earnest and warmhearted. He is never afraid to take challenges, and always fights for what he thinks is the right thing to do. I appreciate all these lessons from him.

In the process of coming up with this slow earthquake project, conducting the research, and turning it into a PhD dissertation, I have received tremendous help and advice from many scientists both in and outside of UC Riverside. I want to thank professor Shiyong Zhou, Hongfeng Yang, Yajing Liu, and Meng (Matt) Wei, who hosted the 2015 summer short course on earthquake source processes at Peking University. As an undergrad, I learned about the big picture of the slow earthquake problem during this course and got motivated by the slow earthquake puzzle. I want to thank my undergrad advisor Haiming Zhang. Professor Zhang always set a high standard for me. Without the training with him, I wouldn't be able to have enough theoretical skills to conduct the derivations in this dissertation. I want to thank my colleague and friends Shukei Ohyanagi, Bo Li, Allie Hutchison, and Satoshi Katakami, who overlapped with me at UC Riverside at the beginning of my dissertation project and was always willing to discuss the latest slow earthquake observations with me.

I also wish to thank those people who I met and discussed with in the 2017 Cargese Summer School in France, in particular, Tomoaki Nishikawa, Satoru Baba, Daisuke Sato, Aitaro Kato, Satoshi Ide, Pierre Romanet, Harsha S. Bhat, and Hans Agurto-Detzel. Their insights into slow earthquake observations and earthquake modeling greatly improved my understanding of this issue, and help me realize the importance of constraining models with observations. In the 2017 SCEC Meeting and AGU Fall meeting, I present some preliminary results of this project received a lot of valuable comments from Ryosuke Ando, Yingdi Luo, Pablo Ampuero, and Kenneth Creager. I want to thank my undergrad roommate and homie Junlin Hua, who is always willing to listen to my ideas and invited me to give a

seminar on my slow earthquake work at Brown University. During my visit to the East coast, I also attent the 2018 Gordon Conference on Rock physics and present my slow earthquake results, I met many scientists who specialized in lab experiments and friction law, in particular Eric Burdette, Nir Badt, Pat Bhattacharya, Sohom Ray, Greg Hirth, and Allan Rubin. My understanding of friction law benefits a lot from the discussion with them. I want to thank Jessica Hawthorne who told me I need to make predictions for my model in order to test it with future observations, during her visit to UC Riverside in late 2019. Lastly, I would like to thank some geologists who I got in touch with in the later stage of my dissertation project: An Yin, Whitney Behr, Adam Beall, Noah Phillips, Christie Rowe, and John Platt. The discussions with them, either in person, over zoom, or on Twitter, help me better appreciate the exhumed fault observations of slow earthquakes. These understandings form the physical picture behind the "friction law" of my model in the present dissertation. This slow earthquake project was stuck in the third year of PhD and I almost gave it up. It is the insights and encouragements from these geologists that motivates me carry on and move forward. In particular, I want to thank professor An Yin, who cheered me up so much during his visit to UC Riverside in February 2019, and urged me to better deliver my results.

Of course, my PhD life is not all about research, and I couldn't have made it without all the love and care from my family and friends. I feel very grateful to have you there during both the tough time and happy time. I want to thank Bo, Kuntal, Matt, Nader, Rachel, Jerlyn, who are always there when I need help in life. I will be, or probably already have been, missing you guys a lot. I want to thank professor Gordon Love, Rich

Minnich, Heather Ford, Roby Douilly, Nic Barth, Maryjo Brounce, Pete Sadler, and Nigel Hughes, who always like to talk to me when seeing me in the department, share with me their advice, and cheer me up. I want to thank my brothers Zhengdong, Yanwei, Boxiao, Chengshuo, Yanxiang, Abu, Baichuan, Mike, and TuKun, with whom I spend most of my non-scientific-discussion and sports time in Riverside. I want to thank my landlord, Uncle Wong and Aunt Wong, who treated me like a family member for five years, feeding me and making sure I am healthy and safe. I want to thank the Starbucks at Blaine, Iowa, and Glen Mor and all the nice stuff there. Nearly all my dissertation texts are written in the above three Starbucks coffee shops. The stuffs in the shop know me well now and will always say hi to me with a big smile, which often prevents me from being too frustrated about the writing. I don't know how I can possibly name all the friends who have so greatly enriched my life for all these years. I only hope that I have been able to give back to you the love you have given me.

Finally, I want to give a special thanks to Xueying. We've been through much together in the last few years, and probably there will be a lot more years to come. This dissertation wouldn't be here without you.

I want to dedicate this dissertation to my mother, Yin'e Xie, and my father, Bingquan Wu. You taught me how to be a good person and how to do the right things. I owe all my achievements to you, and I hope I can make you proud of your son.

To my mother, Yin'e Xie, and my father, Bingquan Wu.

ABSTRACT OF THE DISSERTATION

Explaining Slow Earthquake Phenomena with a Frictional-Viscous Faulting Model

by

Baoning Wu

Doctor of Philosophy, Graduate Program in Geological Sciences
University of California, Riverside, December 2021
Dr. David D. Oglesby, Chairperson

It is well-known that the first-order kinematic characteristics of typical earthquakes, such as slip rate, rupture propagation speed, and moment duration scaling, can be well-explained by a model where the fault experiences a sudden frictional strength drop. In recent decades, a new type of earthquake has been discovered, which has a slower slip rate than a typical earthquake. These earthquakes are now often referred to as slow earthquakes, and those typical earthquakes are referred to as fast earthquakes. The aforementioned sudden strength drop model derived from fast earthquake observations cannot explain the first-order characteristics of slow earthquakes.

In this dissertation, I consider a frictional-viscous fault zone model to explain the puzzling slow earthquake phenomena, with a particular focus on slow slip events (SSEs), which is a type of slow earthquake that is well characterized. The frictional-viscous model is inspired by the recent geological observations that imply the occurrence of SSEs in fault zones with a finite thickness of ∼100s of meters. The bulk matrix of the fault zone deforms viscously, while pervasive frictional surfaces are distributed in the viscous matrix.

To simultaneously consider both the 10s-kilometer-scale rupture propagation and the 100s-meter-scale fault zone features in the same model, I treat a fault zone as a zero-thickness "surface" embedded in an elastic medium. The "frictional-viscous" characteristics are parameterized into a constitutive relation where fault strength is partitioned into a frictional and a viscous component in parallel. Two key parameters in the frictional-viscous model are the viscous coefficient η_v and the event stress drop. The present frictional-viscous model can simultaneously explain various kinematic source parameters for SSEs when the viscous coefficient η_v is about $10^4 - 10^5$ $\mu/(2\beta)$, and the average stress drop in a slip transient is about 10 kPa. Qualitatively, this frictional-viscous model can also explain the shorter inter-event interval and lower average stress drop observed in subduction zone SSEs, compared to what is observed in the fast earthquakes at seismogenic depth. These results imply that the frictional-viscous model is a promising representation of the actual SSE source processes. The present model provides many hypotheses, which can be further tested with future geophysical, geological, and experimental data.

Contents

List of Figures

List of Tables

Chapter 1

Introduction

In this dissertation, I will investigate the physical mechanism of slow earthquakes.

An earthquake, in general, is referred to as the sudden shaking of the Earth's surface caused by a sudden release of energy in or on the Earth's solid body, caused either by humans or by nature, that creates seismic waves. Interchangeably, the source of the seismic energy is often referred to as the earthquake as well. The most common and destructive earthquakes are those shallow ones within the very top layer of the Earth. It is now generally believed that these shallow earthquakes are caused by sudden shear dislocation movement across fractures in the Earth's lithosphere. These fractures and the associated shear dislocation movement are now commonly referred to as faults and fault slip, respectively. These shallow earthquakes that are caused by transient fault slip are the focus of this dissertation. Therefore, in the following text, I will simply use the term "earthquake" to denote a shallow earthquake, whenever it is more convenient.

The seismic energy released in an earthquake is now generally thought to come

from the elastic strain energy stored in Earth's lithosphere, which is divided into a series of plates. Tectonic processes drive these plates to move relative to each other, and elastic strain accumulates when plates move not in accordance with each other. Faults develop and slip occurs to release the excess strain energy, and the slip often happens in an episodic manner. This process is now famously known as elastic rebound (Reid, 1910): during the long period when no earthquake happens, elastic strain slowly accumulates near the fault and the shear stress on fault builds up, while not exceeding the shear strength on fault. At one point, the loading shear stress on fault is so large that the shear strength on fault cannot hold the fault any longer. The shear strength would then suddenly drop from the high value to a lower value. To accommodate the shear strength drop on fault, transient slip would occur on fault as well, which excites seismic waves that propagate outward and release the accumulated elastic strain energy near the fault.

Although exceptions and puzzles exist, the above elastic rebound model is currently the best first-order model to explain various shallow earthquakes observations in gross. Many metrics have been designed based on the vision of this model, including the most widely used metric, moment magnitude, that measures earthquake energy radiation. However, the emerging observations of a new type of transient slip events since early 2000 challenge our existing understandings. These transient slip events are now commonly referred to as slow earthquakes (e.g., Dragert, Wang, & James, 2001; Obara, 2002; Rogers & Dragert, 2003). They are still referred to as "earthquakes" because they are found to be transient slip motions on faults that are caused by shear stress drop. However, they do not generate as much seismic energy as would be predicted by the classic elastic rebound theory

and the related sudden stress drop model. Explaining these discrepancies has become one of the main goals not only for the earthquake science, but also for the Earth sciences as a whole. In a latest study report, *A Vision for NSF Earth Sciences 2020-2030: Earth in Time* by the National Academies of Sciences, Engineering, and Medicine (United States), 12 science priority questions are proposed as "central to the advancement of Earth sciences over the coming decade and could help to transform our scientific understanding of the Earth". The fourth question is stated as "What is an earthquake", stressing the importance of understanding the puzzling slow earthquake phenomenon (National Academies of Sciences & Medicine, 2020).

This dissertation will be devoted to addressing and bridging the discrepancies between slow earthquake observations and the classic elastic rebound theory, and the associated sudden stress drop model. Before I start the detailed analysis from Chapter 2, I will briefly cover the background information in the remainder of this chapter. I will first review the historical development of the classic "elastic rebound theory" and the sudden stress drop model. Then, I will review the discovery of slow earthquakes and introduce several concepts and terminologies that will be constantly used in this dissertation. Lastly, I will briefly lay out the structure of this dissertation.

1.1 The classic "elastic rebound theory" and the sudden stress drop model

The vision that shallow earthquakes are fault slip caused by sudden fault strength drop was proposed as early as in the late 19th and early 20th century (Gilbert, 1884; Reid,

1910), and was mainly inspired by geological and geodetic observations. However, this idea was not fully accepted at the beginning. The "explosion" theory was still thought to be possible, which states that earthquakes come from underground explosions caused by the "fire" of volcanic processes (e.g., Michell, 1760; Mallet, 1862). The fault slip earthquake mechanism became more and more favored in the following century, with accumulating seismic data (e.g., Nakamura, 1922; Byerly, 1926; Honda, 1932; Hodgson, 1957; Honda, 1962), geodetic observations (e.g., Whitten, 1948; Chinnery, 1961), and associated theoretical models that predicted the ground motion of force or force couple(s) (e.g., Lamb, 1904; Love, 1911; Nakano, 1923; Honda & Miura, 1935) and of fault dislocation (e.g., Volterra & Delphenich, 1907; Steketee, 1958; Knopoff & Gilbert, 1960).

Entering the 1960s, the argument that an earthquake is a sudden fault slip mechanism became widely accepted for two main reasons. First, better seismic data implied that earthquake sources are effective double-couple sources (e.g., Aki, 1960), and theoretical studies proved that a fault dislocation can be equivalent to a sudden double-couple force applied in the elastic body in terms of causing elastic deformation (e.g., Maruyama, 1963; Burridge & Knopoff, 1964). This equivalence relation provided the theoretical foundation for using seismically-determined earthquake focal mechanisms to infer fault slip motion. The second reason is the development of plate tectonic theory in the mid-60s. Reviewing the glorious story of plate tectonic discovery is beyond the scope of this discussion, for which I refer readers to the classic textbook *Geodynamics* (Turcotte & Schubert, 2002). One important piece of evidence that supports the plate tectonic theory and is related to earthquakes is the agreement between earthquake focal mechanisms and the predicted

slip direction at mid-ocean transform fault (e.g., Sykes, 1967). In reverse, this agreement could also support the argument that earthquakes correspond fault slip. Perhaps more importantly, as the plate tectonic theory became more and more established, it provided the driving mechanism for the "elastic rebound theory", explaining why elastic strain may slowly build up around faults—it is because of the movement of plates.

The equivalence relation between fault slip and double couple force not only ended the long discussion about the earthquake mechanism; in addition, it provided tools for the community to characterize earthquake processes with seismograms and geodetic measurements, along with the rapid accumulating high-quality data. Quickly, the community found that the "sudden stress drop" argument in the original elastic rebound theory should also be correct for earthquakes, at least in a general sense. The "sudden" here means that the fault strength quickly drops to a low level (dynamic friction) as fault slip starts, and the fault slides at that dynamic friction for most of the slip. This sudden stress model has been shown to be able to reproduce the first-order features of fault slip rate, rupture propagation speed, and earthquake moment-duration scaling. Perhaps most importantly, the sudden fault strength drop model gave rise to the metric of moment magnitude M_w that measures the size and energy release of an earthquake (e.g., Kanamori & Anderson, 1975; Kanamori, 1977; Hanks & Kanamori, 1979; Kanamori, 1983), which has become one of the most important metrics in earthquake science. The basic idea is that, if the fault strength drop is sudden, the amount of seismic energy release E can be grossly approximated via earthquake moment M_0,

$$E = \frac{\Delta\sigma}{\mu} \cdot M_0 \tag{1.1}$$

where $\Delta\sigma$ is the static stress drop and μ is the shear modulus. Since $\Delta\sigma$ is observed to be grossly a constant for earthquakes with different natures (size, slip types, depth), the scaling relation between earthquake moment and the total seismic energy should be grossly the same for all earthquakes. In 1956, Gutenberg and his colleague obtained an empirical relation between earthquake surface wave magnitude M_s and total seismic energy (Gutenberg, 1956; Gutenberg & Richter, 1956),

$$\log E = 1.5M_s + 11.8 \tag{1.2}$$

Therefore, one may construct a magnitude metric based on earthquake moment to measure the total radiation energy of an earthquake, and still make it consistent with the existing surface wave magnitude. This is the moment magnitude M_w,

$$M_w = \frac{2}{3}\left(\log M_0 - 9.05\right) \tag{1.3}$$

where M_0 is in $\mathrm{N} \cdot \mathrm{m}$.

The metric moment magnitude has been shown to be very successful in characterizing earthquakes to first order. In reverse, the success of moment magnitude endorses the assumption that earthquakes slip happens due to a sudden fault strength drop.

It is pretty much safe to say that, by the end of the 20th century, the vision that shallow earthquakes are transient fault slip events caused by sudden fault strength drops, has been widely accepted. Under the umbrella of this gross vision, the major effort

in earthquake science communities has become addressing the variability among different earthquakes. Why are earthquakes different from each other? How do earthquakes slip and rupture start, and how do they stop?

1.2 Discovery of slow earthquakes

Even though the sudden fault strength drop vision can explain most earthquakes, it was recognized at the very early stage that some fault slip transients can be slow and deviate from what is predicted by the sudden fault strength drop model (e.g., Kanamori & Stewart, 1979). However, it was not until the early 21st century that we realized that slip transients are more ubiquitous than we thought.

These slow slip transients are now commonly referred to as slow earthquakes. For convenience, I will denote the most commonly known earthquakes that generate significant ground shaking as "fast earthquakes" in contrast to "slow earthquakes". Different categories of slow earthquakes can be observed in ground motion records at different frequencies, based on which they were given different names. Slow earthquakes are often observed to generate very slow ground movements and thus can only be detected directly using geodetic data. These signals are referred to as "slow slip events", or in abbreviation as SSEs (e.g., Dragert et al., 2001). Other slow earthquakes are also observed to generate seismic signals. The events that generate seismic signals in a range of $\sim 2-8$ Hz are commonly referred to as tectonic tremors, non-volcanic tremors, or tremors (e.g., Obara, 2002). Initially, tremors were detected as a burst of seismic energy while not having clear phase arrivals. As tremors became better characterized, people found that tremors consist of numerous

smaller individual events, which are commonly referred to as low frequency earthquakes, or in abbreviation as LFEs (e.g., Shelly, Beroza, & Ide, 2007). In the literature, people often use tremors and LFEs interchangeably. Some slow slip transients are found to generate seismic energy at a frequency band of $\sim 0.01 - 0.1$ Hz. These events are commonly referred to as very low frequency earthquakes, or in abbreviation as VLFEs (e.g., Ito & Obara, 2006; Ghosh et al., 2015). Although the different events are observed in different frequency bands, they are often observed to occur concurrently. In particular, tremors are now thought to be capable of representing SSE rupture fronts (e.g. Obara & Kato, 2016; Bürgmann, 2018). Since the naming is purely based on the types of signals, these different "events" might still correspond to the same fault slip process, while just manifesting at different portions of the ground motion spectrum.

Obviously, these slow earthquakes are different from fast earthquakes. Many slip characteristics of a slow earthquake (probably except for individual LFE) are different from fast earthquakes, including low inferred slip rate, low rupture propagation speed, and a low ratio of seismic radiation to earthquake moment. These differences are significant enough that they may not be attributed to the internal variability of fast earthquakes. As slow earthquakes have become better characterized in the past 20 years, these first-order differences have been better quantified (see reviews in Obara & Kato, 2016; Bürgmann, 2018; Obara, 2020; Behr & Bürgmann, 2021, and the references therein). At this point, it is clear that the sudden fault strength drop model alone may not explain slow earthquake characteristics well. Modifications and development are needed in order to extend our understanding of fast earthquakes to slow earthquakes. This will be the main topic of this

dissertation.

1.3 Structure of this dissertation

My dissertation will demonstrate a theoretical model to explain the first-order geophysical observations of slow earthquakes. In Chapter 2, I demonstrate how fast earthquakes may be explained with a sudden fault strength drop model, and how slow earthquakes deviate from the model predictions. In Chapter 3, I review existing theoretical models to explain slow earthquakes. In Chapter 4, I show with analytical analysis that a "frictional-viscous mixing" model can simultaneously explain a variety of slow earthquake observations. In Chapter 5, I use numerical dynamic rupture simulations to validate the analytical analysis in Chapter 4. Chapter 6 is the Discussion section, in which I discuss the tectonic implications of my model, provide model predictions, and compare my model with existing models.

a

Chapter 2

Difference in source parameters between fast earthquakes and slow earthquakes

For a long time in human history, the cause of earthquakes was not understood. The idea that earthquakes represent a sudden release of accumulated stress was not documented until the early 20th century during the research on the 1906 San Francisco earthquakes led by Harry Fielding Reid (Reid, 1910). His results led to the elastic rebound theory, in which stress and strain accumulate gradually over a long period and are then released during an earthquake by sudden slip along the fault. This pioneering theory, though derived from limited observations, has been extensively validated in the following century, and has now been widely accepted as the primary cause of earthquakes in the crust. In particular, the first-order kinematic features of fast earthquake co-seismic ruptures, such

as rupture speed, slip rate, and rupture duration, can be quantitatively explained with a sudden stress drop mechanism.

However, as we will show in the later sections, slow earthquakes have kinematic features that are largely different from fast earthquakes. It means that only considering a sudden stress drop cannot explain the slow earthquake characteristics. In the following texts, I am going to list some first-order differences between slow earthquakes and fast earthquakes. Due to the scope of this chapter, I will focus on the characteristics of slow slip events, and only mention other types of seismic slow earthquakes whenever it is necessary. Also, I would only discuss the single event characteristics. The stress accumulation process in the inter-seismic period is not explicitly considered here (pre-stress conditions before the rupture is not a variable in the model). The inter-event process will be qualitatively discussed in Chapter 6.1.

2.1 Static shear stress drop

Although it is still challenging to resolve the detailed spatial-temporal evolution of stress on the fault, estimating the bulk static stress drop in first-order is now common practice for earthquakes. Usually, the static stress drop $\Delta\tau_s$ is estimated using the following equation,

$$\Delta\tau_s = C\mu\frac{D}{L} \tag{2.1}$$

in which μ is shear modulus, D is the characteristic slip on fault, L is the characteristic length of the slipping area. C is a constant that depends on the shape of the slipping area,

the free surface boundary condition, and how L and D are defined in the specific case (for example, whether D is the maximum slip or the average slip).

Static stress drop can be estimated by measuring the parameters on the right-hand side. C can be theoretically derived. It is found to have a value of around 1 in most cases and its variation almost never exceeds an order of magnitude. Shear modulus μ can be measured from lab experiments by deforming rock samples. It is a pressure- and temperature- dependent quantity; yet, for the depth range we care, it is of the order of 10^{10} Pa, and a characteristic value of 3×10^{10} Pa is commonly used. Fault characteristic slip D and length L can be measured in different ways. The most direct way is to use the near-field geodetic data, which can constrain both D and L independently.

If good near-field geodetic data is not available, one may take a somewhat indirect approach using only seismic records. This approach utilizes the fact that seismic moment M_0 has a relation with the spatial average fault slip D as,

$$M_0 = \mu D A \tag{2.2}$$

in which A is the fault area and should be proportional to L^2 for most earthquakes except for those large earthquakes that saturate the seismogenic depth. This exception is important on its own but should not affect our first-order analysis here. If we assume $A = L^2$ and substitute equation (2.2) to (2.1), we have,

$$\Delta\tau_s = C\frac{M_0}{L^3} \tag{2.3}$$

Using equation (2.3), the parameters that need to be measured change from D and

L to M_0 and L. With only seismic records, the seismic moment M_0 of an earthquake can be measured from the long period seismogram within the framework of representation theory (e.g., Aki, 1966, 1967; Aki & Richards, 2002). L can be measured with many different approaches. One common approach is to use the aftershock distribution and assume that it represents the rupture area (e.g., Kanamori & Anderson, 1975). Another common approach is to use the time information in co-seismic seismograms. Theoretical models have suggested that L can be related to the event duration T or body wave phase corner frequency f_c (e.g. Brune, 1970; Shearer, 2019). Both these two seismological estimations of $\Delta\tau_s$ can have large uncertainty in terms of the actual value, since $\Delta\tau_s$'s dependence on L is cubical and the estimation of L can be quite uncertain due to the difficulty in defining the aftershock zone or measuring the time information in a seismogram. Nevertheless, a first-order estimation (i.e., estimation in logarithm scale) should still be reasonably accurate.

In general, static stress drop is now found to be a "constant" for fast earthquakes in a wide range of magnitude, although a large variation of 3 orders of magnitude exists (e.g., Kanamori & Anderson, 1975; Allmann & Shearer, 2009; Shearer, 2019). Though being large, this stress drop variation doesn't appear to systematically depend on any specific parameters (e.g., Allmann & Shearer, 2009). Most earthquakes have comparable static stress drop of $10^0 \sim 10^1$ MPa. Slow earthquakes, however, are found to have static stress drop significantly lower than the value that is typical for fast earthquakes (e.g., Obara & Kato, 2016; Bürgmann, 2018, and the reference therein). The most direct evidence comes from the geodetic measurement of slow slip events. They usually have centimeter-order of slip over several tens of kilometers, yielding a typical SSE shear strain relief of about

$10^{-7} \sim 10^{-6}$ and static stress drop of about $10^3 \sim 10^4$ Pa ($1 \sim 10$ kPa). Other types of slow earthquakes that are detected with seismological methods (e.g., low frequency earthquakes, very low frequency earthquakes) could have low static stress drop as well, although such an estimation could be tricky. All the seismological categorized slow earthquakes are detected in a narrow frequency range. Besides, as we mentioned earlier, estimating static stress drop from seismograms requires many assumptions. Whether these assumptions are valid for slow earthquakes as well has not been thoroughly tested to the best of my knowledge.

I note that, even not considering slow earthquakes, understanding why a fast earthquake would have a MPa level of shear static stress drop is problematic enough, because a typical lithostatic stress level could well be above 100 MPa at a representative earthquake depth of $\sim$ 10km. Many potential mechanisms have been proposed to explain the apparent low shear static stress drop, including an extremely low friction coefficient, non-optimized fault orientation compared to stress tensor, high pore fluid pressure, fault roughness, and so on. What mechanism leads to such an apparent "weak fault" is still an open question. Nevertheless, since slow earthquakes have static stress drop that is even significantly lower than fast earthquakes by about two orders of magnitude, there should probably be an additional mechanism that accounts for the extra low static stress drop in slow earthquakes.

2.2 Slip rate during slip transients

2.2.1 Explaining the $\sim$ m/s co-seismic slip rate in fast earthquakes

Estimating slip rate during a fast earthquake rupture requires good seismic records. Such investigations became possible in the late 20th century as the increasing number of

seismic stations that captured earthquakes in good quality. Although great uncertainty still exists, it is now commonly observed that fast earthquakes rupture have a characteristic slip rate of 10^0 m/s. This characteristic value can be explained with a simple "sudden stress drop" model as illustrated in Figure 2.1. Figure 2.1a shows a fault that is about to rupture. Right near the fault, the elastic loading shear stress τ_{elastic} equals the fault strength (resistance) f. Right before the rupture, $\tau_{\text{elastic}} = \tau_0$ and $f = f_0$.

Rupture starts when there is a sudden drop of fault strength. There are already many quantitative relations that are applied in co-seismic earthquake models to describe the sudden strength drop process, such slip- or time-weakening, rate-and-state friction, strong-rate weakening caused by flash heating, thermo-pressurization, and so on (Scholz, 2019, and the reference therein). Determining which "friction laws" or weakening mechanisms account for the strength drop process has important implications for understanding not only earthquake rupture dynamics but also earthquake cycle mechanisms. However, in the first-order analysis here, I treat the strength drop as almost "immediate" for fast earthquakes because the fault weakening process is usually considerably shorter than the slip duration.

Let's say that fault strength "immediately" drops from f_0 to f_1. The fault starts to slip and the slip rate is V. Even if the strength drop $f_0 - f_1$ happens immediately (or during a very short time), slip cannot speed up without limit due to the immediate damping response from the surrounding block, and V would be confined within a certain bound. Let say during the incremental time Δt right after the rupture, the fault has an incremental slip $\Delta D = V\Delta t$. Due to the limited wave speed, the information of this shear movement only propagates out within a range $\Delta L = \beta\Delta t$, where β is the shear wave speed (Figure

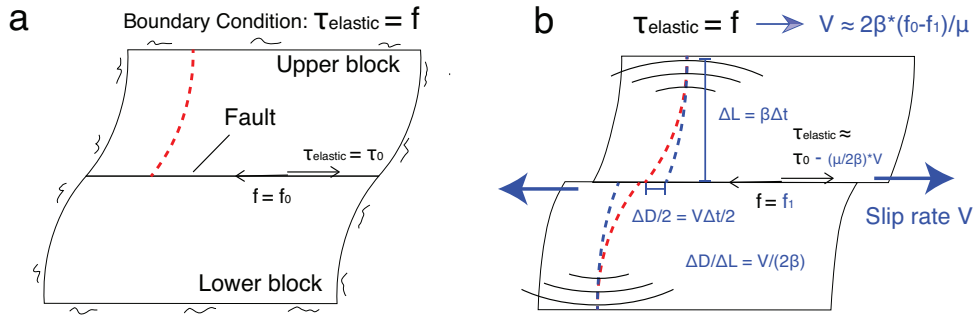

Figure 2.1: 2D schematics that illustrate how to estimate the co-seismic slip rate to first-order by considering the radiation damping effect. **(a)** A fault that is about to rupture. The red dash line shows the strain accumulation near the fault. The tectonic loading stress τ_{elastic} right near the fault should equal the resistance stress from fault f. We denote that $\tau_{\text{elastic}} = \tau_0$ and $f = f_0$ right before the slip starts. **(b)** That fault in (a) suddenly starts to slip because the fault strength (resistance) suddenly drop from f_0 to f_1. The reduction of shear strain in an incremental time Δt is shown with the blue dashed line. The incremental slip on fault $\Delta D = V\Delta t$. Due to the limited wave speed, the shear movement only propagates within a range $\Delta L = \beta\Delta t$, with β as the shear wave speed. Therefore, there is a sudden decrease of elastic loading stress $-(\mu/2\beta)V$ on the fault due to a sudden reduction of shear strain $\Delta D/\Delta L = V/(2\beta)$. The effect of this sudden decrease of elastic loading stress is commonly referred to as "radiation damping" or "shear impedance", which captures the first-order elastic response from the medium. Considering that $\tau_{\text{elastic}} = f$ on fault, the slip rate in response to a sudden fault strength drop can be estimated as $V \approx 2\beta \cdot (f_0 - f_1)/\mu$.

2.1b). Therefore, the elastic loading strain near fault will experience a drop of $\Delta D/\Delta L$, which leads to a decrease of stress on fault,

$$\begin{aligned} \Delta\tau &= -\mu\frac{\Delta D}{2\Delta L} \\ &= -\frac{\mu}{2\beta}V \end{aligned} \tag{2.4}$$

This slip rate dependent elastic stress response is commonly referred to as the radiation damping effect (e.g., Rice, 1993; Zheng & Rice, 1998), or instantaneous traction response in some dynamic rupture modeling research that use Boundary Integral Equation Method (e.g., Cochard & Madariaga, 1994; Tada, 2005). The elasto-dynamic system requires a boundary condition that $\tau_{\text{elastic}} = f$, so the instance change of elastic loading shear stress $\Delta\tau$ should equal the change of fault strength,

$$-\frac{\mu}{2\beta}V = f_1 - f_0$$

which yields the slip rate,

$$V = 2\beta \cdot \frac{f_0 - f_1}{\mu} \tag{2.5}$$

We may use equation 2.5 to estimate fault slip rate. We assume the dynamic stress drop $f_0 - f_1$ has a similar order of magnitude as the static drop σ_s and is about 10^6 to 10^7 Pa, μ is about 10^{10} Pa, and β is about 10^3 m/s. Substituting them into equation 2.5, we can estimate that fault slip rate,

$$
\begin{aligned}
V &\sim 2 \times 10^3 \times \frac{10^6 \text{ to } 10^7}{10^{10}} \text{ m/s} \\
&\sim 10^{-1} \text{ to } 10^0 \text{ m/s}
\end{aligned}
\tag{2.6}
$$

Equations 2.5 and 2.6 indicates that, if stress drop is "magnitude-invariant" for all earthquakes, we may expect the characteristic slip rate V to be "magnitude-invariant" as well, and a typical value should be 10^{-1} to 10^0 m/s if the stress drop is 10^6 to 10^7 Pa (1 to 10 MPa). This theoretical result, though simple, can successfully explain the slip rate observations by modeling seismograms, and thus is thought to have captured the first-order slip rate features of fast earthquake ruptures.

2.2.2 Abnormally low slip rate in slow slip events

However, the above analysis with sudden stress drop cannot satisfactorily explain the low slip rate in slow earthquakes. Let's use slow slip event as an example. Observations suggest that slow slip events have a character stress drop of $10^{3\sim4}$ Pa. If slow slip events share a similar "sudden strength drop" mechanism as fast earthquakes, using equation 2.5, we would estimate the slip rate for slow slip events to be,

$$
\begin{aligned}
V &\sim 2 \times 10^3 \times \frac{10^3 \text{ to } 10^4}{10^{10}} \text{ m/s} \\
&\sim 10^{-4} \text{ to } 10^{-3} \text{ m/s}
\end{aligned}
$$

This value is significantly higher than the characteristic slip rate of slow slip events, which is 10^{-8} to 10^{-7} m/s. Because the sudden stress drop model is thought to be the classic model for earthquakes, this discrepancy suggests that the characteristic slip rate of slow slip

events is abnormally low. Some additional "slow-down" mechanism is needed in order to explain the characteristic slip rate for slow slip events.

2.3 Rupture propagation speed

2.3.1 Explaining the $\sim$ km/s rupture propagation speed in fast earthquakes

During an earthquake, the slip area does not reach its full size immediately; instead, the slip area gradually grows from small to big as the rupture propagates. How fast the rupture propagates plays an important role in many contexts of earthquake physics. In fast earthquakes, the rupture propagation speed is commonly observed to be about a few km/s, which is comparable to the seismic wave speed. This typical propagation speed value is now well explained with theoretical earthquake models. Earthquake rupture propagates because the slipped portion of the fault causes stress perturbations on the un-slipped potion. The rupture propagation speed is then mainly controlled by how fast the stress transfers in space. Elasto-dynamic theories indicate that there are two types of stress transfer that can be caused by fault slip. One is dynamic stress transfer that is carried by elastic waves, and the other is static stress transfer that is permanent but only significant near the slip. The amplitude of dynamic stress is mainly determined by fault slip rate, while the amplitude of static stress is mainly determined by fault slip.

Both the dynamic and static stress transfer mechanisms should affect rupture propagation speed. However, in fast earthquakes, these two stress transfer mechanisms might both have a characteristic transfer speed similar to seismic wave speed, which explains

why the typical rupture propagation speed for fast earthquakes is a few km/s. Figure 2.2 qualitatively demonstrates how a characteristic transfer speed can be estimated for the dynamic and static stress transfer mechanisms (Figure 2.2(a) and 2.2(b), respectively). Figure 2.2a shows a rupture pulse that propagates on a fault plane front left to right. The level of grayness on the fault indicates fault slip rate.

In the dynamic stress transfer mechanism, the slipping region behind the rupture front sends out elastic waves ahead of the rupture front. The dynamic stress carried by the waves triggers the un-ruptured fault, and causes "chain-reaction". If the rupture propagation is mainly controlled by dynamic stress transfer, a characteristic rupture propagation speed V_{rd} would be similar to a seismic wave speed,

$$V_{rd} \approx \beta \tag{2.7}$$

which is typically a few km/s.

In the static stress transfer mechanism, the transfer speed should mainly depend on fault slip rate and stress drop near the rupture front. In the following, I will show a brief derivation for this argument by considering the static stressing rate ahead of the rupture front. A kinematic version of such derivation can be found in Rubin (2011), which, though different in approach, yields very similar results. Let's look at a 1D profile AA' near the rupture front (dashed line in Figure 2.2a). Figure 2.2b qualitatively plots the slip rate and stress rate along the profile AA'. Let's say the high slip rate zone behind the rupture front has a characteristic length of L_p, the high stressing rate zone ahead of the rupture front (near point B') has a characteristic length of L_s. From an energy conservation point of

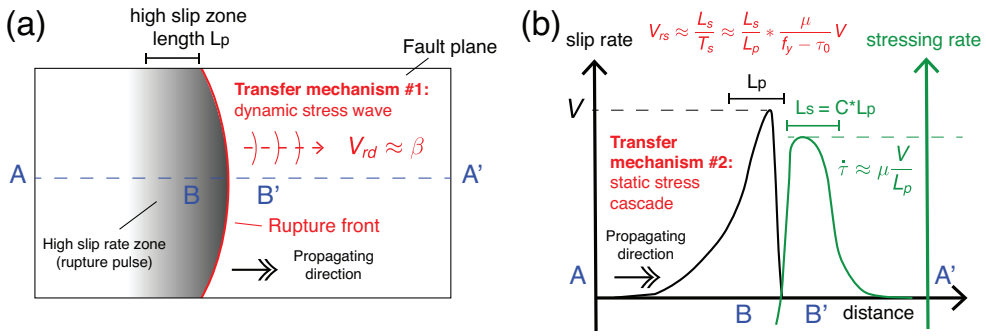

Figure 2.2: Schematics that illustrate two triggering mechanism that affect rupture propagation speed. **(a)** A fault that. **(b)** That fault in (a) suddenly starts to slip because the fault strength (resistance) suddenly drops from f_0 to f_1.

view, L_s should be comparable to L_p ($L_s = CL_p$, and $C \sim 1$), in order for the rupture to propagate stably. Let's next denote V_{rs} as the rupture speed when only the static stress field is driving the rupture propagation. If the loading stress un-ruptured fault ahead of the rupture front takes a time T_s to rise from an initial value τ_0 to the yielding strength f_0, the static stress transfer speed V_{rs} can be approximated as,

$$V_{rs} \approx \frac{L_s}{T_s} \tag{2.8}$$

The stressing time T_s could be estimated by

$$T_s \approx \frac{f_0 - \tau_0}{\dot{\tau}} \tag{2.9}$$

where $\dot{\tau}$ is the characteristic stressing rate ahead of the rupture front. We estimate the stress perturbation ahead of the rupture front as shear modulus μ multiplying the strain across the high slip rate zone D/L_p,

$$\tau \approx \mu \frac{D}{L_p}$$

where D is fault slip. Therefore, the stressing rate $\dot{\tau}$ should be proportional to fault slip rate V as,

$$\dot{\tau} \approx \mu \frac{V}{L_p} \tag{2.10}$$

Substituting equation (2.10) into (2.9), and then substituting the result into equation (2.8), we obtain,

$$V_{rs} \approx \frac{L_s}{L_p} \cdot \frac{\mu}{f_0 - \tau_0} \cdot V \tag{2.11}$$

Let's now use equation (2.11) to estimate the V_{rs} for fast earthquakes. Equation (2.11) yields that the static stress transfer speed should be proportional to slip rate near the rupture front, but to quantitatively estimate V_{rs}, we need to first estimate the strength excess $f_0 - \tau_0$ on the unruptured fault. This can be done more conveniently if we compare it with the static stress drop $\Delta\tau_s$. Let's denote that $f_0 - \tau_0 = S\Delta\tau_s$. The coefficient S here is often referred to as the relative fault strength (e.g., Andrews, 1976). Substituting it into equation (2.11), we have,

$$V_{rs} \approx \frac{L_s}{L_p} \cdot \frac{\mu}{S\Delta\tau_s} \cdot V \tag{2.12}$$

In the last section we have shown that, for a slip instability caused by sudden strength drop, the slip rate should be approximately proportional to the dynamic stress

drop. For convenience, let's denote the dynamic stress drop as $\Delta\sigma_d = f_0 - \tau_0$ in this section, and rewrite equation (2.5) as,

$$V = 2\beta \cdot \frac{\Delta\sigma_d}{\mu}$$

Substitute it into equation (2.12), and consider that $\Delta\sigma_d = (1+S)\Delta\tau_s$, we have,

$$\begin{aligned} V_{rs} &\approx \frac{L_s}{L_p} \cdot \left(1 + \frac{1}{S}\right) \cdot 2\beta \\ &\approx \left(1 + \frac{1}{S}\right) \cdot \beta \end{aligned} \tag{2.13}$$

There are two pieces of information we can directly read from equation (2.13). First, if S is comparable to or significantly larger than 1, V_{rs} would be similar to the elastic wave speed. Second, if S is significantly smaller than 1, V_{rs} would be considerably larger than the elastic wave speed. However, these situations are not all realistic. First of all, S cannot be significantly higher than 1 otherwise the stress perturbation would not be able to provide a high-enough stress increase ahead of the rupture front. Secondly, the static stress transfer speed has an upper bound as elastic wave speed, which means that V_{rs} cannot be considerably larger than β even if S is low. Therefore, even though equation (2.13) explicitly implies a dependency between V_{rs} and S, S should be mostly comparable to or lower than 1, and V_{rs} should always be around the order of β.

To summarize, our analysis above shows that, in a "sudden stress drop" type earthquake model, both the dynamic-stress and the static-stress transfer travel in a speed that is comparable to the elastic wave speed. It explains the prevailing observations that fast earthquake ruptures propagate at a speed around a few km/s.

2.3.2 Abnormally low rupture propagation speed in slow slip events

Although it is still challenging to observe the rupture propagation speed for small seismic slow earthquakes like LFEs or VLFEs, observing the rupture propagation speed for those large slow slip events is possible in many situations. If we assume that the rupture front of an SSE is spatiotemporally colocated with tremors and LFEs, the SSE rupture propagation can then be tracked by locating the seismic slow earthquakes and imaging their migration patterns. It is now found that a typical SSE rupture propagation speed is ~ 10 km/day, or $\sim 10^{-1}$ m/s. Sometimes a main SSE rupture front would trigger secondary rupture fronts that propagate faster in a speed of several to tens of km/h or $\sim 10^{0}$ m/s, which are often referred to as rapid tremor forwards (RTFs), rapid tremor reversals (RTRs), or secondary slip fronts (SSFs).

These rupture propagation speeds are significantly lower than a typical km/s propagation speed in fast earthquakes. Obviously, both the dynamic and static stress transferring speeds shown in equation (2.7) and (2.13) cannot explain this abnormally low rupture speed. It again suggests that a sudden stress drop earthquake model cannot explain SSEs. However, the stress transferring analysis actually still works well even for SSEs. A characteristic SSE slip rate is $10^{-8} - 10^{-7}$ m/s. Since dynamic stress amplitude depends on slip rate while static stress transfer amplitude depends on slip, at such a low slip rate, static stress transfer should be the dominant mechanism that controls the rupture speed. For the derivation from equation (2.12) to (2.13), If we take the abnormally low SSE slip rate as a given condition instead of using equation (2.5), we can estimate the static stress transfer speed V_{rs} as,

$$
\begin{aligned}
V_{rs} &\approx \frac{L_s}{L_p} \cdot \frac{\mu}{S\Delta\tau_s} \cdot V \\
&\approx 1 \times \frac{10^{10}\ \text{Pa}}{1 \times 10^{3\sim4}\ \text{Pa}} \times \left(10^{-8} \sim 10^{-7}\right)\ \text{m/s} \\
&\approx 10^{-2} \sim 10^{0}\ \text{m/s}
\end{aligned}
\tag{2.14}
$$

which is consistent with the observed characteristic SSE rupture propagation speed (e.g., Obara & Kato, 2016; Bürgmann, 2018, and the reference therein).

Equation (2.14) implies a very interesting feature of the static stress transfer rupture propagation mechanism: Since there is a coupling relationship between slip rate and rupture speed, if one can explain the abnormally low slip rate for SSE, the abnormally low rupture propagation speed can be "automatically" explained using the static stress transfer mechanism. This is probably a rationale behind many theoretical models which only focus on explaining the low slip rate feature of SSEs while not going into the details of discussing rupture propagation speed.

I notice that there are some studies that directly use a characteristic speed in a hydraulic framework, such as fluid or pore pressure migration speed, to explain the abnormally low rupture propagation speed in SSEs. This mechanism is possible considering that SSEs slipping zone is often found to be colocated with high pore-pressure zone. Analyzing such a mechanism requires a framework that is very different from the one I set up here, and it will not be discussed in my dissertation.

2.4 Duration T, moment M_0, and their scaling relation

2.4.1 Explaining the $M_0 \propto T^3$ scaling relation in fast earthquakes

Since earthquake duration T can be directly measured from seismograms, this quantity is relatively easy to observe for both small and large earthquakes. Observations show that, to first order, a fast earthquake's duration T increases with its seismic moment M_0, and the scaling relationship is $M_0 \propto T^3$ before the rupture area saturates the seismogenic depth range. A typical Mw6 earthquake would have a duration T of a few seconds. A classic "sudden stress drop" earthquake model can explain this scaling relationship reasonably well. In Chapter 2.1, we have shown that M_0 scales with L^3 if static stress drop is magnitude-invariant. To demonstrate that more clearly, we may re-organize equation (2.3) as

$$M_0 = \frac{1}{C}\Delta\tau_s L^3 \tag{2.15}$$

noting that the special situation where rupture saturates the seismogenic depth is not considered here. An earthquake stops when its slip rate goes back to zero and its rupture stops propagating. Therefore, to first order, earthquake duration T can be estimated as the larger quantity between rupture duration and slip duration,

$$T \approx \max\left(\frac{L}{V_r}, \frac{D}{V}\right) \tag{2.16}$$

where D is final slip, V is slip rate, and V_r is rupture propagation speed. All variables above are characteristic value in first order. For fast earthquakes, we can replace D and V

with expressions of L and β using equation (2.1) and (2.5),

$$\begin{aligned}\frac{D}{V} &\approx \frac{\Delta\tau_s \cdot L}{C \cdot \mu} \cdot \frac{\mu}{2\beta \cdot \Delta\sigma_d} \\ &\approx \frac{\Delta\tau_s}{\Delta\sigma_d} \cdot \frac{L}{2\beta} \\ &\approx \frac{L}{\beta}\end{aligned} \tag{2.17}$$

where we use $\Delta\sigma_d$ instead of $f_0 - f_1$ to represent dynamic stress drop. Since the rupture propagation speed V_r in fast earthquakes is comparable to elastic shear wave speed β, $\frac{D}{V}$ is comparable to $\frac{L}{V_r}$, and equation (2.16) can be written as follows for fast earthquakes,

$$T \approx \frac{L}{\beta} \tag{2.18}$$

Equation (2.18) can explain current earthquake duration observation reasonably well to first order. Besides, by substituting this equation into (2.15), we obtain,

$$M_0 \approx \frac{1}{C}\Delta\tau_s\beta^3 T^3 \tag{2.19}$$

which supports the observed $M_0 \propto T^3$ scaling relation in fast earthquakes.

2.4.2 Abnormally long duration and puzzling moment-duration scaling relation in slow earthquakes

Most slow earthquakes can be categorized into three main types based on the M_0 and T characteristics of their geophysical signals: SSEs that are $\sim$ Mw6 with a duration of days to months, VLFEs that are $\sim$ Mw3 with a duration of tens of seconds, and LFEs that

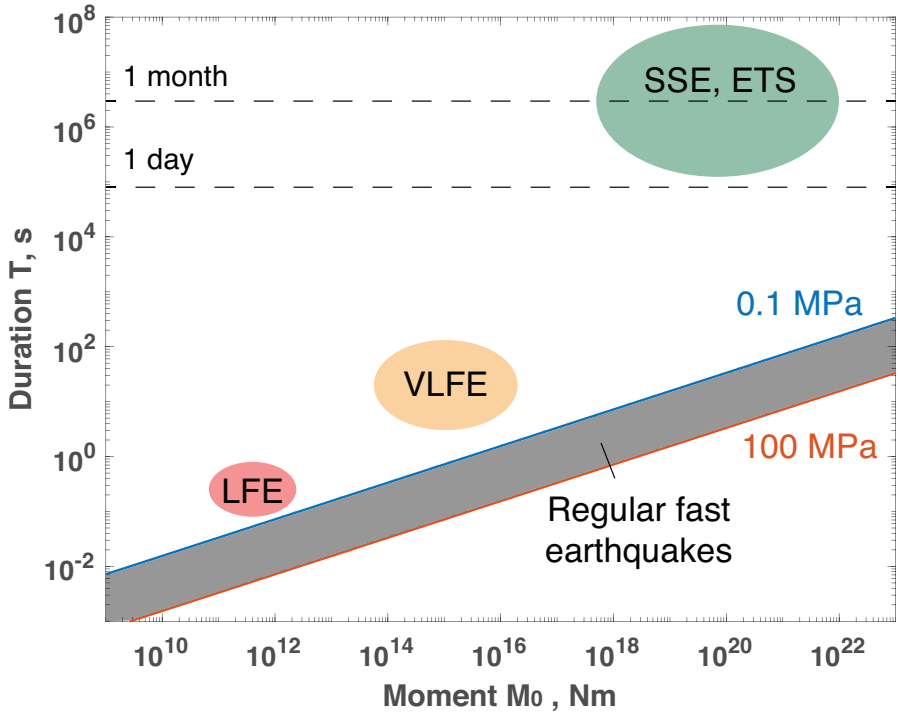

Figure 2.3: Schematic log-log plot that shows the slow earthquake duration T observations versus the corresponding seismic moment M_0. Gray shaded area bounded by two $M_0 \propto T^3$ lines denotes the parameter space of fast earthquakes. The two bounded lines are calculated using equation (2.19) assuming $C = 1$, $\beta = 3$ km/s. $\Delta\tau_s$ is set to be 0.1 MPa for the upper bound (blue line) and 100 MPa for the lower bound (orange line). Ellipse shaded area denotes the approximate location of M_0 and T observations for SSEs and ETSs (green), VLFEs (orange), and LFEs (red).

are $\sim$ Mw1 with a duration of around 1 s. Figure 2.3 shows the approximate location of these three types of slow earthquakes in the moment-duration parameter space. The three types are separated into three different clusters, and all of these events apparently have longer durations than those regular earthquakes that have comparable seismic moment. Because LFEs, VLFEs, and SSEs are often observed in similar locations on faults, some researchers propose that they are fundamentally the same type of slow earthquake, which follows a $M_0 \propto T$ scaling relation (e.g., Ide, Beroza, Shelly, & Uchide, 2007b). However, since these three different categories of slow earthquakes reside as distinct clusters in the "moment-duration" parameter space, some researchers propose that the generation mechanisms of these three categories of earthquake signals are intrinsically different, although they might share the same underlying source process (e.g., Gomberg, Wech, et al., 2016; Luo & Liu, 2021; Behr, Gerya, Cannizzaro, & Blass, 2021). In that case, each category of events should have its own "moment-duration" scaling relation.

So far, deciphering the "moment-duration" scaling relation of slow earthquakes is still challenging and remains an open question. One difficulty comes from the low signal-to-noise ratio of slow earthquake observations. For fast earthquakes, the key source quantities (e.g., slip, slip rate, rupture length, rupture duration, rupture propagation speed) can often be estimated independently from each other using different techniques and data types (e.g., seismogram in different frequencies, geodetic measurements). Therefore, the classic sudden stress drop co-seismic earthquake model can be tested against multiple observations, and has been found to be self-consistent in almost all the cases in first-order (Chapter 2.1, 2.2.1, 2.3.1, and 2.4.1). However, for small seismic slow earthquakes like LFEs and VLFEs,

many key source quantities can not be measured directly due to the limited bandwidth and coverage of their corresponding observations, which makes it difficult to probe its rupture process in detail.

For large slow earthquakes like SSEs, it is possible to constrain different source quantities independently using different geophysical observations, and their source process is better categorized. Using small LFEs and tremors as proxies, we find that the rupture propagation speed for SSEs is around 10 km/day ($10^{-2} \sim 10^{0}$). Geodetic time-series observation suggests that SSEs have a characteristic slip of about 10^{-2} m and slip rate about 10^{-8} m/s ($\sim$ mm/day). The characteristic rupture length L is found to be range around 10^{1} km using either high-frequency seismic observations and geodetic observations. Therefore, scaling relation within SSEs is relatively easy to measure and model. Early observations suggest that SSEs have a close to $M_0 \propto T$ scaling relation (e.g., Gao et al., 2012; Liu, 2014). However, some more recent studies argue that SSEs has a $M_0 \propto T^3$ "moment-duration" similar to fast earthquakes (e.g., Gomberg, Wech, et al., 2016; Michel et al., 2019; Frank & Brodsky, 2019). I include a Figure 2.4 that shows the moment-duration plot in three of the papers mentioned above.

2.5 Summary of the differences in co-seismic rupture between fast earthquakes and SSEs

So far in this section, I have briefly reviewed four characteristics of rupture sources for both fast earthquakes and SSEs. These four characteristics are:

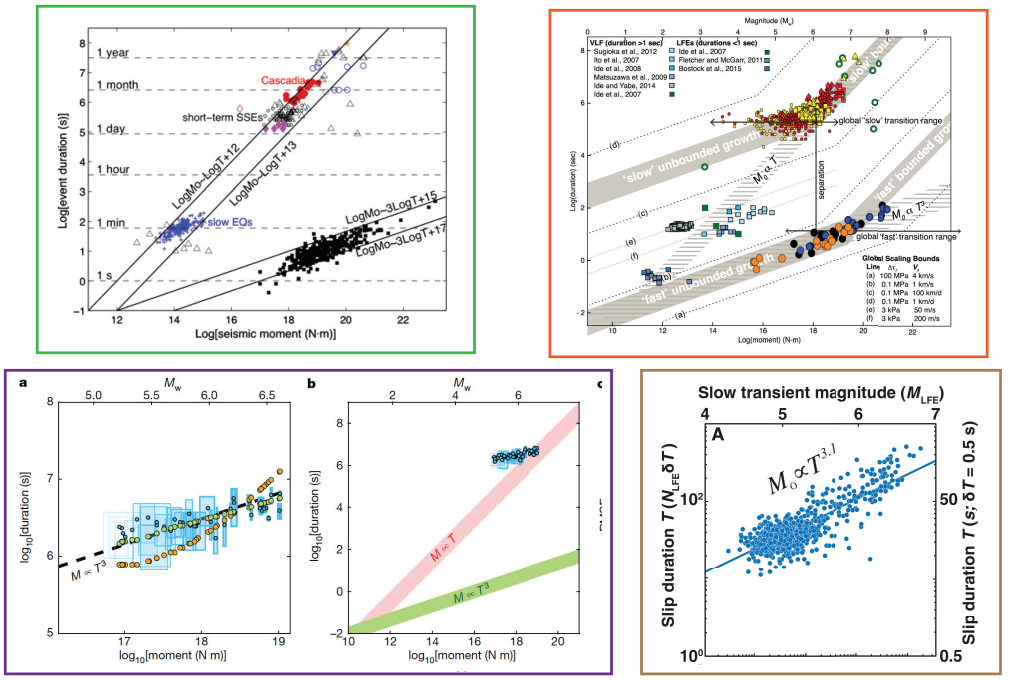

Top left (global): Gao et al., 2012 | Top right (global): Gomberg et al., 2016 | Bottom left (Cascadia): Michel et al., 2019 | Bottom right (Mexico): Frank and Brodsky, 2019

Figure 2.4: Moment-duration observation compilation reported in Gao et al. (2012), Gomberg, Wech, et al. (2016), Michel et al. (2019), and Frank and Brodsky (2019)

1. static stress drop

2. event slip rate

3. rupture propagation speed

4. event duration and moment-duration scaling relation

The quantitative differences of the above four characteristics are summarized in Table 2.1. For fast earthquakes, if we take the observed $\sim$ MPa static stress drop as a given condition and assume that the dynamic stress drop is comparable, a classic sudden stress drop rupture model can self-consistently explain all four characteristics in first order. However, for slow earthquakes, a classic sudden stress drop rupture model would overestimate the slip rate or and rupture propagation speed by several orders even if we take into account that the observed stress drop is $\sim$ 10 kPa. In addition, the durations of SSEs are longer than those of fast earthquakes. Whether the moment-duration scaling relation for SSEs is the same as regular earthquakes is still under investigation. **The purpose of my dissertation is to provide a theoretical model that could address and explain the difference between fast and slow earthquakes.**

I notice that I do mention the small seismic slow earthquakes LFE (tremors) and VLFE here and there while not going into detail. In this dissertation, I will focus on modeling SSEs (Chapter 3, 4, and 5). The model will have implications on those seismic slow earthquakes, which would be discussed in the Discussion chapter (Chapter 6). Also, I did not mention the inter-event characteristics of SSEs (e.g., recurrent interval). Such characteristics will be discussed in Chapter 6 as well.

	fast earthquake	SSEs
Static stress drop	$10^5 \sim 10^7$ Pa, M-invariant	$10^3 \sim 10^4$ Pa, M-invariant?
Slip rate	$10^{-1} \sim 10^0$ m/s, M-invariant	$10^{-8} \sim 10^{-7}$ m/s, M-invariant?
Rupture propagation speed	10^3 m/s, M-invariant	$\sim 10^{-1}$ m/s, M-invariant?
Moment-duration scaling	$M_0 \propto T^3$	$M_0 \propto T$ or T^3?

Table 2.1: Summary of the differences between fast earthquakes and SSE

Chapter 3

Some proposed ingredients to explain the slow behavior in SSEs

In this section, I will briefly review some hypotheses that are proposed to explain the slow behaviors in SSEs and their associated theoretical analysis. Instead of discussing the details of any specific model, I will focus on demonstrating several popular ingredients that are often used in models to make "slow" happen. A model that could reproduce "slow" behaviors may have one or multiple of these ingredients. I aim to use this review to help better illustrate the starting point and novelty of my model which I will present in Chapter 4 and 5. Therefore, even though I will not use some ingredients in my model, I still present them here for the purpose of completeness.

3.1 Making the stress drop less sudden

3.1.1 Elastic stress release during the strength weakening stage

One of the main puzzles that an SSE model needs to explain is why the fault slip rate is abnormally low that it cannot be explained with a classic sudden stress drop model. In Chapter 2.2, we show that if the strength drop is immediate, a radiation damping stress $-\frac{\mu}{2\beta}V$ would arise in response to the sudden strength drop $f_0 - f_1$. Such analysis can explain the "moment-invariant" m/s co-seismic slip rate observations in fast earthquakes. If the transient strength drop in slow earthquakes were immediate as well, assuming that the sudden dynamic strength drop is comparable to the static stress drop (to first order) and a typical static stress drop is ~ 10 kPa, the slip rate V in slow earthquakes would be estimated to be $\sim\ 10^{-3}$ m/s, which is significantly faster than the observed value $10^{-8} \sim 10^{-7}$ m/s.

To achieve a slow slip rate, one way is to make the shear stress drop in a less sudden manner. Depending on the specific fault boundary condition, or "friction law", used in the model, the formulation of the parameters for a less sudden stress drop and slow slip could vary in different cases. For simplicity, let's illustrate this "slow-down" mechanism with a boundary condition formulation of linear slip weakening friction, in which fault strength drops from f_0 to f_1 in a slip weakening distance D_0,

$$\begin{aligned} \Delta f &= -\frac{f_0 - f_1}{D_0} D \\ &= -K_f D \end{aligned} \tag{3.1}$$

in which D is fault slip, Δf is the fault strength change in response to D. For convenience, I denote

$$K_f = \frac{f_0 - f_1}{D_0}$$

as the effective stiffness parameter of strength drop.

While fault slip D increases, the elastic loading shear stress also reduces. Mathematically, the change of loading shear stress $\Delta\tau_D$ due to fault slip can be estimated using an almost identical expression as the static stress drop expression (equation (2.1)), except that the sign is opposite,

$$\begin{aligned} \Delta\tau_D &= -C\mu\frac{D}{L} \\ &= -K_\tau D \end{aligned} \tag{3.2}$$

where C is a geometric factor that is approximately equal to one. C is not affected by the slip process and is determined once the initial and boundary condition is set. μ is shear modulus, and L is the characteristic length of the slip patch. For convenience, I denote

$$K_\tau = \frac{C\mu}{L}$$

as the effective stiffness parameter of elastic shear stress drop.

We may now reconsider our analysis in Chapter 2.2.1. Let's say that there is an incremental fault slip ΔD right after the fault starts to slip. On the fault, the change of fault strength Δf should equal the total change of elastic shear stress $\Delta\tau$,

$$\begin{aligned} \Delta f &= \Delta\tau \\ &= \Delta\tau_D + \Delta\tau_V \end{aligned} \tag{3.3}$$

in which $\Delta\tau_V$ is the elastic shear stress change caused by sudden fault slip rate. I have shown in section 2.2.1 that it can be estimated as $-\frac{\mu}{2\beta}V$ (equation (2.4)). We can then rewrite equation (3.3) as,

$$-K_f \cdot \Delta D = -\frac{\mu}{2\beta}V - K_\tau \cdot \Delta D \tag{3.4}$$

We can solve for slip rate V using the above equation, and we have,

$$V = \frac{2\beta}{\mu}\big(K_f - K_\tau\big) \cdot \Delta D \tag{3.5}$$

Equation (3.5) yields many interesting features. If $K_f < K_\tau$, slip rate V would be negative, and the fault would move backward to accumulate loading shear stress. This solution is obviously unrealistic, as it contradicts our initial assumption that there is a stress drop. The reason why we have this unrealistic solution is that, by having $K_f < K_\tau$, the elastic stress release against slip is faster than the fault strength weakening against slip. Therefore, if the fault strength weakening were to happen, the elastic stress release would be even more than the strength drop. Considering causality, such a sudden stress drop cannot happen. Instead, elastic shear stress will not accumulate, as fault will continuously release the incremental elastic loading stress and be constantly creeping (i.e., undergoing stable slip, even without rate or slip strengthening).

A sudden stress drop, or slip instability, will occur when $K_f > K_\tau$, and slip rate V will be positive. Let's evaluate equation (3.5) at $\Delta D = D_0$ when fault strength has just finished dropping. Fault slip rate V can be expressed as,

$$V = \left(1 - \frac{K_\tau}{K_f}\right) \cdot 2\beta \cdot \frac{f_0 - f_1}{\mu} \tag{3.6}$$

In Chapter 2.2.1, I derive equation (2.5) under the condition that the stress drop is sudden. The sudden stress drop condition can be expressed as $K_f \gg K_\tau$ in equation (3.6). In such case, $\frac{K_\tau}{K_f}$ will be close to zero and equation (3.6) will be close to (2.5), which is shown to explain the slip rate in fast earthquakes reasonably well.

Based on the above analysis, we find that if we want to make a transient slip event while at the same time requiring the fault slip rate to be significantly slower than $2\beta \cdot \frac{f_0 - f_1}{\mu}$, one way is to have K_f larger than K_τ but also comparable to it. In that case, $\frac{K_\tau}{K_f}$ is close to one but still smaller than one, and equation (3.6) would yield a value that is significantly smaller than $2\beta \cdot \frac{f_0 - f_1}{\mu}$. This "slow down" mechanism where K_f is close to K_τ has become a popular ingredient in slow earthquake models. It is sometimes referred to as the "conditionally stable" condition (e.g. Scholz, 2019). Since K_f and K_τ can depend on many parameters, there are multiple ways to realize this mechanism in a specific slow earthquake model. We will briefly demonstrate some common approaches in the rate-and-state friction framework in the following section.

3.1.2 Making K_f close to K_τ in the rate-and-state friction framework

Many models that address slow earthquake issues use a rate-and-state friction law to describe fault strength f instead of a linear slip-weakening friction. The rate-and-state friction law is an empirical relation derived from rock friction experiments (e.g., J. H. Dieterich, 1979; Ruina, 1983). Though derived in laboratories, the rate-and-state friction law

predicts many frictional behaviors that are also commonly observed in natural earthquakes, such as stick-slip behavior, and "Omori-type" aftershock decay (e.g., J. Dieterich, 2007, and the references therein). It has now been widely used in earthquake modeling practice. In a typical rate-and-state friction formulation, fault strength f equals fault normal stress σ_n times the friction coefficient (the same as Coulomb friction),

$$\begin{aligned} f &= \sigma_n \cdot \mu' \\ &= \sigma_n \cdot \left(\mu'_0 + a \ln \left(\frac{V}{V_0} \right) + b \ln \left(\frac{\theta}{\theta_0} \right) \right) \end{aligned} \tag{3.7}$$

here I use μ' to represent friction coefficient to distinguish it from shear modulus μ. μ'_0 is a reference friction coefficient, V_0 is a reference slip rate. θ is state variable and θ_0 is a reference state variable. a and b are two dimensionless parameters that control the contributions of the V-related term and the θ-related term, respectively. A typical value of a and b are about 10^{-3}.

Equation (3.7) is not enough to describe fault strength. State variable θ needs to be described separately using a state evolution law. What specific form of the state evolution law should be used is still an open question, and can depend on the specific application. Here I provide two popular evolution laws that are commonly used: "aging law" and "slip law",

$$\frac{\mathrm{d}\theta}{\mathrm{d}t} = 1 - \frac{\theta V}{D_c} \quad \text{, "aging law"} \tag{3.8}$$

$$\frac{\mathrm{d}\theta}{\mathrm{d}t} = -\frac{\theta V}{D_c} \ln \left(\frac{\theta V}{D_c} \right) \quad \text{, "slip law"} \tag{3.9}$$

in which D_c is commonly referred to as the critical slip weakening distance. These two laws are similar in producing "stick-slip" behaviors to first order, and here I will only focus on their commonalities.

The term $a \ln\left(\frac{V}{V_0}\right)$ increases with slip rate. As shown in equation (3.8) and (3.9), state variable θ has a faster decreasing rate as slip rate increases, so the term $b \ln\left(\frac{\theta}{\theta_0}\right)$ decreases with slip rate. Therefore, $a \ln\left(\frac{V}{V_0}\right)$ and $b \ln\left(\frac{\theta}{\theta_0}\right)$ will compete with each other and the sign of $a - b$ determines whether fault strength decreases or increases as fault slip speeds up: when $a - b < 0$, the fault is referred to as "velocity-weakening" or "rate-weakening"; when $a - b > 0$, the fault is referred to as "velocity-strengthening" or "rate-strengthening". Within the rate-and-state friction framework, a "velocity-strengthening" fault surface cannot have stick-slip behaviors; while, a "velocity-weakening" fault surface can have stick-slip behaviors under certain conditions, as we will discuss below.

Although the "conditionally stable" condition in the earlier section was derived using a linear slip weakening friction, similar model behaviors shall also exist in a rate-and-state friction model. It has been shown that, if a fault is "velocity-weakening", the weakening stiffness K_f of rate-and-state friction should be proportional to $b - a$ and σ_n, and inversely proportional to the critical slip weakening distance D_c,

$$K_f \sim \frac{(b-a)\sigma_n}{D_c} \tag{3.10}$$

Considering that the elastic loading stiffness K_τ is proportional to shear modulus μ and inversely proportional to the characteristic length L of the slip patch,

$$K_\tau = \frac{C\mu}{L}$$

In principle, we may equal K_f and K_τ to find the critical condition of stability. The two above equations suggest that friction parameter ($a-b$, D_c), fault effective normal stress (σ_n), slip patch characteristic size L, and shear modulus μ are affecting this critical condition. Therefore, to facilitate slow slip, a model can create a critical condition through any of the parameters above (though some parameters like D_c and μ are rarely used). On many occasions, this condition is expressed using the L parameter. One may equate K_f and K_τ, and solve for L. For slow slip to occur, L needs to be comparable but not much larger than a critical size L_c,

$$L_c \sim \frac{C\mu D_c}{(b-a)\sigma_n} \tag{3.11}$$

L_c is sometimes represented as h^* instead in the literature. I note that the above derivation uses a "spring-slider" approach; therefore, though correct to first-order, equaling the above two equations may not accurately describe the critical patch size that is needed to nucleate a transient slip event. A more accurate estimate of the critical size L_c can be obtained by considering the transient effects in rate-and-state friction (e.g., Rubin & Ampuero, 2005; Barbot, 2019), and the parameter $\frac{b-a}{b}$ (referred to as R_b in Barbot (2019)) is shown to be important in controlling L_c as well. In that case, L_c need to be written as,

$$L_c = \frac{C\mu b D_c}{(b-a)^2\sigma_n}, \tag{3.12}$$

3.1.3 A brief summary of the "stiffness"-related slow slip mechanism

Many slow earthquake models include the above "stiffness"-related ingredient to facilitate transient slow slip (e.g., Liu & Rice, 2005, 2007; Liu, 2014; Leeman, Saffer, Scuderi, & Marone, 2016; Wei, Kaneko, Shi, & Liu, 2018; Im, Saffer, Marone, & Avouac, 2020). Although similar concepts have been brought up before the emerging observations of slow earthquakes (e.g., Tse & Rice, 1986; J. H. Dieterich, 1992). In summary, a fault should still be able to host transient slip and stress drop ($K_f > K_\tau$). However, the frictional stiffness K_f should only be slightly larger than K_τ. In a rate-and-state framework, this condition is often expressed as a requirement that the characteristic slip area length L be comparable but not much larger than the critical size L_c. Figure 3.1 qualitatively demonstrate how the characteristic length L depends on the shape of the slip patch. For a round shape slip patch, L is better approximated by its diameter; while for a long narrow slip patch, L is better approximated by its width. SSEs are often modeled as long narrow rupture (e.g., Liu & Rice, 2005; Dal Zilio, Lapusta, & Avouac, 2020). When SSEs are modeled as the latter case, the key parameter to tune would be the ratio between slip patch width W and L_c, which is often denoted as W/h^* in the literature.

Within a certain parameter space, the above setup can reproduce many slow earthquake observations. Though successful in many situations, this mechanism to create transient slow slip naturally requires the parameter set to reside in a range that is much narrower than regular both fast earthquakes ($K_f \gg K_\tau$) and constant creep ($K_f > K_\tau$), because K_f needs to smaller than K_τ while very close to it ($K_f \approx K_\tau$). Whether such a narrow range can be applied to the increasing amount of slow slip observations is still a field of active

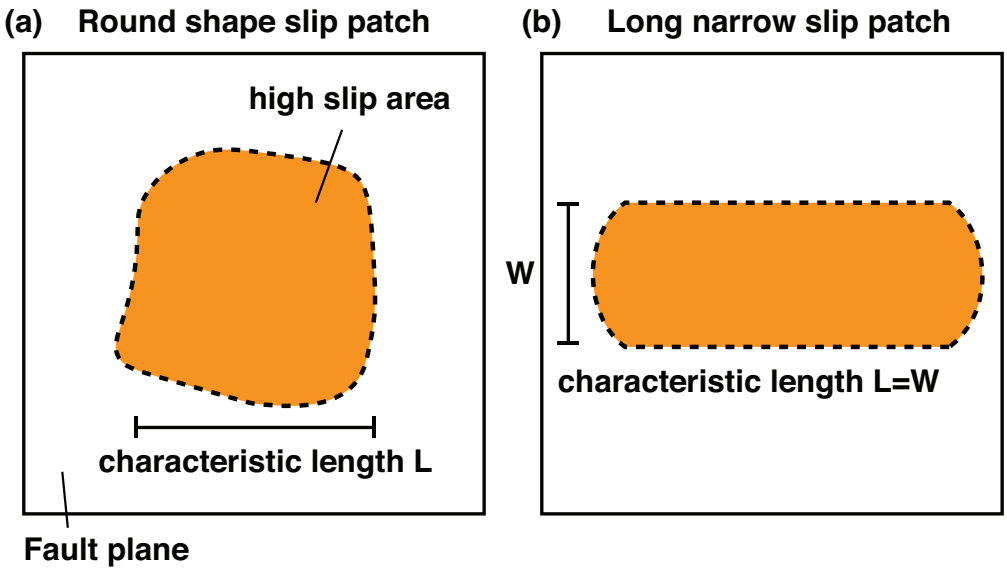

Figure 3.1: Schematic showing the characteristic length L for (a). round shape slip patch and (b) long narrow slip patch. The slip patch area is denoted by the orange shading. L for a round shape slip patch is better approximated with its diameter, while L for a long narrow slip patch is better approximated with its width W.

research.

3.2 Interrupting the stress dropping process as slip rate reaches a certain level

Another commonly used ingredient to quench slip acceleration is interrupting the stress-dropping process as slip rate reaches a certain level. We will briefly introduce two ways to realize the quenching: introducing a cut-off factor in state variable and dilatant strengthening.

3.2.1 A cut-off factor in the state variable

In a rate-and-state framework, quenching slip acceleration can be realized by introducing a constant C in the state variable terms (e.g., Shibazaki & Iio, 2003; Hawthorne & Rubin, 2013),

$$f = \sigma_n \cdot \left(\mu_0' + a \ln \left(\frac{V}{V_0} \right) + b \ln \left(\frac{\theta}{\theta_0} + C \right) \right) \tag{3.13}$$

At slow slip rates, $\frac{\theta}{\theta_0} \gg C$ and the above formulation would have the same behavior as a classic rate-and-state formula. When $a - b < 0$ and $K_f > K_\tau$, transient slip can happen on fault, and slip will accelerate. As slip rate reaches a certain level, $\frac{\theta}{\theta_0}$ would be smaller than C and $b \ln \left(\frac{\theta}{\theta_0} + C \right)$ would cease to decrease. After that, fault friction would switch from "velocity-weakening" to "velocity-strengthening", and the sliding speed is then limited at that level.

Such a model setup to cut off the state variable's influence on stress as slip rate goes high can reproduce some slow slip behaviors as observed. Yet, up till this point, it is more like an artificial "design" in the friction law to slow down slip rather than a physical mechanism. Some evidence about the existence of the constant C in laboratory experiments has been mentioned (James Dieterich, SCEC 2018 plenary talk and personal communication), but is not documented in the literature to the best of my knowledge.

3.2.2 Dilatant strengthening

Another mechanism that is often used to quench slip acceleration is the "dilatant strengthening" mechanism (e.g., Segall, Rubin, Bradley, & Rice, 2010; Liu & Rubin, 2010;

Liu, 2013). Considering a hydraulic system in a fault zone, the effective normal stress on a fault would also depend on the pore pressure P,

$$f = (\sigma_n - P) \cdot \left(\mu_0' + a \ln \left(\frac{V}{V_0} \right) + b \ln \left(\frac{\theta}{\theta_0} \right) \right) \tag{3.14}$$

As slip rate increases, pore space may increase due to a dilatant effect. As a consequence, pore pressure P would decrease, causing an increase of fault strength f. This dilatant strengthening effect eventually helps stabilize fault slip, preventing a seismic slip rate from being reached. Since abundant observations have suggested that the SSE-hosting fault may contain a considerable amount of fluid (e.g., Bürgmann, 2018, and the references therein), such a mechanism could well be possible intuitively. Yet, the hydraulic parameters near-fault are extremely difficult to measure. At present, it is still an open question to what extent this mechanism should account for slow slip phenomena.

3.3 Imposing stress on a stably sliding fault and fault heterogeneity

So far, the "slow-down" ingredients I have introduced have focused on stabilizing fault slip as fault strength weakens. In other words, fault still needs to be able to host transient slip and stress drops as in fast earthquakes; however, the transient slip is slow because the fault strength weakening processes are not fast enough either due to a faster elastic stress release (Chapter 3.1) or an interruption in the weakening process (Chapter 3.2).

There is another approach that does not require the transient stress drop itself

to be slow in order to produce slow slip. If there is a mixture of both sudden stress drop and viscous components on a fault, slow slip behavior can also emerge. This vision is generally supported by the growing body of geological observations of exhumed faults (e.g. Kirkpatrick, Fagereng, & Shelly, 2021; Behr & Bürgmann, 2021, and the references therein). Many theoretical models that were designed with this vision show potential of generating slow slip behaviors. However, compared to the two "slow-down" ingredients explored above, the exploration of this ingredient is still in an early stage. Ways to incorporate such a "heterogeneity" vision are not exclusive. Besides, the quantitative relations between model parameters and the target geophysical observations are still elusive. In the following section, I will review the recent investigations on this alternative "slow-down" ingredient that based on a "heterogeneity" vision. This ingredient is also the major component in the models of this dissertation.

3.3.1 The general concepts

Slow slip can originate when a stress perturbation is imposed on a "viscous" fault. For that to happen, "sudden stress drop" and "viscous" components should coexist on the fault and correspond to separate physical processes. Recently, this hypothesis has been receiving more attention in the context of slow earthquakes, as there is emerging geological evidence suggesting that slow slip shear zones contain both brittle (or frictional) and viscous deformation (e.g., Fagereng & Sibson, 2010; Sibson, 2017; Platt, Xia, & Schmidt, 2018; Phillips, Motohashi, Ujiie, & Rowe, 2020; Behr & Bürgmann, 2021; Kirkpatrick et al., 2021). Many mechanisms have been proposed for both type of deformation. Proposals for brittle deformations include: (1) frictional instabilities on the localized fracture within or at the

boundary of the strong clasts or grains within the shear zone, (e.g., Fagereng & Sibson, 2010; Sibson, 2017; Phillips et al., 2020), (2) viscous flow instabilities in the shear zone, (e.g., Platt et al., 2018) (3) transient pore pressure change (e.g., Shapiro, Campillo, Kaminski, Vilotte, & Jaupart, 2018). Proposals for viscous deformation include cataclastic flow, pressure solution creep, and other types of viscous flow (e.g., Bürgmann, 2018; Kirkpatrick et al., 2021; Behr & Bürgmann, 2021, and the references therein)

To test the above revision against geophysical observations, one needs to incorporate it into a fault rupture model and calculate the resulting ground deformation. Generally speaking, such a vision can be realized by setting up a heterogeneous fault with a mixture of both "sudden stress drop" and "viscous" components (e.g., Ando, Nakata, & Hori, 2010; Nakata, Ando, Hori, & Ide, 2011; Ando et al., 2012; Skarbek, Rempel, & Schmidt, 2012; Lavier, Bennett, & Duddu, 2013; Luo & Ampuero, 2018; Goswami & Barbot, 2018; Beall, Fagereng, & Ellis, 2019; Luo & Liu, 2021; Lavier, Tong, & Biemiller, 2021; Behr et al., 2021). The "sudden stress drop" component causes a sudden stress perturbation on the "viscous" component, and the slip rate on "viscous" component temporally increases in order to relax the extra stress. The magnitude of the resulting slip transient and its relaxation time depend on both the stress perturbation and the viscous property.

3.3.2 Parameterizing the shear zone process as a fault constitutive relation

Although the concept is simple, implementing both brittle and viscous properties together in a rupture model can be non-trivial. Before we go into the details of setting up the heterogeneities in models, it would be convenient that we first go through the rationales

of parameterizing a shear zone as a zero-thickness fault "surface" in rupture models.

Ideally, we want to model the large-scale slow slip ruptures that propagate several tens of kilometers on megathrust as well as the small-scale interaction between the brittle and viscous components within the few hundred meters wide shear zone. However, such a complex dynamic system is very difficult to model due to the multiple orders of magnitude of the length scale and the technical difficulties in incorporating the finite thickness of the fault zone. Even though some exciting efforts have been made to capture the full dynamics of the system in the same model (e.g., Lavier et al., 2021; Behr et al., 2021), most models at the current stage would separate the small-scale process in the shear zone from the large-scale rupture propagation by parameterizing the bulk shear zone deformation as fault slip, as shown in Figure 3.2. In this simplification, fault zone width W is considered to be significantly smaller than both the rupture length and source-instrument distance, and the detailed strain and stress distribution within the fault zone are thought to have minor effects on both the rupture dynamics and on the generation of ground deformation. Therefore, we may simplify the fault zone in Figure 3.2a as a zero thickness fault plane in a rupture model. The relationship between the tractions at the shear zone boundary and the bulk shear deformation is then parameterized as the fault constitutive relation on the hypothetical fault "surface".

Such a "pseudo-3D" approach is suggested to be reasonable as long as the "friction law" approximates the bulk strain release behavior and energy budget in fault zones (e.g., Andrews, 1976, 2005). Since most geophysical signals of earthquakes are mostly related to the large-scale rupture process, this "pseudo-3D" approach is very useful in probing the

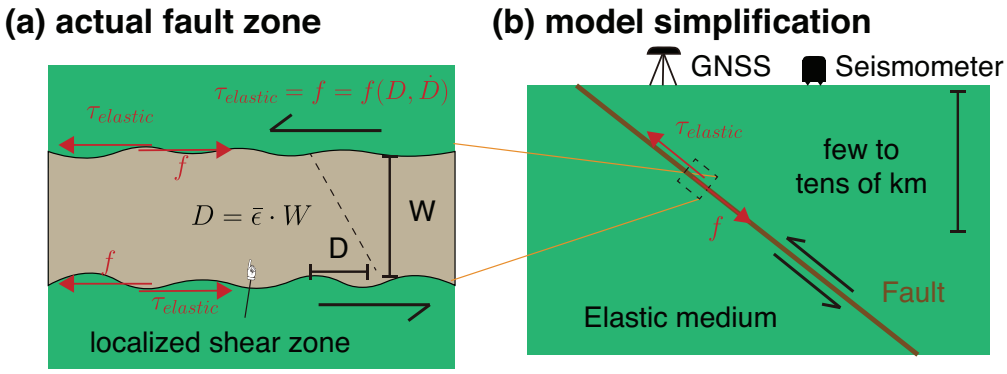

Figure 3.2: Schematics that demonstrate how a fault zone with a finite thickness W is simplified as a zero-thickness fault surface in theoretical models. (a) Diagram of a fault shear zone. Green area is the elastic medium, and the black arrows show the moving direction of the medium. Brown area is the localized shear zone within which rocks deform inelastically. Tractions on the boundaries of the fault zone are marked with red arrows. The elastic loading traction should equal the shear resistance at the fault zone boundary, which may depend on both the bulk slip D and bulk slip rate $\dot{D}$ of the fault zone. (b) Diagram of a simplified zero-thickness fault "surface" in theoretical models. The whole rupture extent and the distance between source and observation should be considerably greater than the fault zone width W.

bulk deformation condition in the shear zone. I note that fault constitutive relations are often also referred to as "friction laws" in the literature, probably because the fault zone in many models is typically parameterized as a zero thickness fault "surface". The "friction law" terminology would be literally correct if the frictional force is the major resistance in the fault zone. However, the term "fault boundary constitutive relation" has a more generalized usage, as it can contain not only frictional resistance but also other types of shear resistance in a fault zone, such as viscous resistance caused by the ductile deformation in the shear zone matrix. To avoid confusion, in the subsequent text, I refer to the fault boundary constitutive relation (generalized friction law) as "friction law" with quotation marks.

Figure 3.3 shows four types of fault constitutive relations that are used in earth-

quake rupture models. The first one is the "only frictional" relation (Figure 3.3a), where only frictional forces are considered. Slip-weakening and rate-and-state friction are two commonly used friction formulations. As we discussed in the previous sections, a sudden frictional resistance drop can explain the first-order fast earthquake features reasonably well (Chapter 2). If the frictional strength drop against fault slip is not sudden enough compared to the unloading of elastic stress, slow slip behavior may emerge (Chapter 3.1). Figure 3.3b shows another type of fault constitutive relation that only has viscous resistance. In this case, fault effective strength increases as the bulk slip rate increases (being rate-strengthening), and cannot suddenly drop by itself; yet, the fault can still slip if there is an either steady or sudden external elastic stress increase. The viscous response could reflect the distributed viscous flow in the shear zone matrix, which might have micro-scale deformation mechanisms such as dislocation creep, cataclastic flow, pressure solution creep, or so on. It is worth noting that the "only viscous" fault constitutive relation can be, and is often, realized within a rate-and-state friction framework by setting $a - b > 0$. It can reflect a vision that the shear zone matrix deformation is achieved by cataclastic flow where there is "velocity-strengthening" frictional sliding between gouge fragments and fragments crushing (e.g., Perfettini & Avouac, 2004; Bürgmann, 2018).

In the wide fault zones that are proposed to host slow earthquakes, both the frictional resistance that can suddenly drop and the viscous resistance that is velocity-strengthening may co-exist in the shear zone. Therefore, the fault constitutive relation of the bulk fault zone could contain both frictional and viscous resistance components. Figure 3.3c and 3.3d show two end-member ways to include both components in the fault

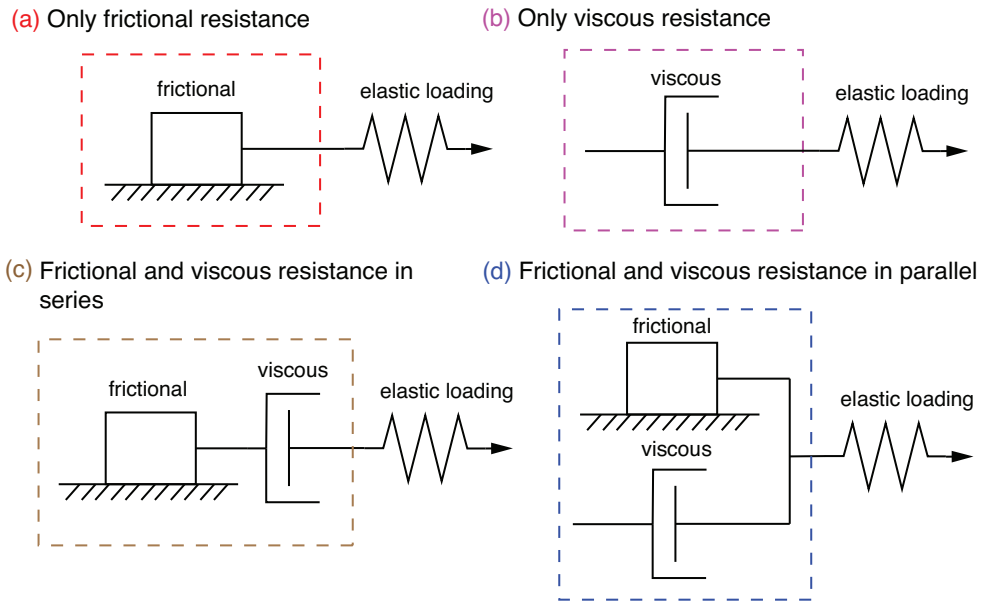

Figure 3.3: Four typical fault constitutive relations used in rupture modeling. (a) "only frictional" relation, where only frictional force is considered. (b) "only viscous" relation, where only viscous force is considered. (c) Friction and viscous resistance both exist and are in series, where the total shear deformation is partitioned into frictional slip and viscous slip. (d) Friction and viscous resistance both exist and are in parallel, where the resistance (or traction) is partitioned into frictional resistance and viscous resistance.

constitutive relation: one is to have the two components in series, where the total shear deformation is partitioned into frictional slip and viscous slip (Goswami & Barbot, 2018); the other is to have the two components in parallel, where the resistance (or traction) is partitioned into frictional resistance and viscous resistance (Ando et al., 2010; Nakata et al., 2011; Ando et al., 2012; Lavier et al., 2013; Beall et al., 2019). Although which end-member setup better represents the actual fault deformation is still unclear, both these two setups are shown to have potential in explaining slow slip behaviors. In my dissertation, I will explore the second end-member, where the fault resistance is partitioned. More discussion of this "friction law" will be made in Chapter 4.

3.3.3 Two types of heterogeneity setup

Within the framework of this "pseudo-3D" approach, there are at least two major ways of parameterization to include the heterogeneity of both "sudden stress drop" and "viscous deformation" (Figure 3.4). One is to have a fault constitutive relation that contains both frictional and viscous resistance as we discussed in section 3.3.2 (Figure 3.3c and 3.3d). In this type of setup, heterogeneities are parameterized in the fault constitutive relation (or "friction law"). Therefore, the "friction" parameters on the fault "surface" do not need to be explicitly heterogeneous (Figure 3.4a).

Another way to create heterogeneities is to distribute different "friction" parameters on the fault "surface". It can be normally achieved by separating fault surface as a mosaic of "sudden-stress-drop-bearing" area and "stable-sliding" areas as shown in Figure 3.4b. If one uses rate-and-state friction as the "friction law", the "sudden-stress-drop"

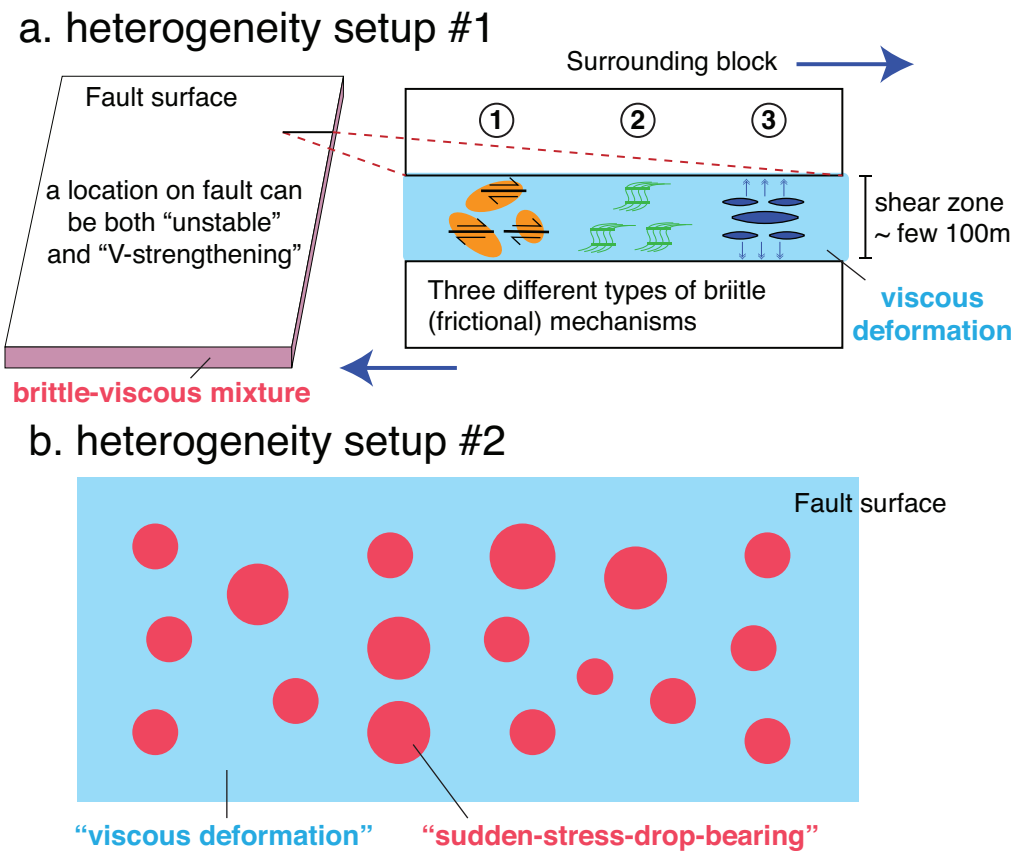

Figure 3.4: Two possible types of heterogeneity setups to realize a “brittle-viscous” mixture. (a) Each location on fault can be both “sudden-stress-drop-bearing” and “viscous”. It represents a physical vision that a fault zone has a finite width, and both brittle (or frictional) and viscous deformation exist and are mixed in the shear zone. The right schematic demonstrates four hypothetical mechanisms that are brought up to explain the brittle deformation in the shear zone that host slow slip: 1. frictional instabilities on the localized fracture within or at the boundary of the strong clasts or grains within the shear zone, 2. viscous flow instabilities in the shear zone, 3. transient pore pressure change. (b) A mosaic fault surface of “viscous deformation” (blue) area and “sudden-stress-drop-bearing” area (blue).

area can be set as "velocity-weakening" ($a - b > 0$), while the 'viscous" area can be set as "velocity-strengthening" ($a - b < 0$) (Skarbek et al., 2012; Luo & Ampuero, 2018; Luo & Liu, 2021). Basically, it is equivalent to having a mosaic pattern of the "only frictional" resistance (Figure 3.3a) and "only viscous" resistance (Figure 3.3b) across the fault "surface".

These two types of heterogeneity setup are not exclusive to each other. Intuitively, it is natural to assume that an implicitly heterogeneous "friction law" and an explicitly heterogeneous "friction" parameters distribution might co-exist. Models have tested where everywhere on a fault has a viscous response to slip rate, while the "sudden-stress-drop-bearing" area is set to have a positive stress drop and linear slip weakening, and the surrounded "viscous" area is set to have zero stress drop (Ando et al., 2010; Nakata et al., 2011; Ando et al., 2012). It is equivalent to having a mosaic pattern of the "frictional and viscous in parallel" resistance (Figure 3.3d) and "only viscous" resistance (Figure 3.3b) across the fault "surface".

In summary, many flavors of heterogeneity setups have been proposed in the current stage, and they all seem to have potential in generating slow slip behavior. These different setups needed to be tested against both geological and geophysical observations, and more theoretical modeling investigations are needed to build up the connections between the observations and the underlying source process.

Chapter 4

A "frictional-viscous in parallel" rupture model and its implication for slow slip events

4.1 Introduction

In the previous two chapters, I summarized the differences in some rupture parameters between slow slip events and fast earthquakes (Chapter 2). I then reviewed some mechanisms that researchers often include in their models to explain the puzzling slow slip observations (Chapter 3). In particular, our understanding of the frictional-viscous mechanism is still poor, although many studies have shown its potentials for generating slow slip behaviors (see references in section 3.3).

In this chapter, I present detailed analysis on one flavor of the frictional-viscous

mixing models—a frictional-viscous in parallel rupture model (Figure 3.3d), where the total fault strength equals the sum of frictional and viscous strength, and the shear (slip) is the same for both the frictional and viscous component. This frictional-viscous mixing setup is different from a frictional-viscous in series rupture model (Figure 3.3c), where the total fault slip is the sum of frictional and viscous shear, while the strength (stress) is the same for both frictional and viscous components (e.g., Goswami & Barbot, 2018; Beall, van den Ende, Ampuero, & Fagereng, 2021). The frictional-viscous in parallel type of model has been investigated by few existing studies (Ando et al., 2010; Nakata et al., 2011; Ando et al., 2012; Lavier et al., 2013; Beall et al., 2019). In particular, Ryosuke Ando and his colleagues explore the farthest in terms of explaining real-world geophysical observations. They innovatively and extensively investigate a "frictional-viscous" model and its potential in generating the observed slow slip behaviors in their three papers: Ando et al. (2010), Nakata et al. (2011), and Ando et al. (2012) (hereafter referred to as "Ando's model").

Though the fault in Ando's model is 2D, it does actually consider the finite-thickness of the fault zone in the parameterization of the "friction law". Yet, Ando's model is sometimes misunderstood by the community as a pure 2D fault model, with the slow slip behaviors in their models mainly due to the mosaic pattern of "frictional" and "viscous" patches on fault (e.g., Yin, Xie, & Meng, 2018; Behr et al., 2021). In my opinion, such misconceptions are partially due to the presentation of Ando's model in the three related papers. The authors did not explain in detail the 3D physical significance (i.e., shear deformation of a shear zone) behind the 2D "friction law" parameterization in dynamic rupture models. In addition, the authors attribute much of the success in producing slow

slip behavior to the mosaic pattern of "frictional" and "viscous" patches, and overlook (at least in the text) the intrinsic "frictional-viscous-mixing" in the "friction law" formalization itself. It makes some of their readers confuse their models with those rate-and-state based models where there are mosaic patterns of "velocity-weakening" and "velocity-strengthen" patches, especially those who are not familiar with earthquake rupture modeling.

From the writer's point of view, the above issue is sort of inevitable when Ando and his colleague derived their models. First of all, geological observations that show the thickness of slow earthquake fault zone within which frictional and ductile deformation coexist were still rare back in the early 2010s. It might be more intuitive for audience to think that it is the "frictional-viscous" heterogeneity across the fault plane that give rise to the slow slip behaviors. Besides, Ando's models are mostly demonstrated with numerical simulations instead of analytical analysis, with only some analytical results in explaining the diffusivity of tremor migration (Ando et al., 2012). From the writer's point of view, a lack of analytical insight might have led them to overlook the importance of the intrinsic frictional-viscous in the "friction law", and thus focus on the discussing the spatial heterogeneity across the fault plane.

In the following chapter, I will revisit, elaborate, and complement Ando's model, extending its implications to incorporate the accumulating new observations after early 2010s. In particular, I will analytically examine the "frictional-vicous mixing" "friction law" that is proposed in Ando's model, providing relations that can relate geophysical observables to the viscous and stress drop properties in the fault zone. I will first demonstrate why we can treat the "frictional-vicous mixing" "friction law" as a 2D parameterization of the actual

3D fault zone. Then, I will show that the frictional-vicous mixing "friction law" is the main reason for generating slow slip behaviors, without necessarily including a mosaic pattern of "frictional" and "viscous" patches on the fault. Eventually, I find that the frictional-viscous model can systematically reconcile the differences between fast earthquake and slow slip event observations.

I note that I will only model the co-seismic rupture. Event-cycles that contain the interseismic period are not considered in my models, and will be discussed in section 6.1.

4.2 Model setup

In all the models presented in this dissertation, I treat the 3D fault shear zone with a finite thickness as a fault "surface" with zero thickness. Such an approach has been widely used in dynamic rupture models and the rationale behind it is explained in section 3.3.2. A "frictional-viscous in parallel" constitutive relation is used as the boundary condition of the hypothetical fault "surface". In addition, the effective frictional strength drop of the fault zone is treated as the local frictional strength drop on brittle components times the ratio between the frictional contact area and the total area. These two setups are not common in dynamic rupture models for fast earthquakes. In this section, I will describe the setup of my models and elaborate the vision and rationale behind it. I will also describe the boundary integral equation framework I use to formularize the problem.

4.2.1 "Frictional-viscous in parallel" fault constitutive relation

The constitutive relation I consider contains both a weakening component and a rate-strengthening component. In a most general formulation, it can be written as,

$$\begin{aligned} \tau_{elastic} &= f \\ &= f_{frictional}(D, V, ...) + f_{viscous}(D, V, ...) \end{aligned} \tag{4.1}$$

in which $f_{frictional}$ and $f_{viscous}$ are the frictional component and the viscous component of the total fault resistance, respectively. Both these two components are treated as functions of different rupture parameters of the bulk shear zone, such as bulk slip D, slip rate V, and other parameters.

Since I focus on the "co-seismic" process of slow slip events, I use a simple linear slip-weakening law to represent the frictional resistance: when elastic loading stress $\tau_{elastic}$ is less than the fault static strength f_0, fault stays still ($D = 0$) and fault behaves like it were not there (i.e. elastic wave can pass through as in the intact medium), and the viscous resistance component equals zero. When $\tau_{elastic}$ reaches f_0, fault strength f quickly drops from a static value f_0 to a residual value f_1 plus the viscous term. It has the following mathematical formulation,

$$\begin{aligned} \tau_{elastic} &= f \\ &= f_0 - (f_0 - f_1) \cdot \frac{D}{D_0} + f_{viscous}(D, V, ...), \text{ when } D \leq D_0 \end{aligned} \tag{4.2}$$

where D_0 is slip weakening distance in the linear slip weakening law. After slip D reach D_0, fault strength will stay at or lower than the the residue level f_1,

$$\begin{aligned} \tau_{elastic} &\leq f \\ &= f_1 + f_{viscous}(D, V, ...), \text{ when } D > D_0 \end{aligned} \tag{4.3}$$

The viscous resistance $f_{viscous}$ needs to increase with slip rate V, but can take various functional forms, such as logarithmic, linear, or a higher-order polynomial. Which functional form better represents the bulk viscous deformation in the fault zone matrix is still an open question. More discussion on the choice of viscous formulation will be discussed in section 6.3, and here we will use a simple linear viscous response for $f_{viscous}$,

$$\begin{aligned} \tau_{elastic} &= f \\ &= f_0 - (f_0 - f_1) \cdot \frac{D}{D_0} + \eta_v \cdot V, \text{ when } D \leq D_0 \end{aligned} \tag{4.4}$$

and,

$$\begin{aligned} \tau_{elastic} &= f \\ &= f_1 + \eta_v \cdot V, \text{ when } D > D_0 \end{aligned} \tag{4.5}$$

where η_v is the parameter that controls the strength of the linear rate-strengthening effect. It has a unit of Pressure $\cdot$ Time $\cdot$ Length^{-1} (e.g., Pa $\cdot$ s $\cdot$ m^{-1}). η_v **is one of the most important variables in our analysis. For convenience, we will referred to** η_v **as viscous coefficient in the subsequent text**. It is different from the unit of viscosity η, which is Pressure $\cdot$ Time (e.g., Pa $\cdot$ s). However, we can relate η_v with η by considering the fact that slip rate V is the bulk shear deformation of the fault zone. V can be expressed as average shear strain $\bar{\epsilon}$ times fault width W, and the linear viscous response can be written as,

$$
\begin{aligned}
f_{viscous} &= \eta_v \cdot V \\
&= \eta_v \cdot W \cdot \bar{\epsilon}
\end{aligned}
\tag{4.6}
$$

and we can define the effective bulk viscosity η of the fault zone as,

$$
\eta = \eta_v \cdot W \tag{4.7}
$$

Figure 4.1a shows the physical conceptualization of this constitutive relation. Brittle structures that are able to host localized frictional slip are embedded in the viscous matrix. Before the slip transient occurs, all stress is loaded in the brittle structures. Once the local stress on the brittle structure exceed the yielding stress, localized frictional slips quickly occur within the brittle structures and the bulk fault zone experiences a sudden drop of shear resistance, inducing a difference between the elastic loading stress and bulk fault strength. This net difference in stress drives the bulk viscous matrix to shear, which, as a whole, can be treated as a viscous response of the fault "surface". Figure 4.1b shows the mechanical equivalent of the constitutive relation. The fault zone with brittle structures embedded in a viscous matrix is parameterized as a system where the frictional response and the viscous response are in parallel. The total fault strength is the sum of the frictional resistance and the viscous resistance, while the deformation of the frictional and viscous component are the same and they both equal to the bulk shear deformation of the fault zone. With this parameterization, the bulk shear deformation in a fault zone with finite thickness can be modeled as slip on a hypothetical zero-thickness fault "surface" (Figure 4.1c), and the associating rupture behaviors can be evaluated in a typical framework of

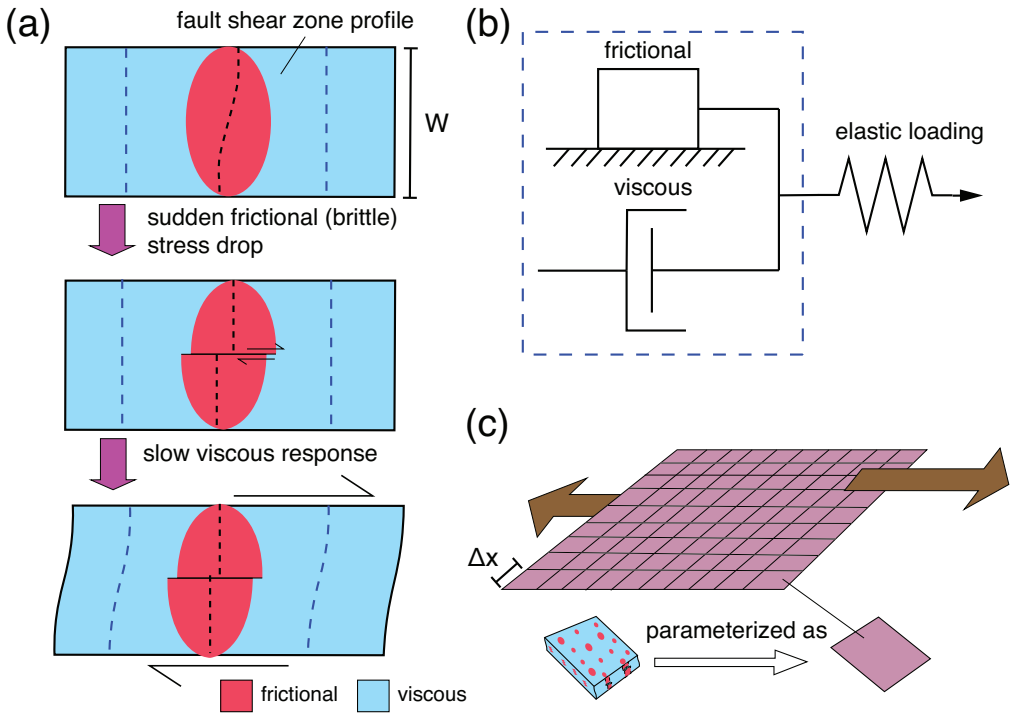

Figure 4.1: Physical conceptualization of the constitutive relation ("friction law") that is used in my models. (a) How a fault zone with brittle structures (red) embedded in a viscous matrix (blue) deform in response to the external elastic loading. (b) The mechanical equivalent of the constitutive relation, where frictional response and viscous response are in parallel. The resistance is partitioned into a frictional resistance component and a viscous resistance component, while the deformation of the frictional and viscous component are identical and they are both equal to the bulk shear deformation of the fault zone. (c) Schematic showing the "pseudo-3D" approach in my models. The deformation of the fault zone with finite thickness is treated as slip on a fault "surface" with zero thickness, and the associated rupture behaviors can then be modeled in a typical framework of dynamic rupture model that uses "friction law".

dynamic rupture model that uses "friction law".

4.2.2 Effective frictional strength drop $\overline{\Delta\tau}$ and local frictional strength drop $\Delta\tau_f$

In the constitutive relation of my models, when fault has not slipped, viscous resistance equals zero because slip rate is zero (equation (4.4)) and frictional resistance takes up all of the loading stress. Frictional strength quickly drops from f_0 to f_1 as slip starts. Since the strength f in the constitutive relation is a parameterization of the bulk fault zone, the frictional strength drop should be treated as an effective strength drop of the whole fault zone instead of a local frictional strength drop on the brittle components. I denote the effective frictional strength drop as $\overline{\Delta\tau}$ and the local frictional strength drop as $\Delta\tau_f$. Considering that the resistance force on a greater fault area A is provided with only the frictional contacts, we have,

$$\overline{\Delta\tau} \cdot A = C_{amp} \cdot \Delta\tau_f \cdot A_f,$$

where A_f is the actual contact area of the brittle component in the fault zone. C_{amp} is a correction factor for the amplification effect. I include C_{amp} to consider that the frictional contact could have a complex 3D structure in the fault zone with finite thickness, and these structure may aid or suppress the stress amplification effect. Here, I assume that this factor is of the order of 1.

We may rearrange the above equation to single out the effective frictional strength drop on the left-hand side,

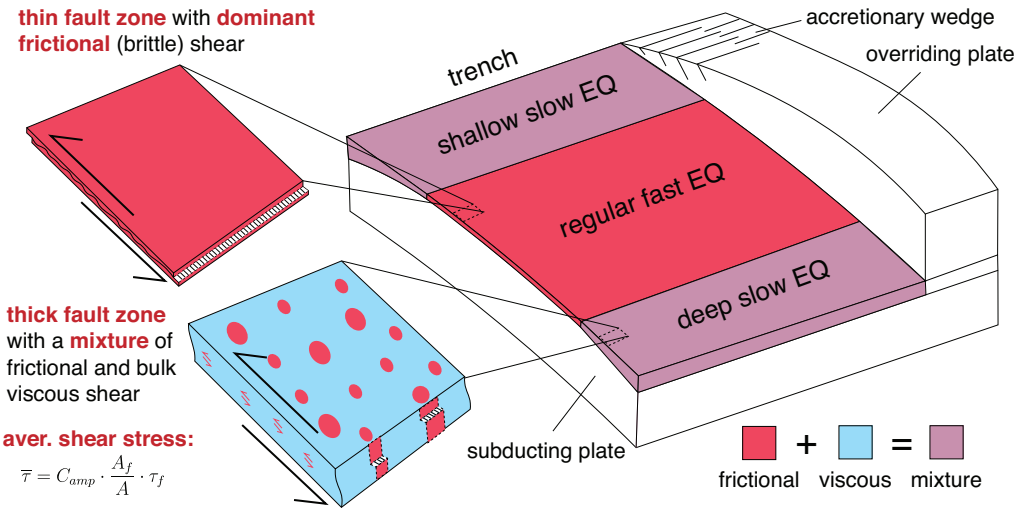

Figure 4.2: Physical vision of the thick frictional-viscous fault zone that hosts slow earthquakes in comparison with the thin "frictional" fault zone that host fast earthquakes. A subduction megathrust setting is used as an example for demonstration. On the fault that host fast earthquakes (red), frictional contacts take up almost all the area of fault ($\frac{A_f}{A} \approx 1$), and the effective frictional strength drop $\overline{\Delta\tau}$ would be similar to the local frictional strength drop $\Delta\tau_f$, and both would be of the order of MPa as suggested by seismological observations. On the fault that hosts slow earthquakes (a mosaic pattern of red and blue in the zoom-in schematic, purple in the zoom-out schematic), frictional contacts are considerably sparser ($\frac{A_f}{A} \ll 1$), and the effective frictional strength drop $\overline{\Delta\tau}$ would be considerably less than the local frictional strength drop $\Delta\tau_f$.

$$\overline{\Delta\tau} = C_{amp} \cdot \frac{A_f}{A} \cdot \Delta\tau_f, \tag{4.8}$$

This relation is used in my models to explain the low effective stress drop on a slow earthquake fault. Figure 4.2 shows the physical conceptualization of my model that uses a subduction zone megathrust setting as an example. Seismological evidence suggests that the effective frictional strength drop $\overline{\Delta\tau}$ (both static and dynamic) for fast earthquakes is of the order of MPa (section 2.1 and 2.2). If we assume that, on the fault that host fast earthquakes, the fault zone is thin and the frictional contacts take almost all of the fault area ($\frac{A_f}{A} \sim 1$), then the effective frictional strength drop $\overline{\Delta\tau}$ would be similar to the

local frictional strength drop $\Delta\tau_f$. In this case, both $\overline{\Delta\tau}$ and $\Delta\tau_f$ would be at a MPa level. On the fault that hosts slow earthquakes, frictional contacts are considerably sparser ($\frac{A_f}{A} \ll 1$), and the effective frictional strength drop $\overline{\Delta\tau}$ would be considerably less than the local frictional strength drop $\Delta\tau_f$. If one assume the local frictional strength drop $\Delta\tau_f$ is the same for both the fast earthquake fault and slow earthquake fault, being $\sim$ MPa, the effective frictional strength drop $\overline{\Delta\tau}$ on the slow earthquake fault would be considerably smaller than MPa. To explain the $\sim$ 10 kPa stress drop observation in slow slip events, we can set $\frac{A_f}{A} \sim 1/100$, then $\overline{\Delta\tau}$ would be about $\Delta\tau_f/100 = 10$ kPa.

Mathematically, the above vision has a similar principle as the relation in laboratory friction experiments between the high stress on local frictional contact ($\sim$ GPa) and low average stress of the fault surface ($\sim$ MPa) (e.g., J. H. Dieterich & Kilgore, 1994; Scholz, 2019). However, the physical meaning of these two relations are different. In the laboratory-scale experiments, the actual frictional contacts area is significantly smaller than the total area due to the small-scale roughness ($\sim$ 100 microns) on the fault surface as reported in J. H. Dieterich and Kilgore (1994)), while the slip surface is still very thin overall. In the vision of my model, the local frictional contacts are more like the total slip surface in the laboratory experiments, instead of the small-scale roughness. The effective frictional strength drop $\overline{\Delta\tau}$ is low on slow earthquake faults because the fault zone is mostly viscous, and the frictional (brittle) components only take up a small portion.

4.2.3 A boundary integral equation framework to formularize the rupture problem

To analytically probe the rupture behaviors under the above fault constitutive law, it is convenient to consider the problem in a boundary integral equation framework, which is commonly used in earthquake mechanics problems. The fault is treated as an internal boundary embedded in the medium, across which shear displacement is discontinuous. The medium outside of the fault is treated as elastic. Fault resistance f is treated as the external traction acting within the fault (outside the elastic medium domain). As a requirement of the continuum system, this external traction needs to equal the internal traction within the medium at the same location, which is usually referred to as the elastic loading stress $\tau_{elastic}$,

$$\tau_{elastic}(\boldsymbol{\xi}, t) = f(\boldsymbol{\xi}, t),$$

which has already been shown in equation (4.1). $\boldsymbol{\xi}$ is a location on fault. In principle, both f and $\tau_{elastic}$ should be vectors in a 3D problem. For simplicity, we require them to be along the same fixed axis in my models, and thus both these parameters and the related slip D are scalars in my models.

Both fault resistance f and elastic loading stress $\tau_{elastic}$ depend on the spatial-temporal evolution of slip $D(\boldsymbol{\xi}, t)$ and its derivatives. The relation between f and slip $D(\boldsymbol{\xi}, t)$ is given by the slip-weakening fault constitutive law (equation (4.4)),

$$f(\boldsymbol{\xi}, t) = f_0 - (f_0 - f_1) \cdot \frac{D(\boldsymbol{\xi}, t)}{D_0} + \eta_v \cdot \dot{D}(\boldsymbol{\xi}, t) \tag{4.9}$$

To solve for slip $D(\boldsymbol{\xi}, t)$, one must know the expression of $\tau_{elastic}$. As a side note, $\tau_{elastic}$ can be numerically evaluated using the finite element or finite difference method by numerically solving the partial differential equations of elastodynamics system. However, in the boundary integral equation framework I use here, the relation between $\tau_{elastic}$ and slip $D(\boldsymbol{\xi}, t)$ is evaluated analytically with a Green's function method, and the expression can be written as the initial elastic loading stress $\tau^0(\boldsymbol{x})$ plus a surface integral that contains the slip rate function $\dot{D}(\boldsymbol{\xi}, t)$,

$$\begin{aligned}\tau_{elastic}(\boldsymbol{\xi}, t) = \tau^0(\boldsymbol{\xi}) - \frac{\mu}{2\beta}\dot{D}(\boldsymbol{\xi}, t) \\ + \int_\Gamma \mathrm{d}S(\boldsymbol{\xi'}) \int_0^t \mathrm{d}\tau \hat{K}(\boldsymbol{\xi}, t-\tau; \boldsymbol{\xi'}, 0)\dot{D}(\boldsymbol{\xi'}, \tau) \quad (\boldsymbol{\xi}, \boldsymbol{\xi'} \in \Gamma),\end{aligned} \tag{4.10}$$

in which Γ is the fault surface. $-\frac{\mu}{2\beta}\dot{D}(\boldsymbol{\xi'}, \tau)$ is often referred to as the instantaneous traction response or radiation damping term (e.g., Rice, 1993; Cochard & Madariaga, 1994; Zheng & Rice, 1998; Tada, 2005), and β is shear wave speed. $t = 0$ is the time when no slip has happened and the elastic stress on fault is $\tau^0(\boldsymbol{\xi})$. $\hat{K}$ is the integral kernel which is a predetermined function once the medium property is set. It includes some differential operator on slip rate $\dot{D}(\boldsymbol{\xi}, t)$. For convenience, I will interchangeably refer to slip rate as both $\dot{D}$ and V, depending on which expression is more suitable for the context.

In theory, one may obtain the spatial-temporal rupture evolution by equating $\tau_{elastic}(\boldsymbol{\xi}, t)$ and $f(\boldsymbol{\xi}, t)$ and solving for $D(\boldsymbol{\xi}, t)$. Since it contains an integral of slip, such equations are commonly referred to as boundary integral equations. Usually, It is difficult to solve the boundary integral equation for $D(\boldsymbol{\xi}, t)$. One common way is to turn to a numerical simulation from here on, which is usually referred to as boundary integral equation method

or boundary element method. However, if the goal is only to probe the first-order rupture characteristics under a certain initial setup, one may simplify the mathematics with some reasonable assumptions, and still be able to solve the equation analytically. My analysis in this dissertation will involve both analytical and numerical approaches of solving the boundary integral equations. In Chapter 4, I will demonstrate the analytical analysis, while in Chapter 5, I will demonstrate the numerical analysis.

4.3 Characteristic slip rate V

In the following section, I will explore the peak slip rate V of the "frictional-viscous in parallel" rupture models. I will first investigate the rupture behaviors analytically with some assumptions to simplify the mathematics. Then, I discuss the analytical analysis's implications for explaining slow slip event observations.

4.3.1 Analytical derivation

Let's first consider a fault at a location $\boldsymbol{\xi}$ with the frictional-viscous constitutive law (equation (4.4)). A drop in the elastic stress causes the slip to speed up. Our goal here is to have an estimate of the peak slip rate V after the stress drop. I refer to this slip rate as the characteristic slip rate under the frictional-viscous constitutive law. Assume that at time $t = t_0$, this location $\boldsymbol{\xi}$ is just about to slip and the slip rate $V(\boldsymbol{\xi}, t_0) = 0$. The elastic loading stress can be expressed as,

$$\begin{aligned}\tau_{elastic}(\boldsymbol{\xi}, t_0) &= \tau^0(\boldsymbol{\xi}) - \frac{\mu}{2\beta} \cdot 0 + \int_\Gamma \mathrm{d}S(\boldsymbol{\xi'}) \int_0^{t_0} \mathrm{d}\tau \hat{K}(\boldsymbol{\xi}, t_0 - \tau; \boldsymbol{\xi'}, 0) \dot{D}(\boldsymbol{\xi'}, \tau) \\ &= \tau^0(\boldsymbol{\xi}) + \int_\Gamma \mathrm{d}S(\boldsymbol{\xi'}) \int_0^{t_0} \mathrm{d}\tau \hat{K}(\boldsymbol{\xi}, t_0 - \tau; \boldsymbol{\xi'}, 0) \dot{D}(\boldsymbol{\xi'}, \tau).\end{aligned} \tag{4.11}$$

At this moment, the combined elastic loading stress, which consists of both the initial stress and the co-seismic stress perturbation due to stress transfer from elsewhere on the fault, reaches a static yielding strength f_0,

$$\tau_{elastic}(\boldsymbol{\xi}, t_0) = f(\boldsymbol{\xi}, t_0) = f_0. \tag{4.12}$$

The fault at this location starts to slip and experience a stress drop. In the linear slip weakening "friction law" I use, the brittle component of the fault strength would drop from f_0 to f_1 linearly as the fault slips a distance D_0 (the second term of equation (4.10)). Let's assume the stress drop process is very sudden, and the fault slip increases to D_0 in a very short amount of time Δt. The fault slip rate increases to $V(\boldsymbol{\xi}, t_0 + \Delta t)$. Our goal now is to estimate this slip rate. It can be done by equating elastic loading stress with fault strength. At time $t = t_0 + \Delta t$, the elastic loading stress can be written as,

$$\begin{aligned}\tau_{elastic}(\boldsymbol{\xi}, t_0 + \Delta t) = \tau^0(\boldsymbol{\xi}) &- \frac{\mu}{2\beta} \cdot V(\boldsymbol{\xi}, t_0 + \Delta t) \\ &+ \int_\Gamma \mathrm{d}S(\boldsymbol{\xi'}) \int_0^{t_0 + \Delta t} \mathrm{d}\tau \hat{K}(\boldsymbol{\xi}, t_0 + \Delta t - \tau; \boldsymbol{\xi'}, 0) \dot{D}(\boldsymbol{\xi'}, \tau)\end{aligned} \tag{4.13}$$

Without a thorough proof, I assert that when Δt is considerably short and D_0 is considerably smaller than the final slip, the incremental difference between the integral term in equation (4.11) and (4.13) would be small enough as well,

$$\int_\Gamma \mathrm{d}S(\boldsymbol{\xi'}) \int_0^{t_0+\Delta t} \mathrm{d}\tau \hat{K}(\boldsymbol{\xi}, t_0+\Delta t-\tau; \boldsymbol{\xi'}, 0)\dot{D}(\boldsymbol{\xi'}, \tau) \approx \int_\Gamma \mathrm{d}S(\boldsymbol{\xi'}) \int_0^{t_0} \mathrm{d}\tau \hat{K}(\boldsymbol{\xi}, t_0-\tau; \boldsymbol{\xi'}, 0)\dot{D}(\boldsymbol{\xi'}, \tau),$$

In that case, combining equation (4.11), (4.12) and (4.13), we may write $\tau_{elastic}(\boldsymbol{\xi}, t_0+\Delta t)$ as,

$$\tau_{elastic}(\boldsymbol{\xi}, t_0 + \Delta t) \approx f_0 - \frac{\mu}{2\beta} \cdot V(\boldsymbol{\xi}, t_0 + \Delta t) \tag{4.14}$$

On the other hand, we need to write out the expression for $f(\boldsymbol{\xi}, t_0 + \Delta t)$. Considering equation (4.10) and $D(\boldsymbol{\xi}, t_0 + \Delta t) = D_0$, it can be written as,

$$\begin{aligned} f(\boldsymbol{\xi}, t_0 + \Delta t) &= f_0 - (f_0 - f_1) \cdot \frac{D_0}{D_0} + \eta_v \cdot V(\boldsymbol{\xi}, t_0 + \Delta t) \\ &= f_1 + \eta_v \cdot V(\boldsymbol{\xi}, t_0 + \Delta t). \end{aligned} \tag{4.15}$$

Equating equation (4.14) with (4.15), we can solve for the slip rate $V(\boldsymbol{\xi}, t_0 + \Delta t)$,

$$\begin{aligned} V(\boldsymbol{\xi}, t_0 + \Delta t) &\approx \frac{f_0 - f_1}{\frac{\mu}{2\beta} + \eta_v} \\ &= \frac{\Delta f}{\frac{\mu}{2\beta} + \eta_v} \end{aligned} \tag{4.16}$$

in which we denote $\Delta f = f_0 - f_1$ as the sudden strength drop from the yielding fault resistance f_0 to the residue resistance f_1 over the slip distance D_0. It is often referred to as the dynamic stress drop in the literature.

To make the physical meaning more clear in the above equation, we can rewrite the right hand side expression as two non-dimension factors times shear wave speed β,

$$V(\boldsymbol{\xi}, t_0 + \Delta t) \approx \left(1 + \frac{\eta_v}{\mu/(2\beta)}\right)^{-1} \cdot \frac{2(f_0 - f_1)}{\mu} \cdot \beta, \tag{4.17}$$

Since slip rate most likely reaches its peak value immediate after the stress drop process, $V(\boldsymbol{\xi}, t_0 + \Delta t)$ can be treated as an estimation of the peak slip rate V under the "frictional-viscous in parallel" fault constitutive law. In a later section, I will demonstrate that the peak slip rate is a good representation of the characteristic slip rate for the model we investigate. Aside from the elastic property μ and β, V also depends on the viscous coefficient η_v and the dynamic stress drop Δf between the yielding strength and residue strength. Since we consider that stress drop happens quickly and over a short distance, the slip weakening distance does not goes into the expression of V.

4.3.2 Implications: dependency on "friction" parameters

We may now perform some first-order analysis on the slip rate using equation (4.17). Two "friction" parameters control the characteristic slip rate: the viscous coefficient η_v and the sudden strength drop $\Delta f = f_0 - f_1$. Figure 4.3 shows how V depends on η_v in a log-log plot when sudden fault resistance drop $\Delta f = f_0 - f_1$ is fixed. Equation (4.17) suggests that η_v affects V through the ratio $\frac{\eta_v}{\mu/(2\beta)}$, and $f_0 - f_1$ affects V through the ratio $\frac{f_0 - f_1}{\mu}$. For a clearer insight into the physical process, I non-dimensionalize η_v, V, and Δf using $\mu/(2\beta)$, β, and μ, respectively. The non-dimensional value of η_v and V are shown on the bottom and left axis (black). To facilitate comparison with observations, I also show η_v and V in their physical units Pa $\cdot$ s/m and m/s on the top and right axis (red), assuming $\mu = 3 \times 10^{10}$ Pa and $\beta = 3.23 \times 10^3$ m/s.

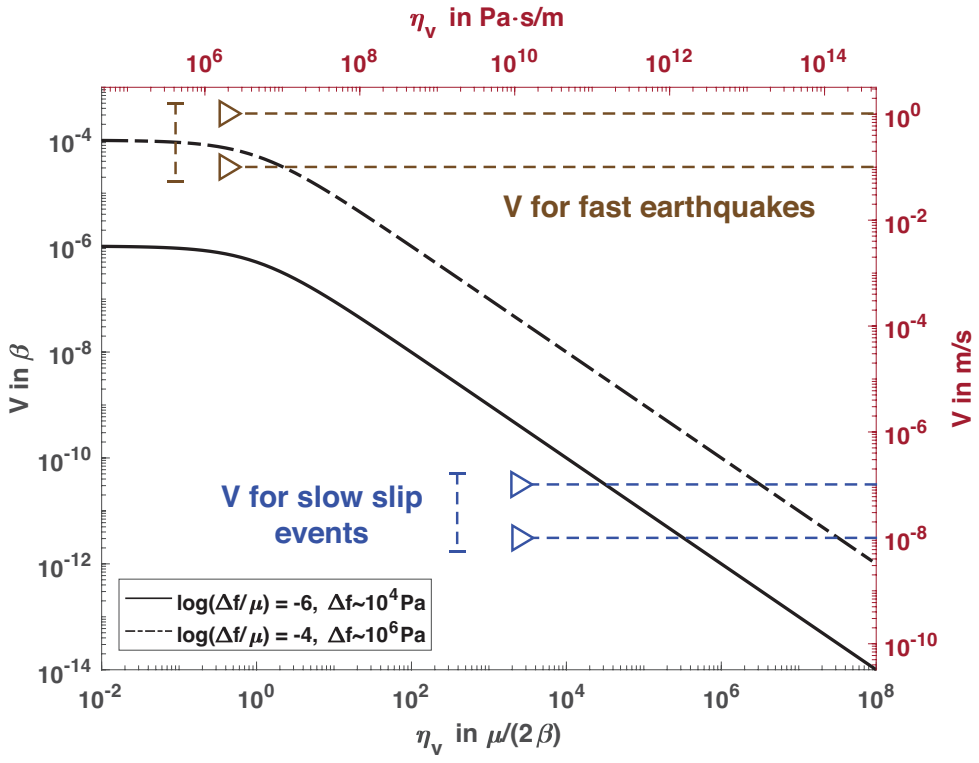

Figure 4.3: The relation between characteristic slip rate V and viscous coefficient η_v yielded by equation (4.17). The sudden strength drop $\Delta f = f_0 - f_1$ is fixed. I show two line where Δf is fixed at 10^{-6} μ (solid black line) and 10^{-4} μ (dashed black line). Considering that μ is normally on the order of 10^{10} Pa, the former case has a Δf of about 10 kPa, while the latter case has a Δf of about 1 MPa. For a clearer insight on the physical process, I non-dimensionalize η_v, V, and Δf using $\mu/(2\beta)$, β, and μ, respectively. The non-dimensional values of η_v and V are shown on the bottom and left axes (black). To facilitate comparison with observations, I also show η_v and V in their physical units Pa $\cdot$ s/m and m/s on the top and right axis (red), assuming $\mu = 3 \times 10^{10}$ Pa and $\beta = 3.23 \times 10^3$ m/s. To compare with observations, I show two sets of horizontal dashed lines with a triangle at the left end to denote the typical V ranges for fast earthquakes (brown dashed lines, $10^{-1} - 10^0$ m/s) and slow slip events (blue dashed lines, $10^{-8} - 10^{-7}$ m/s).

I show two lines along which Δf is fixed at $10^{-6}\mu$ (solid black line) and $10^{-4}\mu$ (dashed black line). Considering that μ is normally on the order of 10^{10} Pa, the former case has a Δf of about 10 kPa, consistent with values inferred for normal fast earthquakes; while the latter case has a Δf of about 1 MPa, consistent with inferred values of slow slip events. V is aways greater for the larger Δf case when η_v is the same. Both lines are relatively flat when η_v is smaller than 1 $\mu/(2\beta)$. This is a region in the parameter space where the radiation damping effect is stronger than the fault viscous effect, and V is mainly controlled by the radiation damping factor. When η_v is greater than 1 $\mu/(2\beta)$, the fault viscous effect becomes the dominant factor that affects V, and V start to decrease with η_v in both lines.

To compare with observations, I show two sets of horizontal dash lines with a triangle at the left end to denote the typical V ranges for fast earthquakes (brown dash lines, $10^{-1} - 10^{0}$ m/s) and slow slip events (blue dash lines, $10^{-8} - 10^{-7}$ m/s). A typical slip rate for fast earthquakes can be explained with a $\sim$ MPa level sudden strength drop Δf and an insignificant fault viscous effect. This result is consistent with our analysis in section 2.2.1 where no viscous effect is considered. In fact, this is not a surprise because equation (4.17) approaches equation (2.5) when η_v is small. A typical slow slip event slip rate can be achieved when η_v is high enough in a corresponding range. For the $\Delta f \sim 10$ kPa case, the corresponding η_v range is $\sim 10^4 - 10^5$ $\mu/(2\beta)$. For the $\Delta f \sim 1$ MPa case, the corresponding η_v range is $\sim 10^6 - 10^7$ $\mu/(2\beta)$. This result suggests that the frictional-viscous fault zone setup I use here is capable of generating the slow slip rate of $10^{-8} - 10^{-7}$ m/s as observed in SSEs.

Another practical interest here is to predict the "friction" parameters η_v and Δf,

if the proposed "friction law" is actually presented in nature. However, It is not possible to constrain both η_v and Δf with only slip rate observations. According to equation (4.17), any Δf should have a range of η_v that can generate a typical slow slip event slip rate. Additional observations are needed to constrain the "friction" parameter, which will be discussed later.

4.4 Characteristic slip D

Our next goal here is to examine the characteristic slip D under the specified fault constitutive relation. Like the previous section, I will first derive a solution analytically and then discuss its implication for slow slip events.

4.4.1 Analytical analysis

The characteristic slip D here is defined as a first-order estimation of the final slip on a fault. Assuming that at $t = 0$, everywhere on fault has not yet started to slip, and the elastic loading stress $\tau_{elastic}$ is at its initial level,

$$\tau_{elastic}(\boldsymbol{\xi}, t = 0) = \tau^0(\boldsymbol{\xi}). \tag{4.18}$$

fault at $\boldsymbol{\xi}$ position starts to slip at some time, which is denoted as t_0 in the previous section. After a long enough time at $t = t_\infty$, all locations on the fault have come back to rest and all the elastic waves have propagated outside the fault region. At that time, we have,

$$\tau_{elastic}(\boldsymbol{\xi}, t = t_\infty) = \tau^0(\boldsymbol{\xi}) - \frac{\mu}{2\beta} \cdot 0 + \int_\Gamma \mathrm{d}S(\boldsymbol{\xi'}) \int_0^{t_\infty} \mathrm{d}\tau \hat{K}(\boldsymbol{\xi}, t_\infty - \tau; \boldsymbol{\xi'}, 0) \dot{D}(\boldsymbol{\xi'}, \tau). \tag{4.19}$$

At the same time, the fault resistance f should be lower than the residual level f_1,

$$\begin{aligned} f(\boldsymbol{\xi}, t = t_\infty) &\leq f_1 + \eta_v \cdot 0 \\ &= f_1 \end{aligned} \tag{4.20}$$

with equality if the elastic loading stress does not go down below f_1 (i.e., no dynamic overshoot). Note that the viscous effect disappears here because slip rate returns to zero in the end. This result indicates that the viscous effect is not important in affecting the net slip. I will also elaborate this point in the discussion later.

For simplicity, we omit the dynamic overshoot effect here and take the equality case of the inequation (4.20), and set it equal to equation (4.19). We have

$$\begin{aligned} \int_\Gamma \mathrm{d}S(\boldsymbol{\xi'}) \int_0^{t_\infty} \mathrm{d}\tau \hat{K}(\boldsymbol{\xi}, t_\infty - \tau; \boldsymbol{\xi'}, 0) \dot{D}(\boldsymbol{\xi'}, \tau) &\approx -\Big(\tau^0(\boldsymbol{\xi}) - f_1\Big) \\ &\approx -\Delta\tau_s \end{aligned} \tag{4.21}$$

in which $\Delta\tau_s$ is the static stress drop, which equals $\tau^0(\boldsymbol{\xi}) - f_1$ when there is no dynamic overshoot effect.

We now need to carry out the integral on the left hand side. If we specify that all slip rate on fault returns to and stays at zero after time $t = t_{end}$ ($t_{end} < t_\infty$), we can change the upper limit of the time integral from t_∞ to t_{end},

$$\begin{aligned} &\int_\Gamma \mathrm{d}S(\boldsymbol{\xi'}) \int_0^{t_\infty} \mathrm{d}\tau \hat{K}(\boldsymbol{\xi}, t_\infty - \tau; \boldsymbol{\xi'}, 0) \dot{D}(\boldsymbol{\xi'}, \tau) \\ &\qquad \approx \int_\Gamma \mathrm{d}S(\boldsymbol{\xi'}) \int_0^{t_{end}} \mathrm{d}\tau \hat{K}(\boldsymbol{\xi}, t_\infty - \tau; \boldsymbol{\xi'}, 0) \dot{D}(\boldsymbol{\xi'}, \tau) \end{aligned} \tag{4.22}$$

Now, the integral can be simplified if we consider that t_∞ is considerably longer than the slip end time t_{end}. In that case, $\hat{K}(\boldsymbol{\xi}, t_\infty - \tau; \boldsymbol{\xi'}, 0)$ would be a constant in time that equals to the static solution. It can then be moved out of the temporal integral,

$$\begin{aligned}
&\int_\Gamma \mathrm{d}S(\boldsymbol{\xi'}) \int_0^{t_\infty} \mathrm{d}\tau \hat{K}(\boldsymbol{\xi}, t_\infty - \tau; \boldsymbol{\xi'}, 0) \dot{D}(\boldsymbol{\xi'}, \tau) \\
&\qquad \approx \int_\Gamma \mathrm{d}S(\boldsymbol{\xi'}) \hat{K}(\boldsymbol{\xi}, t_\infty; \boldsymbol{\xi'}, 0) \int_0^{t_{end}} \mathrm{d}\tau \dot{D}(\boldsymbol{\xi'}, \tau) \\
&\qquad = \int_\Gamma \mathrm{d}S(\boldsymbol{\xi'}) \hat{K}(\boldsymbol{\xi}, t_\infty; \boldsymbol{\xi'}, 0) D(\boldsymbol{\xi'}, t_\infty).
\end{aligned} \tag{4.23}$$

The above expression can be estimated using the static solution of a slip patch,

$$\int_\Gamma \mathrm{d}S(\boldsymbol{\xi'}) \int_0^{t_\infty} \mathrm{d}\tau \hat{K}(\boldsymbol{\xi}, t_\infty - \tau; \boldsymbol{\xi'}, 0) \dot{D}(\boldsymbol{\xi'}, \tau) \approx -C \cdot \frac{\mu}{L} \cdot D(\boldsymbol{\xi}) \tag{4.24}$$

in which C is a constant that depends on slip mode, free surface condition, and the shape of the slip patch. It is of the order of one (and close to one). μ is shear modulus and L is the characteristic length of the slip patch (rupture area). I note that, since we only care about the first-order quantitative results, how L is controlled by the shape of the slip patch should not affect our analysis here, and one may treat L as an order-of-magnitude estimate of the rupture area dimension. Substitute equation (4.24) to (4.20), we can solve for the characteristic slip $D(\boldsymbol{\xi})$,

$$\begin{aligned}
D(\boldsymbol{\xi}) &\approx \frac{1}{C} \cdot \frac{L}{\mu} \cdot \left(\tau^0(\boldsymbol{\xi}) - f_1 \right) \\
&\approx \frac{1}{C} \cdot \frac{L}{\mu} \cdot \Delta\tau_s
\end{aligned} \tag{4.25}$$

This solution is the same as a typical final slip expression for regular earthquakes. Slip is proportional to the static stress drop $\Delta\tau_s$ and the characteristic length L of slip patch,

and inversely proportional to the shear modulus μ. It is worth noting that the final slip is not affected by the viscous coefficient η_v, even though η_v is a major factor in controlling peak slip rate. This results is understandable, because the viscous effect is more related to the transient process, while the net slip should be more controlled by the net difference in stress.

4.4.2 Implications: small static stress drop for slow slip event

In this part, I will discuss the implication of the above analytical results for slow earthquakes. Figure 4.4 shows the relation between D and L yielded in equation (4.25). The static stress drop $\Delta\tau_s$ is fixed and μ is set to be 3×10^{10} Pa. I show two line where $\Delta\tau_s$ is fixed at 10^4 Pa (solid black line) and 10^6 Pa (dash black line). To compare with observations, I show two shaded area denoting the typical rupture parameters D and L for observed fast earthquakes (brown shaded area) and slow slip events (blue shaded area).

Since equation (4.17) is the same as a classic solution without viscous effect, a $\sim$ MPa level of stress drop in the above model is able to explain the "D-L" observations for regular fast earthquakes, which is consistent with the abundant existing static stress drop studies (e.g., Wells & Coppersmith, 1994; Allmann & Shearer, 2009). For slow slip events, observations of L are concentrated in a range around $\sim$ 10 km, and the detailed $D - L$ scaling is not as well-constrained as in fast earthquakes. However, a first-order D for slow slip events is around the order of $\sim$ cm (e.g., Bürgmann, 2018). Therefore, a static stress drop of $\sim$ 10 kPa is needed to explain slow slip events.

The above static stress drop results are identical to the results in section 2.1, where no viscous effect is considered. However, the physical significance is different, because

viscous effect is included in the analysis here while not in section 2.1. The viscous effect does not show up in the final results because it does not contribute to the strength of "end" state (equation (4.20)). In another word, the results of equation (4.25) has an important yet hidden implication, that is, the final slip D is not controlled by η_v. Since the final slip D and the rupture dimension L for slow slip events can be measured from geodetic data to the first order, the static stress drop $\Delta\tau_s$ can be directly estimated from data.

In section 4.3, I show that the characteristic slip rate V in my model is controlled by the dynamic strength drop Δf and the viscous coefficient η_v. Although the V for slow slip events can be directly measured from geodetic data, we can not estimate Δf and V simultaneously due to the trade-off (equation (4.17) and Figure 4.3). To resolve this trade-off, one assumption we can make is that the dynamic strength drop Δf has the same order of magnitude as the static stress drop $\Delta\tau_s$, similar to what is observed for regular earthquakes (section 2.1 and 2.2). In that case, both Δf and $\Delta\tau_s$ for slow slip events would be as low as ~ 10 kPa, which are significantly smaller than the $\sim$ MPa level for fast earthquakes. If our model is indeed a good representation of the actual process, with this constraint, we can estimated the η_v to be $\sim 10^4 - 10^5\ \mu/(2\beta)$ (solid black line in Figure 4.3).

I note that I mentioned two stress drop concepts in section 4.2.2: "effective frictional strength drop $\overline{\Delta\tau}$" and "local frictional strength drop $\Delta\tau_f$". Both the dynamic strength drop Δf and the static stress drop $\Delta\tau_s$ I discuss here should belong to the "effective frictional strength drop $\overline{\Delta\tau}$" category. This is because we were estimating both Δf and $\Delta\tau_s$ with the geophysical observations that can only capture the holistic picture of slow slip event ruptures. Therefore, to explain the apparent low stress drop value, it is possible

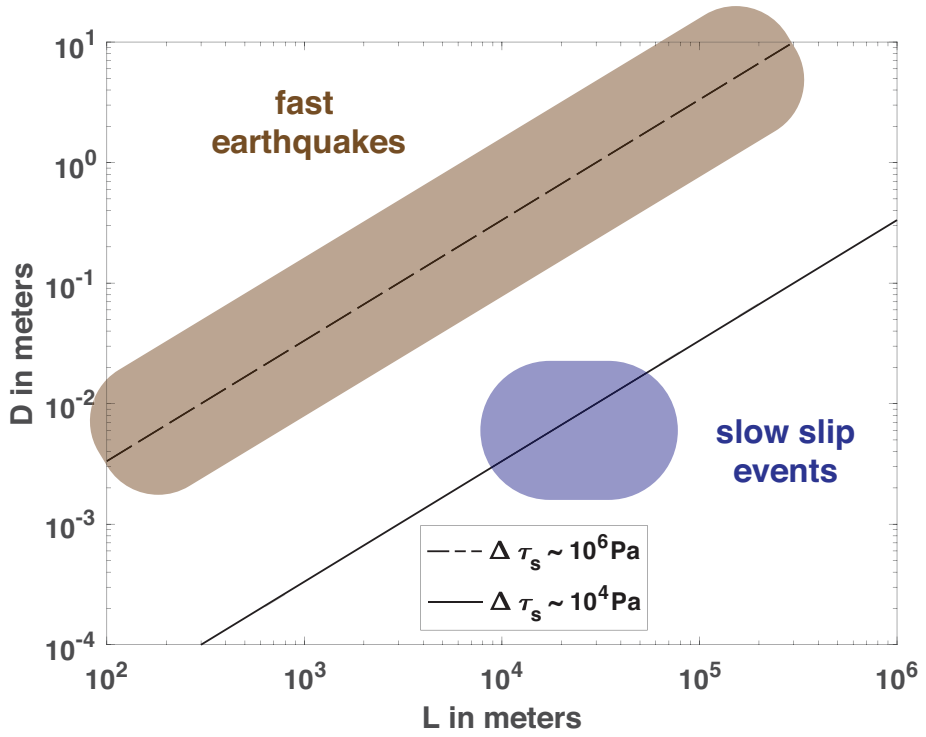

Figure 4.4: The relation between characteristic slip rate D and characteristic slip patch length L yielded in equation (4.25). The static stress drop $\Delta\tau_s$ is fixed. I show two lines where $\Delta\tau_s$ is fixed at 10^4 Pa (solid black line) and 10^6 Pa (dash black line). μ is set to be 3×10^{10} Pa. To compare with observations, I show two shaded area denoting the typical rupture parameters D and L for observed fast earthquakes (brown shaded area) and slow slip events (blue shaded area).

that it is not because the actual frictional strength drop is low (although it can be); instead, it is because the frictional contacts are considerably sparse, which, I envision, corresponds to vision that the distribution of brittle deformation in the viscous substrate is relatively sparse ($\frac{A_f}{A} \ll 1$) in the SSE fault zones. In that case, if we assume that $\frac{A_f}{A} \approx 1$ for regular fast earthquakes that has a $\sim$ MPa level stress drop, we can estimated that $\frac{A_f}{A}$ for slow slip events is about 1/100. This result can possibly explain why the "LFE" features observed geologically in fault zone is sparse but they still seems able to connect and rupture together

in slow slip events. I will discuss more about this point in section 6.1.

4.5 Characteristic slip rate decay time T_d

In the following section, I will investigate the characteristic time T_d it takes for slip rate to slow down after the sudden frictional strength drop in the current model. This quantity is of particular interest here because for slow slip events, T_d can be independently measured using different geophysical observations. Using geodetic data, one can directly measure the characteristic slip rate decay time T_d from the surface displacement time-series across the study area, and at the same time obtain the slip D and slip rate V of slow slip events. If we assume that tremor and LFE locations represent the fault area that is slipping, we can estimate the characteristic slip rate decay time T_d using high-frequency seismic data, without needing to know the slip D or slip rate V of slow slip events. Similar to previous sections, I will first derive the dependence of T_d in our model, and then discuss its implication for slow slip events.

4.5.1 Analytical derivation

Consider an idealized situation. Assume there is a patch on fault with a characteristic length L. At some time, the elastic loading stress $\tau_{elastic}$ reaches the yielding friction strength f_0 everywhere on the patch, and the whole patch starts to slip simultaneously. Although the stress and slip on patch should in principle be heterogeneous, for the convenience of obtaining a characteristic value, we may assume that the evolution of elastic loading stress $\tau_{elastic}$ and slip rate V are homogeneous across the patch, and thus can be

treated as functions that depend solely on time. In addition, we may assume that the slip weakening distance D_0 is considerably smaller than the final slip, and that the frictional strength drop process can be treated as immediate. Let us denote that at time $t = 0$, the frictional strength drops from f_0 to f_1. At this moment, the slip rate $V(t = 0)$ on the patch is V_0 (i.e., the initial slip rate right after the immediate stress drop is V_0).

To obtain the evolution of $V(t)$ and $\tau_{elastic}(t)$, we may equate $\tau_{elastic}(t)$ with $f(t)$. We may write $\tau_{elastic}(t)$ as,

$$\tau_{elastic}(t) = \tau_0 - \frac{\mu}{2\beta} \cdot V(t) + \int_\Gamma \mathrm{d}S(\boldsymbol{\xi'}) \int_0^t \mathrm{d}\tau \hat{K}(\boldsymbol{\xi}, t-\tau; \boldsymbol{\xi'}, 0)\dot{D}(\boldsymbol{\xi'}, \tau) \tag{4.26}$$

To form an ordinary differential equation, we want to rewrite the integral term into a function that solely depends on slip or slip rate. In section 4.4, we have shown that when only considering the static contribution, the integral can be written as a function of slip (equation (4.24)). In the case here, the dynamic component may not be insignificant in general. However, inspired by the static analysis, we may separate the integral kernel $\hat{K}$ into a static part and a dynamic part,

$$\begin{aligned} &\hat{K}(\boldsymbol{\xi}, t-\tau; \boldsymbol{\xi'}, 0) \\ &= \hat{K}(\boldsymbol{\xi}, t_\infty - \tau; \boldsymbol{\xi'}, 0) - \left(\hat{K}(\boldsymbol{\xi}, t_\infty - \tau; \boldsymbol{\xi'}, 0) - \hat{K}(\boldsymbol{\xi}, t-\tau; \boldsymbol{\xi'}, 0) \right) \end{aligned} \tag{4.27}$$

in which $t = t_\infty$ is a long enough time after when all location on fault has come back at rest and all the elastic waves have propagated outside the fault region. Substituting equation (4.27) into the integral in (4.26), we can separate the integral into two parts, and the first part can be expressed as a linear function of slip $D(t)$,

$$
\begin{aligned}
&\int_\Gamma \mathrm{d}S(\boldsymbol{\xi'}) \int_0^t \mathrm{d}\tau \hat{K}(\boldsymbol{\xi}, t-\tau; \boldsymbol{\xi'}, 0)\dot{D}(\boldsymbol{\xi'}, \tau) \\
&= \int_\Gamma \mathrm{d}S(\boldsymbol{\xi'}) \int_0^t \mathrm{d}\tau \hat{K}(\boldsymbol{\xi}, t_\infty-\tau; \boldsymbol{\xi'}, 0)\dot{D}(\boldsymbol{\xi'}, \tau) + \phi(t) \\
&\approx -C \cdot \frac{\mu}{L} \cdot D(t) + \psi(t)
\end{aligned}
\tag{4.28}
$$

in which,

$$
\psi(t) = \int_\Gamma \mathrm{d}S(\boldsymbol{\xi'}) \int_0^t \mathrm{d}\tau \Big(\hat{K}(\boldsymbol{\xi}, t_\infty-\tau; \boldsymbol{\xi'}, 0) - \hat{K}(\boldsymbol{\xi}, t-\tau; \boldsymbol{\xi'}, 0) \Big) \dot{D}(\boldsymbol{\xi'}, \tau). \tag{4.29}
$$

The term $\psi(t)$ here represents the difference between the static and the dynamic solution with instantaneous response $-\frac{\mu}{2\beta} \cdot V(t)$ excluded.

To carry on our analysis, we assert that $\psi(t)$ is considerably smaller than $-C \cdot \frac{\mu}{L} \cdot D(t)$. Physically, it is equivalent to assuming the temporal change in stress plays a smaller role than the static stress in terms of affecting the rupture process. This assumption should be proper when slip rate is small. With this assumption, equation (4.26) can be written as,

$$
\tau_{elastic}(t) = \tau_0 - \frac{\mu}{2\beta} \cdot V(t) - C \cdot \frac{\mu}{L} \cdot D(t) \tag{4.30}
$$

To form an equation, we also need to write out the fault resistance expression, which can be achieved using the "friction law". Considering that the frictional stress on fault has completely dropped to f_1, we have

$$
f(t) = f_1 + \eta_v \cdot V(t). \tag{4.31}
$$

Equating (4.30) with (4.31), we have,

$$\tau_0 - \frac{\mu}{2\beta} \cdot V(t) - C \cdot \frac{\mu}{L} \cdot D(t) = f_1 + \eta_v \cdot V(t),$$

taking differentials on both sides, we obtain an ordinary differential equation,

$$-\frac{\mu}{2\beta} \cdot \mathrm{d}V(t) - C \cdot \frac{\mu}{L} \cdot V(t)\,\mathrm{d}t = \eta_v \cdot \mathrm{d}V(t), \tag{4.32}$$

in which we write out $D(t)$ as $V(t)\,\mathrm{d}t$. This is an ordinary differential equation in which separation of variables is possible. We can write $V(t)$ and t on two sides of the equation separately.

$$\begin{aligned} \mathrm{d}t &= -\frac{1}{C} \cdot \frac{L}{\mu} \cdot \left(\frac{\mu}{2\beta} + \eta_v\right) \cdot \frac{\mathrm{d}V(t)}{V(t)} \\ &= -\frac{1}{C} \cdot \frac{L}{\mu} \cdot \left(\frac{\mu}{2\beta} + \eta_v\right) \mathrm{d}\ln V(t). \end{aligned} \tag{4.33}$$

Integrating (4.33) from $t = 0$ to $t = t$, we have,

$$t = -\frac{1}{C} \cdot \frac{L}{\mu} \cdot \left(\frac{\mu}{2\beta} + \eta_v\right) \cdot \ln\left(\frac{V(t)}{V_0}\right).$$

Solving for $V(t)$, we may obtain the evolution of slip rate,

$$\begin{aligned} V(t) &= V_0 \cdot \exp\left(-\frac{C\mu}{L} \cdot \left(\frac{\mu}{2\beta} + \eta_v\right)^{-1} \cdot t\right) \\ &= V_0 \cdot \exp\left(-C \cdot \left(1 + \frac{\eta_v}{\mu/2\beta}\right)^{-1} \cdot \frac{t}{L/2\beta}\right) \end{aligned} \tag{4.34}$$

Equation (4.34) gives the solution of $V(t)$. It shows that the slip rate will experience an exponential decay after reaching the peak level V_0. From the derivation we know that the exponential form of decay originates from the choice of linear viscous resistance.

A different functional form of viscous resistance (e.g., logarithm, polynomial) will lead to another functional form of decay, which will be discussed in section 6.3. Here, we focus on the slip rate decay time under linear viscous resistance. Based on (4.34), the characteristic slip rate decay time T_d can be defined as,

$$T_d = \frac{1}{C} \cdot \left(1 + \frac{\eta_v}{\mu/2\beta}\right) \cdot \frac{L}{2\beta}. \tag{4.35}$$

This result suggests that, aside from the elastic property μ and β and the patch geometry factor C, the characteristic slip rate decay time T_d is mainly controlled by both the characteristic slip patch length L and the viscous coefficient η_v. At the same time, stress conditions, such as static stress drop $\Delta\tau_s$ and dynamic frictional strength drop Δf, or slip parameters, such as final slip D and initial slip rate V_0, do not go into the expression for T_d. Again, I note that how L is controlled by the shape of the slip patch should not affect our analysis here, and thus one may treat L as an order-of-magnitude estimate of the rupture area dimension, because we only care about the first-order quantitative results.

Another way to obtain a characteristic decay time T_d is to divide the characteristic slip D (equation (4.26)) by the characteristic slip rate V (equation (4.17)),

$$\begin{aligned} T_d &= \frac{D}{V} \\ &= \frac{\Delta\tau_s}{\Delta f} \cdot \frac{1}{C} \cdot \left(1 + \frac{\eta_v}{\mu/2\beta}\right) \cdot \frac{L}{2\beta}, \end{aligned} \tag{4.36}$$

Equation (4.35) and (4.36) are almost the same except for a factor $\Delta\tau_s/\Delta f$ in (4.36). However, the physical significance of the similar results is more than a mere agreement. The expression of (4.35) is obtained from the $V(t)$ solution (4.34), which actually depicts

how slip rate decays, and T_d is the factor with a dimension of time in the exponent. The expression of (4.36), on the other hand, is obtained simply by dividing final slip D with the peak slip rate V right after the stress drop process. There is no guarantee that such an approach would yield an answer similar to (4.35), because the peak slip rate can be different from the average, or characteristic slip rate. In fact, it is at this point I demonstrate why the peak slip rate V derived in section 4.3 can be also treated as the characteristic slip rate. From this point of view, (4.35) is a more rigorous solution.

However, the derivation of (4.35) is not completely rigorous either, because we ignore the transient stress interaction $\psi(t)$ that is mediated by waves. If the patch is brought to failure by a transient stress wave (loading stress from τ_0 to f_0), this wave contribution may only be present during the slip rate decay process for a short amount of time. When the wave is gone, the slip rate may experience a drop as well. Not considering such effect may lead to an overestimate of T_d. Such effects are implicitly considered in the derivation of (4.36), and that's probably why the factor $\Delta\tau_s/\Delta f$ does not show in (4.35) but in (4.36).

Nevertheless, equation (4.36) would be the same as (4.35) to first-order if the static stress drop $\Delta\tau_s$ is of the same order as the dynamic strength drop Δf. This is probably the case for slow slip events because the stress interactions from elastic waves might not be strong in slow rupture propagation, and the triggering mechanism within a spontaneous slow slip event rupture might be dominated by static stress transfer. In the following order-of-magnitude analysis, I will assume $\Delta\tau_s/\Delta f \sim 1$ and use equation (4.35) for convenience. I note that if the frictional failure is almost entirely triggered by a transient stress ($\Delta\tau_s/\Delta f \ll 1$; e.g., tele-seismic surface wave, sudden pore pressure change), the

above assumption might not be correct.

4.5.2 Implications: T_d for slow slip event ruptures

We have just obtained some theoretical relations of the characteristic slip rate decay time T_d, the next step is to test whether the above theoretical relation can explain observations. Measuring the slip rate decay time in slow slip events can be challenging. With geodetic data, it is more convenient to measure the event duration T, which is how long the whole event lasts, due to its limited spatial resolution on fault. However, the event duration T is not only related to the slip rate decay time T_d, but also related to how long in time the rupture front propagates. If the rupture propagation time is longer than the slip rate decay time, the event duration T would be more closely related to the rupture propagation time. This complication is more convenient to discuss in a later section (section 4.8), after we derive the relation for the characteristic rupture propagation speed V_r of the current model. Therefore, in this section I focus on seismic observations.

With seismic data, it is possible to measure T_d more accurately than with geodetic data, if we assume that area with high slip rate (i.e., slipping fault) coincides with tremors and LFE locations. In that case, we may estimate T_d by measuring the duration of tremor activity at one location, and estimate the slipping area length by measuring the concurrent tremor activity length. This length is then treated as the characteristic slipping area dimension L that is used in equation (4.35). Figure 4.5 shows tremor migration patterns along strike in three subduction zones: (a) Tremors in the Cascadia subduction zone under northern Washington during the 2011 episodic tremor and slip event (Ghosh et al., 2015,

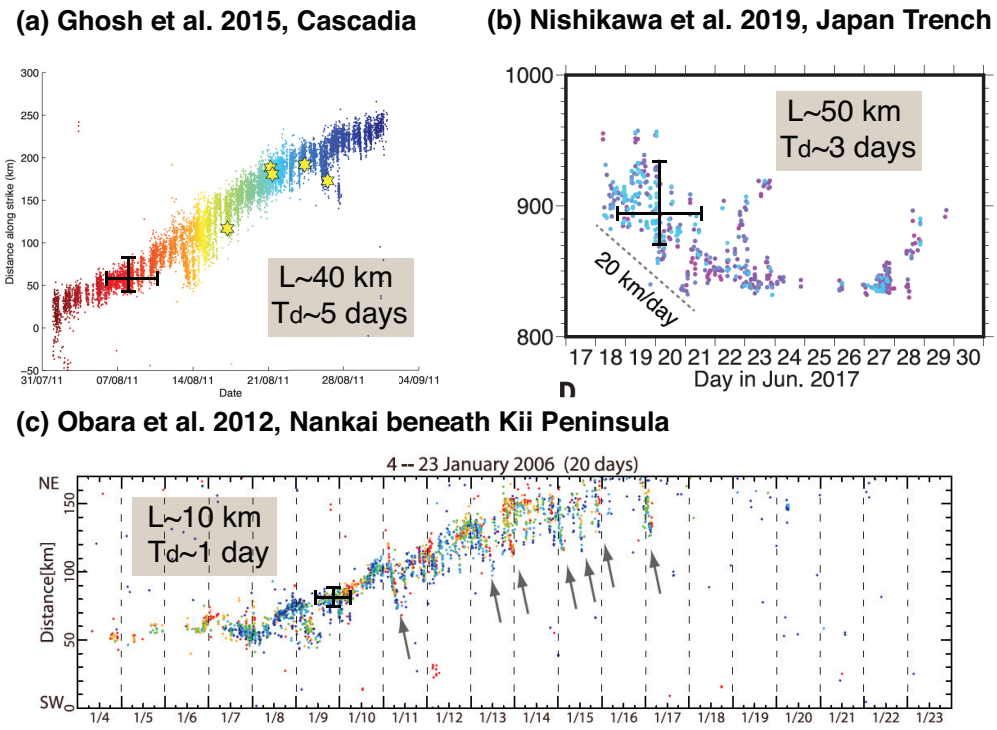

Figure 4.5: Three example tremor migration patterns reported in different subduction environments. I estimate the concurrent slipping area length L and slip rate decay time T_d from the three published figures and mark my estimations on the original figure using two black bars, one vertical and one horizontal. The numbers of my estimation are written on the side. (a). Tremors in the Cascadia subduction zone under northern Washington during the 2011 episodic tremor and slip event (Ghosh et al., 2015, Figure 5). (b). Tremors near the Japan Trench in 2017 (Nishikawa et al., 2019, Figure 1C). (c). Tremors in the Nankai subduction zone under Kii Peninsula in 2006 (Obara et al., 2012, Figure 1c).

Figure 5). (b) Tremors near the Japan Trench in 2017 (Nishikawa et al., 2019, Figure 1C). (c) Tremors in the Nankai subduction zone under Kii Peninsula in 2006 (Obara et al., 2012, Figure 1c). Since the purpose here is only first-order estimation, I roughly estimate L and T_d for the three published results directly on their figures using the drawing software Adobe Illustrator. For the Cascadia case, I estimate $L \sim 40$ km and $T_d \sim 5$ days. For the Japan Trench case, I estimate $L \sim 50$ km and $T_d \sim 3$ days. For the Nankai case, I estimate $L \sim 10$ km and $T_d \sim 1$ day.

As a side note, my theoretical relation of T_d does not explain why L would be of a certain value; instead, L is thought to be a given condition. L are all about a few tens of kilometers in the above observations. I suspect that it is related to the along-dip width of rupture area, which is also about a few tens of kilometers. Theoretically, when a rupture propagates along the strike of a long-narrow fault, the width of the high slip rate pulse behind the rupture front is of the same order of magnitude with the narrow side width (e.g., Dalguer & Day, 2009). The hypothesis of along-dip with controlling L is also supported by my numerical simulation in Chapter 5. Nevertheless, figuring out what control L is not the focus here. We can treat the measured value as a given condition and carry on with our analysis.

The above estimation all estimate T_d to be on the order of a few days, which is about 10^5 seconds. Such a long slip rate decay time cannot be explained by a traditional dynamic rupture model with only sudden weakening. In our model with a viscous response, a significantly longer decay time can be achieved with a high viscous coefficient η_v. Figure 4.6 plots T_d against η_v (in log-log space) using the theoretical relation (4.35) with C set to

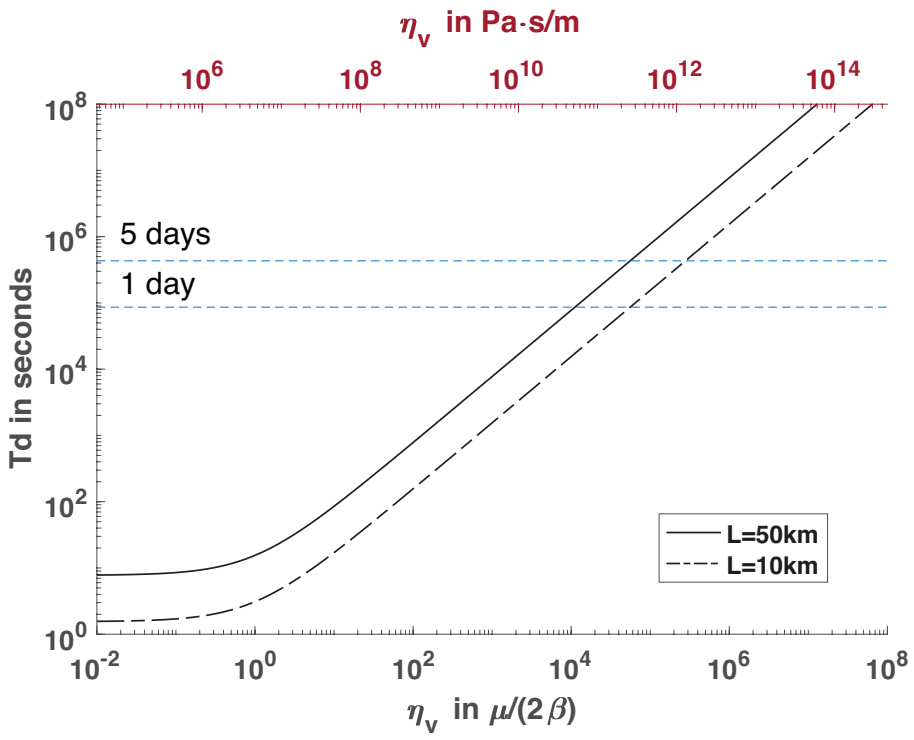

Figure 4.6: T_d against η_v (in log-log space) using the theoretical relation (4.35) with C set to be one and L fixed. The black solid line shows the case where L is fixed at 50 km, and the black dash line shows the case where L is fixed at 10 km. Two blue horizontal dashed lines are plotted indicating the location of 5 days and 1 day. Similar to Figure 4.3, I show the non-dimensional value of η_v on the bottom axis (black), and show the value in the physical units $\text{Pa} \cdot \text{s/m}$ on the top axis (red).

be one and L fixed. Since the estimated slip area length is about few tens of km, we show two cases with L fixed at 50 km (black solid line) and with L fixed at 10 km (black solid line). Two blue horizontal dashed line are plotted indicating the location of 5 days and 1 day. Figure 4.6 implies that, to generate a slip rate decay time T_d as long as a few days, η_v needs to be about $10^4 - 10^5$ $\mu/(2\beta)$.

Importantly, the estimation of η_v here using T_d is consistent with the estimation in previous sections. In section 4.3, I derive an expression of the characteristic slip rate V (equation (4.17)). Since V depends on both η_v and the dynamic stress drop Δf, we cannot simultaneously estimate both parameters using only the V observation. In section 4.4, I derive an expression of the characteristic final slip D (equation (4.25)). Using that expression, we may estimate the bulk static stress drop $\Delta\tau_s$ to be ~ 10 kPa. If we assume that Δf is of the same order as $\Delta\tau_s$, we may then substitute the ~ 10 kPa level into equation (4.17) to estimate η_v, and the corresponding η_v would be about $\sim 10^4 - 10^5$ $\mu/(2\beta)$.

Because the estimation of η_v using (4.35) does not involve any stress drop value, the estimation of η_v in this section should be an independent constraint. All our theoretical estimations have achieved reasonable agreement with observations so far. It suggests that the model setup we have here has potential to explain the first-order features of SSEs in a self-consistent manner.

4.6 Characteristic rupture propagation speed V_r

In this section, I will discuss the rupture propagation speed V_r under our "frictional-viscous" model setup. We are interested in V_r because it can be estimated using tremor

migration speed, if we assume that tremors and LFEs coincide with the SSE rupture front. For the main SSE rupture front, the rupture propagation speed is estimated to be on the order of ~ 10 km/day. This value is significantly lower than the typical rupture propagation speed ($\sim$ km/s) in fast earthquakes, and cannot be explained with a classic "sudden stress drop" earthquake rupture model. In the following text, I will first derive the theoretical relation for V_r under the "frictional-viscous" model setup, and then discuss its implications for SSEs.

4.6.1 Analytical results

In the dynamic rupture model we explore here, there is no migration of an external forcing (like fluid migration). Rupture propagates due to a slip cascade: the slipping fault area causes a stress change in the un-slipped fault area, and triggers it to slip. The rupture speed would then depend on how fast the stress transfers on fault. In section 2.3, we show that the slipping fault area would cause two types of stress perturbation to the nearby fault: the dynamic stress perturbation and the static stress perturbation. The dynamic stress perturbation travels at the speed of seismic waves. As shown in equation (2.7), a propagating rupture that is mainly triggered by dynamic stress perturbations would have a propagation speed V_{rd} that is similar to a seismic wave speed,

$$V_{rd} \approx \beta,$$

where β is the shear wave speed. On the other hand, the traveling speed of the propagating rupture that is mainly triggered by the static stress perturbation depends on the slip rate of

the slipping area. As shown in equation (2.12), if the rupture is mainly triggered by static stress perturbation, the propagation speed V_{rs} can be expressed as,

$$V_{rs} \approx \frac{L_s}{L_p} \cdot \frac{\mu}{S\Delta\tau_s} \cdot V,$$

in which L_p is the characteristic length of the high slip rate zone behind the rupture front, and L_s is the characteristic length of the high stressing rate zone ahead of the rupture front (Figure 2.2). L_s should be comparable to L_p ($\frac{L_s}{L_p} \approx 1$). S is the ratio between strength excess $f_0 - \tau_0$ and static stress drop $\Delta\tau_s$, so $S\Delta\tau_s$ is the strength excess. V is the characteristic slip rate at the rupture front.

In section 2.3, we have shown that for an earthquake rupture model that only considers a sudden stress drop component, both V_{rd} and V_{rs} will be similar to seismic wave speed, which is of the order of km/s. It means that a "sudden stress drop model" will always have a rupture propagation speed at a km/s level. Since it is consistent with the rupture speed observations of fast earthquakes, we may conclude that a "sudden stress drop" model is a decent first-oder description for fast earthquakes.

For the "frictional-viscous" model, the above two triggering mechanisms should also exist, and therefore we may directly use equations (2.7) and (2.12) to analyze the rupture propagation speed in the the "frictional-viscous" model. The dynamic-stress-led rupture speed V_{rd} would still be $\sim \beta$. For the static-stress-led rupture speed V_{rs}, we need to substitute the characteristic slip rate V of the "frictional-viscous" model (equation (4.17)) into equation (2.12), and we will obtain,

$$
\begin{aligned}
V_{rs} &\approx \frac{L_s}{L_p} \cdot \frac{\mu}{S\Delta\tau_s} \cdot \frac{2\Delta f}{\mu} \cdot \left(1 + \frac{\eta_v}{\mu/(2\beta)}\right)^{-1} \cdot \beta \\
&\approx \frac{L_s}{L_p} \cdot \left(1 + \frac{1}{S}\right) \cdot \left(1 + \frac{\eta_v}{\mu/(2\beta)}\right)^{-1} \cdot 2\beta,
\end{aligned}
\tag{4.37}
$$

in which we makes use the relation that $\Delta f/\Delta\tau_s = 1+S$. Since $\frac{L_s}{L_p}$ and $1+\frac{1}{S}$ are both about the order of 1 and are not likely to have a variation of several orders of magnitude, V_{rs} is mostly controlled by the viscous coefficient η_v through the ratio $\frac{\eta_v}{\mu/(2\beta)}$. If η_v is high, V_{rs} can be quite low, and there will a η_v that corresponds to the observed rupture propagation speed for SSEs.

4.6.2 Implications for slow slip event

In the "frictional-viscous" model, the dynamic stress transfer speed V_{rd} would always be of seismic wave speed, while the static stress transfer speed V_{rs} can be significantly lower due to a lower characteristic slip rate V. Can the "frictional-viscous" model explain the abnormally low rupture propagation speed in SSEs?

It should. If the static stress transfer is the dominant rupture triggering mechanism, since V_{rs} decreases with η_v, we may find a η_v that corresponds to the observed rupture speed for SSEs. However, one thing we have not considered yet is the relative amplitude of the two types of stress transfer. The amplitude of the dynamic stress transfer mainly depends on the slip rate of the slipping area. In general, the greater the slip rate, the stronger the dynamic stress perturbation. On the other hand, the amplitude of the static stress transfer is mainly controlled by the slip. In general, the greater the slip, the stronger the static stress perturbation. In the "frictional-viscous" model, the slip rate de-

creases significantly as η_v increases, while the final slip is not affected by η_v. Therefore, the amplitude of dynamic stress transfer should decrease as η_v increases, while the amplitude of static stress transfer is not affected. As a result, V_{rs} should outweigh V_{rd} in representing the rupture propagation speed V_r when η_v is large, and V_r can be significantly lower than a typical seismic wave speed.

Figure 4.7 shows how rupture propagation speed V_r changes with η_v in our theoretical model. The black dashed line shows the V_r when the dynamic stress transfer is in control (referred to as V_{rd}), and the black solid line shows the V_r when the static stress transfer is in control (referred to as V_{rs}). Since dynamic stress transfer always travels at a seismic wave speed, V_{rd} is not affected by η_v. V_{rs} stay at the seismic wave level when η_v is smaller than 1 $\mu/(2\beta)$. As η_v increases, V_{rs} decreases significantly. When one of the mechanisms is dominant, the rupture speed V_r curve should be better represented by the corresponding curve.

When η_v is small, both static and dynamic stress are important, and both V_{rd} and V_{rs} are of the order of km/s. Therefore, V_r should also be of the order of km/s. To first order, this theoretical result is consistent with the observed rupture speed in fast earthquakes (roughly bounded by the two brown dashed lines, $2 - 7$ km/s). When η_v is large, V_r should be better represented by V_{rs} because static stress transfer becomes the dominant triggering mechanism. To explain the low observed rupture propagation speed in SSEs (roughly bounded by the two blue dashed lines, $4 - 40$ km/day), η_v need to be $\sim 10^4 - 10^5$ $\mu/(2\beta)$.

This η_v value is consistent with the η_v estimation using other SSE observables in

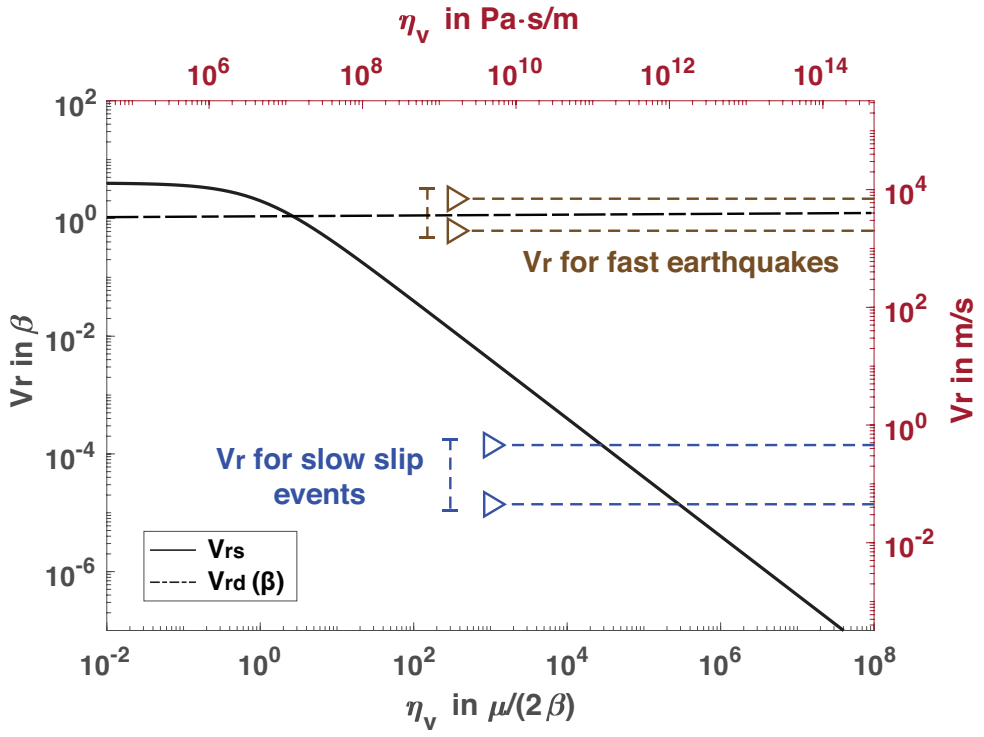

Figure 4.7: The relation between rupture propagation speed V_r and viscous coefficient η_v yielded in equation (2.7) for the dynamic stress transfer speed V_{rd} (black dashed line) and in equation (4.37) for the static stress transfer speed (black solid line). For a clearer insight on the physical process, I non-dimensionalize η_v and V_r using $\mu/(2\beta)$ and β, respectively. The non-dimensional value of η_v and V_r are shown on the bottom and left axis (black). To facilitate comparison with observations, I also show η_v and V in their physical units Pa $\cdot$ s/m and m/s on the top and right axis (red), assuming $\mu = 3 \times 10^{10}$ Pa and $\beta = 3.23 \times 10^3$ m/s. To compare with observations, I show two sets of horizontal dashed lines with a triangle at the left end to denote the typical V_r ranges for fast earthquakes (brown dash lines, $2 - 7$ km/s) and slow slip events (blue dashed lines, $4 - 40$ km/day).

previous sections. Importantly, since the V_r observations for SSEs are independent from other observations that we discussed earlier, the agreement between model and observations here should be independent from the agreement we demonstrate earlier. Our results here again imply that the "frictional-viscous" model has the potential to be a useful representation of the actual SSE process, and thus explain different SSE observations in a self-consistent way.

4.7 Diffusive behavior of tremor migrations

4.7.1 Observations of diffusive tremors behavior

Tremors are sometimes found to have a diffusive migration pattern: the time t it takes for tremors to propagate is proportional to the square of the propagation distance x,

$$t = (D_f)^{-1} \cdot x^2 \tag{4.38}$$

in which I use D_f to denote diffusivity instead of D to distinguish it from the final slip.

The diffusive behavior of tremor migrations has been reported in the Nankai subduction zone (Ide, 2010; Ando et al., 2012; Poiata, Vilotte, Shapiro, Supino, & Obara, 2021). Recently, Creager, Ulberg, and Houston (2020) report diffusive behaviors of tremor in the Cascadia subduction (Creager et al. (2020) is an abstract in AGU Fall Meeting 2020 and their paper haven't come out by the time I write this manuscript). Figure 4.8 shows two examples of diffusive tremor migration in the Nankai subduction zone reported by Ide (2010) (his Figure 3a) and Ando et al. (2012) (their Figure 1a). In both cases, the initial tremor burst has a length about 10 to 20 km, and propagates outwards for several tens

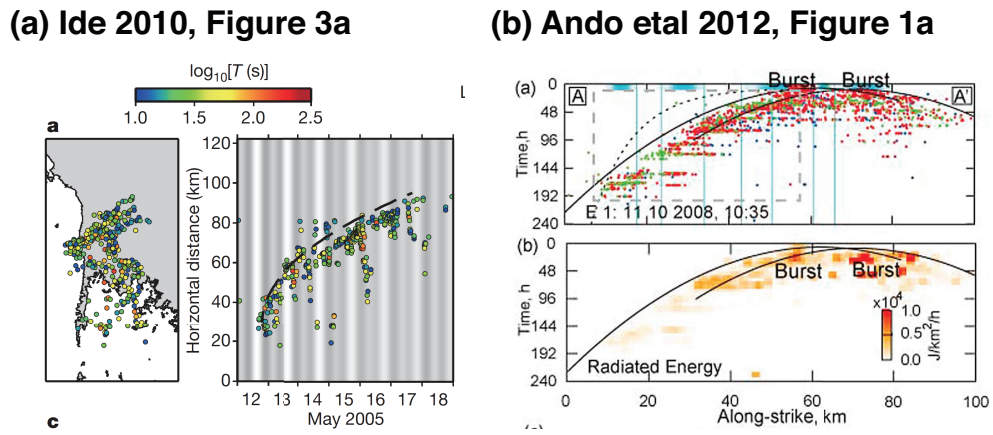

Figure 4.8: Two examples of diffusive tremor migration in Nankai subduction zone reported by Ide (2010) (Figure 3a) and Ando et al. (2012) (Figure 1a)

of kilometers in a diffusive manner. The diffusivities reported in these two studies are 10^4 m^2/s and 0.5×10^4 m^2/s, respectively. Creager et al. (2020) reports that the diffusivity for the diffusive tremor migration in the Cascadia subduction zone is 2 to 5×10^3 m^2/s. In summary, the few reported diffusivities for diffusive tremor migration are of the order of $10^3 - 10^4$ m^2/s.

4.7.2 Explanation in Ando et al. (2012)

If we assume that tremor activities coincide with the SSE rupture front, the above observations would suggest that the SSE ruptures are diffusive. Such a diffusive rupture propagation is seldom reported for fast earthquakes, except for those earthquake swarms that are thought to be controlled by the migration of external forcing such as fluids. Ando et al. (2012), which is one of the three papers related to the Ando's model (see section 4.1 for definition), demonstrates that the diffusive rupture pattern can be reproduced with the "frictional-viscous" model discussed here. Ando et al. (2012) consider a situation where

there is a strong patch in the central position of the fault with a high stress drop. The strong patch is surrounded by a weaker area of fault, and rupture propagates from the strong patch outward into the un-ruptured, weaker area. In contrast to section 4.6, where we consider that the rupture propagates due to a cascade of fault slip at the rupture front, Ando et al. (2012) consider that the slip outside the strong patch is too weak to push itself forward and cascade; instead, the rupture propagation outside the strong patch is still driven by the static stress field of the strong patch, and thus would yield diffusive response.

In addition to numerical simulations, Ando et al. (2012) provide an analytical quasi-static solution of stress evolution in 2D, where a concentrated point source has a stress drop at the origin, and the shear stress propagates outward to a pure velocity-strengthening (viscous) fault (Figure 4.9a). They obtain the solution by directly solving the boundary integral equations. The solution implies a diffusive stress evolution. Using the solution, Ando et al. (2012) obtain a relation that can associate η_v with the observed diffusivity D_f (equation 4 in Ando et al. (2012)),

$$D_f = \frac{\mu \Delta\tau L_i}{2\pi\eta_v \tau_e} \tag{4.39}$$

in which I switch the original variable name D with D_f. $\Delta\tau$ is the prescribed stress drop at the origin. L_i is the effective length of the concentrated point source. τ_e is the difference between yielding strength and initial stress on the fault except for the origin.

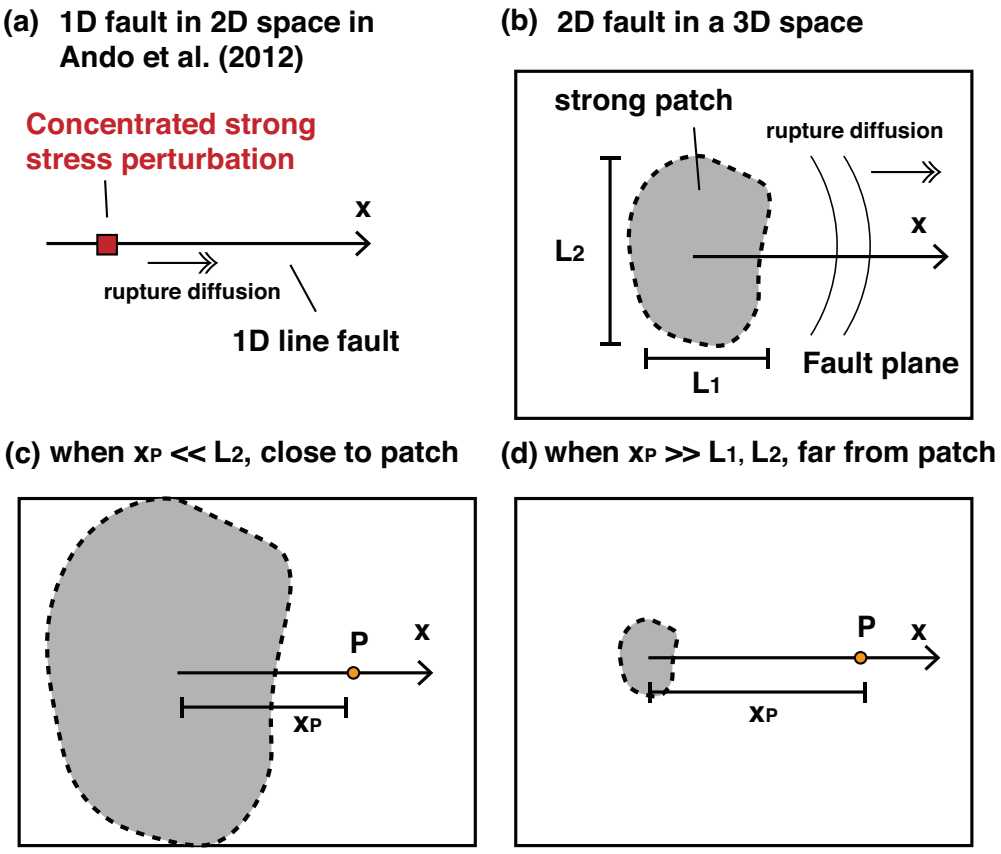

Figure 4.9: (a) Schematic of the 2D analytical model setup in Ando et al. (2012). (b) Schematic of the 3D analytical model setup in this research. Rupture that propagates along the x direction is considered. The strong patch dimension parallel to x is L_1, and the dimension perpendicular to x is L_2. (c) Schematic showing the situation when point P is close to the patch and $x_P \ll L_2$. (d) Schematic showing the situation when point P is far away from the patch and $x_P \gg L_1$ and L_2.

4.7.3 My analytical solution

In this part, I will illustrate the diffusive behavior of tremor migrations (and thus SSE rupture propagations) and derive the relation between η_v and D_f using a slightly different approach from Ando et al. (2012). The new derivation may not be as rigorous as in Ando et al. (2012), but would fit better to the demonstration flow here from a holistic point of view. As I will show in the end, my derivation here yields the same D_f-η_v relation as in Ando et al. (2012) (equation (4.39)). Instead of considering a 2D model with stress drop concentrated at the origin, I consider a general 3D model with a strong patch that has finite area (Figure 4.9b). I consider that the rupture propagates along the x direction. The strong patch dimension parallel to x is L_1, and the dimension perpendicular to x is L_2. Within the strong patch, the initial stress is set to be the same as the yielding stress, and the whole patch starts to slip simultaneously with a sudden stress drop of Δf. Outside the strong patch, the fault needs an incremental stress increase of $\tau_e = f_0 - \tau_0$ in order to start slip. Similar to Ando et al. (2012), I ignore the stress cascade outside the strong patch, and consider that the rupture propagation outside the strong patch is entirely controlled by the stress influence from the strong patch. Everywhere on the fault is "frictional-viscous" with a viscous coefficient of η_v.

Let's consider a point P on the x axis outside of the strong patch. Its distance to the center of the patch is x_P. We are interested in the stress perturbation on P received from the patch. In section 4.6, we demonstrate that the slipping fault would send out two types of stress to the un-ruptured area: dynamic stress and static stress. Dynamic stress always travels at seismic wave speeds. So if the fault at P is triggered by a dynamic stress

perturbation, a diffusive rupture propagation will not be plausible. However, we have shown that when η_v is large, the slip rate decreases significantly while final slip is not affected. In this case, the static stress transfer becomes the dominant mechanism, and the stress perturbation on P might be evaluated by only considering the static stress transfer.

At time t, the strong patch slip is $D(t)$. The stress perturbation at point P at time t can be evaluated using a static stress transfer solution (e.g., Okada, 1992). By doing this, I assume that the stress increase due to the patch's increasing slip is slow enough that the wave travel time from the patch to point P is negligible. Since we are interested in the diffusive behavior, what we care about the static solution is how fast the stress decay with distance. If P is close to patch, the stress perturbation should be close to the stress drop $\Delta\tau(t)$ on fault, which can be written as,

$$\Delta\tau(t) = C \cdot \mu \cdot \frac{D(t)}{L} \tag{4.40}$$

where C is a constant close to 1 that depends on the geometry of the patch. L is the characteristic length of the patch in terms of stress drop. It tends to be the shortest dimension of the patch.

Let's first consider this situation: Point P is close to the patch and $x_P \ll L_2$ (Figure 4.9c). This is most likely when L_2 is considerably greater than L_1 (the extreme condition is a 2D model). If we ignore the short travel time of the static stress propagation, the stress perturbation $\tau(x_P, t)$ at point P at time t could be roughly estimated as $\Delta\tau(t)$ times a decay factor that depends on the distance x_P. For case 1 where $x_P \ll L_2$, solutions in Okada (1992) suggest that the decay is $\sim 1/(x_P)^2$. We will have,

$$\begin{aligned}\tau(x_P,t) &\approx \Delta\tau(t)\cdot\frac{(L_1)^2}{(x_P)^2}\\ &= C\cdot\mu\cdot\frac{D(t)}{L}\cdot\frac{(L_1)^2}{(x_P)^2}\end{aligned} \tag{4.41}$$

To obtain $\tau(x_P,t)$, we need to have the expression of $D(t)$. In section 4.5, we have obtained the slip rate $V(t)$ evolution of a fault patch in equation (4.34). $D(t)$ can be obtained simply by integrating $V(t)$ from 0 to t,

$$\begin{aligned}D(t) &= \int_0^t V(\tau)\,\mathrm{d}\tau\\ &= V_0\cdot\int_0^t \exp\left(-C\cdot\left(1+\frac{\eta_v}{\mu/2\beta}\right)^{-1}\cdot\frac{\tau}{L/2\beta}\right)\mathrm{d}\tau\\ &= V_0\cdot\frac{1}{C}\cdot\left(1+\frac{\eta_v}{\mu/2\beta}\right)\cdot\frac{L}{2\beta}\cdot\left[1-\exp\left(-C\cdot\left(1+\frac{\eta_v}{\mu/2\beta}\right)^{-1}\cdot\frac{t}{L/2\beta}\right)\right]\end{aligned} \tag{4.42}$$

in which V_0 is the initial slip rate of the patch. Since the initial stress on the patch is the same as the yielding stress, we may estimated V_0 using the characteristic slip rate V (equation (4.17)),

$$V_0 \approx \left(1+\frac{\eta_v}{\mu/(2\beta)}\right)^{-1}\cdot\frac{2\Delta f}{\mu}\cdot\beta.$$

Substituting into (4.42), we may obtain an expression for $D(t)$,

$$D(t) \approx \frac{1}{C}\cdot\frac{\Delta f}{\mu}\cdot L\cdot\left[1-\exp\left(-C\cdot\left(1+\frac{\eta_v}{\mu/2\beta}\right)^{-1}\cdot\frac{t}{L/2\beta}\right)\right]. \tag{4.43}$$

Then, substituting equation (4.43) into (4.41) and assuming $L\approx L_1$, we will obtain,

$$\tau(x_P,t) \approx \Delta f\cdot\frac{L^2}{(x_P)^2}\cdot\left[1-\exp\left(-C\cdot\left(1+\frac{\eta_v}{\mu/2\beta}\right)^{-1}\cdot\frac{t}{L/2\beta}\right)\right] \tag{4.44}$$

Equation (4.44) implies that the stress perturbation at point P would gradually increase with time. However, there is an upper limit of the stress perturbation, which is approximately the stress drop on the strong patch times the decay factor $L^2/(x_P)^2$.

We have specified that outside the strong patch, the fault needs an incremental stress increase of $\tau_e = f_0 - \tau_0$ in order to start slip. We may substitute τ_e into the left hand side of equation (4.44), and solve for the relation between t and x_P. We obtain,

$$t \approx \frac{1}{C} \cdot \left(1 + \frac{\eta_v}{\mu/2\beta}\right) \cdot \frac{L}{2\beta} \cdot \ln\left(\frac{1}{1 - \frac{\tau_e}{\Delta f} \cdot \frac{(x_P)^2}{L^2}}\right) \tag{4.45}$$

Since logarithms cannot have negative variable, the ratio $\frac{\tau_e}{\Delta f} \cdot \frac{(x_P)^2}{L^2}$ cannot be larger than 1. Physically, it means that the static stress transfer distance cannot be so large such that even the highest possible stress perturbation $\Delta f \cdot \frac{L^2}{(x_P)^2}$ is still smaller than the required stress increment τ_e. Let us assume for now that the strong patch stress drop Δf is 10 times larger than the required stress increment τ_e ($\Delta f = 10\tau_e$), the maximum rupture propagation distance would be,

$$\begin{aligned} \max x_P &\approx \sqrt{\frac{\Delta f}{\tau_e}} \cdot L \\ &\approx 3L. \end{aligned} \tag{4.46}$$

This equation suggests that the strong patch static stress forcing can only influence the surrounding fault within a few patch lengths, depending on how much larger the stress drop on the patch is compared to the ambient stress outside. It is consistent with what is observed in case of the diffusive tremor migration (Ide, 2010; Ando et al., 2012; Creager et al., 2020; Poiata et al., 2021).

Although we have obtained a relation between t and x_P, it does not have a strict form of diffusive behavior as $t = (D_f)^{-1} \cdot (x_P)^2$. Instead, the diffusion is in a complicated logarithmic form. However, the $t = (D_f)^{-1} \cdot (x_P)^2$ type of diffusive behavior is actually contained in the complex expression. There are two ways to see it. One way is to simplify our derivation all the way back starting from (4.41). Rather than seeking a solution for $D(t)$, we may take a time-derivative on both sides of the (4.41) and assume $L \approx L_1$. We can obtain an expression for the stressing rate,

$$\begin{aligned} \dot{\tau}(x_P, t) &\approx C \cdot \mu \cdot \frac{\dot{D}(t)}{L} \cdot \frac{L^2}{(x_P)^2} \\ &= C \cdot \mu \cdot \frac{V(t)}{L} \cdot \frac{L^2}{(x_P)^2} \end{aligned} \tag{4.47}$$

Noted that the denominator is not simplified in order to keep the equation in a clear format to perform dimension analysis. Next, we may substitute the initial slip rate V_0 into (4.47), and use the resulting stressing rate as a representative value,

$$\begin{aligned} \dot{\tau} &\approx C \cdot \mu \cdot \frac{V_0}{L} \cdot \frac{L^2}{(x_P)^2} \\ &= C \cdot \frac{2\beta}{L} \cdot \Delta f \cdot \left(1 + \frac{\eta_v}{\mu/(2\beta)}\right)^{-1} \cdot \frac{L^2}{(x_P)^2} \end{aligned} \tag{4.48}$$

This assumption is similar to the assumption Ando et al. (2012) make in their derivation where they only consider the situation at the "initial moment" (text below their equation 3). We may then calculate the time t simply by dividing the required stress incremental τ_e with the representative stressing rate,

$$
\begin{aligned}
t &\approx \frac{\tau_e}{\dot{\tau}} \\
&= \frac{1}{C} \cdot \frac{1}{L \cdot 2\beta} \cdot \frac{\tau_e}{\Delta f} \cdot \left(1 + \frac{\eta_v}{\mu/(2\beta)}\right) \cdot (x_P)^2
\end{aligned}
\tag{4.49}
$$

The above equation has a form of diffusion relation, $t = (D_f)^{-1} \cdot (x_P)^2$. We may get the diffusivity expression as,

$$
\begin{aligned}
D_f &= C \cdot \frac{\Delta f}{\tau_e} \cdot \left(1 + \frac{\eta_v}{\mu/(2\beta)}\right)^{-1} \cdot L \cdot 2\beta \\
&= \frac{C\mu\Delta f L}{\eta_v \tau_e} \cdot \left(\frac{\mu/(2\beta)}{\eta_v} + 1\right)^{-1}
\end{aligned}
\tag{4.50}
$$

This expression is almost identical to that derived by Ando et al. (2012) (equation (4.39)). A major difference is the factor $\left(\frac{\mu/(2\beta)}{\eta_v} + 1\right)^{-1}$, which contains a comparison between the viscous coefficient η_v and the radiation damping factor $\mu/(2\beta)$. I suspect that this difference exists because Ando et al. (2012) considers a quasi-static model, while I consider a quasi-dynamic model with the radiation damping term. My solution approaches their solution when η_v is significantly larger than $\mu/(2\beta)$ and the geometric constant $C = 1/(2\pi) \approx 0.16$.

Another way to extract the $t = (D_f)^{-1} \cdot (x_P)^2$ type diffusive behavior from equation (4.45) is to use the a Taylor series expansion of the logarithmic function in (4.45). We may treat $\frac{\tau_e}{\Delta f} \cdot \frac{(x_P)^2}{L^2}$ as the variable in the logarithmic function, and the domain of the function is [0 1). We perform a Taylor series expansion of the function $\ln\left(\frac{1}{1-x}\right)$ near zero, and we obtain,

$$\begin{aligned}\ln\left(\frac{1}{1-\frac{\tau_e}{\Delta f}\cdot\frac{(x_P)^2}{L^2}}\right) &= 0+\frac{\frac{\tau_e}{\Delta f}\cdot\frac{(x_P)^2}{L^2}}{1-\frac{\tau_e}{\Delta f}\cdot\frac{(x_P)^2}{L^2}}+o\left(\frac{\tau_e}{\Delta f}\cdot\frac{(x_P)^2}{L^2}\right)\\ &\approx \frac{\frac{\tau_e}{\Delta f}\cdot\frac{(x_P)^2}{L^2}}{1-\frac{\tau_e}{\Delta f}\cdot\frac{(x_P)^2}{L^2}}.\end{aligned} \tag{4.51}$$

To further simplify the expression, we may assume $1-\frac{\tau_e}{\Delta f}\cdot\frac{(x_P)^2}{L^2}\approx 1$ when $\frac{\tau_e}{\Delta f}\cdot\frac{(x_P)^2}{L^2}$ is close to zero, and we will have,

$$\ln\left(\frac{1}{1-\frac{\tau_e}{\Delta f}\cdot\frac{(x_P)^2}{L^2}}\right)\approx\frac{\tau_e}{\Delta f}\cdot\frac{(x_P)^2}{L^2}. \tag{4.52}$$

Substituting (4.52) into (4.39), we will obtain a $t=(D_f)^{-1}\cdot(x_P)^2$ type equation that is exactly the same as equation (4.49), and thus leads to the same result as the "constant-stressing rate" assumption. The benefit of having the "Taylor series expansion" derivation is that we know x_P needs to be close to the strong patch in order for the diffusive behavior to exist. In practice, when we try to fit a parabolic curve to the tremor migration observation, we are mainly fitting the early part, because a parabolic curve predicts an infinite rupture distance, while the observed ruptures always slow down and stop at a certain distance.

The above derivation can also be applied to another situation, where Point P is far away from the patch, and x_P is significantly larger than both L_1 and L_2 (Figure 4.9d). This case is most likely to occur when L_1 is similar to L_2. In that case, the only thing different is the decay factor, which changes from a squared decay to a cubic decay,

$$\begin{aligned}\tau(x_P,t) &\approx \Delta\tau(t)\cdot\frac{(L_1)^3}{(x_P)^3}\\ &= C\cdot\mu\cdot\frac{D(t)}{L}\cdot\frac{L^3}{(x_P)^3}\end{aligned} \tag{4.53}$$

This difference in the decay factor does not affect all the other steps in the previous derivation. Following similar steps, we may obtain the $t - x_P$ relation for the cube decay case as,

$$t \approx \frac{1}{C} \cdot \left(1 + \frac{\eta_v}{\mu/2\beta}\right) \cdot \frac{L}{2\beta} \cdot \ln\left(\frac{1}{1 - \frac{\tau_e}{\Delta f} \cdot \frac{(x_P)^3}{L^3}}\right) \tag{4.54}$$

and similarly, we can write out the approximate diffusion pattern near the strong patch as,

$$t \approx \frac{1}{C} \cdot \frac{1}{L^2 \cdot 2\beta} \cdot \frac{\tau_e}{\Delta f} \cdot \left(1 + \frac{\eta_v}{\mu/(2\beta)}\right) \cdot (x_P)^3 \tag{4.55}$$

I note that the "near strong patch" assumption is seemly contradicted by the "$x_P \gg L_1$ and L_2" assumption. However, these two assumptions do not have to be exclusive. The "$x_P \gg L_1$ and L_2" assumption is satisfied when the static stress drop decay changes from a squared decay to a cubic decay. This change can happen while the "near strong patch" assumption is still satisfied.

4.7.4 Discussions and Implications

In the text above, I have discussed how a "frictional-viscous" model is able to generate diffusive rupture behaviors with a stronger patch surrounded by weaker fault area. This type of diffusive rupture behavior is controlled by the static stress transfer. Therefore, it can only be dominant when the slip rate is slow and the dynamic stress transfer is weak. This is probably why the diffusive rupture behavior is rare for fast earthquakes but often observed in SSEs.

In the model we discuss, we require that the rupture outside the strong patch can

only be driven by the static stress field of the patch. This is different from the situation we discuss in section 4.6, where the rupture front can cascade by itself. These two mechanisms can be treated as two modes of rupture propagations for SSEs. In reality, both modes may exist, and switch back-and-forth. As demonstrated in the previous derivation, whether the propagation is diffusive does not depend on the whether a part of the fault is viscous or frictional. The main factor is the stress distribution condition at the time under consideration. Since the stress condition evolves with time, the same place can have diffusive or constant speed rupture at different time (e.g., in different ETS events). This is consistent with the tremor migration observations in Nankai subduction zone (Ide, 2010). For the same reason, both modes can exist in the same tremor migration sequence at different stages. As reported by Creager et al. (2020), the episodic tremor and slip (ETS) events in the northern Cascadia subduction zone often start as diffusive ruptures, and experience a transition to constant speed ruptures later on.

In the previous sections, I have shown that a viscous coefficient η_v of the order of $\sim 10^4 - 10^5\ \mu/(2\beta)$ can simultaneously explain different independent SSE observations. A good parameter we may model with the diffusive tremor migration observations is the diffusivity D_f. In the "frictional-viscous" model, the relation between D_f and η_v is given by equation (4.50). In the Nankai and Cascadia subduction zones where diffusive tremor migration behaviors have been reported, D_f is measured to be about $10^3 - 10^4$ m^2/s. We may then use this observation to estimate η_v.

Figure 4.10 shows how D_f changes with η_v in the theoretical relation (4.50). For each line in the plots, the characteristic strong patch length L, the constant C, and the ratio

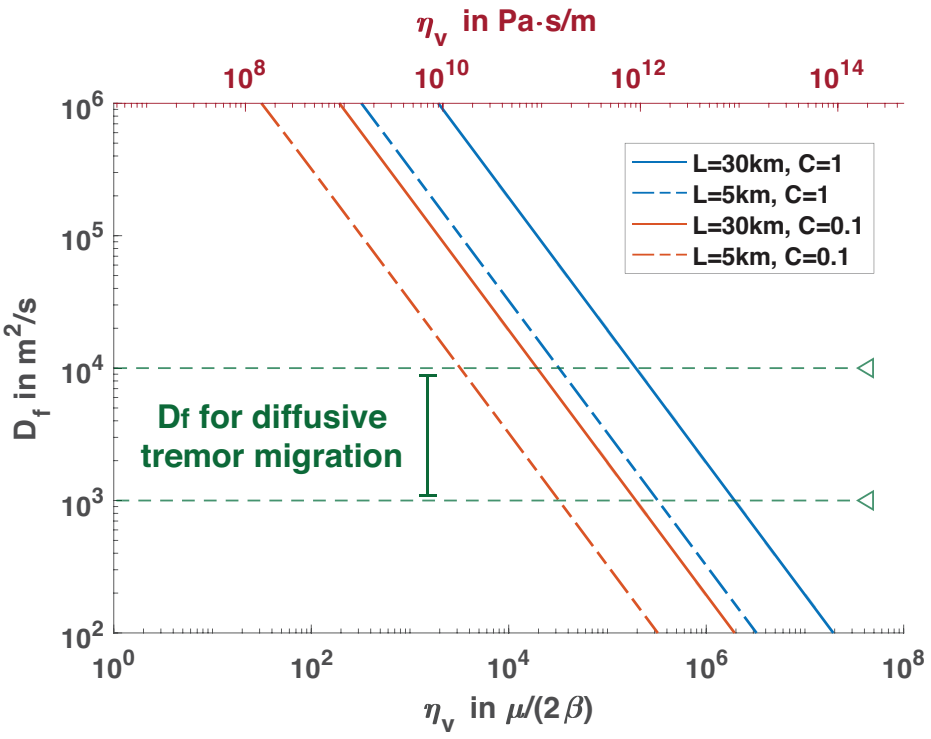

Figure 4.10: How D_f changes with η_v in the theoretical relation (equation (4.50)). For each line in the plots, characteristic strong patch length L, the constant C, and the ratio $\Delta f/\tau_e$ are fixed. Cases with different L and C are shown, while $\Delta f/\tau_e$ is kept as 10. Different values of L are denoted by different line styles: solid lines show the cases where $L = 30$ km, while dash lines show the cases where $L = 5$ km. Different C are denoted by different line colors: blue lines show the cases where $C = 1$, while orange lines show the cases where $C = 0.1$. The space between the two green horizontal dashed lines denote the range of observed D_f for diffusive tremor migrations.

$\Delta f/\tau_e$ are fixed. Cases with different L and C are shown, while $\Delta f/\tau_e$ is kept as 10. We picked 5 km and 30 km as two typical values of L, and pick 1 and 0.1 as two typical value of C. As shown in the figure, the observed $D_f \approx 10^3 - 10^4$ m^2/s corresponds to a η_v in the range of $\sim 10^3 - 10^6$ $\mu/(2\beta)$, which is consistent with our previous estimation. I note that Ando et al. (2012) made an estimation of η_v assuming $D_f = 10^4$ m^2/s, $L = 10$ km, $C = 0.1$ (since $1/(2\pi) \approx 0.16$), $\Delta f/\tau_e = 10$, and $\mu = 10^{10}$ Pa. They obtain that $\eta = 10^{10}$ Pa $\cdot$ m/s, which is the same as the estimation here. Although it is not a surprise that the two estimates agree since we are literally using the same relation, the agreement at least assure me that the calculation I have is correct.

As a quick summary for this rather long section of diffusive tremor migration behavior, I revisit, complement, and extend the analytical analysis in Ando et al. (2012) and demonstrate that a "frictional-viscous" model can produce diffusive rupture with a stronger patch surrounded by weaker fault area. Most importantly, we may estimate the viscous coefficient η_v that is required to explain the D_f observation to be $\sim 10^3 - 10^6$ $\mu/(2\beta)$, which is consistent with the η_v that is required to explain other independent observations. These consistency, again, strongly imply the potential of the frictional-viscous model as a realistic representation of the SSE rupture process.

4.8 The scaling relation between moment M_0 and event duration T

The scaling relation between moment M_0 and event duration T is among the most debated puzzles for the problem of slow earthquakes. Here, we will focus on the scaling of

slow slip events (SSEs). Fast earthquakes are known to have a $M_0 \propto T^3$ scaling to first order (e.g. Allmann & Shearer, 2009). However, it has been proposed that slow slip events could have a moment-duration scaling of $M_0 \propto T$ (e.g. Ide, Beroza, Shelly, & Uchide, 2007a; Gao et al., 2012; Liu, 2014). Recently, some studies reported that slow slip events have $M_0 \propto T^3$ scaling similar to fast earthquakes, only with the duration being longer (e.g. Gomberg, Wech, et al., 2016; Michel et al., 2019; Frank & Brodsky, 2019). From an observational point of view, these seemly contradictory arguments could well be due to sparse and poor datasets. However, they could also highlight the complexity of the SSE rupture process.

Theoretically, the scaling relation between moment M_0 and event duration T has been discussed in many rate-and-state based models (e.g. Colella, Dieterich, & Richards-Dinger, 2011; Liu, 2014; Dal Zilio et al., 2020). However, the theoretical scaling-relation of the frictional-viscous model has not been addressed before in the literature. At this point, since we have obtained many analytical relations for different observables (or the derived parameters), the scaling relation of the frictional-viscous model is possible to derive to first order.

4.8.1 Theoretical moment-duration scaling

A most critical "observable" in the scaling relation discussion is the event duration T. However, relating it to the quantity of source process is non-trivial. This is because T may have defferent expressions for different types of source process. Both the duration of slip and the duration of rupture propagation can contribute to the event duration T, and T should be the sum of the two contributions. When one is longer than the another, the longer one of the two is more representative of the event duration. If the slip rate decay

time is shorter than the rupture propagation time (rupture being pulse like), T can be approximated as the total rupture length L divided by rupture propagation speed V_r, and expressed as,

$$T \approx \frac{L}{v_r}. \tag{4.56}$$

For simplicity, we ignore the saturation effect of available fault width here. Substituting the characteristic V_r (equation (4.37)) into (4.56), we have,

$$T \approx \frac{L_s}{L_p} \cdot \left(1 + \frac{1}{S}\right) \cdot \left(1 + \frac{\eta_v}{\mu/(2\beta)}\right) \cdot \frac{L}{2\beta}$$

For the purpose of a first order study, we may approximate $\frac{L_s}{L_p}$, $\left(1 + \frac{1}{S}\right)$, and the factor 2 as 1,

$$T \approx \left(1 + \frac{\eta_v}{\mu/(2\beta)}\right) \cdot \frac{L}{\beta} \tag{4.57}$$

There could be some cases where the slip rate decay time is longer than the rupture propagation time. Such cases happen when the rupture is crack like, or some external force triggers a portion of the fault simultaneously. In these cases, the event duration would be better approximated with the slip rate decay time T_d. In addition, the simultaneously slipping area length should be of the same order as the total rupture length L. Using equation (4.35), we may obtain the T in this case as,

$$T = \frac{1}{C} \cdot \left(1 + \frac{\eta_v}{\mu/2\beta}\right) \cdot \frac{L}{2\beta}.$$

Similarly, we may approximate both C and the factor 2 as 1 for the purpose of first order study. We obtain,

$$T \approx \left(1 + \frac{\eta_v}{\mu/2\beta}\right) \cdot \frac{L}{\beta}. \tag{4.58}$$

Equation (4.57) is the same as (4.58) to first order (ignoring the difference in constants that is of the order of one). It suggests that the event duration T derived using different assumptions are of the same order. In another word, whether the rupture is crack-like or pulse-like, to the first order, does not affect the theoretical event duration expression in the frictional-viscous model.

Another important quantity of the scaling is the seismic moment M_0. It can be expressed as the product of shear modulus μ, the final slip D, and the slip area A. We may use our analytical results in section 4.4 to write out the expression for M_0 (equation (4.25)),

$$\begin{aligned} M_0 &= \mu \cdot D \cdot A \\ &\approx \mu \cdot \frac{1}{C} \cdot \frac{L}{\mu} \cdot \Delta\tau_s \cdot L^2 \\ &\approx \Delta\tau_s \cdot L^3 \end{aligned} \tag{4.59}$$

in which we approximate $C = 1$ and $A = L^2$ for the purpose of first-order investigation.

We may now solve for L using (4.58) and substitute it into (4.59) to obtain the theoretical moment-duration relation for the frictional-viscous model,

$$M_0 \approx \Delta\tau_s \cdot \left(1 + \frac{\eta_v}{\mu/2\beta}\right)^{-3} \cdot \beta^3 \cdot T^3 \tag{4.60}$$

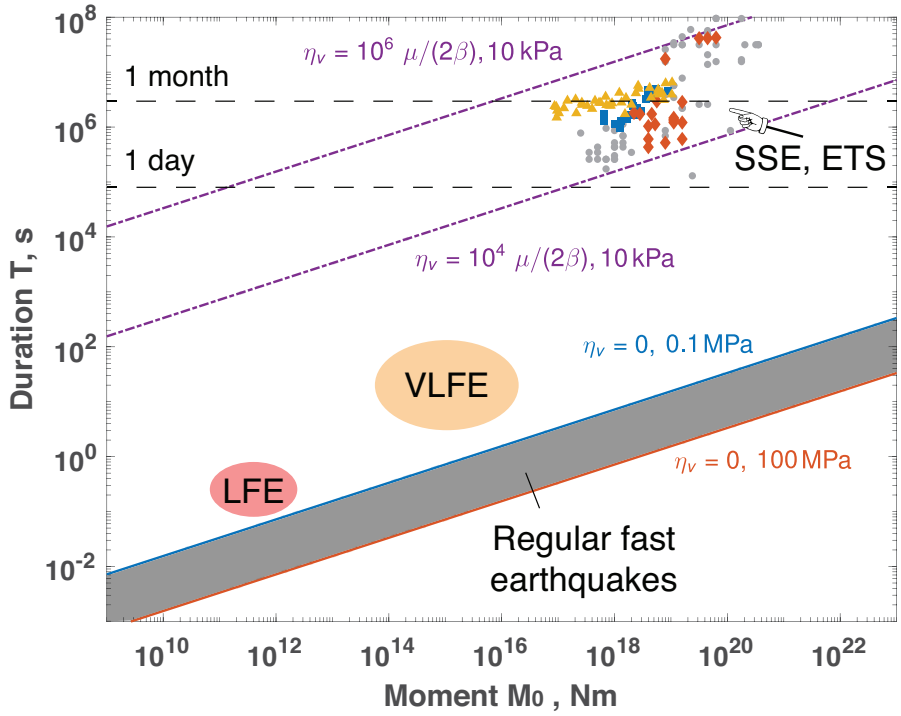

Figure 4.11: The moment-duration relation for slow and fast earthquakes, after Figure 2.3. The gray shaded area bounded by two $M_0 \propto T^3$ lines denotes the parameter space of fast earthquakes. The two bounded lines are calculated using equation (2.19) assuming $C = 1$, $\beta = 3$ km/s. It is equivalent to equation (4.60) when $\eta_v = 0$. $\Delta\tau_s$ is set to be 0.1 MPa for the upper bound (blue line) and 100 MPa for the lower bound (orange line). Shaded ellipse areas denote the approximate location of M_0 and T observations for VLFEs (orange), and LFEs (red). The purple dashed lines denote the theoretical moment-duration relation in the frictional-viscous model, and are calculated using equation (4.60). η_v for the two lines are $\sim 10^4$ $\mu/(2\beta)$ and 10^6 $\mu/(2\beta)$ (noted besides the lines). $\Delta\tau_s$ is set to be 10 kPa for both the purple dash lines. In contrast to Figure 2.3, I show some actual moment-duration observations for SSEs/ETSs instead of using a general shaded ellipse. The yellow triangles are the SSEs in Cascadia subduction zone reported by Michel et al. (2019). Michel et al. (2019) provides a minimum and a maximum estimate for each data point, and what I plot here is the mean of the two values. The blue squares are the SSEs in the Cascadia subduction zone measured by Gao et al. (2012). The orange diamonds are the SSEs in the Higurangi subduction zone originally measured by Wallace and Beavan (2010) and Wallace et al. (2012), and compiled in Liu (2014). Grey circles are other SSEs and ETSs compiled in Gao et al. (2012) and Liu (2014) that are measured by various authors in Japan (40 in Gao et al. (2012), 7 in Liu (2014)), Mexico (9 in Gao et al. (2012), 1 in Liu (2014)), Alaska (1 in Gao et al. (2012), 2 in Liu (2014)), and Costa Rica (1 in Gao et al. (2012), 2 in Liu (2014)).

As equation (4.60) suggests, the frictional-viscous model has a $M_0 \propto T^3$ scaling similar to fast earthquakes. In fact, the only difference between equation (4.60) and the moment-duration relation of fast earthquakes (equation (2.19)) is a factor $\left(1 + \frac{\eta_v}{\mu/2\beta}\right)^{-3}$ that contains a dependency on η_v. For the convenience of comparison, here I demonstrate equation (2.19) again,

$$M_0 \approx \frac{1}{C}\Delta\tau_s\beta^3 T^3$$

We can see that when $\eta_v = 0$, equation (4.60) would be identical to equation (2.19).

Figure 4.11 plots the theoretical scaling relation (4.60) in a moment-duration diagram similar to Figure 2.3, except that I substitute the green ellipse shaded area that roughly denotes the SSEs/ETSs location with actual data points (details in the figure caption). The two purple dashed lines show the two moment-duration relations yielded by equation (4.60) when η_v is set to be 10^4 $\mu/(2\beta)$ and 10^6 $\mu/(2\beta)$, respectively. $\Delta\tau_s$ for the two purple lines is fixed at 10 kPa. As shown in the figure, having a viscous effect in addition to the "sudden stress drop" would only increase the event duration T, while not changing the slope of the moment-duration relationship.

The $M_0 \propto T^3$ prediction in our model agrees with the observed SSE moment-duration relation in general, although significant scatter exists. The agreement would show more clearly if we look at two recent investigations in Cascadia and Mexico, both of which show a clear trend of $M_0 \propto T^3$ scaling (Michel et al., 2019; Frank & Brodsky, 2019). In particular, we note that these two studies both use a catalog in which M_0 and T are measured in a consistent manner. This is different from many earlier studies that use a

compilation of data points from various authors. The consistency in the catalogs definitely adds weight to their $M_0 \propto T^3$ estimates.

Figure 4.11 also reveals that when η_v is $\sim 10^4 - 10^6$ $\mu/(2\beta)$, the frictional-viscous model can explain the moment-duration observations for SSEs. This estimated η_v range is consistent with our estimations in the previous section, although it might not be a big surprise since both the M_0 and T observations can both be derived from the observations we mentioned earlier. Nonetheless, the fact that our estimation earlier matches the observed moment-duration scaling suggests that our analytical derivations for the scaling relation is self-consistent with our previous derivations.

4.8.2 Possible complications in measuring L and T caused by the diffusive tremor migrations

In section 4.7, we discussed diffusive rupture behaviors that are sometimes observed in tremor migrations using high-frequency seismic data. We showed that the frictional-viscous model is able to explain the diffusive rupture behavior with a high stress drop patch surrounded by a low stress drop fault area. If the frictional-viscous model is indeed a good representation of the SSE source process, our derivation would suggest some complications in measuring L and T, which might eventually result in a different scaling from fast earthquakes.

Let us assume we have a strong patch that is configured as in section 4.7 with a length L. When the strong patch ruptures, it drives the surrounding fault to slip and triggers diffusive tremor migration. The slip outside the strong patch might not be resolvable with geodetic data. However, if we use tremor as a proxy to measure the length L, we would end

up with a larger value for L than the actual size of the strong patch. This seismologically estimated size could be a few times greater than L, depending on the strength of the strong-weak contrast (equation (4.46)). If we denote the seismologically estimated length in the diffusive migration case as L_{td}, using equation (4.49) and (4.55), we may obtain a theoretical relation between L_{td} and T as,

$$T \approx \frac{1}{C} \cdot \frac{1}{L \cdot 2\beta} \cdot \frac{\tau_e}{\Delta f} \cdot \left(1 + \frac{\eta_v}{\mu/(2\beta)}\right) \cdot (L_{td})^2 \propto (L_{td})^2, \tag{4.61}$$

for the end-member case of a $1/(x_P)^2$ static stress decay, or,

$$T \approx \frac{1}{C} \cdot \frac{1}{L^2 \cdot 2\beta} \cdot \frac{\tau_e}{\Delta f} \cdot \left(1 + \frac{\eta_v}{\mu/(2\beta)}\right) \cdot (L_{td})^3 \propto (L_{td})^3, \tag{4.62}$$

for the end-member case of a $1/(x_P)^3$ static stress decay.

The above result suggests that, if we use L_{td} as the slip area length instead of L, the duration-length relation would be $T \sim L^n$, with n =2 or 3, which is different from fast earthquakes. If we went on to use L_{td} to estimate M_0 using a moment-length scaling relation,

$$M_0 \propto (L_{td})^3 \tag{4.63}$$

we would end up with two different scaling relations as,

$$M_0 \propto T^{1.5} \tag{4.64}$$

for the end-member case of a $1/(x_P)^2$ static stress decay, or,

$$M_0 \propto T \tag{4.65}$$

for the end-member case of a $1/(x_P)^3$ static stress decay.

Considering that we have made many assumption in deriving the diffusive behavior relations, the above two scaling relation (4.64) and (4.65) should not be treated as an explanation of the observation; instead, they may better be interpreted as a warning of the potential complications in investigating the scaling relation for SSEs. Because of these complications, measuring M_0 accurately with only high-frequency seismic data may be non-trivial, which could cause scattering of data points in the moment-duration diagram. An analog to the phenomenon discussed here is the afterslip-aftershock relation in fast earthquakes. If a large earthquake triggers some afterslip that can induce its own aftershock clusters, the total aftershocks extent would be larger than the actual co-seismic rupture area. Nevertheless, this complication of measuring M_0 and L may not be as troublesome if geodetic data that has good quality and good spatial coverage is available.

4.9 Summary of Chapter 4

In Chapter 4, I explore a frictional-viscous model, where a fault zone with finite thickness and a mixture of viscous and frictional deformation is treated as a fault "surface" with zero thickness in the rupture model. The frictional and viscous behavior are parameterized into a "friction law", which is mechanically equivalent to having frictional resistance and viscous resistance in parallel (Figure 4.1). In this vision, a sudden stress drop can occur due to the sudden frictional (brittle) deformation in the fault zone. The bulk

viscous matrix would deform slowly in response to the sudden stress drop, causing "slow slip" of the bulk fault zone. I explore the rupture behaviors of the frictional-viscous model to first-order with extensive analytical analysis. I find that the frictional-viscous model can self-consistently explain and reproduce many of the quantities estimated for slow slip events based on data, including slip rate (section 4.3), final slip (section 4.4), slip rate decay time (section 4.5), rupture propagation speed (section 4.6), diffusive tremor migration (section 4.7), and moment-duration scaling (section 4.8). My analytical results show that the slow slip behaviors can be stably generated in the frictional-viscous model with a wide range of parameters. To simultaneously explain different observations, the viscous coefficient η_v needs to be about $\sim 10^4 - 10^5\ \mu/(2\beta)$, which can be tested against future observations on viscous properties in SSE fault zones.

The formalization of the frictional-viscous "friction law" I explore here has been proposed and analyzed in a few previous studies (Ando et al., 2010; Nakata et al., 2011; Ando et al., 2012; Lavier et al., 2013; Beall et al., 2019). In particular, Ryosuke Ando and his colleagues have extensively explored the rupture behavior under this "friction law" in a three-paper series back in the early 2010s, and use it to explain slow earthquake observations (Ando et al., 2010; Nakata et al., 2011; Ando et al., 2012). Since Ando's models are mostly numerical, the parameter space that can be explored by the authors is limited. Therefore, the authors were mainly demonstrating a prototype friction setup, in which it is possible to produce slow slip behaviors. Additionally, because Ando's models include spatial heterogeneities of stress and viscous properties on fault asides from the frictional-viscous "friction law", it is not clear whether it is the "friction law" or the spatial

heterogeneity that fundamentally causes slow slip behaviors. In Chapter 4, I derived a plenty of analytical relations to depict the rupture behavior under the frictional-viscous "friction law" setup. These analytical results allow us to efficiently explore the parameter space in a much larger range and, as a result, enable us to quantitatively compare the viscous and frictional model parameter with SSE observations. With the insight gained from the comprehensive analytical results, I show that the frictional-viscous "friction law" itself is the fundamental cause of the slow slip behavior. Various phenomena (e.g., diffusive tremor migration) would appear when one adds into the models some spatial heterogeneities on the fault. My analytical results also reveal some rupture behaviors that haven't been explored before (e.g., slip rate decay time). Numerical analysis of those previous un-explored rupture behaviors will be shown in Chapter 5.

At the beginning of Chapter 4, I demonstrate the physical image behind the "friction law" parameterization where both frictional and viscous resistance are collocated. I show that the "friction law" could actually represent the behaviors of the bulk fault zone with finite thickness, instead of merely representing a frictional force dependency in-between sliding surfaces (section 4.2). Such a vision has gathered more attention recently, as emerging geological observations have implied that both viscous and frictional deformation may exist in the slow-earthquake-bearing fault zone, and the fault zone thickness could be large. Therefore, this frictional-viscous "friction law" is actually beyond the framework of traditional "surface contact based" friction laws such as rate-and-state friction, which is commonly used in models to address slow earthquake problems. In this Chapter, I have shown that the frictional-viscous model can generate stable slow slip behavior within a wide range

of parameter space. This is different from a typical rate-and-state model that might required the friction parameters to reside in a narrow range of parameter space (e.g., Liu & Rice, 2007; Scholz, 2019).

In summary, we have shown in Chapter 4 that the frictional-viscous model is a promising representation of the actual SSE source process. The analytical results in this Chapter 4 will be numerically validated in Chapter 5, and more discussion that is inspired by the results here will be saved for Chapter 6.

Chapter 5

Numerical validation of the analytical results

In Chapter 4, I show with an analytical analysis that a frictional-viscous rupture model can yield slow slip characteristics consistent with those of real-world SSEs. These characteristics include slip rate, stress drop, slip rate decay time, rupture propagation speed, diffusive behavior, and moment-duration scaling. The analytical results are useful in demonstrating rupture behaviors in a wide parameter space and revealing the mechanisms. However, I often make two assumptions to simplify the expressions and to allow further derivation. One assumption is that the elastic waves generated during the rupture are insignificant in affecting the rupture, and that the inertial effect can be accomodated by considering only the "radiation damping" term. This assumption is made in most of the derivation in Chapter 4 except in the stress drop analysis. The other assumption is that the static shear strain perturbation generated by a slipping area on itself can be

simplified as the average shear slip divided by the characteristic length of the slipping area. By doing so, we ignore the spatial distribution of stress perturbations, and the analysis can be simplified to be pseudo-one-dimensional. This assumption is made in most of the derivations in Chapter 4 except in the slip rate analysis.

As discussed in Chapter 4, these two assumptions may be proper for the scope of our analysis. Firstly, as the viscous coefficient η_v becomes several orders of magnitude greater than the radiation damping factor $\mu/(2\beta)$, slip rate V decreases significantly, and the elastic wave amplitude should also diminish. Therefore, omitting elastic waves is appropriate. In addition, what we are interested in is the first-order rupture behavior, and the spatial distribution of slip and stress is not important in affecting the first-order "characteristic" relations derived in Chapter 4.

However, to validate our results, it is desirable to relax these two assumptions. Due to the complicated nature of the problem, a numerical approach is more suitable for this task. In this chapter, I conduct a few numerical models to validate the conclusions in Chapter 4 that are obtained by analytical analysis. A complete inertial effect, including elastic wave propagations, and a non-trivial spatial distribution of slip and stress are considered in the numerical models. By comparing the few "data points" of numerical models with the "lines" predicted by analytical analysis, we may see how appropriate the aforementioned assumptions are. In addition, numerical analysis enables us to visualize the spatio-temporal evolution of rupture, which provides a more intuitive demonstration of the slow slip behaviors yielded in the analyticalfrictional-viscous model.

5.1 Numerical method

The numerical method I use for the analysis is the boundary integral equation method (BIEM), which is often also referred to as the boundary element method (BEM). This is a semi-analytical-semi-numerical method for linear elasticity problems. The analytical part of the framework is the same as in our analytical analysis and has been demonstrated in section 4.2.3. Here I will give a brief introduction of the numerical scheme, and describe some details of the code I use. The BIEM scheme I use is primarily based on Tada (2009). More details can be found in that paper.

5.1.1 Discretizing BIEs and "friction law"

Unlike finite element method (FEM) or finite difference method (FDM), BIEM does not have discretization for the governing equations directly. Instead, BIEM requires that we first analytically derive the Green's function of the system. Using the Green's function, one may write the traction-displacement relation at the domain boundary in the form of an integral equation, which is often referred to as boundary integral equation (BIE). For the earthquake problem in particular, the boundary we care about is the fault, and the BIE we obtain is a relation between the traction and the slip on fault. For simplicity, here we consider a simple setup with only a single planar fault, and slip is fixed in one direction,

$$\tau_{elastic}(\boldsymbol{\xi}, t) = \tau^0(\boldsymbol{\xi}) + \int_\Gamma \mathrm{d}S(\boldsymbol{\xi'}) \int_0^t \mathrm{d}\tau \hat{K}(\boldsymbol{\xi}, t-\tau; \boldsymbol{\xi'}, 0) \dot{D}(\boldsymbol{\xi'}, \tau) \quad (\boldsymbol{\xi}, \boldsymbol{\xi'} \in \Gamma), \tag{5.1}$$

in which $\tau_{elastic}(\boldsymbol{\xi}, t)$ is the shear traction, or shear stress, on fault. $\tau^0(\boldsymbol{\xi})$ is the initial shear stress. $\dot{D}(\boldsymbol{\xi}, t)$ is slip rate. $\hat{K}(\boldsymbol{\xi}, t-\tau; \boldsymbol{\xi'}, 0)$ is a factor that contains the Green's function

of the problem, and it can be derived beforehand. I note that, in contrast to the from its representation in equation (4.10) in section 4.2.3, I put the instantaneous response term into the integral for now.

To numerically solve the integral equation 5.1, we need to discretize both the fault surface and integral time range. Assume the fault is discretized into N_x elements, and the nth element is denoted as Γ_n. The time range is discretized into N_T time steps, and the end moment of the qth time step is denoted as t_q (i.e., the qth time step covers a time range $t_{q-1} < t < t_q$). We require that all points in the same element during a certain time step have the same slip rate. In that case, the slip rate distribution can be written as,

$$\Delta\dot{D}(\boldsymbol{\xi}, t) = \sum_{n=1}^{N_X} \sum_{q=1}^{N_T} V_{nq} H(\boldsymbol{\xi} \in \Gamma_n)[H(t - t_{q-1}) - H(t - t_q)] \tag{5.2}$$

in which V_{nq} is the discretized slip rate; when $\boldsymbol{\xi}$ is in Γ_n, $H(\boldsymbol{x} \in \Gamma_n)$ equals one, otherwise it equals zero; when $t_{q-1} < t < t_q$, $H(t - t_{q-1}) - H(t - t_q)$ equals one, otherwise it equals zero.

We may substitute (5.2) into (5.1), and we will obtain a discretized BIE,

$$\begin{aligned} \tau_{elastic}(\boldsymbol{\xi}, t) = \tau^0(\boldsymbol{\xi}) + \sum_{n=1}^{N_X} \sum_{q=1}^{N_T} V_{nq} \int_\Gamma dS(\boldsymbol{\xi}') \int_0^t d\tau \hat{K}(\boldsymbol{\xi}, t - \tau; \boldsymbol{\xi}', 0) \\ H(\boldsymbol{\xi}' \in \Gamma_n)[H(\tau - t_{q-1}) - H(\tau - t_q)] \quad (\boldsymbol{\xi}, \boldsymbol{\xi}' \in \Gamma) \end{aligned} \tag{5.3}$$

To conduct numerical simulations, for the mth fault element, we need to select one or more points $\boldsymbol{\xi}$ in the Γ_m to represent the receiver point(s) of the element. How we choose the representative points may affect the simulation results in some cases (e.g., for an element near a fault geometry complexity). Fortunately, for the planar fault problem in

full space, such an issue shall not be a big problem, and we may simply choose the center point of the element as the representative point. Let say the representative point for the mth element is $\boldsymbol{\xi_m}$. We may let $\boldsymbol{\xi} = \boldsymbol{\xi_m}$, $t = t_p$, and substitute into equation (5.3),

$$T_{mp} = T_m^0 + \sum_{n=1}^{N_X} \sum_{q=1}^{p} V_{nq} K_{mp/nq} \tag{5.4}$$

in which $T_{mp} = \tau_{elastic}(\boldsymbol{\xi_m}, t_p)$, $T_m^0 = \tau^0(\boldsymbol{\xi_m})$. T_{mp} is the stress at fault element m at time step p, due to the entire slip history over the entire fault. I note that the upper limit of the time summation is p instead of N_T now. This is because we consider the causality requirement: the slip rate after time step p cannot have influence on the traction at time step p. $K_{mp/nq}$ is the discrete integration kernel, which relates fault slip rate distribution with traction distribution. It has the following expression,

$$K_{mp/nq} = \int_\Gamma dS(\boldsymbol{\xi'}) \int_0^t d\tau \hat{K}(\boldsymbol{\xi_m}, t_p - \tau; \boldsymbol{\xi'}, 0) H(\boldsymbol{\xi'} \in \Gamma_n)[H(\tau - t_{q-1}) - H(\tau - t_q)] \tag{5.5}$$

In practice, obtaining the integration kernel $\hat{K}(\boldsymbol{\xi}, t - \tau; \boldsymbol{\xi'}, 0)$ and $K_{mp/nq}$ can be non-trivial. Usually, a proper regularization process is needed in the derivation to remove singularities. For a full space problem, a proper $\hat{K}(\boldsymbol{\xi}, t - \tau; \boldsymbol{\xi'}, 0)$ and $K_{mp/nq}$ have already been derived by many authors (e.g., Fukuyama & Madariaga, 1998; Aochi, Fukuyama, & Matsu'ura, 2000; Tada, 2005, 2006, 2009).

Considering time translation symmetry, $K_{mp/nq} = K_{m(p-q)/n0}$, and (5.4) can be written as,

$$T_{mp} = T_m^0 + \sum_{n=1}^{N_X} \sum_{q=1}^{p} V_{nq} K_{m(p-q)/n0} \tag{5.6}$$

To solve for the slip evolution, one more equation is needed to relate shear traction and slip. This is given by the fault boundary condition ("friction law"). In my dissertation, the "friction law" is a frictional-viscous relation, which is a combination of a sudden weakening (brittle) resistance and a linear rate-strengthening (viscous) resistance. In our numerical simulations, we realize the above "friction law" in the following manner: when shear traction of an fault element is lower than the yielding level f_y, the element stays un-ruptured and no slip happens; when shear traction of this element exceeds f_0, the shear traction becomes a residual level f_1 plus a viscous resistance $\eta_v \cdot V_{mp}$ over the following time step. The discretized fault boundary condition can be written as,

$$T_{mp} = f_1 + \eta_v \cdot V_{mp} \tag{5.7}$$

A formulation like this means that shear traction can have a sudden drop, and the frictional (brittle) part of this "friction law" is equivalent to a one-time-step time-weakening. I note that such a short weakening time might causes numerical issues in other numerical method like FEM and FDM. However, it does not cause noticeable numerical issues in all our BIEM experiments, as I will show later. Previous numerical studies with similar "sudden stress drop" setting in BIEM also do not seem to have significant numerical issues (Ando et al., 2010; Nakata et al., 2011; Ando et al., 2012). I suspect that BIEM can handle such a short weakening time because the intrinsic semi-analytical component in the method, i.e., the discrete integration kernel $K_{mp/nq}$ is analytically calculated in a closed form before

the numerical simulation.

5.1.2 Time-marching scheme of simulations

We may now design a numerical scheme to conduct simulations based on equations (5.6) and (5.7). I will use a time-marching scheme for my numerical simulations. This is a commonly used numerical scheme, in which we start from the initial condition, use the recurrence relation to march advance in time, and eventually obtain the solution. To use a time-marching scheme, we need to separate the second term in the right hand side of (5.6) into two parts: one part is only related to the current time step, and the other part is related to all of the previous slip history,

$$T_{mp} = T_m^0 + \sum_{n=1}^{N_X} V_{nq} K_{m0/n0} + \sum_{n=1}^{N_X} \sum_{q=1}^{p-1} V_{nq} K_{m(p-q)/n0} \tag{5.8}$$

Combining with (5.7), we may obtain N_x equations that are related to the slip rate at the pth time step (V_{1p}, V_{2p},..., $V_{N_x p}$),

$$-\eta_v \cdot V_{mp} + \sum_{n=1}^{N_X} V_{np} K_{m0/n0} = -T_m^0 + f_1 - \sum_{n=1}^{N_X} \sum_{q=1}^{p-1} V_{nq} K_{m(p-q)/n0} \\ , \ (m = 1, 2, ..., N_X) \tag{5.9}$$

In principle, one may start a simulation using (5.9). However, this set of equations is implicit, because the slip rate in the same time-step but of different elements can affect each other. Therefore, the simulation with the above equation needs to involve finding the inverse of a matrix, which greatly increases the complexity of coding. Here I adopt a different approach to avoid finding the inverse of a matrix. We can formalize (5.9) into an

explicit equation by setting a small enough time-step size. We need to introduce a CFL (Courant–Friedrichs–Lewy) parameter, which, in our case, is defined as,

$$\mathrm{CFL} = \frac{c\Delta t}{\Delta x_{min}} \tag{5.10}$$

where c is the maximum elastic wave speed in the medium. For a full-space simulation, it should be the P wave speed. Δt is the time-step size. Δx_{min} is the minimum distance among all elements from the representative point to the element edge. For a homogeneous discretization with squares, Δx_{min} should be half of the element side length. If we choose a CFL parameter smaller than one, no elastic wave can propagate out of any element within a time-step, and equation (5.9) can be re-written as,

$$-\eta_v \cdot V_{mp} + K_{m0/m0} \cdot V_{mp} = -T_m^0 + f_1 - \sum_{n=1}^{N_X} \sum_{q=1}^{p-1} V_{nq} K_{m(p-q)/n0} \\ , \ (m = 1, 2, ..., N_X) \tag{5.11}$$

$K_{m0/m0}$ is the instantaneous response factor, which equals $-\mu/(2\beta)$ for a full-space problem. Substituting it into (5.11) and solving for V_{mp}, we have,

$$V_{mp} = \left(T_m^0 - f_1 + \sum_{n=1}^{N_X} \sum_{q=1}^{p-1} V_{nq} K_{m(p-q)/n0} \right) \cdot \left(\eta_v + \frac{\mu}{2\beta} \right)^{-1} \\ , \ (m = 1, 2, ..., N_X) \tag{5.12}$$

Equation (5.12) provides an explicit recurrence relation to conduct the time marching scheme simulation for a specific model setup. At time step zero, slip rate equals zero everywhere and shear stress equals the initial condition. In a typical dynamic rupture simulation, to facilitate rupture, the initial shear stress would be greater than the yielding

strength within an area on the fault, which is commonly referred to as the nucleation zone. Fault elements within the nucleation zone would start to slip at time step one, and the slip rate can be calculated using equation (5.12). Step by step, the rest of the rupture evolution can then be obtained using the explicit recurrence relation.

5.1.3 Other simulation details

For simplicity, in my dissertation, I will consider the most simple case where there is a single planar fault embedded in an elastic full space. The discretization elements I will use are squares. The analytical expressions of the discrete integration kernel $K_{mp/nq}$ I use are given by (Tada, 2009), which were originally obtained in an earlier paper of the same author Tada (2005). The code I ran is written in C, and parallelized with openMPI. The code was originally developed in my undergraduate thesis with Dr Haiming Zhang.

5.2 Model A: spontaneous rupture on an elongated fault

5.2.1 Simulation setup

I will first present a set of simulations that test the effect of viscous coefficient η_v on rupture dynamics on an elongated fault. This set of simulations is named 'Model A'. All the settings in these simulations are kept the same, except for the viscous coefficient η_v. Figure 5.1 shows the schematics that demonstrate the general setup of the Model A simulations. Figure 5.1a shows the geometry and discretization of the fault in Model A. The fault is set to be a planar rectangle, with a length of 20 km and a width of 5 km. The fault is discretized with small squares whose side $\Delta x = 0.1$ km. The fault is treated as a

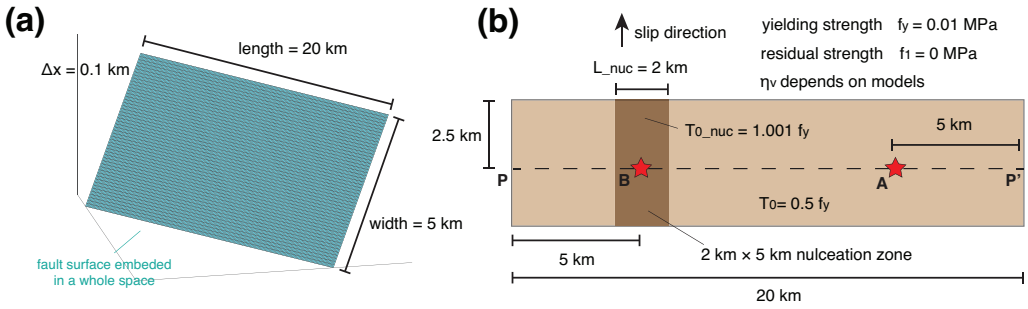

Figure 5.1: Schematics showing the setup of Model A simulations that test the effect of the viscous coefficient η_v on rupture dynamics. (a) The geometry and discretization of the fault in Model A. The fault is set to be a planar rectangle, with a length of 20 km and a width of 5 km. The fault is discretized with small squares whose side $\Delta x = 0.1$ km. The fault is treated as a displacement discontinuity embedded in an elastic whole (full) space. The fault is viewed from an angle from the top. (b) The generic setup of "friction" and initial stress setting. The yielding shear strength f_y and residual shear strength f_1 are set to be homogeneous on the fault: $f_y = 0.01$ MPa and $f_1 = 0$ MPa. The initial shear stress T_0 is prescribed in the along-width direction. It is set to be $T_0 = 0.5 f_y$ everywhere on fault (light brown area), except for within the nucleation zone, which is a 2 km narrow band across the whole fault width whose center is 5 km away from one short side the rectangle fault (dark brown area). Within the nucleation zone, initial stress $T_{0nuc} = 1.001 f_y$, which is just above the yielding strength. The aforementioned settings are kept the same for all simulations of Model A. The viscous coefficient η_v is set to be homogeneous on fault for a given simulation, and its value varies among different models. The dashed line PP' is a profile along the x-axis that will be used in the later analysis, and it is at the central location along the width of the fault. Red stars show two points A and B on faults that will be used in the later analysis.

Parameter	Fixed value
shear modulus μ	3.13×10^{10} Pa
P wave speed α	5.6×10^{3} m/s
S wave speed β	3.23×10^{3} m/s
medium density ρ	3×10^{3} kg/m^3
f_y	10^4 Pa
f_1	0 Pa
T_0 outside the nucleation zone	0.5×10^4 Pa
T_0 within the nucleation zone	1.001×10^4 Pa

Table 5.1: Summary of the fixed parameters used in different simulations in Model A.

displacement discontinuity embedded in an elastic whole (full) space. Figure 5.1b shows the generic setup of "friction" and initial stress setting. The yielding shear strength f_y and residual shear strength f_1 are set to be homogeneous on fault: $f_y = 0.01$ MPa and $f_1 = 0$ MPa. The initial shear stress T_0 are prescribed in the along-width direction. It is set to be $T_0 = 0.5 f_y$ everywhere on fault (light brown area), except for within the nucleation zone, which is a 2 km narrow band across the whole fault width whose center is 5 km away from one short side the rectangle fault (dark brown area). Within the nucleation zone, initial stress $T_{0nuc} = 1.001 f_y$, which is just above the yielding strength. A summary of the general parameters in Model A is shown in Table 5.1.

The aforementioned settings are kept the same for all simulations of Model A. The viscous coefficient η_v is set to be homogeneous on the fault for a given simulation, and its value varies between different models. In total I present eight different simulations for Model A, and their η_v values are shown in Table 5.2. The η_v value I test range from 0 to 165000 MPa $\cdot$ s/km, which corresponds to a range from 0 to 34.0 when normalized by $\mu/(2\beta)$.

Model number	η_v in MPa $\cdot$ s/km	η_v in $\mu/(2\beta)$
Model A1	0	0
Model A2	15000	3.1
Model A3	35000	7.2
Model A4	65000	13.4
Model A5	105000	21.7
Model A6	165000	34.0
Model A7	5000	1.0
Model A8	10000	2.1

Table 5.2: Summary of η_v used in different simulations in Model A.

I note that this range does not cover the proposed η_v range in Chapter 4 for SSEs, which is $\sim 10^4$ $\mu/(2\beta)$. This is because the computation capacity available to me at this time can not allow for such big simulations. For dynamic rupture simulations that include elastic wave propagations (i.e., full inertial effects), the simulation time step is determined by the size of the discretization (as discussed in section 5.1.2). However, a simulation with greater η_v usually needs a longer simulation duration in order to capture the slower rupture. Therefore, a simulation with greater η_v requires a greater number of simulation time steps. Currently, the $\eta_v = 34.0$ $\mu/(2\beta)$ simulation needs 18000 time steps to capture the whole rupture (Model A6), and the runtime is about two days when run on the Mingus cluster of the UCR Geophysics group with 64 cores. A simulation with $\eta_v = 10^4$ $\mu/(2\beta)$ may require a ~ 300 times longer runtime. Nevertheless, as I show later, our numerical simulations are sufficient to support the trend of rupture behavior as proposed in Chapter 4.

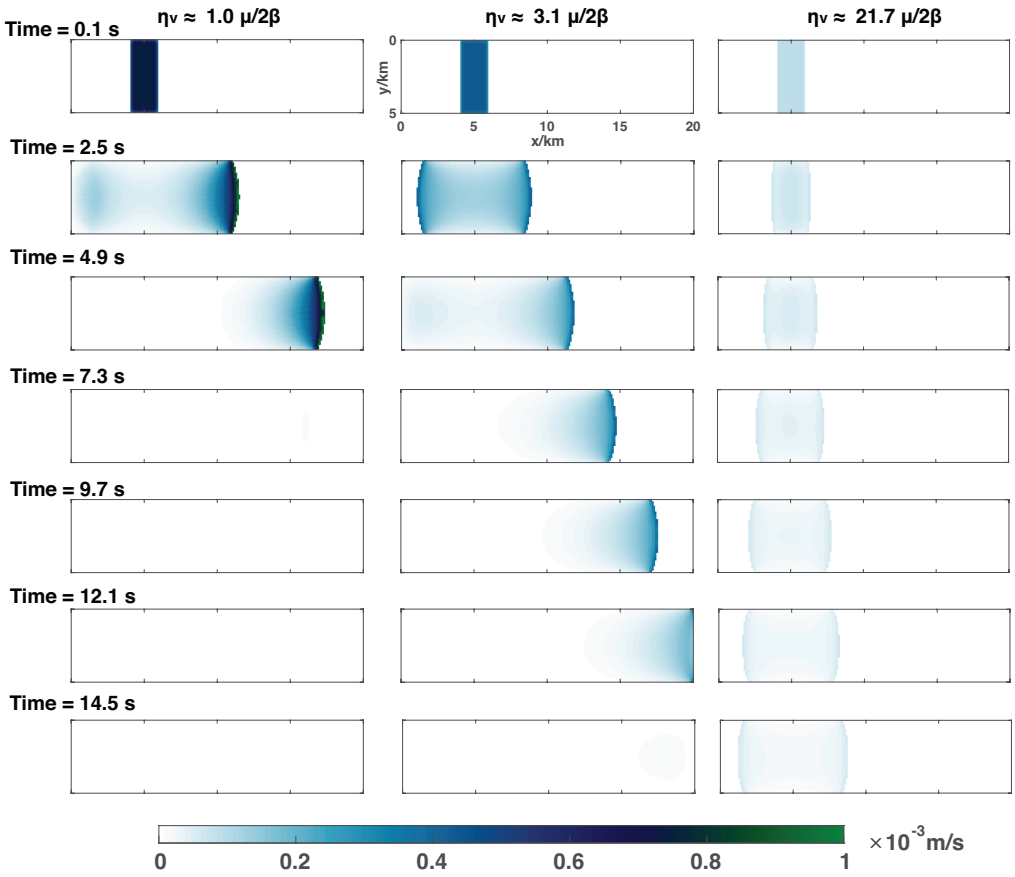

Figure 5.2: Slip rate snapshots of the three models with different viscous coefficient η_v. Each column corresponds to a model with specific η_v, and the η_v increases from left to right: the left column is Model A7 with $\eta_v = 1.0\ \mu/(2\beta)$, the middle is Model A2 with $\eta_v = 3.1\ \mu/(2\beta)$, and the right is Model A5 with $\eta_v = 21.7\ \mu/(2\beta)$. Each row corresponds to a time step, and the time increases from top to bottom. For each snapshot, the x-axis is the long-side direction of the rectangle fault and y-axis is the short side direction of the rectangle fault. Slip rate is color-coded, with white equaling zero and dark green equaling 1×10^{-3} m/s. This figure shows that, as η_v increases, both the maximum slip rate and the rupture propagation speed decrease.

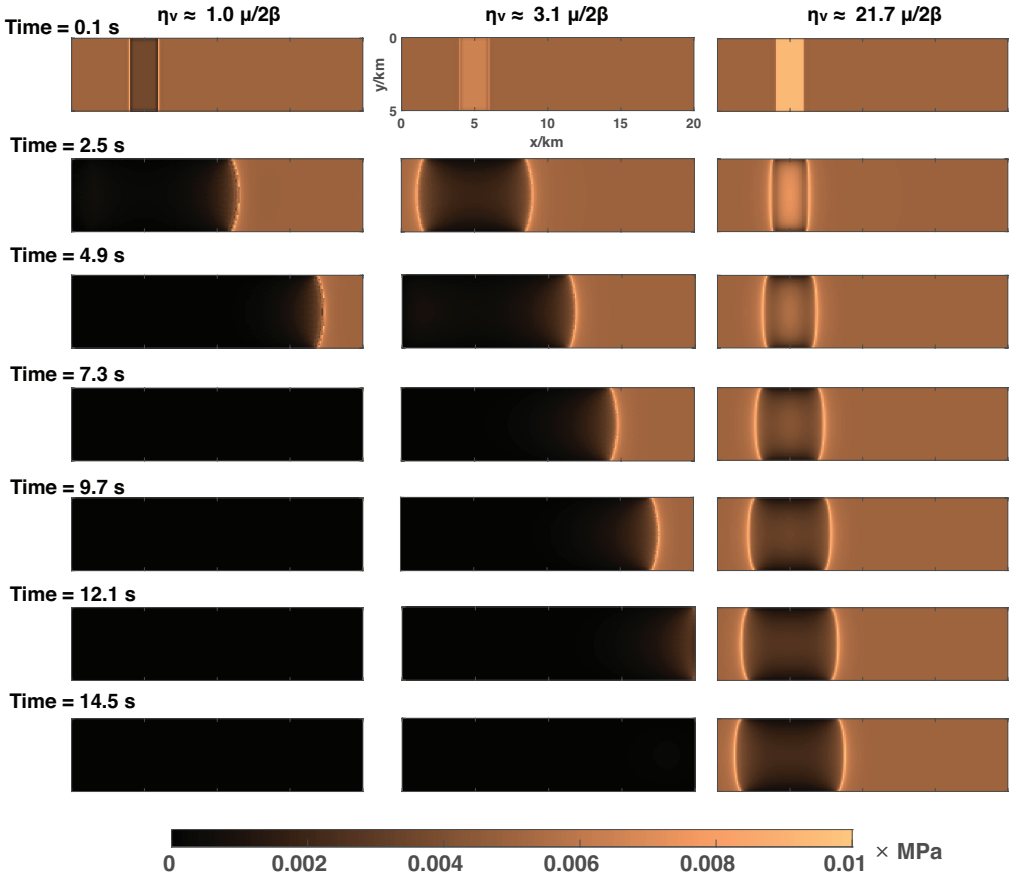

Figure 5.3: Shear stress snapshots of the three models with different viscous coefficient η_v. Each column corresponds to a model with specific η_v, and the η_v increases from left to right: the left column is Model A7 with $\eta_v = 1.0\ \mu/(2\beta)$, the middle is Model A2 with $\eta_v = 3.1\ \mu/(2\beta)$, and the right is Model A5 with $\eta_v = 21.7\ \mu/(2\beta)$. Each row corresponds to a time step, and the time increases from top to bottom. For each snapshot, the x-axis is the long-side direction of the rectangle fault and y-axis is the short side direction of the rectangle fault. Shear stress is color-coded, with black equals zero and the brightest color equals 0.01 MPa. This figure shows that, as η_v increases, the rupture propagation speed decreases and the stress drop process becomes slower.

5.2.2 Simulation results: rupture propagation speed and maximum slip rate

To better demonstrate the effect of η_v, I select three out of the eight simulations to demonstrate in detail: Model A7 ($\eta_v = 1.0\ \mu/(2\beta)$), Model A2 ($\eta_v = 3.1\ \mu/(2\beta)$), and model A5 ($\eta_v = 21.7\ \mu/(2\beta)$). Figures 5.2 and 5.3 show the slip rate snapshots and stress snapshots of these three simulations. Each column corresponds to a model with specific η_v, and the η_v increases from left to right: the left column is Model A7 with $\eta_v = 1.0\ \mu/(2\beta)$, the middle is Model A2 with $\eta_v = 3.1\ \mu/(2\beta)$, and the right is Model A5 with $\eta_v = 21.7\ \mu/(2\beta)$. For all three simulations, rupture propagates bilaterally along the x-axis (long-side of the rectangle) after nucleation. The nucleation zone is located 5 km away from the fault center to the left, so rupture has a longer distance to propagate on the right hand side. The rupture fronts are shown in the slip rate snapshots (Figure 5.2) by the high slip rate area and shown in the shear stress drop (Figure 5.3) by the contrast between high and low stress. After a rupture finishes, both slip rate and shear stress become zero everywhere on fault.

Figure 5.2 shows that the maximum slip rate of the rupture front decreases as η_v increases. In addition, both snapshots show that rupture propagation speed is slower when η_v is higher. For the $\eta_v = 1.0\ \mu/(2\beta)$ case (left column), rupture finishes its propagation between 4.9 seconds and 7.3 seconds. For the $\eta_v = 3.1\ \mu/(2\beta)$ case (middle column), rupture finishes its propagation between 12.1 seconds and 14.5 seconds. For the $\eta_v = 21.7\ \mu/(2\beta)$ case (right column), rupture does not finish its propagation in the time steps I show. Both the maximum slip rate and rupture propagation speed trends agree with the analytical analysis we have in Chapter 4.

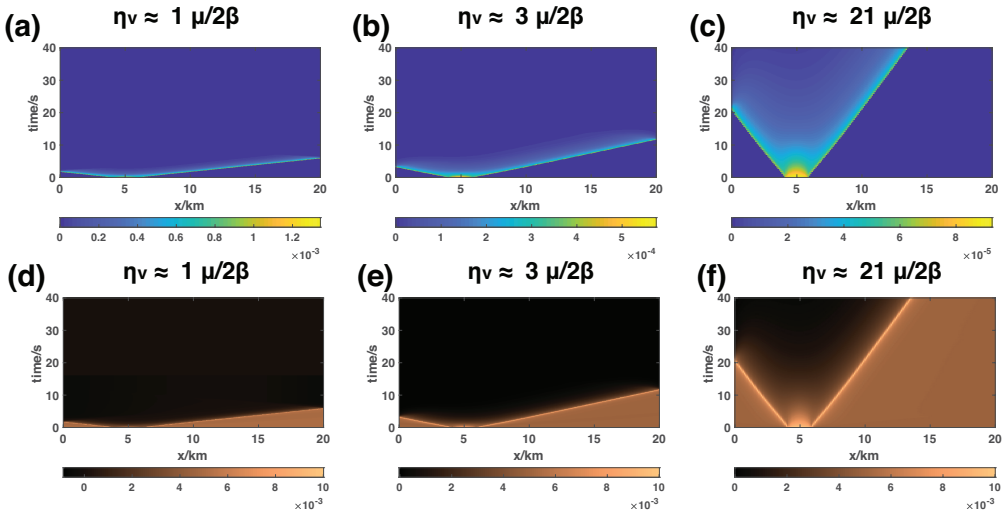

Figure 5.4: The space-time evolution of slip rate and shear stress along the PP' profile shown by the dashed line in Figure 5.1b. The slip rate evolution for η_v equals 1.0, 3.1, and 21.7 $\mu/(2\beta)$ cases are shown in (a), (b), and (c), respectively. The maximum value of the colormap is the maximum slip rate value in the corresponding simulation, and the minimum value is zero. The shear stress evolution for η_v equals 1.0, 3.1, and 21.7 $\mu/(2\beta)$ cases are shown in (d), (e), and (f), respectively. For each space-time plot, x-axis is the along profile distance, with zero at point P, and y-axis denotes time. The maximum value of the colormap is 0.01 MPa, and the minimum value is zero.

5.2.3 Simulation results: slip rate and shear stress decay in space and time

My analytical results in Chapter 4 also give relations on how slip rate and shear stress decay, so we want to see if those features can be reproduced by the numerical simulations. Figure 5.4 shows the space-time evolution of slip rate and shear stress along the PP' profile shown by the dashed line in Figure 5.1b. This figure also shows the decrease of rupture propagation speed as η_v becomes larger. In addition, Figure 5.4 shows an increase of slip rate decay time and stress drop decay time as η_v increases, which is qualitatively consistent with my analytical result in section 4.5.

To better illustrate how slip rate decays in space, I pick a given timestep to show the slip rate distribution along PP'. The corresponding figures are shown in Figure 5.5(a), (b), and (c), which show the slip rate profile of the η_v equals 1.0, 3.1, and 21.7 $\mu/(2\beta)$ model, respectively, at the time step when Point A (location shown in Figure 5.1b) just ruptures. The profiles for the three models are almost the same, suggesting that the slip rate decay distance behind the rupture front is not affected by the viscous coefficient η_v. I do a visual measure of the characteristic distance and my measure is 5 km. I did not have a rigorous analytical derivation for this characteristic distance, and thus document it in Chapter 4. I suspect that it may be controlled by the width (shorter dimension) of the fault, as suggested by many previous dynamic rupture modeling studies (e.g., Day, 1982; Dalguer & Day, 2009). Also, this characteristic distance may be controlled by the initial nucleation size under the "frictional-viscous-mixing" "friction law" I used here. A better understanding of the characteristic distance requires more investigations, and will be left for a future study.

To better illustrate how slip rate decays in time, I also show the time evolution of point A in Figure 5.5(d), (e), and (f) for the η_v equals 1.0, 3.1, and 21.7 $\mu/(2\beta)$ model, respectively. Because the rupture propagation speed is different in different models, the start time of the high slip rate is different. Yet, the initial speed-up process is similar for all three models. The slip rate decay gradually after reaching the peak value, and the decay is very similar to the exponential decay that is suggested in section 4.5. Most importantly, the slip rate decay time increases with η_v, which is consistent with the conclusion in section 4.5.

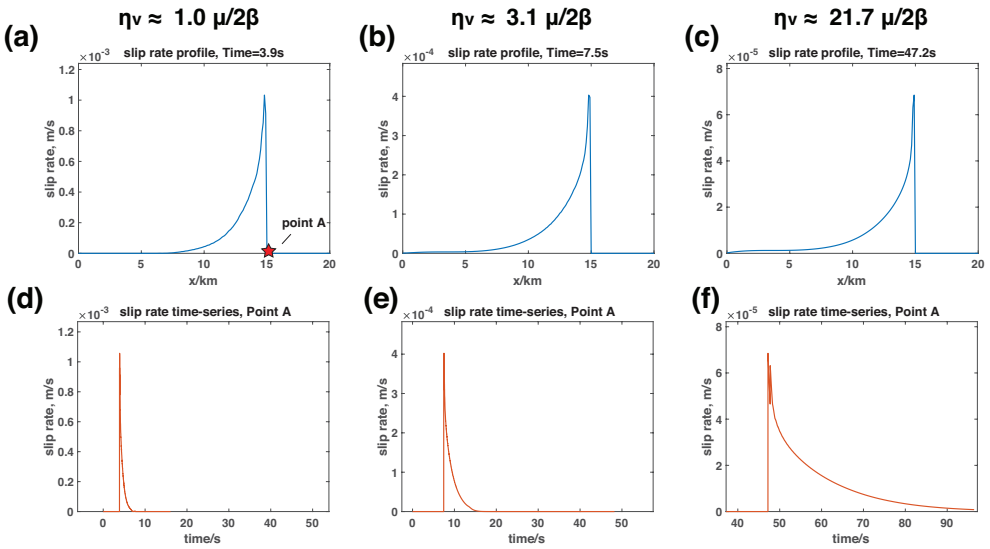

Figure 5.5: (a), (b) and (c) show the slip rate distribution along PP' for the η_v equals 1.0, 3.1, and 21.7 $\mu/(2\beta)$ model, respectively, at the time step when Point A (location shown in Figure 5.1b) just ruptures. These three plots suggest that the width of slip rate pulse behind the rupture front is not affected by η_v. (d), (e), and (f) show the slip rate time evolution of point A for the η_v equals 1.0, 3.1, and 21.7 $\mu/(2\beta)$ model, respectively. These three plots suggest that slip rate decay time increases with η_v.

For the purpose of completeness, I also show a set of figures similar to Figure 5.5, but instead for the shear stress evolution (Figure 5.6). The main result is similar to what I discussed in the previous paragraph.

5.2.4 Simulation results: shear stress-slip relation

How shear stress changes in response to slip can reflect the energy budget of ruptures, i.e., how the total elastic strain energy partitions into radiated energy and dissipated energy on the fault. Using the analytical framework in Chapter 4, in principle, I can derive the analytical relation between shear stress and slip. I choose not to do that in Chapter 4 because my main goal there is to explain SSE observations. Therefore, I just vaguely assert

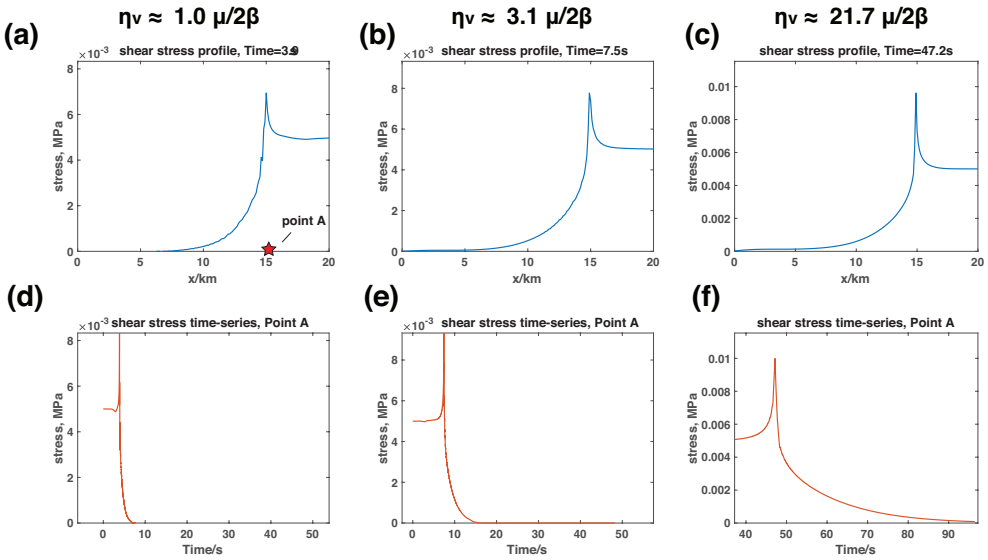

Figure 5.6: (a), (b) and (c) show the shear stress distribution along PP' for the η_v equals 1.0, 3.1, and 21.7 $\mu/(2\beta)$ model, respectively, at the time step when Point A (location shown in Figure 5.1b) just ruptures. These three plots suggest that the width of stress pulse behind the rupture front is not affected by η_v. (d), (e), and (f) show the shear stress time evolution of point A for the η_v equals 1.0, 3.1, and 21.7 $\mu/(2\beta)$ model, respectively. These three plots suggest that stress decay time increases with η_v.

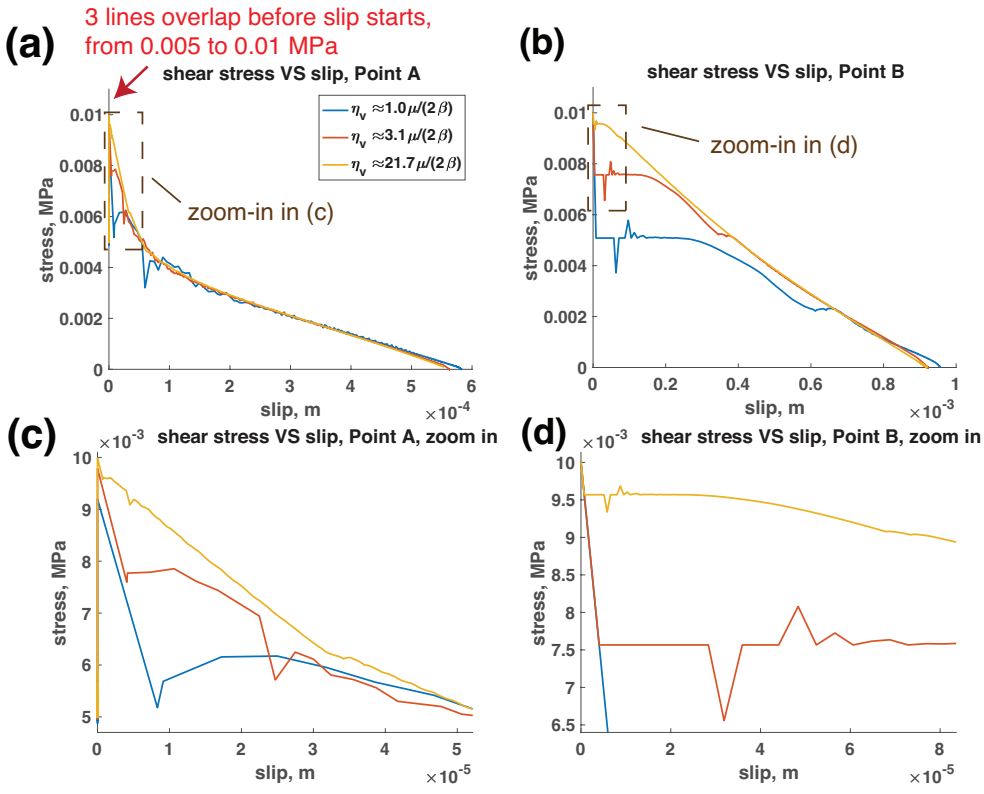

Figure 5.7: Shear stress-slip relation for the η_v equals 1.0, 3.1, and 21.7 $\mu/(2\beta)$ models. (a) shear stress-slip relation at point A outside the nucleation zone, and (b) shear stress-slip relation at point B inside the nucleation zone (locations shown in Figure 5.1b). The dashed box are the range of the zoom-in figures in (c) and (d). (c) and (d): the same as (a) and (b) but zoom into the beginning portion of the stress drop.

that, since a larger η_v causes smaller slip rate V, the radiated energy should also be smaller as η_v becomes larger. However, from a theoretical point of view, it is important to discuss the shear stress-slip relation, in order to better illustrate the physical process behind the ruptures. Here, since I have already demonstrated the simulations, it would be convenient that I also demonstrate the numerical shear stress-slip relation. Readers may skip this small section without losing important information.

Figure 5.7 show the shear stress-slip relation for the three simulations: η_v equals

1.0, 3.1, and 21.7 $\mu/(2\beta)$. Two representative points are selected for demonstration: point A outside the nucleation zone and point B inside the nucleation zone. The location of A and B are shown in Figure 5.1b. Figure 5.7(a) shows the shear stress-slip relation for point A. For all three models, initial stress at point A is 0.005 MPa. As the rupture front approaches point A, shear stress builds up and eventually reaches the yielding strength $f_y = 0.01$ MPa. Shear stress experiences a sudden drop immediately after yielding, and then gradually decays with slip. The stress decay curves of all three simulations approach a straight line after a certain amount of slip, and the stress decay follows this line until it drops to zero. When extrapolating this line, we find that the line intersects the y-axis roughly at 0.005 MPa, which is the initial shear stress. It suggests that the shear stress decay along the straight line is almost a quasi-static stress decay.

Figure 5.7(c) shows a zoomed-in version of Figure 5.7(a), focusing on the initial process. As the figure shows, stress decays more slowly with slip when η_v is larger. It suggests that more energy is dissipated on the fault when η_v is larger, and less energy is radiated out.

Figure 5.7(b) shows the stress-slip relation at point B, which is located within the nucleation zone. Since the initial shear-stress is higher than the yielding strength within nucleation zone, shear stress immediately starts to drop at the beginning (from $T_0 = 0.01001$ MPa). All three curves experience a sudden drop after the first time step, after which the stress decay becomes nearly flat. A larger η_v case has a smaller sudden stress drop, which leads to a smaller slip rate, as has been shown in section 5.2.2. Some oscillations in stress appear after a small amount of slip, probably due to the elastic waves radiated

from the top boundary or nucleation boundaries. A larger η_v case has the oscillations at a smaller slip, and the oscillation has a smaller amplitude. This is because a larger η_v case has a slower slip rate, and thus less radiated wave energy. At one point, stress starts to decay faster with slip until shear stress drops to zero. This last part of the decay curve is almost straight. When extrapolating the straight line, the line approximately intersects the y-axis at 0.01 MPa, which is the initial stress level. It suggests that, similar to what we find for point A, the last part of shear stress decay here is almost a quasi-static decay.

From an energy budget point of view, the stress-slip relation shows that a smaller amount of energy is released when η_v is larger. It means that more energy is dissipated in the viscous process on the fault, and the radiated seismic waves would have a smaller amplitude. Looking at the point A results may reveal a clearer picture of the energy transfer process. Stress slowly builds up as rupture approaches point A, implying that strain energy is transferred from other parts of the fault behind the rupture front to near point A. After point A ruptures, it starts to do work to the other part of the fault in front of the rupture front and release strain energy. Based on the nearly quasi-static stress decay, we infer that point A almost does not "release energy" into the system. It implies that, for a case when η_v is large, point A is mostly acting like a "pipe" that passes energy.

As noted, the discussion here contain much speculation and intuition, and I do believe more analysis and experimentation are needed. However, it shall not affect the SSE analysis I have—it is just an issue about how we should understand this model from an energy point of view.

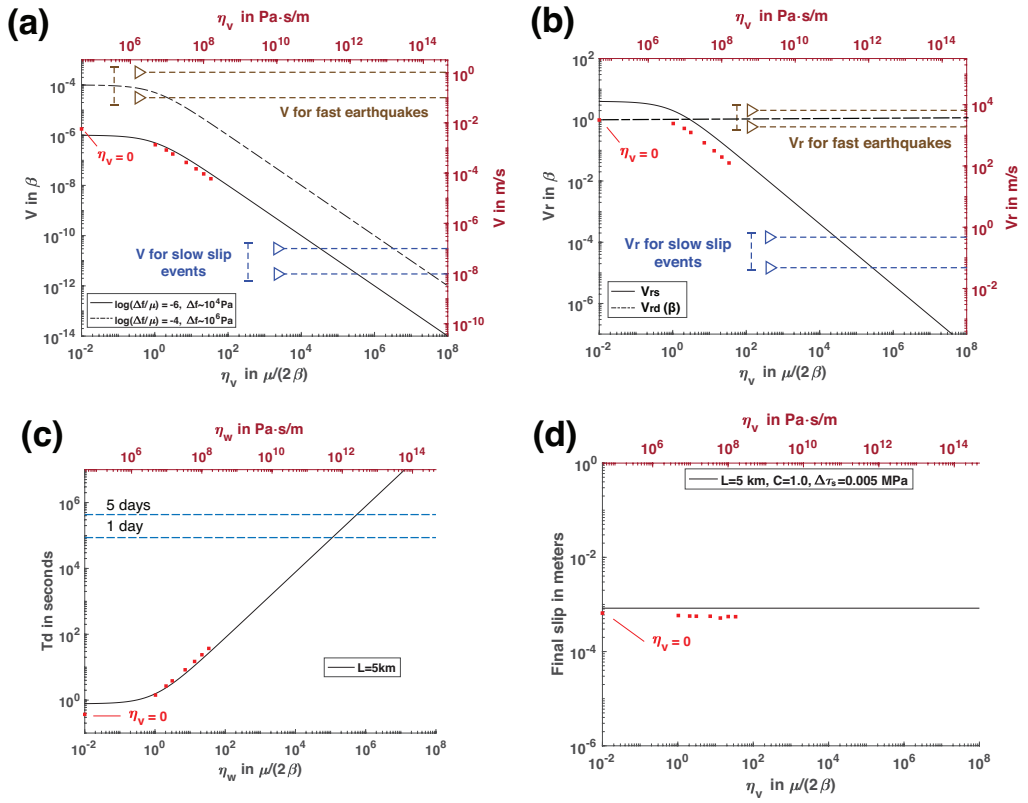

Figure 5.8: How (a) maximum slip rate, (b) rupture propagation speed, (c) slip rate decay time, and (d) final slip depends on the viscous coefficient η_v in my numerical simulations and analytical relations. The dashed and solid black lines in the figures are analytical relations obtained in Chapter 4. The red squares are the eight numerical simulations for Model A. The red squares on the y-axis represent the case when $\eta_v = 0$. The numerical shows trends that are broadly consistent with the analytical relations. Detailed discussion in the main text.

5.2.5 Comparison between numerical model A and analytical results

We may now quantitatively compare the numerical simulations with the analytical relations identified in Chapter 4. Figure 5.8 shows how different rupture quantities change with η_v in both the numerical simulations above and the analytical results from Chapter 4. The dashed and solid black lines in the figures are analytical relations obtained in Chapter 4. The red squares are the eight numerical simulations in Model A.

Figure 5.8(a) shows the comparison for maximum slip rate V. The corresponding analytical analysis is presented in section 4.3 and the analytical relation is also shown in Figure 4.3. The analytical results suggest that V decreases as η_v increases, and the V-η_v relation depends on the dynamic stress drop Δf. The dashed black line plots the analytical V-η_v relation when $\Delta f = 10^6$ Pa, and the solid black line plots the analytical V-η_v relation when $\Delta f = 10^4$ Pa. In our Model A simulations, $\Delta f = 10^4$ Pa, which is the same as the solid line case. The $\eta_v = 0$ case is plotted on the y-axis, due to the limitation of a log-log plot. The trend shown by the numerical data points fits the corresponding analytical relation (the solid black line) very well, suggesting a good fit between numerical and analytical models.

Figure 5.8(b) shows the comparison for rupture propagation speed V_r. The corresponding analytical analysis is presented in section 4.6 and the analytical relation is also shown in a similar Figure 4.7. The analytical results suggest that, if rupture propagation is mainly controlled by elastic (dynamic) stress waves, V_r should be close to the elastic wave speed and should not be affected by η_v. I referred to this "elastic wave" controlled rupture propagation speed as V_{rd}, and it is plotted as a horizontal dashed black line in 5.8(b). When slip rate V is slower, the elastic wave amplitude is smaller, and I suggest that rupture propagation would then be mainly controlled by static stress transfer. I refer to the rupture propagation speed that is controlled by static stress as V_{rs}. Since the propagation speed of static stress transfer depends on slip rate V and V depends on η_v, V_{rs} depends on η_v as well. The analytical relation between V_{rs} and η_v is shown by the solid black line.

The rupture propagation speed V_r in the eight numerical simulations are calculated by dividing the maximum propagation distance along the PP' profile (from the edge of the

nucleation zone to P', 14.5 km) by the rupture time of P'. Due to the limitation of a log-log plot, I plot the $\eta_v = 0$ case on the y-axis. The rupture propagation speed for the $\eta_v = 0$ case is very close to β. For numerical simulations with a larger η_v, the rupture propagation speed is slower, and the trend is consistent with the analytical relation. I note that there is a small offset between the numerical and analytical results. Considering the nature of log-log plots, this discrepancy should be minor.

Figure 5.8(c) shows the comparison for slip rate decay time T_d. The corresponding analytical analysis is presented in section 4.5 and the analytical relation is also shown in a similar Figure 4.6. The analytical results suggest that T_d is controlled by both the characteristic slipping area length L and the viscous coefficient η_v. For a given L, T_d increases as η_v increases. The solid black line shows the analytical T_d-η_v relation when $L = 5$ km. I choose 5 km because this is roughly the slip rate decay distance we obtained in the numerical simulations. T_d is measured at point A, and it is defined as the time it takes for slip rate to drop from its top value to 1/10 of it. As shown in the figure, the trend shown with the numerical simulations agrees well with the trend of the analytical relation.

Figure 5.8(d) shows the comparison for characteristic slip D. The corresponding analytical analysis is presented in section 4.4. The analytical results suggest that the characteristic slip D is not affected by η_v. Therefore, I only mention this relation in the text and do not include a figure similar to Figure 5.8(d) to show it in section 4.4. The slip value is measured as the final slip at point A. The slip of the analytical model is calculated using equation (4.25),

$$D = \frac{1}{C} \cdot \frac{L}{\mu} \cdot \Delta\tau_s$$

The parameters I use are $C = 1$, $L = 5$ km, $\mu = 3 \times 10^{10}$ Pa, and $\Delta\tau_s = 0.005$ MPa. All parameters are the same as the numerical models, except μ being slightly different ($\mu = 3.13 \times 10^{10}$ Pa in the numerical models). I didn't notice this minor difference before I made the figures. Since this slight difference barely makes any difference to the comparison, I decide not to remake the figure. (Maybe I would if I have time in the end).

As shown in Figure 5.8(d), both analytical and numerical results demonstrate that the final slip D is not affected by η_v. In adition, the simplified derivation in section 4.4 can predict the slip in numerical simulations reasonably well.

As a quick summary of the above comparisons, the overall good agreement suggests that the simplifications and idealizations that allowed the analytical models to be developed in Chapter 4 are valid, because we are getting consistent results via a numerical model that does not make nearly so many assumptions.

5.3 Model B: sudden rupture of a square patch

One factor we have not tested in Model A is the effect of characteristic slipping area length L. Also, Model A does not directly validate the analytical relations of moment-L and moment-duration scaling. To test them, I run another set of numerical simulations, which I refer to as Model B. I note that some results of Model B have been presented in my earlier paper Wu, Oglesby, Ghosh, and Li (2019). In this prior publication, the results were used to explained VLFEs, while here I reference these results to validate the robustness of

my analytical derivations in Chapter 4.

I note that, in this particular section and the following section (section 5.4), I will use the unit MPa/(km/s) instead of Pa/(m/s) for η_v, although Pa/(m/s) is used in the all the other portion. I switch unit only because many figures in this section are made in my prior publication, and those figures use MPa/(km/s) for η_v. As I write the dissertation, I run out of the time to modify the unit and make thing homogeneous. This difference in unit makes no difference to my results.

5.3.1 Simulation setup

The generic setting of Model B is shown in Figure 5.9. As shown in Figure 5.9(a), the fault is set to be a planar square, with a side length of 10 km. The fault is discretized with small squares whose side $\Delta x = 0.1$ km, the same as in Model A. Figure 5.9(b) shows the generic setup of "friction" and initial stress setting. A square patch is located near the top edge of the fault (light and dark brown area). It has a side length of L, which is a fixed parameter for a given simulation but tunable across simulations. Within the patch, The yielding shear strength f_y and residual shear strength f_1 are set to be homogeneous and kept the same for all Model B simulations: $f_y = 0.01$ MPa and $f_1 = 0$ MPa. The initial shear stress T_0 on the patch is set to be 0.0095 MPa (light brown area), except for the very top row of the elements (dark brown area). That row of elements are used as a "nucleation zone" where the initial shear stress is 0.01001 MPa, which is just above the yielding strength. Outside the square patch (blue area), f_y, f_1, and T_0 are all set to be zero. The viscous coefficient η_v is set to be homogeneous on the fault for a given simulation, and its value

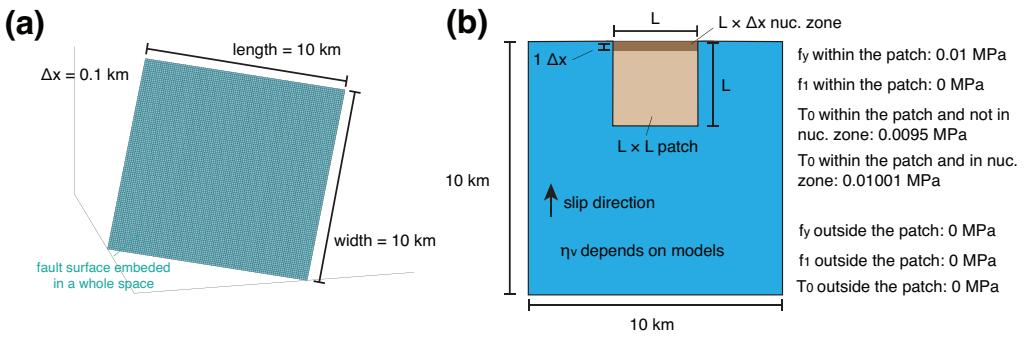

Figure 5.9: Schematics showing the setup of Model B simulations that test the effect of viscous coefficient L and η_v on rupture dynamics. (a) The geometry and discretization of the fault in Model B. The fault is set to be a planar square, with a side length of 10 km. The fault is discretized with small squares whose side $\Delta x = 0.1$ km. The fault is treated as a displacement discontinuity embedded in an elastic whole (full) space. The fault is viewed from an angle from the top. (b) The generic setup of "friction" and initial stress setting. A square patch is located near the top edge of the fault (light and dark brown area). It has side length of L, which is a fixed parameter for a given simulation but tunable across simulations. Within the patch, The yielding shear strength f_y and residual shear strength f_1 are set to be homogeneous and kept the same for all Model B simulations: $f_y = 0.01$ MPa and $f_1 = 0$ MPa. The initial shear stress T_0 is prescribed in the direction (shown by the arrow). The initial shear stress T_0 on the patch is set to be 0.0095 MPa (light brown area), except for the very top row of the elements (dark brown area). That row of elements is used as a "nucleation zone" where the initial shear stress is 0.0101 MPa, which is just above the yielding strength. Outside the square patch (blue area), f_y, f_1, and T_0 are all set to be zero. The viscous coefficient η_v is set to be homogeneous on the fault for a given simulation, and its value varies among different models.

Parameter	Fixed value
shear modulus μ	3.13×10^{10} Pa
P wave speed α	5.6×10^{3} m/s
S wave speed β	3.23×10^{3} m/s
medium density ρ	3×10^{3} kg/m^3
f_y within the patch	10^4 Pa
f_1 within the patch	0 Pa
f_y outside the patch	0 Pa
f_1 outside the patch	0 Pa
T_0 within the patch and outside the nucleation zone	0.95×10^4 Pa
T_0 within the patch and within the nucleation zone	1.001×10^4 Pa
T_0 outside the patch	0 Pa

Table 5.3: Summary of the fixed parameters used in different simulations in Model B.

varies among different models. These fixed parameters of Model B are summarized in Table 5.3. The patch side length L and the viscous coefficient η_v are two tunable parameters in Model B. Table 5.4 summarizes all of the parameter combinations I test with Model B. L ranges from 0.6 km to 9 km, and η_v ranges from 0 to 35000 MPa $\cdot$ s/km.

	$\eta_v = 0$	$\eta_v = 5000$	$\eta_v = 15000$	$\eta_v = 25000$	$\eta_v = 35000$
L=0.6	√	√		√	
L=1	√	√			
L=2	√	√			
L=3	√	√		√	
L=4	√	√			
L=5	√	√	√	√	√
L=6	√	√			
L=7	√	√		√	
L=8	√	√			
L=9	√	√		√	

Table 5.4: The table shows all the parameter combinations of L and η_v I test. A check mark means this combination is tested, while blank means not tested. The unit of L is km, and the unit of η_v is MPa $\cdot$ s/km. ($\mu/2\beta$ is about 5000 MPa $\cdot$ s/km)

5.3.2 Simulation results: general effect of η_v on rupture characteristics

Before discussing the effect of L, I first demonstrate the general effect of η_v on the rupture characteristics under this specific fault setting. Figure 5.10 shows the rupture snapshots of two simulations in Model B: 1. $L = 5$ km and $\eta_v = 0$ MPa/(km/s) (1st and 3rd column). 2. $L = 5$ km and $\eta_v = 25000$ MPa/(km/s) (2nd and 4th column). The 1st and 2nd column are slip rate snapshots, while the 3rd and 4th column are slip snapshots. In both simulations, the rupture starts propagating from the upper edge of the patch at close to a seismic wave speed, because the initial shear stress is very close to the yielding strength. Rupture stops when it reaches the lower edge of the patch, because the fault outside the patch does not allow a significant stress drop to facilitate further shear slip rupture. Therefore, high slip and slip rate area are confined within the patch.

As shown in both the slip and slip rate snapshots of the $\eta_v = 0$ MPa/(km/s) simulation, the fault stops slipping (i.e., the slip rate goes back to zero and slip stops increasing) soon after rupture stops propagating. For the $\eta_v = 25000$ MPa/(km/s) simulation, although rupture finishes its propagation at the same time as in the fast earthquake analog model, it does not stop slipping immediately afterward (shown in snapshots after 0.91 s). The patch still has considerable slip rate at 5.0 s, which is 5 times larger than the rupture propagation duration. The maximum slips of the $\eta_v = 0$ MPa/(km/s) and $\eta_v = 25000$ MPa/(km/s) simulation are ~ 1.3 mm and ~ 1 mm, respectively. The two numbers are of the same order, suggesting that these two models have similar moment release. However, the $\eta_v = 0$ MPa/(km/s) simulation has a maximum slip rate of ~ 3 mm/s (color scale saturated) while the $\eta_v = 25000$ MPa/(km/s) simulation only has ~ 0.3 mm/s,

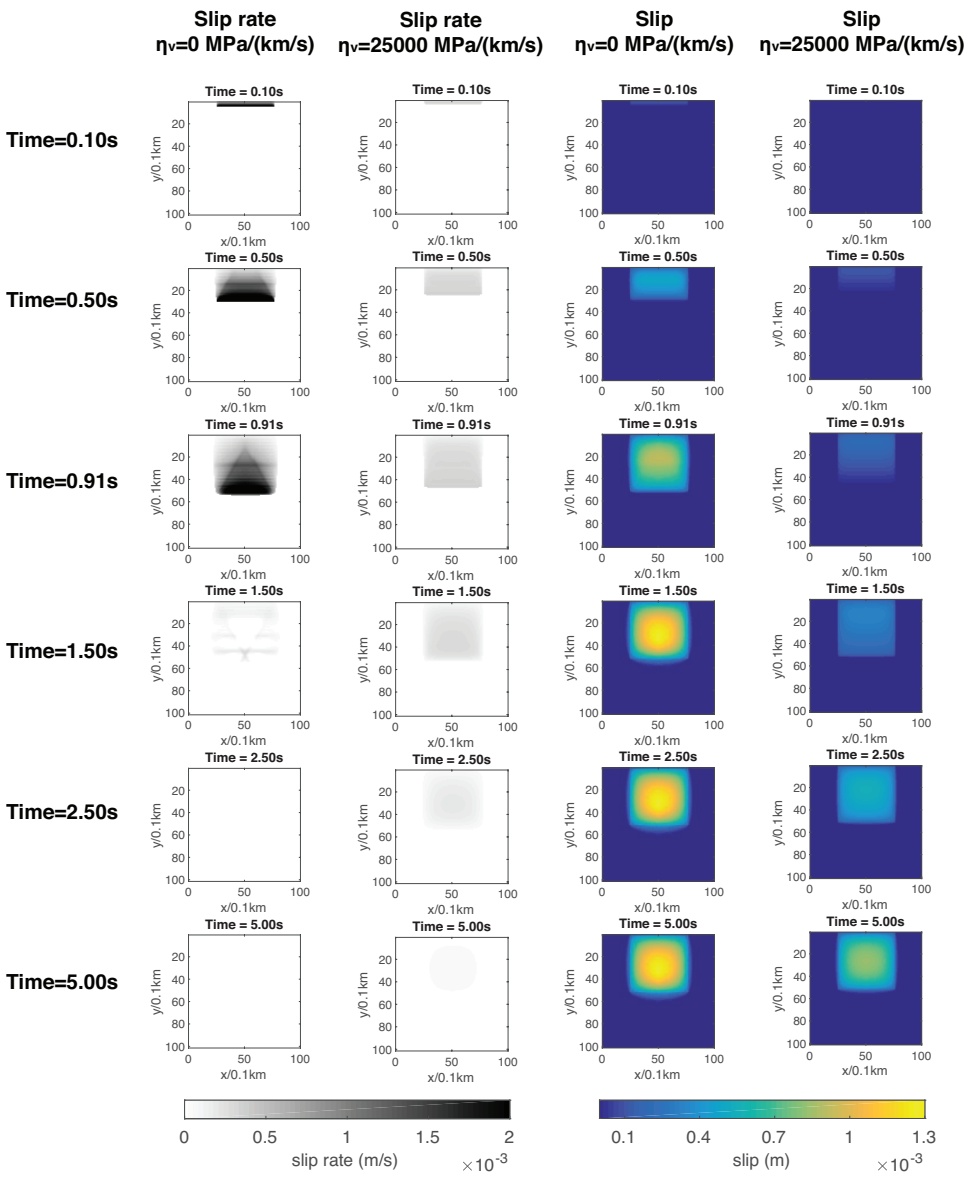

Figure 5.10: Slip and slip rate snapshots of two of Model B simulations: 1. An $L = 5$ km patch ruptures with rate strengthening friction coefficient $\eta_v = 0$ MPa/(km/s). (1st and 3rd column) 2. A $L = 5$ km patch ruptures with rate strengthening friction coefficient $\eta_v = 25000$ MPa/(km/s) (2nd and 4th column).

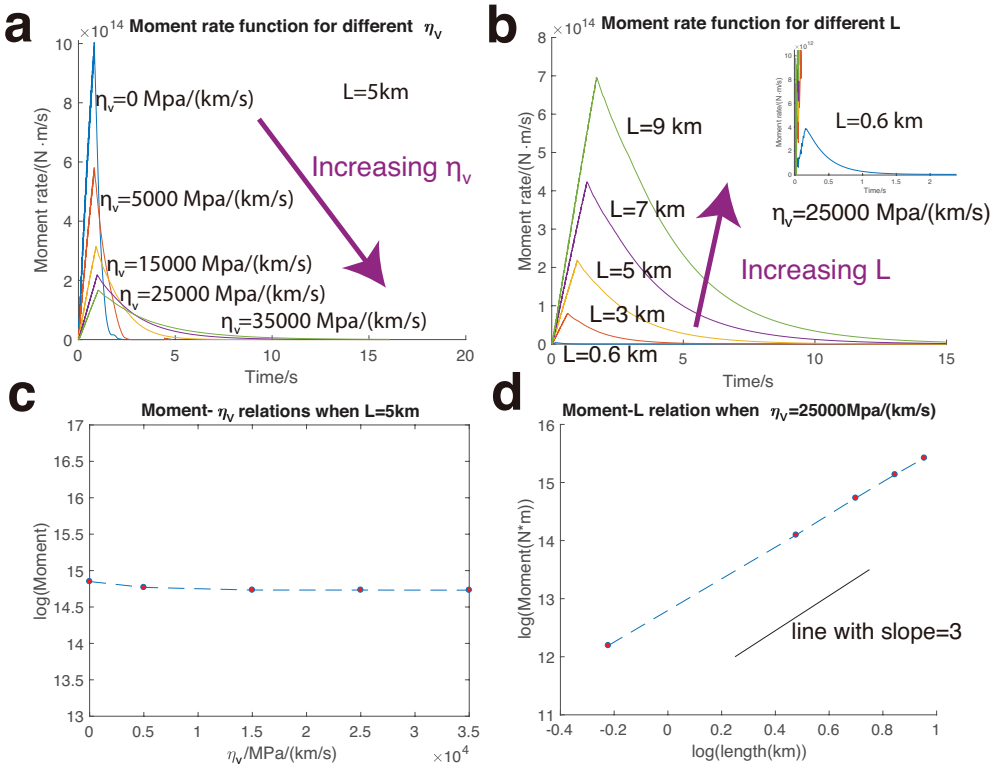

Figure 5.11: Results of Model B simulation **(a)** Moment rate functions of models with different rate strengthening coefficient η_v while the patch side length is fixed at 5 km. **(b)** Moment rate functions of models with different patch side length while the rate strengthening coefficient η_v is fixed at 25000 MPa/(km/s). The moment rate function when $L = 0.6$ km is not clear in the main figure, thus it is also shown in the inset map with an extended scale for a close look. **(c)** Moment-η_v relation when patch side length L is fixed at 5 km. **(d)** Moment-L relation when rate strengthening coefficient η_v is fixed at 25000 MPa/(km/s).

suggesting a lower amount of seismic radiation. The prolonged slip rate decay time caused due to increasing η_v is consistent with those we discussed for Model A in the previous section.

5.3.3 Simulation results: moment rate function

To demonstrate the effect of L and consider the "moment-L" and "moment-duration" relation, I investigate the moment rate function of the numerical simulations.

Figure 5.11 shows two sets of moment rate function comparisons where I keep either η_v or L fixed while varying the other parameter.

Figure 5.11(a) shows the moment rate functions of models with different viscous coefficient η_v while the patch side length L is fixed at 5 km. The moment at a time step k, M_0^k, is defined as,

$$M_0^k = \sum_i^N \mu \cdot D_i^k \cdot (\Delta x)^2 \tag{5.13}$$

and the moment rate at a time step k $\dot{M}_0^k$ is defined as,

$$\dot{M}_0^k = \sum_i^N \mu \cdot V_i^k \cdot (\Delta x)^2 \tag{5.14}$$

in which D_i^k and V_i^k are the slip and slip rate at the ith element at time step k (a total number element is N).

A typical moment rate function under a rate strengthening effect will start with a rapid linear increase, which corresponds to the rupture propagation process. The increase of moment rate is followed by a slow decay, which corresponds to a long-duration slip rate decay process. This characteristic can be quantitatively explained by considering the rupture front propagation at the beginning and an exponential slip rate decay (the exponential decay property has been discussed in section 4.5). As η_v increases, the maximum moment rate decreases while the event duration increases. Figure 5.11(b) shows the moment rate functions of models with different patch side length L while the viscous coefficient η_v is fixed at 25000 MPa/(km/s). It shows that both maximum moment rate and duration increase with patch length L.

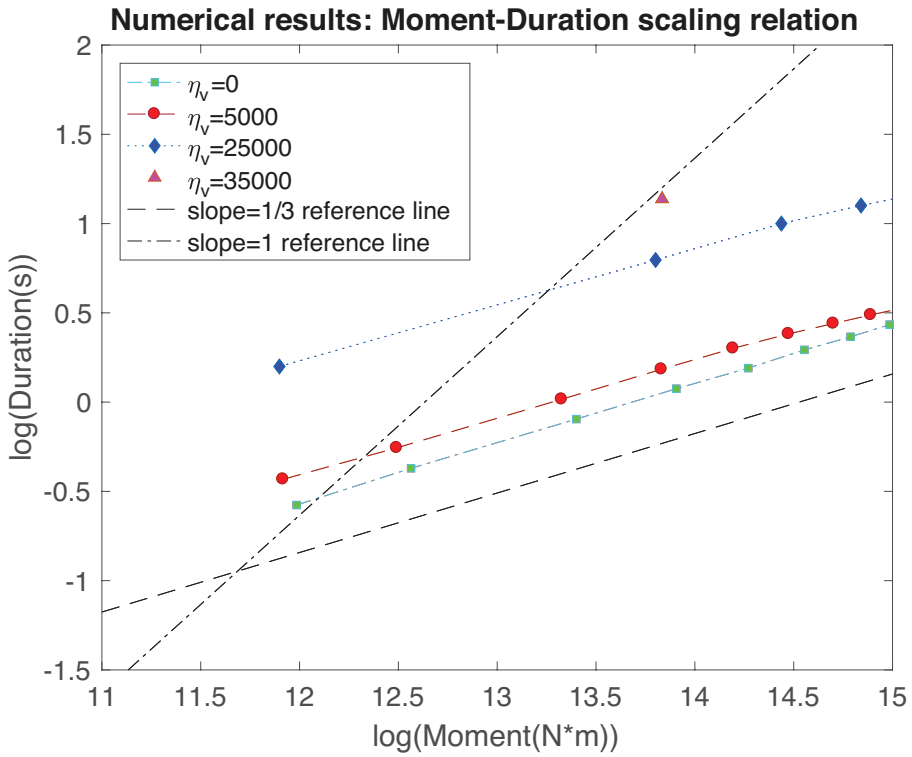

Figure 5.12: Moment-duration (M-T) scaling relation of the numerical simulations in Model B (in log-log). Each point in the plot represents one test result, and the different shapes and colors represent different η_v setting. Data points are connected with dashed line if they have the same η_v. All the η_v in this figure and its caption has a unit of MPa/(km/s) ($\mu/2\beta$ in my models is about 5000 MPa $\cdot$ s/km). Green square represents $\eta_v = 0$, red circle represents $\eta_v = 5000$, blue diamond represents $\eta_v = 25000$, and magenta triangle represents $\eta_v = 35000$. For reference, I also plot a "slope=1/3" line (dashed) and a "slope=1" line (dot-dashed).

Figure 5.11(c) shows how the final moment of simulations depends on η_v. The result shows that final moment does not change with η_v, which is consistent with the results from Model A that final slip does not change with η_v (Figure 5.8(d)). Figure 5.11(d) shows how the final moment of simulations depends on L. It shows that final moment increases with patch length L, and the slope of moment-L relation in a log-log plot is a straight line with a slope close to three. This scaling relation is the same as the one in a classic fast earthquake model, and it is consistent with my analytical results in Chapter 4 (discussion in section 4.8 around equation (4.59)).

Figure 5.12 plots the duration against moment for all the simulations in Model B. Duration is measured as the time taken for the moment rate function to drop to 1/10 of its peak value. Each dot represent one simulation. Data points are connected with dashed line if they have the same η_v. As shown in Figure 5.12, moment scales with the cube of duration when η_v is fixed at a certain value (0, 5000, and 25000 MPa/(km/s)). However, as η_v increases, the absolute location of the "1/3" line changes, moving from short duration to long duration in the moment-duration diagram. Although the simulations here cannot reach the parameter space of a typical SSE, they suggest a trend that is consistent with my analytical analysis in section 4.8, where I derive a $M_0 \propto T^3$ relation in equation (4.60). It again implies that my derivation in Chapter 4, though with some assumptions, should be robust for the problem we study here.

5.4 Model C: diffusive behavior of rupture

One last rupture behavior I will explore with the numerical models is the diffusive rupture propagation. As demonstrated in section 4.7, diffusive rupture propagation emerges in the "frictional-viscous" model framework when there is a patch with large stress drop surrounded by fault area that has a smaller stress drop. In that case, the rupture front outside the strong patch is too weak to push itself forward; instead, the rupture propagation outside the strong patch is still driven by the static stress field of the strong patch, and thus would yield a diffusive behavior. Ando et al. (2012) has demonstrated this diffusive rupture behavior with BIEM numerical simulations. However, the setup in Ando et al. (2012) includes very heterogeneous spatial distribution of stress and η_v. In section 4.7, I propose that a much simpler setup should also be able to produce diffusive rupture behaviors, where η_v is homogeneous and stress is almost homogeneous except for the difference between within and outside the strong patch. In this section, I explore this possibility with my own numerical simulations. This set of numerical simulations is referred to as Model C.

5.4.1 Model setup

Figure 5.13 shows the schematic of the setup of Model C. The fault geometry and fault discretization is the same as Model A. The friction and stress setting is almost the same as Model A, except that in Model C we have a different yielding strength f_y and residual shear stress f_1 between within the nucleation zone (dark brown area) and outside the nucleation zone (gray area). The yielding shear strength f_y and residual shear strength f_1 within the nucleation zone are set to be 0.01 MPa and 0 MPa, respectively. the initial

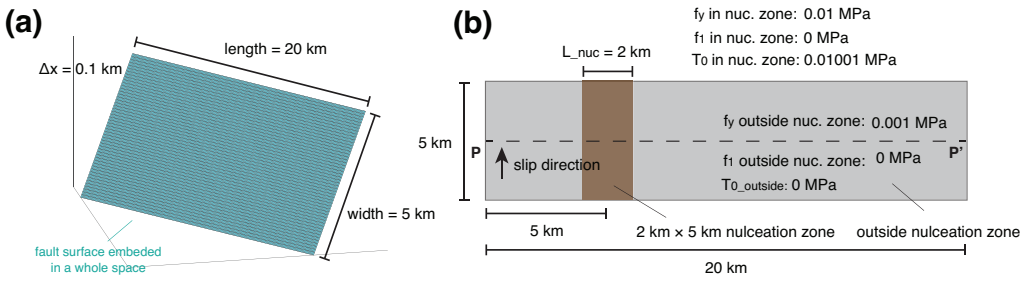

Figure 5.13: Schematics showing the setup of Model C simulations that test the diffusive rupture behaviors in the "frictional-viscous-mixing" "friction" framework. (a) The geometry and discretization of the fault in Model C. It is the same as in Model A (section 5.2). The fault is set to be a planar rectangle, with a length of 20 km and a width of 5 km. The fault is discretize with small squares whose side $\Delta x = 0.1$ km. The fault is treated as a displacement discontinuity embedded in an elastic whole (full) space. The fault is viewed from an angle from the top. (b) The generic setup of "friction" and initial stress setting. The initial shear stress T_0 is prescribed in the along-width direction. Similar to Model A, there is a rectangle nucleation zone (2 km $\times$ 5 km) whose center is 5 km away from a short side of the rectangular fault (dark brown area). The yielding shear strength f_y and residual shear strength f_1 within the nucleation zone are set to be 0.01 MPa and 0 MPa, respectively. Within the nucleation zone, initial stress $T_{0nuc} = 0.001001$ MPa, which is just above the yielding strength. Outside the nucleation zone, the yielding shear strength f_y and residual shear strength f_1 are set to be 0.001 MPa and 0.001, which results in a ten-times smaller dynamic stress drop $f_y - f_1$ compared to within the nucleation zone (gray area). The initial shear stress T_0 outside the nucleation zone is set to be 0 MPa. The viscous coefficient η_v is set to be homogeneous on the fault for a given simulation, and its value varies among different models. The dashed line PP' is a profile along x-axis that would be used in the later analysis, and it is at the central location along the width of the fault.

stress within the nucleation zone $T_{0nuc} = 0.001001$ MPa, which is just above the yielding strength. Outside the nucleation zone, the yielding shear strength f_y and residual shear strength f_1 are set to be 0.001 MPa and 0, which results in a ten-times smaller dynamic stress drop $f_y - f_1$ compared to within the nucleation zone. The initial shear stress T_0 outside the nucleation zone is set to be 0 MPa. η_v is set to be the same everywhere on the fault.

The common parameters in Model C simulations are summarized in Table 5.5. By

Parameter	Fixed value
shear modulus μ	3.13×10^{10} Pa
P wave speed α	5.6×10^{3} m/s
S wave speed β	3.23×10^{3} m/s
medium density ρ	3×10^{3} kg/m^3
f_y outside the nucleation zone	10^{3} Pa
f_y within the nucleation zone	10^{4} Pa
f_1 outside the nucleation zone	0 Pa
f_1 within the nucleation zone	0 Pa
T_0 outside the nucleation zone	0 Pa
T_0 within the nucleation zone	1.001×10^{4} Pa

Table 5.5: Summary of the fixed parameters used in different simulations in Model C.

Model number	η_v in MPa $\cdot$ s/km	η_v in $\mu/(2\beta)$
Model C1	165000	34.1
Model C2	85000	17.5

Table 5.6: Summary of η_v used in different simulations in Model C.

having this setup, the rupture propagation outside the nucleation zone would be mostly driven by the nucleation zone slip, instead of its own slip. We want to investigate the effect of η_v on the diffusive rupture behaviors, so I run two simulations of this generic setup with two different η_v: $\eta_v = 165000$ MPa $\cdot$ s/km, and $\eta_v = 85000$ MPa $\cdot$ s/km (summarized in Table 5.6).

5.4.2 Simulation results

Figure 5.14 shows the slip rate and shear stress snapshots of the two Model C simulations: Model C1 with $\eta_v \approx 34.1\ \mu/(2\beta)$ and Model C2 with $\eta_v \approx 17.5\ \mu/(2\beta)$. Each column corresponds to an output of the model (slip rate or shear stress) with a specific η_v.

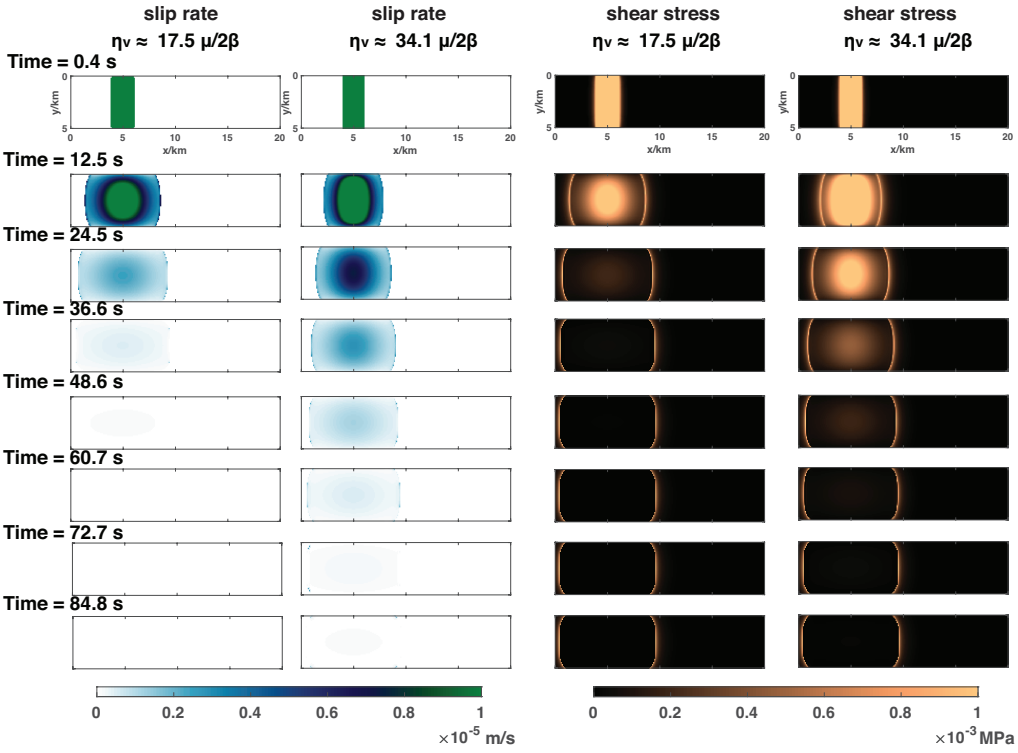

Figure 5.14: Slip rate and shear stress snapshots of the two models (Models C1 and C2) with different viscous coefficients η_v. Each column corresponds to an output of the model (slip rate or shear stress) with a specific η_v. The first and second column are the slip rate snapshots for the $\eta_v \approx 17.5\ \mu/(2\beta)$ model and the $\eta_v \approx 34.1\ \mu/(2\beta)$ model, respectively. The third and forth column are the shear stress snapshots for the $\eta_v \approx 17.5\ \mu/(2\beta)$ model and the $\eta_v \approx 34.1\ \mu/(2\beta)$ model, respectively. Each row corresponds to a time step, and the time increases from top to bottom. For each snapshot, the x-axis is the long-side direction of the rectangle fault and the y-axis is the short side direction of the rectangle fault. Slip rate is color-coded with white equals zero and dark green equals 1×10^{-5} m/s. Shear stress is color-coded with black equals zero and the brightest color equals 0.001 MPa. Both of these colormaps are saturated when the output is within the nucleation zone, in order to better show the diffusive rupture propagation outside the nucleation zone. This figure shows that the Model C setup can generate diffusive rupture behaviors, and the rupture diffuses more slowly as η_v increases.

The first and second columns are the slip rate snapshots for the $\eta_v \approx 17.5\ \mu/(2\beta)$ model and the $\eta_v = 34.1\ \mu/(2\beta)$ model, respectively. The third and forth column are the shear stress snapshots for the $\eta_v \approx 17.5\ \mu/(2\beta)$ model and the $\eta_v = 34.1\ \mu/(2\beta)$ model, respectively.

As shown in Figure 5.14, rupture propagation in both simulations naturally dies out when the rupture propagates a certain distance away from the nucleation zone, and this distance is the same for both simulations. When rupture dies out, slip rate goes back to zero (first and second column) and a permanent static shear stress increase is left near the edges of the slipped area (third and forth column). Both simulations show a diffusive-type rupture behavior in a general sense, where rupture propagates slower when propagating further. The rupture in the model with $\eta_v \approx 17.5\ \mu/(2\beta)$ ends between 36.6 s and 48.6 s, while in the $\eta_v \approx 34.1\ \mu/(2\beta)$ model, the rupture ends between 72.7 s and 84.8 s. It implies that a slower diffusive rupture when η_v is higher. In addition, the peak slip rate becomes smaller as the rupture get away from the nucleation zone.

The diffusive rupture can be seen more clearly in the space-time evolution plot. Figure 5.15 shows the space-time evolution of slip rate and shear stress along the PP' profile (the dashed line in Figure 5.13b). Both the two colormaps for slip rate and shear stress are saturated when the output is within the nucleation zone, in order to better show the diffusive rupture propagation outside the nucleation zone. For the slip within the nucleation zone, the rise time is larger when η_v is higher, which is consistent with the results in section 4.5 and 5.2. Both ruptures end near $x = 0$ km and $x = 10$ km, and the rupture propagation outside the nucleation zone is diffusive-like. The slip rate gradually decreases to zero as rupture diffuses out. The diffusive speed is slower when η_v is higher.

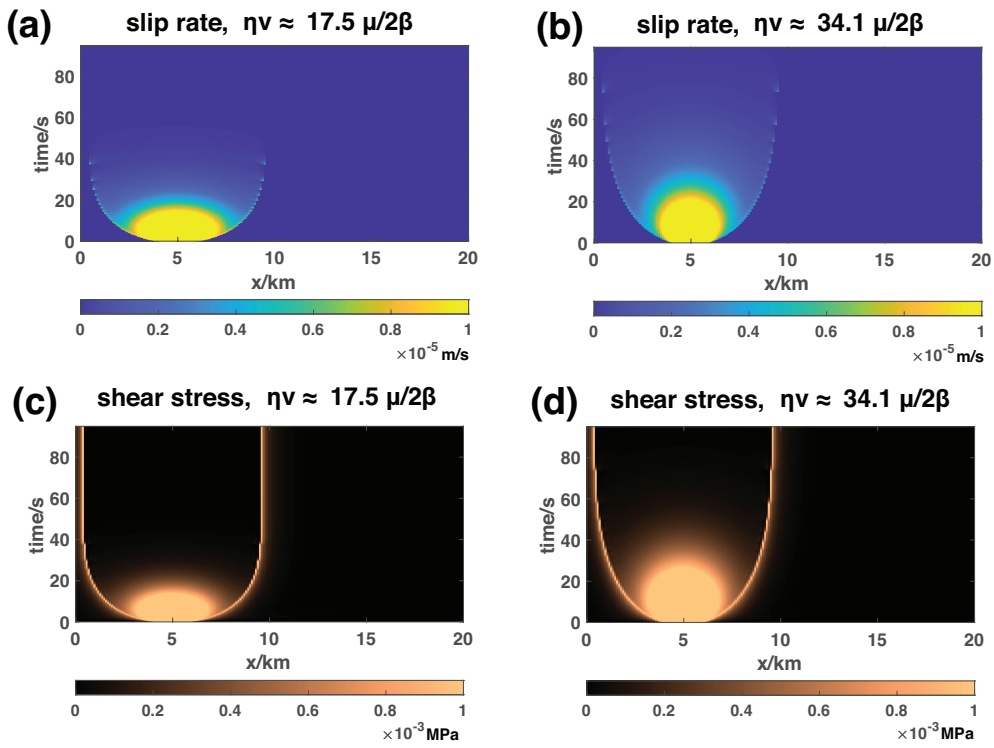

Figure 5.15: The space-time evolution of slip rate and shear stress along the PP' profile shown by the dashed line in Figure 5.13b. The slip rate evolution for $\eta_v = 17.5$ and 34.1 $\mu/(2\beta)$ cases are shown in (a) and (b), respectively. The shear stress evolution for $\eta_v = 17.5$ and 34.1 $\mu/(2\beta)$ cases are shown in (c) and (d), respectively. For each space-time plot, x-axis is the along profile distance, with zero at point P, and y-axis denotes time. The maximum value of the slip rate colormap is 10^{-5} m/s, and the minimum value is zero. The maximum value of the colormap is 0.001 MPa, and the minimum value is zero. Both these two colormap are saturated when the output is within the nucleation zone, in order to better show the diffusive rupture propagation outside the nucleation zone.

5.4.3 Comparison between numerical Model C and analytical results

Before we compare between numerical Model C and analytical results, it would be helpful we first review the analytical results in section 4.7. In section 4.7, we obtain several analytical relations to predict and describe the diffusive rupture behavior, and find that it depends on different ways of simplification and approximation. To obtain the analytical relation, I need to simplify the complicated static stress decay relation as either $\sim r^{-2}$ or $\sim r^{-3}$. For both decay assumptions, we may obtain a corresponding relation between rupture time t and distance x_P that is in a logarithmic form. The corresponding equation for $\sim r^{-2}$ and $\sim r^{-3}$ are (4.45) and (4.54), respectively. For convenience, I will show them here again. Equation (4.45) is

$$t \approx \frac{1}{C} \cdot \left(1 + \frac{\eta_v}{\mu/2\beta}\right) \cdot \frac{L}{2\beta} \cdot \ln\left(\frac{1}{1 - \frac{\tau_e}{\Delta f} \cdot \frac{(x_P)^2}{L^2}}\right)$$

and equation (4.54) is

$$t \approx \frac{1}{C} \cdot \left(1 + \frac{\eta_v}{\mu/2\beta}\right) \cdot \frac{L}{2\beta} \cdot \ln\left(\frac{1}{1 - \frac{\tau_e}{\Delta f} \cdot \frac{(x_P)^3}{L^3}}\right)$$

To simplify the expressions, one may utilize a Tyler series expansion near $x_P = 0$ to approximate the logarithmic relation as a polynomial. For the $\sim r^{-2}$ assumption case, the logarithmic relation can be approximated as a $t \sim (x_P)^2$ relation, and it has been shown in equation (4.49),

$$t \approx \frac{1}{C} \cdot \frac{1}{L \cdot 2\beta} \cdot \frac{\tau_e}{\Delta f} \cdot \left(1 + \frac{\eta_v}{\mu/(2\beta)}\right) \cdot (x_P)^2$$

and for the $\sim r^{-3}$ assumption case, the logarithmic relation can be approximated as a $t \sim (x_P)^3$ relation, and it has been shown in equation (4.55),

$$t \approx \frac{1}{C} \cdot \frac{1}{L^2 \cdot 2\beta} \cdot \frac{\tau_e}{\Delta f} \cdot \left(1 + \frac{\eta_v}{\mu/(2\beta)}\right) \cdot (x_P)^3$$

The purpose of making this simplification is to compare my theoretical results with the $t = (D_f)^{-1} \cdot x^2$ diffusive tremor migration behavior observed in real world. In particular, this observed empirical relation has a one-to-one correspondence with the theoretical relation equation (4.49), based on which one can find a theoretical expression for D_f in equation (4.50),

$$\begin{aligned} D_f &= C \cdot \frac{\Delta f}{\tau_e} \cdot \left(1 + \frac{\eta_v}{\mu/(2\beta)}\right)^{-1} \cdot L \cdot 2\beta \\ &= \frac{C\mu\Delta\tau L}{\eta_v \tau_e} \cdot \left(\frac{\mu/(2\beta)}{\eta_v} + 1\right)^{-1} \end{aligned}$$

This relation is consistent with the theoretical relation derived in Ando et al. (2012) when η_v is significantly larger than $\mu/(2\beta)$ and $C = 1/(2\pi)$. Since the solution in Ando et al. (2012) is derived for a 2D fault with quasi-static assumption, my solution here might be more general.

We may now compare between numerical model C and the analytical results. I choose the slip rate space-time evolution plot Figure 5.14(a) and (b) as the numerical outputs to compare against. Figure 5.16 shows the comparison between the numerical results and the analytical relation where a r^{-2} decay of static stress is assumed. The analytical relations are shown by lines with different colors and line-styles. For all the

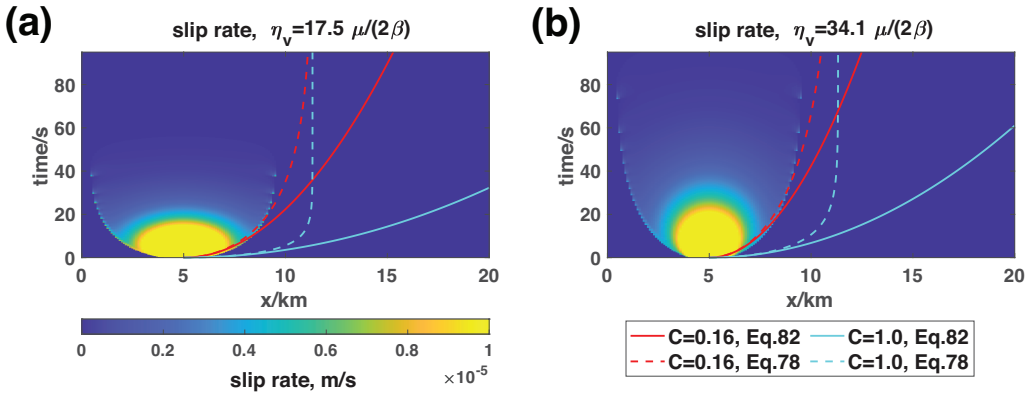

Figure 5.16: Comparison between the numerical results and the analytical relation derived in section 4.7 where a r^{-2} decay of static stress is assumed. The numerical space-time evolution of slip rate along the PP' of the $\eta_v = 17.5\ \mu/(2\beta)$ model and the $\eta_v = 34.1\ \mu/(2\beta)$ model are used for comparison, and they are the same as Figure 5.14(a) and (b). The analytical relations in section 4.7 are shown by lines with different colors and line-styles. The logarithmic-form theoretical relations (equation (4.45)) are shown by dashed lines, and the $t \sim x^2$ approximations (equation (4.49)) are shown by solid lines. For all lines, the strong patch length L is set to be 2 km and $\tau_e/\Delta f$ is set to be 0.1, which are consistent with the numerical simulations. For the constant C, the lines use two values: when plotting the blue lines, I assume a most generic value $C = 1$. When plotting the red lines, I fine-tune C to make the analytical relations best match the numerical results visually. The best C I find is 0.16, which is similar to the 2D theoretical value $1/(2\pi)$ given in Ando et al. (2012).

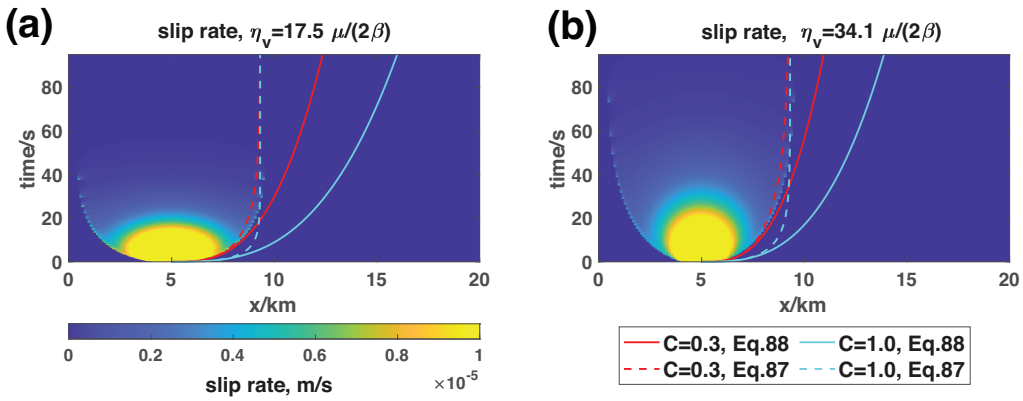

Figure 5.17: Comparison between the numerical results and the analytical relation derived in section 4.7 where a r^{-3} decay of static stress is assumed. The numerical space-time evolution of slip rate along the PP' of the $\eta_v \approx 17.5\ \mu/(2\beta)$ model and the $\eta_v \approx 34.1\ \mu/(2\beta)$ model are used for comparison, and they are the same as Figure 5.14(a) and (b). The analytical relations in section 4.7 are shown by lines with different colors and line-styles. The logarithm-form theoretical relations (equation (4.54)) are shown by dash lines, and the $t \sim x^3$ approximation (equation (4.55)) is shown by solid lines. For all lines, the strong patch length L is set to be 2 km and $\tau_e/\Delta f$ is set to be 0.1, which are the consistent with the numerical simulations. For the constant C, The lines use two value: when plotting the blue lines, I assume a most generic value $C = 1$. When plotting the red lines, I fine-tune C to make the analytical relations best match the numerical results visually. The best C I find is 0.3.

analytical results, the strong patch length L is set to be 2 km and $\tau_e/\Delta f$ is set to be 0.1, which are the consistent with the numerical simulations. For the constant C, I use two value: a most generic value $C = 1$ (blue lines) and a fine-tune C to make the analytical relations best match the numerical results visually (red lines).

As shown in Figure 5.16, the analytical relations also show a slower diffusive rupture as η_v increases, which is consistent with the numerical results. The logarithm relation (dashed lines) is very similar to the $t \sim x^2$ approximation (solid lines) when the rupture distance is short. This is expected because the $t \sim x^2$ approximation is derived by only using the first-order term in the Tyler series expansion of the logarithmic relation. However, the more rigorous logarithmic relation can predict the diffusive propagation boundary, while the $t \sim x^2$ approximation cannot. A most generic constant C value of one can produce a diffusive rupture behavior (blue lines), but the fit is relatively poor. When $C = 0.16$, the fit is much improved, especially at the beginning of the diffusive rupture. This C value is very similar to $1/(2\pi)$ that is derived in Ando et al. (2012). Considering that the rupture setup is close to a 2D situation just outside the nucleation zone, such agreement is as expected.

Figure 5.17 shows the comparison between the numerical results and the analytical relation where a r^{-3} decay of static stress is assumed. The logarithmic-form theoretical relations (equation (4.54)) are shown by dashed lines, and the $t \sim x^3$ approximation (equation (4.55)) is shown by solid lines. The results are very similar to in Figure 5.16, where diffusion becomes slower when η_v increases, and the logarithmic relation converges to the $t \sim x^3$ approximation when propagation distance is small. The generic C value of one fits the diffusion poorly, while the fit is much improved when $C = 0.3$. In contrast to the r^{-2} de-

cay case, the logarithm form r^{-3} decay relation can better predict the diffusive propagation boundary. This is as expected since a r^{-3} decay of static stress is a better approximation as rupture moves away from the stress source (Okada, 1992).

The comparison above suggests that the analytical relations in section 4.7, no matter whether they are based on r^{-2} or r^{-3} static stress decay, all can explain the diffusive rupture behavior in the numerical simulations to a certain degree. It again suggests that our analytical derivation in section 4.7 is reasonable to first-order, though with many assumptions. Different from the numerical results in Ando et al. (2012), I did not include any smaller-scale spatial heterogeneity of friction or stress parameters. It implies that the drastic contrast between a strong patch and a weak surrounding fault, together with the frictional-viscous "friction law", is the key to produce the diffusive rupture behavior.

For both the r^{-2}- and the r^{-3}- based analytical relations, the logarithmic form seems to be better than the polynomial ($t \sim x^3$ or $t \sim x^3$) approximations in all cases. The logarithmic form would predict a natural stop of the diffusive rupture, while the polynomial approximations cannot. This feature has not been pointed out in Ando et al. (2012), though it is likely buried in their numerical simulations. Nevertheless, I note that the polynomial approximations should still be very important, especially from an observational point of view. First of all, a good property of the simple polynomial approximations is that, they are more convenient to use when measuring and quantifying the diffusive rupture in observations, compared to the complicated logarithmic form. In fact, all existing reports on the diffusive tremor migrations assume a $t = (D_f)^{-1} \cdot x^2$ relation and measure the corresponding diffusivity D_f. Therefore, using the simple polynomial approximations shall

be easier for the practice of comparing between models and observations.

Secondly, although the polynomial approximations depart from the logarithmic form predictions as x increases, the polynomial approximations actually approach the logarithmic form when x is small. The polynomial approximations also fit the numerical results reasonably well at the beginning stage of the diffusive rupture. Since the slip rate dies out as rupture diffuses to a greater distance, the beginning stage of the diffusive rupture should be most visible in observations, which is exactly what the polynomial approximations are good at explaining. Figure 5.18 shows rupture time against rupture distance in a log-log plot for the two simulations we investigate above. The numerical results are plotted in blue solid curves, and the slope of $t \sim x^2$ and $t \sim x^3$ relation are shown in red and brown dashed lines for reference. The plot shows that both a $t \sim x^2$ and $t \sim x^3$ can be reasonable representations for a considerable portion of the early diffusive rupture.

At the end of the discussion of Model C, I want to note that the model setup here is very simple with not much spatial heterogeneity of friction and stress parameter. I am using it to highlight the mechanism of diffusive rupture. Were I to include a high prestress region at a certain distance away from the nucleation zone, the rupture may switch from a diffusive rupture to a constant propagation speed rupture, as shown in Model A. Such a transition has been observed in ETS events in the Cascadia subduction zone, as reported by Creager et al. (2020). Nevertheless, a detailed modeling of the actual SSE is beyond the scope of my dissertation, and shall be the subject of future study.

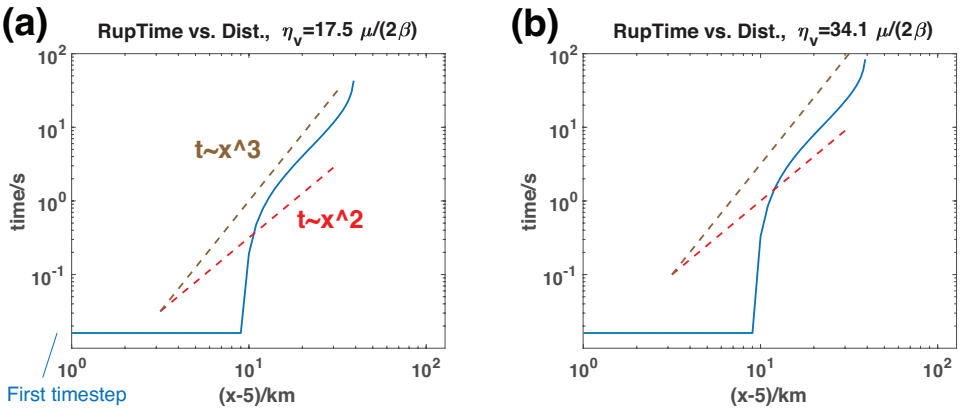

Figure 5.18: Rupture time against rupture distance for one branch of the rupture along the PP' profile ($x > 5$ km) in (a) Model C2, $\eta_v \approx 17.5\ \mu/(2\beta)$ and (b) Model C1, $\eta_v \approx 34.1\ \mu/(2\beta)$. X-axis is the along profile distance minus $x = 5$ km, which is the center coordinate of the nucleation zone. Y-axis is the time when a certain fault element just ruptures (rupture time). The plot is shown in a log-log form in order to demonstrate the first-order dependence. Blue solid lines are numerical model results. Within the nucleation zone, all rupture time values equal the first time step. Blue lines disappear after a certain time/distance because rupture dies out. The brown and red dashed lines show the slope of $t \sim x^2$ and $t \sim x^3$ relation for reference purpose. The figure suggests that either $t \sim x^2$ or $t \sim x^3$ could be a reasonably well approximation of the simulation results here.

5.5 Summary of Chapter 5

In Chapter 5, I conduct numerical simulations to test the "frictional-viscous" models that are described and analytically investigated in Chapter 4. In numerical solutions, I am able to include the full elastodynamic effects with inertia and waves, and as well consider the spatial distribution of slip and stress on the fault. These two features are simplified in the analytical derivations. Therefore, with the advantage of numerical solutions, I can test the robustness of my analytical derivations. The good agreement between the numerical and analytical results implies that both my analytical derivations and numerical implications for the targeted "friction law" framework should be robust.

In particular, the set of simulations in **Model A** (section 5.2) provides numerical results that can be compared with the analytical results in section 4.3 for maximum slip rate, in section 4.4 for final slip, in section 4.5 for slip rate decay time, in section 4.6 for rupture propagation speed, and in section 4.8 for "moment-duration" scaling relation when rupture propagation duration controls the event duration. Secondly, the set of simulations in **Model B** (section 5.3) provides numerical results that can be compared with the analytical results for the effect of characteristic slipping area length L in section 4.4 for final moment, and in section 4.8 for "moment-duration" scaling relation when rise time (slip rate decay time) controls the event duration. Lastly, the set of simulations in **Model C** (section 5.4) provides numerical results that can be compared with the analytical results of diffusive rupture propagation in section 4.7. Combining the discussions of Model A, B, and C, all the analytical relations derived in Chapter 4 have been tested against numerical simulations.

I note that, due to limited computational capacity, I cannot simulate an event

that matches the observed characteristics of SSEs, as it would require η_v to be at least 10^4 $\mu/(2\beta)$, and the fault area needs to be larger. Those simulations would requires several orders of magnitude greater computational capacity. However, these numerical simulations support the trend predicted by the analytical relations in Chapter 4. The agreement in trends between numerical and analytical results helps to validate the derivations I have made in Chapter 4. With the analytical solutions, we may easily extend the model to examine the parameter space of observed SSEs. As has already been shown in Chapter 4, we find that a stress drop of $\sim$ 10 kPa and a viscous coefficient η_v of $\sim 10^4 - 10^5$ $\mu/(2\beta)$ can simultaneously explain all the SSE "co-seismic" observations that are discussed above. As a bonus, the numerical simulations provide many visualizations that are more intuitive than the analytical equations in Chapter 4, which could help readers better understand the physical process I discuss in my dissertation.

Chapter 6

Discussion: implications and limitations of my analysis

I notice that some potentially important topics have not been fully addressed in the previous chapters. In Chapter 4 and 5, my main focus is to derive the slip and rupture behaviors under the frictional-viscous faulting system. I did not expand the discussion on the physical picture behind the model in terms of the whole tectonic process and deliberate on the physical meaning of the associated parameters. In addition, I mainly focused on explaining the kinematic characteristics of slow slip events (SSEs), but, did not extend discussion to other slow earthquakes, such as low frequency earthquakes (LFEs), tectonic tremors, very low frequency earthquakes (VLFEs), and rapid tremor migrations. Lastly, I did not compare my model to other slow earthquake models in detail. For a better flow of demonstration, these discussions are not expanded in the previous chapters on purpose.

However, these discussions may still be good supplements to the demonstration

in my dissertation. In the following chapter, I will discuss these topics in greater detail, and each section will correspond to a distinct topic. I hope these discussions may better illustrate the implications and limitations of the model in my dissertation.

6.1 Physical image of the frictional-viscous model in terms of the whole tectonic process

In Chapters 4 and 5, I demonstrate how the fault with frictional-viscous "friction" can give rise to slow slip events, In these chapters, I focus more on the process that generates the slow slip event signals, and less on the tectonic consequence of such setup in terms of the stress accumulating process. A thorough discussion of the latter part requires more quantitative analysis and is out of the scope of this paper. Still, we may still at least discuss the associated process conceptually and qualitatively, which will be the content of this section.

6.1.1 Stress concentration on the frictional contact

As the elastic rebound theory suggests, when two tectonic blocks move against each other, frictional force on the fault tends to hold the two blocks together. Shear strain would increase near the fault, and so would the applied shear stress on the fault. No slip (offset) takes place across the fault until the shear stress on the fault is so large that the fault can no longer provide an equivalent frictional force to prohibit slip. Then, a sudden drop of frictional force (or shear strength) happens on the fault, resulting in a release of the strain energy in the nearby rock, and causing earthquakes.

This framework should also apply to the frictional-viscous model that I am investigating here. In my model, stress is partitioned into a frictional part and a viscous part. When shear stress is applied to such a fault, it would not slip until the shear stress is high enough to break the frictional contact, which is similar to the classic "friction-only" model. However, because the fraction of frictional contact area is small compared to the total fault area, the actual shear stress τ_f on these contacts needs to be larger than the average shear stress $\overline{\tau}$, in order to hold the fault and prevent the two sides from slipping. We denote the actual frictional contact area as A_f and the total area as A. τ_f and $\overline{\tau}$ should have the following relation,

$$\overline{\tau} = C_{amp} \cdot \frac{A_f}{A} \cdot \tau_f \tag{6.1}$$

in which C_{amp} is a correction factor for the amplification effect. It is included to consider that the frictional contact could have a complex 3D structure in the fault zone that has finite thickness, which may modify the stress amplification effect.

This physical picture is demonstrated in the schematics in Figure 6.1. For a fault zone where frictional contact area is dominant (Figure 6.1(a)), the average stress on the fault would be similar to the frictional stress on the contact,

$$\overline{\tau} \approx \tau_f, \text{ when } C_{amp} \cdot \frac{A_f}{A} \approx 1 \tag{6.2}$$

For the frictional-viscous model in my dissertation, the frictional contact is assumed to be only a small fraction of the total fault zone volume (Figure 6.1(b)). In that case the average stress on the fault would be significantly smaller than the frictional stress

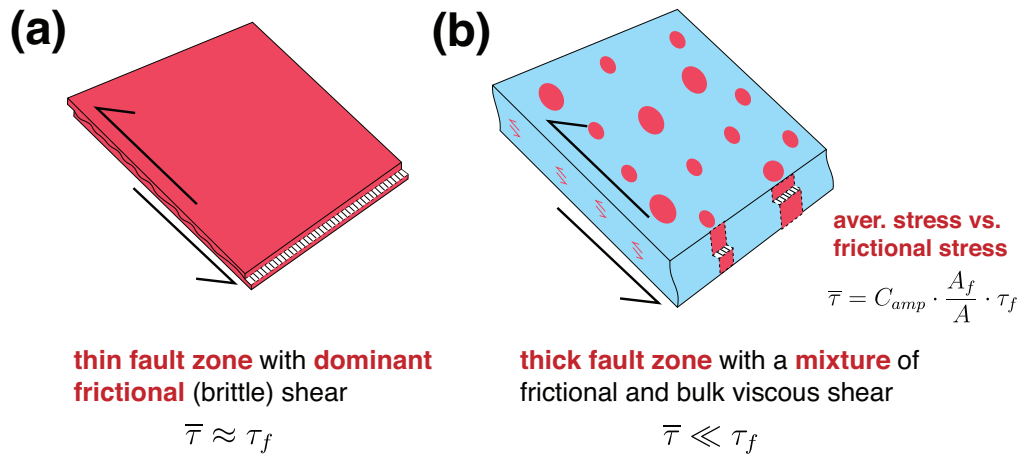

Figure 6.1: Schematics of fault zone showing two cases: (a) the fault zone is thin and frictional contacts dominate the shear zone; and (b) the fault zone is wide and frictional contacts is only a small fraction of the total fault area. (a) is more representative of the fault zone at seismogenic depths. (b) is the physical vision of the frictional-viscous model in my dissertation, which I suggest can be representative of the shear zones that host slow earthquakes.

on the contact,

$$\overline{\tau} \ll \tau_f, \text{ when } C_{amp} \cdot \frac{A_f}{A} \ll 1. \tag{6.3}$$

This mechanical property would lead to a stress concentration/amplification effect for the frictional-viscous model: when tectonic shear strain accumulates around the fault due to plate movement, the actual shear stress on the frictional contact builds up significantly faster than the average shear stress on fault. This is because the small fraction of area that is frictionally locked needs to bear the load for a considerably greater area. As a result, a frictional-viscous fault would have a shorter event interval and a smaller average shear drop, compared to a fault where the frictional contact area fraction is high.

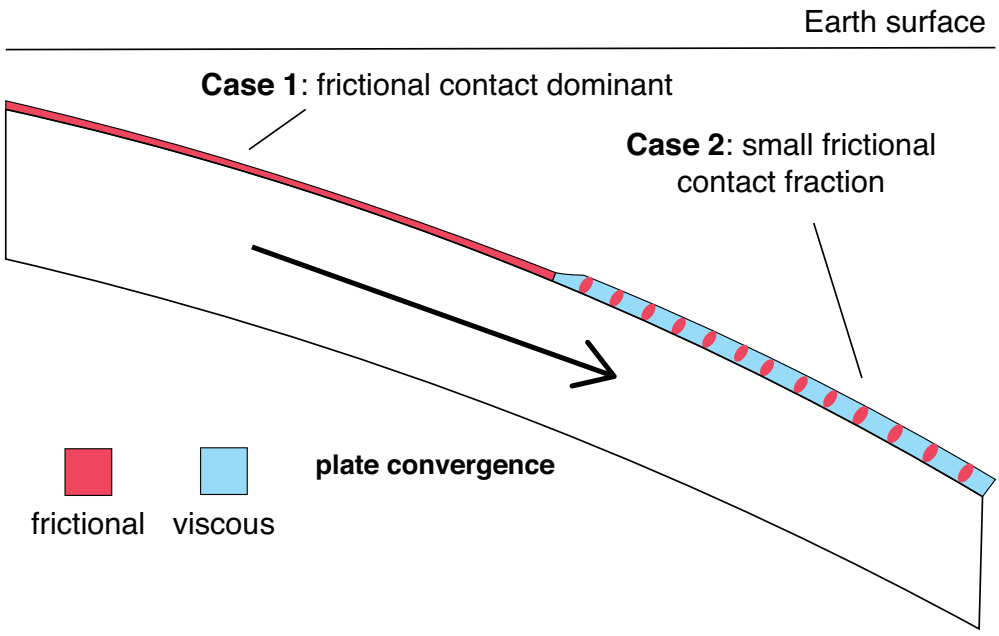

Figure 6.2: Schematic of the two conceptual cases that I consider when evaluating the tectonic consequence of the frictional-viscous model. The figure sketches a cross-section of a subduction zone. Case 1 represents Figure 6.1(a) and depicts the updip portion of the subduction interface, where the fault zone is thin and the frictional contact covers most of the fault area. Case 2 represents Figure 6.1(b) and shows the downdip portion of the subduction zone, where the fault zone is thick and the frictional contact area fraction is small. The schematic is just for illustrating concepts and is not to scale.

6.1.2 The tectonic consequence of the stress concentration effect: a smaller shear stress drop and a shorter event interval

For convenience, I use a subduction zone setting as an example to demonstrate the tectonic consequence of the stress concentration effect. The same mechanism should also be applicable to other tectonic environments. Figure 6.2 shows the schematic of the two conceptual cases that I consider. The figure sketches out a 2D profile of a subduction zone. Case 1 is shown in the updip portion of the subduction interface, where the fault zone is thin and the frictional contact covers most of the fault area, representing Figure 6.1(a).

Case 2 represents Figure 6.1(b) and is shown in the downdip portion of the subduction zone, where the fault zone is thick and the frictional contact area fraction is small. We may consider a very simple model where a fault starts to slip when the actual frictional shear stress τ_f reaches the yielding frictional strength f_y, and assume that f_y is the same for the fault zone in both cases.

Figure 6.3 shows the two conceptual diagrams that demonstrate how the shear stress on the fault evolves with plate convergence. Figure 6.3(a) and (b) correspond to Cases 1 and 2 described in the previous paragraph, respectively. In both figures, the purple solid line represents the average shear stress on fault, while the orange dashed line represents the actual shear stress on the frictional contact. For simplicity, I assume that both cases have the same far-field stressing rate. In Case 1, the average stressing rate is similar to the actual stressing rate on the frictional contact. Therefore, when a sudden stress drop (an earthquake) happens, the average stress drop is similar to the actual frictional stress drop. In Case 2, the average stressing rate is set to be the same as in Case 1. However, the actual stressing rate on the frictional contact is significantly larger due to the stress concentration effect. Therefore, the frictional contact may reach the yielding strength sooner than in Case 1, and the event interval in Case 2 is much shorter. In addition, the average stress drop in Case 2 is smaller than in Case 1, which also produce less final slip per event.

The transient stress drop events in Case 1 and Case 2 are considered to correspond to large megathrust earthquakes and large slow slip events, respectively. Therefore, the results above are qualitatively consistent with the observed differences between large megathrust earthquakes and large slow slip events. That is, slow slip events tend to have

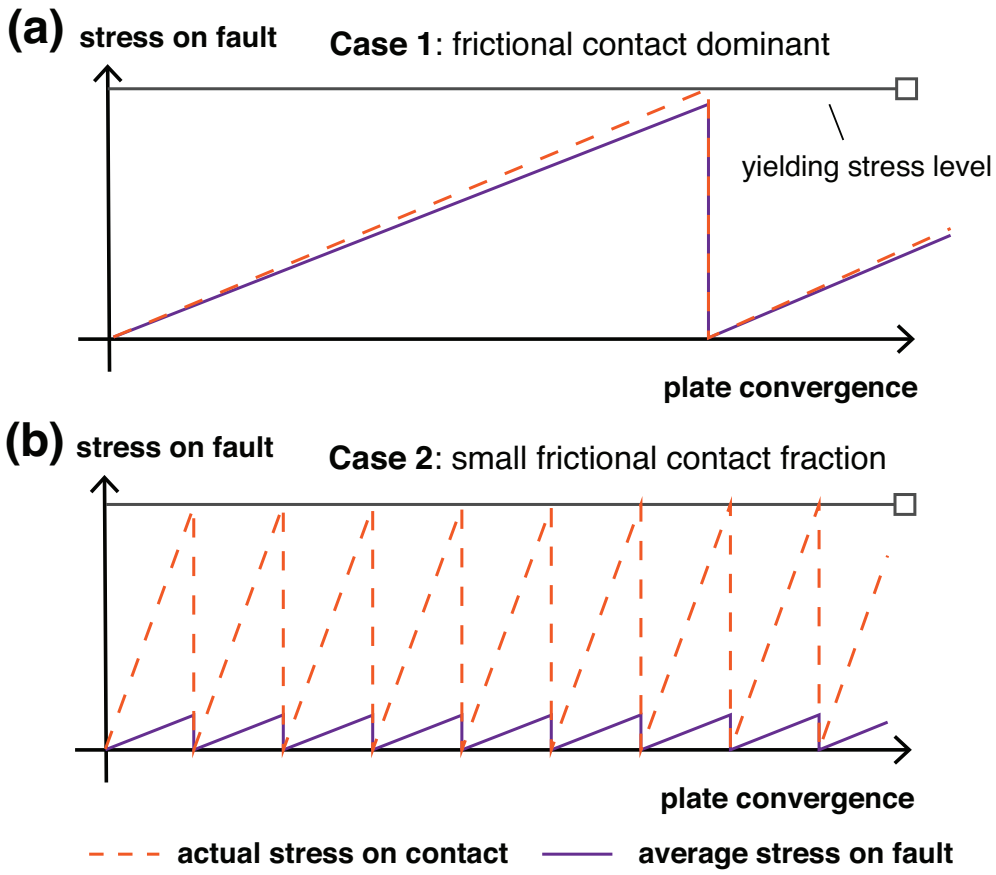

Figure 6.3: Conceptual diagrams that demonstrate how the stress on the fault evolves with plate convergence. Figure 6.3(a) and (b) correspond to Cases 1 and 2 described in section 6.1, respectively. X-axis denotes plate convergence and y-axis denotes shear stress on the fault. In both (a) and (b), purple solid line represents the average shear stress on the fault, while orange dashed line represents the actual shear stress on the frictional contact. I set the purple solid lines in both (a) and (b) to have the same slope to indicate the same stressing rate for both cases. The figures demonstrate how the stress amplification effect may reduce both the average stress drop and the inter-event interval in the frictional-viscous model. The schematic is just for illustration purposes and is not to scale. I note that the x-axis looks tilted but it is not—this is only a visual illusion.

smaller stress drops as well as shorter inter-event intervals. I note that the above analysis is about the long term tectonic process. The transient stress drop events, either in Case 1 or Case 2, are considered to be effectively instantaneous in the long term and can be plotted as vertical lines. However, their short term features, or "co-seismic" features, should be very different, depending on whether we consider the existence of the viscous shear resistance components. As shown in Chapter 4 and 5, since the fault zone in Case 2 also contains a viscous (rate-strengthening) layer, the transients in Case 2 should have smaller slip rates and rupture propagation speeds compared to Case 1, making them slow slip events.

6.1.3 A quick summary for section 6.1

In the above discussion, I demonstrate a conceptual model to show that, under the frictional-viscous framework I use in this dissertation, both the inter-event interval and the average stress drop would be smaller than those in the regular earthquake model, where frictional contact area covers most of the fault. These results are consistent with the SSE observations. Most importantly, the simple analysis above suggests that a smaller average shear stress drop is a natural tectonic consequence of the frictional-viscous framework. It does not require the high pore fluid pressure that many theoretical models require to get low stress drop. In Chapter 4 and 5, I have shown that a low average shear stress drop is a requirement for the co-seismic frictional-viscous model to fit the SSE observations. Therefore, the inference in the long term analysis is consistent with the required prescribed condition in the short term co-seismic analysis. This agreement suggests that the frictional-viscous framework can, or at least has a great potential to, explain both the long term and short term SSE observations in a self-consistent manner.

6.2 A testable hypothesis on the viscous coefficient η_v and its physical meaning

In my dissertation, a most critical parameter is the viscous coefficient η_v. It is a parameter that controls how the viscous resistance $f_{viscous}$ of the bulk fault shear zone is related to the slip rate V,

$$f_{viscous} = \eta_v \cdot V \tag{6.4}$$

In Chapter 4 and 5, I demonstrate that by considering this viscous resistance together with frictional/brittle stress drop in a model, a transient slip event can have a slower slip rate and rupture propagation speed, compared to the typical frictional/brittle-only models that is commonly used to explain fast earthquakes. Importantly, I find that a viscous coefficient η_v of $\sim 10^4 - 10^5$ $\mu/(2\beta)$ can simultaneously explain many first order characteristics of slow slip events (SSEs), which strongly suggests that the frictional-viscous model is promising to be a decent representation of the actual SSE source processes.

My analysis provides a quantitative prediction of the viscous coefficient η_v: $\sim 10^4 - 10^5$ $\mu/(2\beta)$. This value is purely derived from the need of explaining geophysical observations. Based on this, we may naturally come up the following hypothesis for future observations to test: **if the frictional-viscous model is indeed the mechanism behind the SSE source process, we should find that the micro-scale shear deformation mechanism of SSEs has a linear slip rate strengthening characteristic, and the associated viscous coefficient η_v is about $\sim 10^4 - 10^5$ $\mu/(2\beta)$.** This hypothesis, in principle, can be independently tested with geological observations on SSE hosting faults

(in-situ or exhumed) and with laboratory experiments.

It is worth noting that, at this point, the viscous process I refer to does not need to be related to any specific viscous mechanism. In other words, any fault-zone-scale process could be responsible, as long as a it can provide an average resistance against slip movement that increases with slip rate (i.e., rate-strengthening). I have to confess that my current understanding of rock mechanics may not be enough to fully address this issue, but I do believe more thorough investigations across disciplines are necessary to answer this question. Nevertheless, It is possible to expand the discussion a bit on the micro-scale viscous process as follows, based on the results above and my limited knowledge on this topic. This is mostly for reference purposes, to let the readers (including the future me myself) to know what I had in mind as I wrote the dissertation.

I am thinking the viscous resistance of a fault zone is provided by distributed viscous deformation within the fault zone. This distributed viscous deformation can either correspond to the viscous flow in the volume or rate-strengthening creep on countless discrete slip surfaces. In either case, we may define a effective viscosity η_{eff} for the viscous deformation within the fault zone as the viscous coefficient η_v times the width W of the fault zone,

$$\eta_{eff} = \eta_v \cdot W \tag{6.5}$$

Considering that the viscous coefficient η_v is about $\sim 10^4 - 10^5$ $\mu/(2\beta)$, $\mu/(2\beta)$ is about 5×10^7 Pa $\cdot$ s/m (based on our model setting, see Table 5.1), and a fault zone width W is ~ 100 meters, we may estimate the effective viscosity η_{eff} to be,

$$\begin{aligned}\eta_{eff} &= [10^4 \text{ to } 10^5] \cdot [5 \times 10^7 \text{ Pa} \cdot \text{s/m}] \cdot 100 \text{ m} \\ &\sim 10^{13} \text{ to } 10^{15} \text{ Pa} \cdot \text{s}\end{aligned} \tag{6.6}$$

A typical rock viscosity in the lithosphere is about 10^{17} to 10^{22} Pa $\cdot$ s. Therefore, the predicted effective viscosity for the fault zone is significantly smaller than the typical viscosity in the ambient rock, even for the hottest part. This order-of-magnitude result suggests that the viscous deformation within the high-strain-rate fault zone might be intrinsically different from the viscous flow in the ambient rock.

Based on a review of recent literature on geological observations of potential SSE sources (e.g., Bürgmann, 2018; Phillips et al., 2020; Kirkpatrick et al., 2021; Behr & Bürgmann, 2021; Schmidt & Platt, 2022), I suspect some viscous/rate strengthening mechanisms within the fault zone may be responsible for this "low" effective viscosity. Two of the mechanisms are most impressive to me. One mechanism is a "dissolution-precipitation" creep, by which grains change shape through dissolution at high stress sites, accompanied by fluid-assisted diffusive mass transfer towards, and reprecipitation at, low-stress sites (Kirkpatrick et al., 2021). Another mechanism is "brittle creep" or "cataclastic flow", in which a volume of rock deforms by frictional sliding and grain rolling combined with fracture, causing an overall change in shape (Perfettini & Avouac, 2004; Kirkpatrick et al., 2021). I could not find a robust estimation of the effective viscosity for the above two mechanisms; yet, I do think they can potentially produce an "expected low" effective viscosity for the model in my dissertation, since these two mechanisms are different from the viscous flow mechanism in the ambient lithosphere and may be unique for the fault zone. Besides, these two mechanisms, seem to me to be closely related to the presence of abundant fluid

in the fault zone, which makes them seem more attractive.

Nevertheless, I will leave these open questions to future investigations. In fact, I think this "unsolved" question may actually make my dissertation attractive to geologists and rock physicists.

6.3 A different form of viscous resistance instead of linear, and why a logarithmic form would allow slow slip only in a narrow range of parameter space

In this dissertation, I adopt a linear form for the viscous resistance in my models. Indeed, the initial choice of a linear form is mainly for simplicity. Nevertheless, this linear form is very successful in explaining SSE observations in first order, as I have shown in Chapter 4 and 5. These analyses, together with the results in Ando et al. (2010), Nakata et al. (2011), and Ando et al. (2012), suggest that the linear viscous resistance is an attractive formulation for SSEs, at least from the point of view of explaining geophysical observations.

However, I notice that other forms of viscous (or rate-strengthening) resistance, could be, or has been, proposed to explain slow slip events. Perhaps the most popular form is the logarithmic form. This is the form of the slip rate dependence in the rate-and-state friction formulation (e.g., J. H. Dieterich, 1979; Ruina, 1983), and it has been proposed to be the mathematical form of the viscous resistance for brittle creep (cataclastic flow) mechanism (e.g., Perfettini & Avouac, 2004; Perfettini & Ampuero, 2008). Other forms of rate-strengthening forces, like a higher order polynomial dependence on slip rate, are also

possible.

Determine which form serves as the best representation for the SSE source process is outside the scope of my dissertation. However, from a purely theoretical point of view, I may still provide some derivations to rudimentarily show the slip and rupture characteristics under these alternative rate-strengthening formulations. For simplicity, I will only derive the expressions of initial slip rate and slip rate decay relations using the 1D approximation in secions 4.3 and 4.5. These derivations are demonstrated as below, and in particular, I will show that a logarithmic form may always need to occupy a narrow parameter range in its parameter space to explain the observed slow slip behaviors.

6.3.1 A general form of rate-strengthening

To make a general discussion, we may start from the general form of viscous resistance, and assume it only depends on slip rate V,

$$f_{viscous} = f_v(V) \tag{6.7}$$

The frictional (brittle) part of the setup is left the same as in Chapter 4. To see how slip rate evolves under the general form of viscous resistance, we may reproduce the derivation in section 4.5 before equation (4.31), only except that we change (4.31) to a general form of rate strengthening,

$$f(t) = f_1 + \eta_v \cdot f_v\big(V(t)\big). \tag{6.8}$$

By equating (4.31) and (6.8), we will obtain,

$$-\frac{\mu}{2\beta}\cdot \mathrm{d}V(t) - C\cdot\frac{\mu}{L}\cdot V(t)\,\mathrm{d}t = \eta_v \cdot f_v'\big(V(t)\big)\,\mathrm{d}V(t), \tag{6.9}$$

where L is the characteristic length of the slipping area.

It is possible to separate the variables V and t in the above ODE, and we can obtain,

$$\mathrm{d}t = -\frac{1}{C}\cdot\frac{L}{\mu}\cdot\frac{f_v'(V)+\mu/(2\beta)}{V}\cdot\mathrm{d}V \tag{6.10}$$

Performing indefinite integration on both sides, we obtain,

$$\begin{aligned} t &= \int -\frac{1}{C}\cdot\frac{L}{\mu}\cdot\frac{f_v'(V)+\mu/(2\beta)}{V}\cdot\mathrm{d}V + \text{Const.} \\ &= \left(\int -\frac{1}{C}\cdot\frac{L}{\mu}\cdot\frac{f_v'(V)}{V}\cdot\mathrm{d}V\right) + \left(-\frac{1}{C}\cdot\frac{L}{2\beta}\ln V\right) + \text{Const.} \end{aligned} \tag{6.11}$$

In principle, we may use (6.11) to obtain the slip rate decay in any specific form. In practice, for earthquake modeling, we are most interested in one form: the logarithmic form, because it appears in the rate-and-state formula and is now most widely used. In the following part of section 6.3, I will expand the discussion on the logarithmic form of viscous resistance.

6.3.2 A logarithmic form of viscous resistance: how does slip rate decay?

Let us now investigate a logarithmic form of viscous resistance,

$$f_v(V) = \tau_{ref} + a\sigma\ln\left(\frac{V}{V_{ref}}\right) \tag{6.12}$$

in which τ_{ref} is the viscous resistance when V is at a reference slip rate V_{ref}. $a\sigma$ is included to quantify the strength of the logarithmic form rate-strengthening. It is set to be a product of a and σ in order to mimic the classic logarithmic form rate strengthening in the rate-and-state friction law, in which a is the dimensionless coefficient that controls the direct response term (the $a\ln(\frac{V}{V_0})$ term in equation (3.7)), and σ is the normal stress. I note that V is not allowed to be zero in this form (meaning that it is not regularized).

Taking derivative on both sides of (6.12), we have,

$$f_v'(V) = \frac{a\sigma}{V} \tag{6.13}$$

Substitute (6.13) into (6.12), we have,

$$\begin{aligned} t &= \left(-\int \frac{1}{C}\cdot\frac{a\sigma L}{\mu}\cdot\frac{1}{V^2}\cdot \mathrm{d}V\right) + \left(-\frac{1}{C}\cdot\frac{L}{2\beta}\ln V\right) + \text{Const.} \\ &= \frac{1}{C}\left(\frac{a\sigma L}{\mu V} - \frac{L}{2\beta}\ln V\right) + \text{Const.} \end{aligned} \tag{6.14}$$

Assuming at $t = 0$, $V(t = 0) = V_0$, and substituting them into (6.14), we have,

$$t = \frac{a\sigma L}{C\mu}\left(\frac{1}{V(t)} - \frac{1}{V_0}\right) - \frac{1}{C}\cdot\frac{L}{2\beta}\ln\left(\frac{V(t)}{V_0}\right) \tag{6.15}$$

This is a transcendental equation for V. However, when $V(t)$ is significantly smaller than $\frac{a\sigma}{\mu}\cdot 2\beta$, the first term should be significantly larger than the second term (which is related to radiation damping). So it is possible to leave out the second term. Assuming a typical $a = 10^{-3}$, $\frac{\sigma}{\mu} = 10^{-4}$, $\beta = 10^3$ m/s, the value of $\frac{a\sigma}{\mu}\cdot 2\beta$ under the

rate-and-state is $\sim 10^{-4}$ m/s. This is considerably larger than the typical SSE speed, and suggests that it might be safe to leave out the second term.

Anyway, if we neglect the second term, we will obtain,

$$V(t) = V_0 \cdot \frac{1}{1 + \frac{C\mu V_0}{a\sigma L} \cdot t} \tag{6.16}$$

this formula is essentially the same as what is derived in Perfettini and Avouac (2004) with the same setting, although it is not explicitly shown and one needs to take the limit of stress rate $\dot{\tau} \to 0$ ($t_r \to \infty$) in their equation (24). Also, they were deriving this formula to explain afterslip instead of SSEs.

Equation (6.16) shows a $1/t$ decay of the slip rate, and a characteristic decay time T_{lnd} can be extracted from (6.16),

$$T_{lnd} = \frac{a\sigma L}{C\mu V_0} \tag{6.17}$$

Since $a\sigma$ represents the strength of rate-strengthening effect, equation (6.17) suggests that a stronger rate-strengthening effect would lead to a longer slip rate decay time here, similar to what is found in section 4.5.

6.3.3 A logarithmic form of viscous resistance: characteristic slip rate

We may now investigate the characteristic slip rate under the logarithmic formulation. Based on equation (6.17), the characteristic slip rate should be well represented with the initial slip rate V_0, similar to what we found in Chapter 4. Following the procedure in

section 4.3, we can estimate the V_0 for the logarithmic case, except that we need to change equation (4.15) to the logarithmic form,

$$f(\boldsymbol{\xi}, t_0 + \Delta t) = f_1 + \tau_{ref} + a\sigma \ln\left(\frac{V(\boldsymbol{\xi}, t_0 + \Delta t)}{V_{ref}}\right). \tag{6.18}$$

Equating (6.18) with (4.14), we can obtain a equation to solve for $V(\boldsymbol{\xi}, t_0 + \Delta t)$ (and thus V_0, since we assume $V(\boldsymbol{\xi}, t_0 + \Delta t) = V_0$),

$$f_0 - \frac{\mu}{2\beta} \cdot V_0 = f_1 + \tau_{ref} + a\sigma \ln\left(\frac{V_0}{V_{ref}}\right) \tag{6.19}$$

Again, this is a transcendental equation for V_0 and can not be solved analytically. However, we know $-\frac{\mu}{2\beta} \cdot V_0$ is the radiation damping factor, so if V_0 is considerably small, $-\frac{\mu}{2\beta} \cdot V_0$ may be ignored. We may than solve for V_0 as,

$$V_0 \approx V_{ref} \cdot \exp\left(\frac{\Delta f - \tau_{ref}}{a\sigma}\right) \tag{6.20}$$

in which we denote $\Delta f = f_0 - f_1$,

Equation (6.20) suggests that the characteristic slip rate depends exponentially on the sudden frictional (brittle) stress drop, when the viscous resistance is in a logarithmic form. It implies that if the sudden frictional (brittle) stress drop Δf has a certain level of variation, the resulting characteristic slip rate V_0 would have a much greater variation. To be more specific, even if the variation of Δf is within the same order of magnitude, the variation of V_0 could still be as large as several orders of magnitude. It may still be possible

to use equation (6.20) to explain SSE observations. However, the range of parameters that can explain the observations would be narrow in parameter space, and this may be almost inevitable due to the exponential relation.

As shown in our derivation, the exponential equation essentially originates from the logarithmic formula of the slip-rate-strengthening dependence. Therefore, although I did not explore other slip and rupture behaviors, I suspect that a similar "narrow range" of results may be achieved, as long as a logarithmic formula is used to describe the viscous (rate-strengthening) response. I note that a "narrow range" of parameter space does not necessarily mean it is not possible. However, as there is growing evidence suggesting that SSE is more ubiquitous than we used to think (e.g., Obara & Kato, 2016; Bürgmann, 2018), I would favor a viscous formulation that is not in a logarithmic form.

6.4 How do LFEs, VLFEs, tremors, and rapid tremor migration fit in the frictional-viscous model framework?

In the frictional-viscous model framework of this dissertation, I focus on explaining slow slip event (SSE) signal. The model does not explicitly address the signals of other seismic types of slow earthquakes, that is, those events that can generate detectable seismic waves and are thought to be associated with slow slip processes. These seismic slow earthquakes include tremors, low frequency earthquakes (LFEs), very low frequency earthquakes (VLFEs or VLFs), and rapid tremor migrations.

Ultimately, my opinion is that a complete slow earthquake model needs to explain all the phenomena and their associated signals during the slow slip process across different

scales. This task could be difficult because it is challenging to consider the physical process across multiple scales all at once. Take my model for example: since I am focusing on SSE rupture propagation that extends for several kilometers on the fault, I choose to ignore the detailed distribution of frictional (brittle) heterogeneities, and only treat the parameter in my "friction law" as an spatial-average property on fault. Therefore, I am not able to directly generate the signals for these seismogenic events in my dissertation, and compare them to specific seismic observations. However, I may still qualitatively describe my vision on how these seismic slow earthquakes may fit in the frictional-viscous model framework. In particular, I propose some hypotheses to relate the actual physical property to the parameterization scheme in my "spatial-average" model. These hypotheses can be tested in a future finer-scale model that can address slow earthquakes across multiple scales.

6.4.1 Tremors and LFEs: recap of observations

Tectonic tremors, or non-volcanic tremors, are usually referred to as tremors in the context of slow earthquakes research. A good summary of tremors can be found in many review papers such as Peng and Gomberg (2010) and Obara and Kato (2016). A tremor is a burst of high amplitude signals observed in a continuous seismogram filtered at 2-8 Hz. Unlike signals for a single regular earthquake event, tremor signals usually do not have clear P and S arrivals, and are usually located with techniques like envelope cross-correlation or signal beam-forming (Obara & Kato, 2016, and the reference therein). Tremors are found to consist of many small seismic events that can have clear P and S arrivals (usually after stacking), and these small events are usually referred to as low frequency earthquakes (LFEs) (e.g., Shelly et al., 2007). Based on this, people often use LFEs and tremors interchangebly.

Some LFEs are found to appear in clusters, and these clusters are now commonly referred to as LFE families (e.g., Sweet, Creager, & Houston, 2014).

From the beginning of their study, tremors have often been found to be accompanying aseismic slow slip events (e.g., Rogers & Dragert, 2003). Although counter-examples exist, the correlation between aseismic SSE and seismic tremors is very commonly observed, which suggests that their relationship is very close. In recent years, researchers have found that one may detect more SSEs in noisy geodetic data with the guidance of tremor time and location (e.g., Frank et al., 2015), which further supports the correlation. It is now commonly thought that tremor activity could highlight the slipping area in SSE rupture propagation.

However, the causality relation between SSE and tremors is still an open question. The higher-frequency radiation spectrum of tremors (compared to SSEs), low local magnitude of LFEs, and the delineation of their spatial distribution imply that tremors originate from sudden frictional (brittle) ruptures within the fault zone . One popular hypothesis is these sudden frictional ruptures are triggered by the slowly propagating SSE rupture front. A physical rationale behind it is that the SSE are usually measured to have significantly greater moment than the associated tremors, and it is reasonable that the smaller events are triggered by the larger event. In recent years, another hypothesis has emerged, indicating that SSE and tremor signals belong to the same rupture process, and the different deformation modes that respectively generate SSE and tremors signal are actually interacting with each other during the rupture (e.g., Nakata et al., 2011; Ando et al., 2012; Luo & Ampuero, 2018; Luo & Liu, 2021). For example, the small-magnitude tremor sources could actually

drive the large-magnitude slow slip events as well.

6.4.2 Relations between tremors and SSE in my model: the "chain reaction"

The frictional-viscous model in my dissertation belongs to second hypothesis in section 6.4.1, that is, SSEs and tremors may correspond to the same rupture process, and the two types of events aid the occurrence of each other.

I consider that the total resistance provided by the fault zone to act against the plate movement is the sum of a frictional (brittle) part and a viscous part (equation (4.1)),

$$\begin{aligned}\tau_{elastic} &= f \\ &= f_{frictional}(D, V, ...) + f_{viscous}(D, V, ...),\end{aligned}$$

In my vision, the frictional (brittle) strength part corresponds to the brittle contacts that can generate tremor and LFE signals. As shown in section 6.1, this frictional strength would hold the two plates adjacent to the fault still and allow tectonic strain to accumulate in the plates. Eventually, at some point, the frictional (brittle) strength will not be able to resist the tectonic loading, and will suddenly drop. These sudden strength drop at the local frictional contact have two consequences: first, they generate high-frequency signals that are detected as tremors or LFEs; second, they quickly cause a difference in stress between the average tectonic loading stress and the fault zone resistance stress.

The sudden gap in stress would cause slip motion not only on the local frictional contact but also on the fault as a whole. If no viscous component exists in the fault zone ($f_{viscous}(D, V, ...) = 0$), the slip rate would be mainly limited by the radiation damping

effect, as I show in section 2.2.1 and Figure 2.1. When there is viscous resistance in the fault zone, the gap in average stress would also cause the viscous portion to be loaded and deformed. Due to the existence of viscous deformation, the slip rate of the whole fault zone would not be as fast as the the local slip rate on frictional contacts. In my vision, these bulk viscous deformations are SSEs. Because of the slow slip rate, the bulk deformation in the fault zone does not generate detectable seismic radiation and is aseismic. However, it can still be detected by geodetic instruments and be categorized as an SSE.

The above mixed modes of shear deformation may start near a certain location on the fault. At the same time, other locations on the fault should remain still because the frictional (brittle) strength has not been reached. Then, the initial bulk viscous deformation would causes an increase in elastic loading stress at the nearby fault. Due to the stress amplification effect as discussed in section 6.1, this increase in elastic loading stress would cause an even greater increase in local frictional stress, and eventually lead the nearby fault to experience a sudden frictional strength drop. As described above, this sudden frictional strength drop, again, would cause a wider-scale viscous deformation, contributing to a "chain reaction". As a result, the rupture propagates out on the fault and manifests itself as both tremors (local frictional strength drop) and an SSE (bulk viscous deformation).

The above "chain reaction" processes are summarized in the flow chart in Figure 6.4. In my model framework, tremors and LFEs are thought to correspond to the sudden brittle strength drop on the local frictional contacts, while SSEs are thought to correspond to the bulk viscous deformation of the fault zone. Both the local frictional failure and the bulk viscous deformation are a part of the same rupture process, and they should have influence

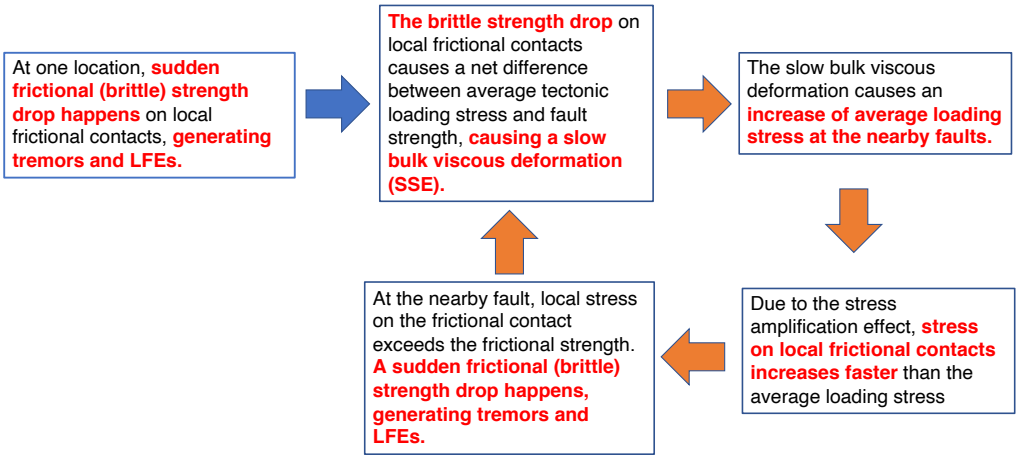

Figure 6.4: Flow chart that demonstrate the "chain reaction" that controls the rupture propagation process in the frictional-viscous model. Details in section 6.4.2

on each other. However, the associated tremors and the SSE could manifest themselves differently in geophysical observations, which could lead to different categorizations.

In addition, this "chain reaction" vision here can explain the puzzling geological observations that the frictional (brittle) features observed in the potential SSE exhumed fault zone are usually too small to link up in the plane of the fault (Behr & Bürgmann, 2021). It leads Behr and Bürgmann (2021) to pose the following question,

> ...what mechanisms (e.g. fluid−pressure diffusion, viscoelastic stress transfer) allow transient deformation features to communicate within a more distributed shear zone to form a coherent LFE 'patch', and to reliably participate in frequently recurring SST (slow slip and tremor) events that propagate over 10s of km distances?

This question can be well-explained with the "chain reaction" process described above.

Finally, I want to note that my model here cannot explicitly generate the tremor signals that can fit seismograms. This is because my model does not explicitly consider the stress amplification effect in the fault zone. Instead, the average stress is set as a prescribed parameter in the model, and the stress amplification effect is approximated by prescribing a

low average stress drop. In this setting, high-frequency radiation is artificially filtered-out. To generate high-frequency tremor-like seismic radiation (compared to the extreme long-period SSE signals), one needs to explicitly consider the distribution of brittle deformation in the 3D fault zone. This not only requires one to have better observational constraints on the fault zone structures, but also requires a more complex theoretical model that captures and characterizes the detailed interaction between viscous and brittle deformation in the 3D fault zone.

6.4.3 VLFEs

Very low frequency earthquakes (VLFEs) are another type of seismic slow earthquake signal. Unlike tremors and LFEs, they are usually observed in the frequency band below 0.1 Hz and above 0.01 Hz, and usually have a duration of a few to a few tens of seconds. The present model does not have a direct explanation for VLFE. However, if one considers some specific conditions, VLFE signals may be produced within the framework of my models. Previous research has implied two specific setups that may explain these phenomena. I will demonstrate both hypotheses here, more thorough research is needed in future.

The first hypothesis is that VLFEs correspond to the bulk viscous deformation or clusters of frictional slip, and emerge due to the natural fluctuation of SSE slip rate or tremor activities. These fluctuations can generate ground deformation signals that have a "white" spectrum (the spectrum being flat). Because the seismic noise is naturally low between 0.01 to 0.1 Hz, the fluctuation of ground motion is most easily observed in that particular frequency band. Similar ideas have also been suggested in many other studies (e.g., Ide &

Yabe, 2014; Gomberg, Agnew, & Schwartz, 2016; Masuda, Ide, Ohta, & Matsuzawa, 2020). This hypothesis would predict that VLFEs are likely to co-appear with SSEs or tremors. I do not have a model in my dissertation to show such effects since my model here does not specify any heterogeneity length scale. Yet, were I to include a "random" fluctuation in the spatial distribution of viscous or stress setting, the "white" spectrum of ground motion might emerge. Such a possibility was suggested by (Nakata et al., 2011) as well.

The second hypothesis is that, VLFEs correspond to the bulk viscous deformation, but take place within some special fault area where the viscous coefficient η_v is lower than $\sim 10^4 - 10^5\ \mu/(2\beta)$. This hypothesis is proposed in my earlier paper (Wu et al., 2019). I show that when the characteristic slip rate decay time in the frictional-viscous model is comparable to the filtered period (0.01 to 0.1 Hz), VLFE signals may be detected. However, this would require the viscous coefficient η_v (denoted as η in (Wu et al., 2019)) to be $\sim 10^2\ \mu/(2\beta)$, which is significantly lower than the value that is needed to explain SSEs.

Up till this point, it is still hard to determine which one of the above two hypotheses is correct, or either of them is not correct. I think more observations are needed to characterize the source process of VLFEs.

6.4.4 Rapid tremors migration

The main SSE rupture front, highlighted by tremor migration, usually has a propagation speed of several km/day. This $\sim$ km/day speed is used as the fitting target in my main analysis of SSE rupture propagation speed in section 4.6. However, some tremor migrations are observed to have a speed of around km/h, which is an order of magnitude faster than the main SSE rupture propagation (e.g., Ghosh et al., 2010). Similar to VLFEs,

these rapid tremor migration phenomena cannot be explained with the first order features in the frictional-viscous model. However, they may still be explained with my model if we consider variations in stress or friction parameters. Based on our analysis in section 4.6, the rupture propagation speed under the frictional-viscous model framework can be expressed as (equation (4.37)),

$$V_{rs} \approx \frac{L_s}{L_p} \cdot \left(1 + \frac{1}{S}\right) \cdot \left(1 + \frac{\eta_v}{\mu/(2\beta)}\right)^{-1} \cdot 2\beta,$$

in which L_p is the characteristic length of the high slip rate zone behind the rupture front, L_s is the characteristic length of the high stressing rate zone ahead of the rupture front (Figure 2.2). S is the ratio between strength excess $f_0 - \tau_0$ and static stress drop $\Delta\tau_s$, so $S\Delta\tau_s$ is the strength excess.

Variations in the associated parameters in the above equation can cause the rupture speed to vary by an order of magnitude. In particular, the parameter S is an attractive option. S represents how close the fault is to frictional (brittle) failure: the smaller the S, the weaker the fault. Based on the above equation, we may see that if S is one order of magnitude smaller, V_{rs} could be one order of magnitude higher. It suggests that, under the frictional-viscous model framework, if we prescribe some fault area that has an S that is one order of magnitude smaller than the background, the rupture on this area may propagate one order of magnitude faster. This design has been shown to be capable of generating rapid tremors migration in Ando et al. (2012). Physically, the smaller S area on fault may correspond to the linear fault area that is intrinsically weaker than normal due to its special structure. For example, the linear weaker fault area may have an S of around 0.1, while the

background area may have an S of around 0.1. This weaker area may correspond to some special structure on the subduction interface, such as seamounts.

I note that other parameters are also possible to give a higher rupture propagation speed, including η_v and $\frac{L_s}{L_p}$. However, I prefer not to use the variation in η_v to explain the variation in rupture speed. For η_v, a change in its value will also affect the prediction of other observables, unlike S. For $\frac{L_s}{L_p}$, I do not have a good physical justification of why this ratio might vary in space.

6.5 Comparison with other theoretical slow earthquake models: differences and connections

I have almost finished the demonstration of my theoretical model. As summarized in Chapter 3, there here have been many theoretical studies addressing the puzzling slow earthquakes observations. It is useful to look back and compare my model with other theoretical models, describing their differences and connections. I note that, due to the limitations of my knowledge, there may be some mistake or inaccuracies in the comparison. I hope this honest documentation of my opinion can help future readers (including myself) better understand my thinking process and better position this theoretical work in their own framework of understanding slow earthquakes.

6.5.1 Comparison with the "less sudden stress drop" models

In section 3.1, I reviewed the models that slow down slip rate by incorporating a less sudden stress drop. This slow-down mechanism only requires a frictional resistance in the

"friction law". The fault needs to be slip weakening, or rate-weakening. In this framework, the weakening rate with slip is only slightly faster than the elastic stress release rate with slip. This is a so-called "conditionally stable" or "conditionally unstable" condition, under which slow slip behaviors would emerge in models.

This general mechanism can have various realizations in different models depending on the specific setup. A classic setup in a rate-and-state friction framework is to set the characteristic slip patch length be slightly smaller than the intrinsic critical slip patch length. Both parameters can depend on many factors. The characteristic slip patch length depends on fault geometry, the type of slip motion, the shape of initial stress and friction distribution, the proximity to the Earth's surface, etc.; while the intrinsic critical slip patch length can depend on critical slip weakening distance, effective normal stress, frictional parameters a and b, and so forth. The wide range of tunable parameters allow modelers to generate slow slip behaviors in many different apparent settings (e.g., Liu & Rice, 2005, 2007; Liu, 2014; Leeman et al., 2016; Wei et al., 2018; Im et al., 2020).

The mechanism utilized in my model to generate slow slip behavior is fundamentally different from this mechanism. Similar to the "less sudden stress drop" models, my model does have a frictional resistance component that may drop with slip and give rise to a slip transient. However, the weakening rate with slip would always be significantly faster than the the elastic stress release rate with slip. In another words, if only considering the frictional resistance, my model would always generate fast earthquakes. The key component in my model to generate the slow slip behaviors is the viscous component. Therefore, my model does not belong to the "less sudden stress drop" models.

6.5.2 Comparison with the "limiting slip rate" models

In section 3.2, I reviewed the models that slow down slip rate by somehow limiting the slip acceleration process. This can be done by artificially setting a hard limit to the slip rate (Colella et al., 2011), incorporating a constant term in the state term of rate-and-state formulation (e.g., Shibazaki & Iio, 2003; Hawthorne & Rubin, 2013), or considering a dilitant process in the framework of poroelasticity (e.g., Segall et al., 2010; Liu & Rubin, 2010; Liu, 2013). In these models, it has been shown that once the slip rate is slowed down, other event characteristics like rupture propagation speed would also start to fit the actual SSE observations.

The present model is similar to these models in that the slow average slip rate of the fault zone produces a variety of slow slip behaviors. However, the underlying physical image is different. In the aforementioned models, the fault zone is still envisioned as frictional-dominant, and it is due to either the frictional parameter or an external process that the slip acceleration is limited. However, in the vision of my model, the fault zone consists of countless small frictional (brittle) contacts embedded in a bulk viscous shear zone. The slip rate on the local frictional (brittle) contacts can still be fast, generating tremors and LFEs. Meanwhile the bulk shear deformation is slow because it is mainly viscous. Therefore, the present model should be intrinsically different from the "limiting slip rate" models, since no mechanism is adopted to limit the frictional slip rate: the slip rate on local contacts can still be high, while the bulk slip rate is slow because it is the intrinsic property of a viscous shear zone.

6.5.3 Comparison with models that have spatial heterogeneous rate-strengthening and rate-weakening rate-and-state parameters on the fault

In section 3.3, I reviewed a mechanism to slow down slip rate that is different from the previous two mechanisms: if we can somehow impose a transient stress perturbation on a viscous or rate-strengthening fault, the slip on the rate-strengthening fault can exhibit slow slip characteristics. This idea can be realized in multiple ways, and in this section I will first discuss the way where the idea is realized within a typical rate-and-state friction framework.

In a typical rate-and-state formulas, $a-b>0$ means the fault is rate-strengthening while $a-b<0$ means the fault is rate-weakening. To realize the above general mechanism, one may set the $a-b$ parameter to be heterogeneous on the fault, with some part being rate-strengthening and some part being rate-weakening (e.g., Skarbek et al., 2012; Luo & Ampuero, 2018; Luo & Liu, 2021). Such a model would give rise to slip instability (slip transients) because the existence of rate-weakening friction, and transient stress perturbations are imposed on the rate-strengthening area. The rate-strengthening area would slip slowly due to its intrinsic stability. Most importantly, the slow slipping rate-strengthening fault would load the un-ruptured rate-weakening regions, driving them to rupture. The newly ruptured rate-weakening region would again transfer stress perturbations onto the nearby rate-strengthening fault. These processes together form a "chain-reaction" that drives the rupture to propagate. The resulting slip rate and rupture propagation speed is controlled by how the heterogeneity is set up.

From a mathematical stand point, my model has a very similar general mechanism

to generate slow slip behavior to the above model. The "chain-reaction" above is very similar to what is described in section 6.4.2. However, the physical pictures behind the formulations are quite different. The aforementioned model is still in a framework that considers only frictional resistance. Therefore, each location on fault can either be rate-strengthening or rate-weakening. To include both the transient stress drop and viscous component in the same model, one has to distribute the heterogeneity on the fault surface, setting some part to have $a - b > 0$ while some other parts have $a - b < 0$. In contrast, the framework of the present model includes both frictional resistance and viscous resistance, and these two resistances might or might not co-exist at the same location on the fault. This setup may seem unrealistic if we consider the fault is a frictional surface; yet, it actually seems more reasonable if we consider that a fault is a shear zone with a finite thickness. In addition, the present model can consider a different viscous resistance formulation than the logarithmic form. In summary, my model envision a more general situation than the rate-and-state-based heterogeneity model, although the general mathematical structure that gives rise to slow slip may be similar in both.

6.5.4 Comparison with the "frictional-viscous mixing in series" model

In my model, I consider the frictional resistance and viscous resistance acting in parallel (Figure 3.3(d)), where the bulk slip only has a single value, and the total resistance (strength or stress) on fault is the sum of frictional resistance and viscous resistance. An alternative way to realize frictional-viscous is to have the two types of resistance acting in series (Figure 3.3(c)), where the bulk resistance (strength or stress) on fault only have a single value, and the total shear strain is the sum of viscous strain and frictional strain

(slip).

Obviously, this type of models is quite different from the present, and such models to explain SSE are rare in literature. To the best of my knowledge, only Goswami and Barbot (2018) examined this setup. Goswami and Barbot (2018) have shown that a frictional-viscous in series setup can aid the generation of slow slip events. Yet, my impression is that they still require other types of mechanism (such as a "less sudden stress drop") to act as a major role to generate slow slip behaviors. My another concern about this mechanism is its inability to explain the lack of SSE slip during the inter-event period. For a frictional-viscous in series model, the fault may be alway slipping.

6.5.5 Comparison with other "frictional-viscous mixing in parallel" models

My model is not the first to adopt the "frictional-viscous mixing in parallel" framework to explain SSE. Before me, many pioneering works have already explored this setups and accumulated an abundance of valuable understanding (Ando et al., 2010; Nakata et al., 2011; Ando et al., 2012; Lavier et al., 2013; Beall et al., 2019; Lavier et al., 2021), upon which the study of this dissertation is built. My dissertation moves this research area forward by providing plenty of new theoretical analyses and results that show it can explain a number of SSE phenomena, help the community better appreciate the "frictional-viscous mixing in parallel" model, and better apply it to explain other observations. In the following section, I will briefly discuss how the current work builds on prior work in the "frictional-viscous mixing in parallel" formalism.

I will first start the comparison with Ando's model (definition of "Ando's model"

in section 4.1) (Ando et al., 2010; Nakata et al., 2011; Ando et al., 2012). There is actually much discussion on this comparison in Chapter 4 and Chapter 5, since my model here has an identical "friction law" setup to Ando's model, and thus owes a debt to this prior work. Therefore, I refer readers to Chapter 4 for more detailed information. Here I will only briefly summarize the advancement of my theoretical development. First, I have derived a wealth of analytical relations that can depict the physical image in a deeper manner. With the analytical relations, we may gain an understanding of parameter space that might not be currently explorable with numerical simulations. Second, I have shown that the frictional-viscous "friction law" itself is enough to generate slow slip behaviors; it is not required that one explicitly place heterogenous stress and "friction" parameter on the fault "surface", as is suggested in Ando's model, either implicitly or explicitly. Finally, Ando's model obtains an estimate of η_v to be $10^4 - 10^5\ \mu/(2\beta)$ by explaining diffusive tremor migration. With the newly derived analytical relation, I can extend the estimation to other observables, and I find that a viscous coefficient η_v of $10^4 - 10^5\ \mu/(2\beta)$ can also simultaneously explain many other SSE observations, including their slip rates, rupture propagation speeds, slip rate decay times, and moment duration scaling.

Aside from Ando's model, there are other studies that also imply that a "frictional-viscous mixing in parallel" framework can possibly produce SSE behaviors, including Lavier et al. (2013), Beall et al. (2019), and Lavier et al. (2021). Compared to the setup in my models and Ando's model, these three above studies are more focused on exploring the frictional-viscous interaction within the fault zone, instead of explaining the geophysical observations. In these three models, the dimension of the model domain is too small to

thoroughly consider the interaction between the fault zone and the elastic medium, such as inertia and wave effects. Therefore, it is naturally difficult for them to analyze some of geophysical observations, such as rupture propagation speed and moment-duration scaling. It would be ideal if we can have a model that cover multiple scales; yet, as we have suggested earlier, it is non-trivial to consider both a fault zone scale of $\sim$ 100 meters and the SSE rupture scale of $\sim$ 10 kilometers in the same model. Such theoretical analysis will be a direction for future studies.

6.5.6 Connections with the Brownian walk model

In addition to mechanical models, some statistically-based models are also brought up to explain slow earthquakes. One statistical model that is of particular interest here is the Brownian Walk model developed by Satoshi Ide and others (e.g. Ide, 2008; Ide & Yabe, 2019). This model describes the slow earthquake propagation in a statistical framework. A key component that makes the Brownian Walk model generate slow earthquake signals is that, for each location on fault, whether it would slip at a given time step depends on whether its nearby fault was slipping in the last time step (with some probability) (Ide & Yabe, 2019).

This assumption is actually consistent with the physical image of the frictional-viscous model that explored in my dissertation. As demonstrated earlier, elastic wave amplitude becomes smaller as slip rate decreases. Therefore, when slip rate is low, static stress transfer would be the dominant mechanism that controls the rupture propagation, instead of dynamic stress transfer by seismic waves. Since static stress is fundamentally a force that only affects nearby areas within the slipping fault, the static stress transfer-

controlled rupture propagation might have a very similar behavior as described in the Brownian Walk model. More detailed comparisons can be done in the future with the analytical relations I have obtained in my dissertation. Nevertheless, I believe, though this potential relation is tantalizing, more careful work is necessary to understand the relationship between these two models.

Chapter 7

Summary and Conclusion

In this dissertation, I consider a frictional-viscous fault zone model to explain puzzling slow earthquake phenomena. Here, "frictional" means that fault strength can suddenly drop and host transient frictional slip. The strength drop is treated as sudden when the strength dropping rate with slip is considerably faster than the elastic loading stress dropping rate with slip. In Chapter 2, I show that many first-order characteristics of fast earthquakes (e.g., slip rate, rupture propagation speed, moment duration scaling) can be explained by a frictional-only model, with a stress drop of the order of magnitude of MPa. Corresponding first-order characteristics of slow slip events (SSEs) cannot be explained by a frictional-only model with a stress drop of the order of magnitude of 10 kPa, which is a typical value constrained by geodetic and seismic data.

To explain SSEs, I consider adding a viscous component to the fault boundary condition, which is one of the potential mechanisms that have been proposed by earlier studies (Chapter 3). In this frictional-viscous model, the total fault strength equals the sum

of the frictional and viscous strength components. This model reflects the physical picture that the 3D fault zone mostly consists of viscous deformation, while frictional (brittle) deformation sparsely exists in the fault zone as well. In the present model, the viscous strength increases linearly with slip rate,

$$f_{viscous} = \eta_v \cdot V,$$

Where η_v is the viscous coefficient. Therefore, when the fault has not yet slipped, the viscous strength is zero, and the applied elastic loading stress is completely taken up by the frictional strength. Because such a boundary condition is equivalent to a mechanical system where the frictional and viscous force act in parallel (Figure 3.3d, 4.1b), I also refer to this model as a "frictional-viscous in parallel" model in this dissertation.

At some point, the frictional strength cannot keep up with the increased elastic loading stress, and experiences a sudden drop. This strength drop causes a sudden imbalance between the elastic loading stress and the total fault strength. In response to the imbalance, the fault slips until the gap is remedied, resulting in a slip transient. In Section 6.1, I show that such a transient would happen more frequently in the frictional-viscous model than the frictional-only slip transient. This is because the frictional contacts are sparsely distributed in the fault zone in the frictional-viscous model. For the same bulk plate loading rate, the frictional contacts in the frictional-viscous model would experience a higher stressing rate than in the frictional-only model, and thus would reach the yielding stress faster. As a result, the average strength drop in the frictional-viscous model during each slip transient would be smaller than the local strength drop on the frictional contacts. If we assume

that the local strength drop is the same for both the frictional-viscous and the frictional-only model, the frictional-viscous model would have a smaller average strength drop than the frictional-only model. This physical picture is qualitatively consistent with what we observed for the subduction zone SSEs. To first order, a 100 times smaller average stress drop in the frictional-viscous model corresponds to a 100 times more frequent slip transient occurrence.

In Chapters 4 and 5, I explore the first-order "coseismic" characteristics of the slip transient under the frictional-viscous setting. In Chapter 4, I derive analytical relations to relate the parameters in the frictional-viscous model (e.g., viscous coefficient η_v, sudden frictional strength drop Δf, characteristic length of slipping patch L) with some kinematic source parameters that can be inferred from the geophysical observations (e.g., slip rate V, rupture propagation speed V_r, slip rate decay time T_d). I find that the frictional-only is a degenerate case of the fractional-viscous model when $\eta_v = 0$. When the viscous coefficient η_v becomes larger, the slip rate V and the rupture propagation speed V_r of the slip transient become slower. The magnitude of the reduction is controlled by the ratio between η_v and the radiation damping factor $\mu/(2\beta)$. In particular, I find that when the viscous coefficient η_v and the stress drop are of the order of magnitude of 10^4 to 10^5 $\mu/(2\beta)$ and 10 kPa, respectively, the frictional-viscous model can simultaneously produce the first-order slip rate V, rupture propagation speed V_r, slip rate decay time T_d, and the moment-duration scaling for SSEs that are inferred from geophysical observations. The moment-duration scaling relation in the frictional-viscous model is $M_0 \propto T^3$, which is the same as the frictional-only model. However, the duration in the frictional-viscous model can be several orders

of magnitude greater than in the frictional-only model. These results are validated by the numerical simulations in Chapter 5.

Because the slip rate V becomes slower as η_v increases, the radiated dynamic wave energy of the slip transient also reduces. Therefore, when η_v is large, the mechanism of fault interaction and rupture propagation would be static stress transfer, instead of dynamic stress perturbation. Such a condition would produce a unique type of rupture propagation, the diffusive rupture migration (Ando et al., 2012), when there is also a spatial contrast in stress drop on the fault. The diffusive rupture migration is unlikely to emerge in a model when dynamic stress perturbation dominates the fault interaction. In section 4.7, I derive analytical relations to relate the viscous coefficient η_v with the apparent diffusivity D_f that can be estimated from geophysical observations. The analytical relation that describes the diffusive rupture migration is validated by numerical simulations in section 5.4. To explain the observed $D_f \sim 10^3 \mathrm{m}^2/\mathrm{s}$, η_v needs to be $\sim 10^3 - 10^6 \ \mu/(2\beta)$, which is consistent with the η_v that is required to explain other independent observations, and agrees with the analysis in (Ando et al., 2012).

To conclude, the present frictional-viscous model can simultaneously explain various observed kinematic source parameters for SSEs, when the viscous coefficient η_v is about $10^4 - 10^5 \ \mu/(2\beta)$, and the average stress drop in a slip transient is about 10 kPa. Qualitatively, this frictional-viscous model can also explain the shorter inter-event interval and lower average stress drop observed in subduction zone SSEs, compared to what is observed in the fast earthquakes at seismogenic depth. These results imply that the frictional-viscous model is a promising representation of the actual SSE source process for two main reasons.

First, the estimations of the multiple kinematic source parameters for SSEs are mostly independent of each other. Having a single model setting that can simultaneously explain different independent estimates usually suggests a good applicability of the model. Second, the agreements between the present models and SSE observations are first-order agreements. This is because the relationship between the model parameters and the "observables" are linear (Chapter 4 and section 6.3). Therefore, a set of model parameters within two orders of magnitude range can all produce the first-order observables for SSEs. This result suggests that the frictional-viscous model can generate stable slow slip behavior within a wide range of parameter space.

The present model focuses on quantitatively explaining SSE observations, and therefore does not explicitly address other seismic slow earthquake signals, such as tremors, LFEs, VLFEs, and rapid tremor migrations. However, the physical picture of the present model may still qualitatively explain the generation of these seismic slow earthquake signals (section 6.4). Tremors and LFEs are thought to correspond to the sudden frictional strength drop in the frictional-viscous model. In the physical picture, these individual sudden frictional strength drops are thought to be sparsely distributed within the viscous fault zone; although in the model, they are parameterized and "smoothed" into the average strength drop parameter that represents the bulk slip behaviors of the fault, for simplicity. My results suggest that these sudden frictional strength drops (tremors) are crucial in driving the propagation of the bulk viscous deformation of the fault zone, which is thought to correspond to SSEs. In return, the bulk viscous deformation would trigger more sudden frictional strength drops. These interactions together form a "chain-reaction", and manifest

in the geophysical observations as the coexistence of tremors and SSEs. Within the present model framework, I propose different potential directions to explain the signals of VLFE and rapid tremor migrations; yet, the questions of whether and how they can be explained with the present frictional-viscous model are still open.

There are many potential future studies that could be undertaken to test the hypotheses made in the present dissertation, or to improve the present model. First, the present work suggests that the viscous response of the SSE fault zone increases linearly with slip rate, and the viscous coefficient η_v is about $10^4 - 10^5$ $\mu/(2\beta)$ to explain the kinematic source parameters for SSEs estimated from the geophysical observations. This hypothesis, in principle, can be independently tested with geological observations on SSE-hosting faults (in-situ or exhumed) and with laboratory experiments. Also, the present models are simplified in a way that does not explicitly address the heterogeneity in the fault zone. A future fine-scale model that can explicitly include a spatial distribution of viscous and frictional contacts in 3D and simulate the slow earthquakes across multiple scales would be able to test whether the parameterization scheme in the present model is proper or not. Lastly, since this dissertation has suggested that the present frictional-viscous setup can reproduce the first-order characteristics of SSEs, it is promising that a future model may utilize this model framework to model the geophysical observations of a real SSE scenario.

References

Aki, K. (1960). Study of earthquake mechanism by a method of phase equalization applied to rayleigh and love waves. *Journal of Geophysical Research (1896-1977)*, *65*(2), 729-740. Retrieved from https://agupubs.onlinelibrary.wiley.com/doi/abs/10.1029/JZ065i002p00729 doi: https://doi.org/10.1029/JZ065i002p00729

Aki, K. (1966, jul). Generation and propagation of g waves from the niigata earthquake of june 16, 1964. : Part 2. estimation of earthquake moment, released energy, and stress-strain drop from the g wave spectrum. *Bulletin of the Earthquake Research Institute, University of Tokyo*, *44*(1), 73-88. Retrieved from https://ci.nii.ac.jp/naid/120000871042/en/ doi: info:doi/10.15083/0000033586

Aki, K. (1967). Scaling law of seismic spectrum. *Journal of Geophysical Research (1896-1977)*, *72*(4), 1217-1231. Retrieved from https://agupubs.onlinelibrary.wiley.com/doi/abs/10.1029/JZ072i004p01217 doi: https://doi.org/10.1029/JZ072i004p01217

Aki, K., & Richards, P. G. (2002). *Quantitative seismology*. University Science Books. Retrieved from https://books.google.com/books?id=sRhawFG5_EcC

Allmann, B. P., & Shearer, P. M. (2009). Global variations of stress drop for moderate to large earthquakes. *Journal of Geophysical Research: Solid Earth*, *114*(B1). Retrieved from https://agupubs.onlinelibrary.wiley.com/doi/abs/10.1029/2008JB005821 doi: https://doi.org/10.1029/2008JB005821

Ando, R., Nakata, R., & Hori, T. (2010). A slip pulse model with fault heterogeneity for low-frequency earthquakes and tremor along plate interfaces. *Geophysical Research Letters*, *37*(10). Retrieved from https://agupubs.onlinelibrary.wiley.com/doi/abs/10.1029/2010GL043056 doi: https://doi.org/10.1029/2010GL043056

Ando, R., Takeda, N., & Yamashita, T. (2012). Propagation dynamics of seismic and aseismic slip governed by fault heterogeneity and newtonian rheology. *Journal of Geophysical Research: Solid Earth*, *117*(B11). Retrieved from

https://agupubs.onlinelibrary.wiley.com/doi/abs/10.1029/2012JB009532 doi: https://doi.org/10.1029/2012JB009532

Andrews, D. J. (1976). Rupture velocity of plane strain shear cracks. *Journal of Geophysical Research (1896-1977)*, *81*(32), 5679-5687. Retrieved from https://agupubs.onlinelibrary.wiley.com/doi/abs/10.1029/JB081i032p05679 doi: https://doi.org/10.1029/JB081i032p05679

Andrews, D. J. (2005). Rupture dynamics with energy loss outside the slip zone. *Journal of Geophysical Research: Solid Earth*, *110*(B1). Retrieved from https://agupubs.onlinelibrary.wiley.com/doi/abs/10.1029/2004JB003191 doi: https://doi.org/10.1029/2004JB003191

Aochi, H., Fukuyama, E., & Matsu'ura, M. (2000, Dec 01). Spontaneous rupture propagation on a non-planar fault in 3-d elastic medium. *pure and applied geophysics*, *157*(11), 2003-2027. Retrieved from https://doi.org/10.1007/PL00001072 doi: 10.1007/PL00001072

Barbot, S. (2019). Slow-slip, slow earthquakes, period-two cycles, full and partial ruptures, and deterministic chaos in a single asperity fault. *Tectonophysics*, *768*, 228171. Retrieved from https://www.sciencedirect.com/science/article/pii/S0040195119302781 doi: https://doi.org/10.1016/j.tecto.2019.228171

Beall, A., Fagereng, Å., & Ellis, S. (2019). Fracture and weakening of jammed subduction shear zones, leading to the generation of slow slip events. *Geochemistry, Geophysics, Geosystems*, *20*(11), 4869-4884. Retrieved from https://agupubs.onlinelibrary.wiley.com/doi/abs/10.1029/2019GC008481 doi: https://doi.org/10.1029/2019GC008481

Beall, A., van den Ende, M., Ampuero, J.-P., & Fagereng, A. (2021). Viscous fault creep controls the stress-dependence of modelled earthquake statistics.

Behr, W. M., & Bürgmann, R. (2021). What’s down there? the structures, materials and environment of deep-seated slow slip and tremor. *Philosophical Transactions of the Royal Society A: Mathematical, Physical and Engineering Sciences*, *379*(2193), 20200218. Retrieved from https://royalsocietypublishing.org/doi/abs/10.1098/rsta.2020.0218 doi: 10.1098/rsta.2020.0218

Behr, W. M., Gerya, T. V., Cannizzaro, C., & Blass, R. (2021). Transient slow slip characteristics of frictional-viscous subduction megathrust shear zones. *AGU Advances*, *2*(3), e2021AV000416. Retrieved from https://agupubs.onlinelibrary.wiley.com/doi/abs/10.1029/2021AV000416 (e2021AV000416 2021AV000416) doi: https://doi.org/10.1029/2021AV000416

Brune, J. N. (1970). Tectonic stress and the spectra of seismic shear waves from earthquakes. *Journal of Geophysical Research (1896-1977)*, *75*(26), 4997-5009. Retrieved from

https://agupubs.onlinelibrary.wiley.com/doi/abs/10.1029/JB075i026p04997 doi: https://doi.org/10.1029/JB075i026p04997

Bürgmann, R. (2018). The geophysics, geology and mechanics of slow fault slip. *Earth and Planetary Science Letters*, *495*, 112-134. Retrieved from https://www.sciencedirect.com/science/article/pii/S0012821X18302760 doi: https://doi.org/10.1016/j.epsl.2018.04.062

Burridge, R., & Knopoff, L. (1964, 12). Body force equivalents for seismic dislocations. *Bulletin of the Seismological Society of America*, *54*(6A), 1875-1888. Retrieved from https://doi.org/10.1785/BSSA05406A1875 doi: 10.1785/BSSA05406A1875

Byerly, P. (1926, 12). The Montana earthquake of June 28, 1925, G.M.C.T. *Bulletin of the Seismological Society of America*, *16*(4), 209-265. Retrieved from https://doi.org/10.1785/BSSA0160040209 doi: 10.1785/BSSA0160040209

Chinnery, M. A. (1961, 07). The deformation of the ground around surface faults. *Bulletin of the Seismological Society of America*, *51*(3), 355-372. Retrieved from https://doi.org/10.1785/BSSA0510030355 doi: 10.1785/BSSA0510030355

Cochard, A., & Madariaga, R. (1994, Sep 01). Dynamic faulting under rate-dependent friction. *pure and applied geophysics*, *142*(3), 419-445. Retrieved from https://doi.org/10.1007/BF00876049 doi: 10.1007/BF00876049

Colella, H. V., Dieterich, J. H., & Richards-Dinger, K. B. (2011). Multi-event simulations of slow slip events for a cascadia-like subduction zone. *Geophysical Research Letters*, *38*(16). Retrieved from https://agupubs.onlinelibrary.wiley.com/doi/abs/10.1029/2011GL048817 doi: https://doi.org/10.1029/2011GL048817

Creager, K. C., Ulberg, C. W., & Houston, H. (2020, December). Initiation and Propagation Phases of Northern Cascadia Episodic Tremor and Slip Events. In *Agu fall meeting abstracts* (Vol. 2020, p. T005-03).

Dalguer, L. A., & Day, S. M. (2009). Asymmetric rupture of large aspect-ratio faults at bimaterial interface in 3d. *Geophysical Research Letters*, *36*(23). Retrieved from https://agupubs.onlinelibrary.wiley.com/doi/abs/10.1029/2009GL040303 doi: https://doi.org/10.1029/2009GL040303

Dal Zilio, L., Lapusta, N., & Avouac, J.-P. (2020). Unraveling scaling properties of slow-slip events. *Geophysical Research Letters*, *47*(10), e2020GL087477. Retrieved from https://agupubs.onlinelibrary.wiley.com/doi/abs/10.1029/2020GL087477 (e2020GL087477 10.1029/2020GL087477) doi: https://doi.org/10.1029/2020GL087477

Day, S. M. (1982, 06). Three-dimensional finite difference simulation of fault dynamics: Rectangular faults with fixed rupture velocity. *Bulletin of the Seismological Society of America*, *72*(3), 705-727. Retrieved from https://doi.org/10.1785/BSSA0720030705 doi: 10.1785/BSSA0720030705

Dieterich, J. (2007). Applications of rate-and state-dependent friction to models of fault slip and earthquake occurrence. *Treatise on Geophysics*, 107-129.

Dieterich, J. H. (1979). Modeling of rock friction: 1. experimental results and constitutive equations. *Journal of Geophysical Research: Solid Earth*, *84*(B5), 2161-2168. Retrieved from https://agupubs.onlinelibrary.wiley.com/doi/abs/10.1029/JB084iB05p02161 doi: https://doi.org/10.1029/JB084iB05p02161

Dieterich, J. H. (1992). Earthquake nucleation on faults with rate-and state-dependent strength. *Tectonophysics*, *211*(1), 115-134. Retrieved from https://www.sciencedirect.com/science/article/pii/004019519290055B doi: https://doi.org/10.1016/0040-1951(92)90055-B

Dieterich, J. H., & Kilgore, B. D. (1994, Mar 01). Direct observation of frictional contacts: New insights for state-dependent properties. *pure and applied geophysics*, *143*(1), 283-302. Retrieved from https://doi.org/10.1007/BF00874332 doi: 10.1007/BF00874332

Dragert, H., Wang, K., & James, T. S. (2001). A silent slip event on the deeper cascadia subduction interface. *Science*, *292*(5521), 1525-1528. doi: 10.1126/science.1060152

Fagereng, Å., & Sibson, R. H. (2010, Aug 01). Mélange rheology and seismic style. *Geology*, *38*(8), 751-754. Retrieved from https://doi.org/10.1130/G30868.1 doi: 10.1130/G30868.1

Frank, W. B., & Brodsky, E. E. (2019). Daily measurement of slow slip from low-frequency earthquakes is consistent with ordinary earthquake scaling. *Science Advances*, *5*(10). Retrieved from https://advances.sciencemag.org/content/5/10/eaaw9386 doi: 10.1126/sciadv.aaw9386

Frank, W. B., Radiguet, M., Rousset, B., Shapiro, N. M., Husker, A. L., Kostoglodov, V., ... Campillo, M. (2015). Uncovering the geodetic signature of silent slip through repeating earthquakes. *Geophysical Research Letters*, *42*(8), 2774-2779. Retrieved from https://agupubs.onlinelibrary.wiley.com/doi/abs/10.1002/2015GL063685 doi: https://doi.org/10.1002/2015GL063685

Fukuyama, E., & Madariaga, R. (1998, 02). Rupture dynamics of a planar fault in a 3D elastic medium: Rate- and slip-weakening friction. *Bulletin of the Seismological Society of America*, *88*(1), 1-17.

Gao, H., Schmidt, D. A., & Weldon, I., Ray J. (2012, Feb 01). Scaling relationships of source parameters for slow slip events. *Bulletin of the Seismological Society of America*, *102*(1), 352-360. Retrieved from https://doi.org/10.1785/0120110096 doi: 10.1785/0120110096

Ghosh, A., Huesca-Pérez, E., Brodsky, E., & Ito, Y. (2015). Very low frequency earthquakes in cascadia migrate with tremor. *Geophysical Research Letters*, *42*(9), 3228-3232. Retrieved from

https://agupubs.onlinelibrary.wiley.com/doi/abs/10.1002/2015GL063286 doi: https://doi.org/10.1002/2015GL063286

Ghosh, A., Vidale, J. E., Sweet, J. R., Creager, K. C., Wech, A. G., Houston, H., & Brodsky, E. E. (2010). Rapid, continuous streaking of tremor in cascadia. *Geochemistry, Geophysics, Geosystems*, *11*(12). Retrieved from https://agupubs.onlinelibrary.wiley.com/doi/abs/10.1029/2010GC003305 doi: https://doi.org/10.1029/2010GC003305

Gilbert, G. K. (1884). A theory of the earthquakes of the great basin, with a practical application. *American Journal of Science*, *s3-27*(157), 49–53. Retrieved from https://www.ajsonline.org/content/s3-27/157/49 doi: 10.2475/ajs.s3-27.157.49

Gomberg, J., Agnew, D., & Schwartz, S. (2016). Alternative source models of very low frequency events. *Journal of Geophysical Research: Solid Earth*, *121*(9), 6722–6740.

Gomberg, J., Wech, A., Creager, K., Obara, K., & Agnew, D. (2016). Reconsidering earthquake scaling. *Geophysical Research Letters*, *43*(12), 6243-6251. Retrieved from https://agupubs.onlinelibrary.wiley.com/doi/abs/10.1002/2016GL069967 doi: https://doi.org/10.1002/2016GL069967

Goswami, A., & Barbot, S. (2018, Apr 18). Slow-slip events in semi-brittle serpentinite fault zones. *Scientific Reports*, *8*(1), 6181. Retrieved from https://doi.org/10.1038/s41598-018-24637-z doi: 10.1038/s41598-018-24637-z

Gutenberg, B. (1956). The energy of earthquakes. *Quarterly Journal of the Geological Society*, *112*(1-4), 1–14. Retrieved from https://jgs.lyellcollection.org/content/112/1-4/1 doi: 10.1144/GSL.JGS.1956.112.01-04.02

Gutenberg, B., & Richter, C. F. (1956, 04). Earthquake magnitude, intensity, energy, and acceleration: (Second paper). *Bulletin of the Seismological Society of America*, *46*(2), 105-145. Retrieved from https://doi.org/10.1785/BSSA0460020105 doi: 10.1785/BSSA0460020105

Hanks, T. C., & Kanamori, H. (1979). A moment magnitude scale. *Journal of Geophysical Research: Solid Earth*, *84*(B5), 2348-2350. Retrieved from https://agupubs.onlinelibrary.wiley.com/doi/abs/10.1029/JB084iB05p02348 doi: https://doi.org/10.1029/JB084iB05p02348

Hawthorne, J. C., & Rubin, A. M. (2013). Laterally propagating slow slip events in a rate and state friction model with a velocity-weakening to velocity-strengthening transition. *Journal of Geophysical Research: Solid Earth*, *118*(7), 3785-3808. Retrieved from https://agupubs.onlinelibrary.wiley.com/doi/abs/10.1002/jgrb.50261 doi: https://doi.org/10.1002/jgrb.50261

Hodgson, J. H. (1957, 05). NATURE OF FAULTING IN LARGE EARTHQUAKES. *GSA Bulletin*, *68*(5), 611-644. Retrieved from

https://doi.org/10.1130/0016-7606(1957)68[611:NOFILE]2.0.CO;2 doi: 10.1130/0016-7606(1957)68[611:NOFILE]2.0.CO;2

Honda, H. (1932). On the initial motion and the types of the seismograms of the north idu and ito earthquakes. *J. Met. Soc. Japan, ii*, *9*, 293-314. Retrieved from https://ci.nii.ac.jp/naid/10003775681/en/

Honda, H. (1962). Earthquake mechanism and seismic waves. *Journal of Physics of the Earth*, *10*(2), 1-97. doi: 10.4294/jpe1952.10.2_1

Honda, H., & Miura, T. (1935). On the strain produced in a semi-infinite elastic solid by statical surface force, with some applications to seismology. *Geophys. Mag*, *9*, 61–81.

Ide, S. (2008). A brownian walk model for slow earthquakes. *Geophysical Research Letters*, *35*(17).

Ide, S. (2010, Jul 01). Striations, duration, migration and tidal response in deep tremor. *Nature*, *466*(7304), 356-359. Retrieved from https://doi.org/10.1038/nature09251 doi: 10.1038/nature09251

Ide, S., Beroza, G. C., Shelly, D. R., & Uchide, T. (2007a). A scaling law for slow earthquakes. *Nature*, *447*(7140), 76.

Ide, S., Beroza, G. C., Shelly, D. R., & Uchide, T. (2007b, May 01). A scaling law for slow earthquakes. *Nature*, *447*(7140), 76-79. Retrieved from https://doi.org/10.1038/nature05780 doi: 10.1038/nature05780

Ide, S., & Yabe, S. (2014). Universality of slow earthquakes in the very low frequency band. *Geophysical Research Letters*, *41*(8), 2786–2793.

Ide, S., & Yabe, S. (2019, Mar 01). Two-dimensional probabilistic cell automaton model for broadband slow earthquakes. *Pure and Applied Geophysics*, *176*(3), 1021-1036. Retrieved from https://doi.org/10.1007/s00024-018-1976-9 doi: 10.1007/s00024-018-1976-9

Im, K., Saffer, D., Marone, C., & Avouac, J.-P. (2020, Oct 01). Slip-rate-dependent friction as a universal mechanism for slow slip events. *Nature Geoscience*, *13*(10), 705-710. Retrieved from https://doi.org/10.1038/s41561-020-0627-9 doi: 10.1038/s41561-020-0627-9

Ito, Y., & Obara, K. (2006). Very low frequency earthquakes within accretionary prisms are very low stress-drop earthquakes. *Geophysical Research Letters*, *33*(9).

Kanamori, H. (1977). The energy release in great earthquakes. *Journal of Geophysical Research (1896-1977)*, *82*(20), 2981-2987. Retrieved from https://agupubs.onlinelibrary.wiley.com/doi/abs/10.1029/JB082i020p02981 doi: https://doi.org/10.1029/JB082i020p02981

Kanamori, H. (1983). Magnitude scale and quantification of earthquakes. *Tectonophysics*, *93*(3), 185-199. Retrieved from

https://www.sciencedirect.com/science/article/pii/0040195183902731 (Quantification of Earthquakes) doi: https://doi.org/10.1016/0040-1951(83)90273-1

Kanamori, H., & Anderson, D. L. (1975, 10). Theoretical basis of some empirical relations in seismology. *Bulletin of the Seismological Society of America*, *65*(5), 1073-1095. Retrieved from https://doi.org/10.1785/BSSA0650051073 doi: 10.1785/BSSA0650051073

Kanamori, H., & Stewart, G. S. (1979). A slow earthquake. *Physics of the Earth and Planetary Interiors*, *18*(3), 167-175. Retrieved from https://www.sciencedirect.com/science/article/pii/0031920179901122 doi: https://doi.org/10.1016/0031-9201(79)90112-2

Kirkpatrick, J. D., Fagereng, Å., & Shelly, D. R. (2021, Apr 01). Geological constraints on the mechanisms of slow earthquakes. *Nature Reviews Earth & Environment*, *2*(4), 285-301. Retrieved from https://doi.org/10.1038/s43017-021-00148-w doi: 10.1038/s43017-021-00148-w

Knopoff, L., & Gilbert, F. (1960, 01). First motions from seismic sources. *Bulletin of the Seismological Society of America*, *50*(1), 117-134. Retrieved from https://doi.org/10.1785/BSSA0500010117 doi: 10.1785/BSSA0500010117

Lamb, H. (1904). I. on the propagation of tremors over the surface of an elastic solid. *Philosophical Transactions of the Royal Society of London. Series A, Containing Papers of a Mathematical or Physical Character*, *203*(359-371), 1-42. Retrieved from https://royalsocietypublishing.org/doi/abs/10.1098/rsta.1904.0013 doi: 10.1098/rsta.1904.0013

Lavier, L. L., Bennett, R. A., & Duddu, R. (2013). Creep events at the brittle ductile transition. *Geochemistry, Geophysics, Geosystems*, *14*(9), 3334-3351. Retrieved from https://agupubs.onlinelibrary.wiley.com/doi/abs/10.1002/ggge.20178 doi: https://doi.org/10.1002/ggge.20178

Lavier, L. L., Tong, X., & Biemiller, J. (2021). The mechanics of creep, slow slip events, and earthquakes in mixed brittle-ductile fault zones. *Journal of Geophysical Research: Solid Earth*, *126*(2), e2020JB020325. Retrieved from https://agupubs.onlinelibrary.wiley.com/doi/abs/10.1029/2020JB020325 (e2020JB020325 2020JB020325) doi: https://doi.org/10.1029/2020JB020325

Leeman, J. R., Saffer, D. M., Scuderi, M. M., & Marone, C. (2016, Mar 31). Laboratory observations of slow earthquakes and the spectrum of tectonic fault slip modes. *Nature Communications*, *7*(1), 11104. Retrieved from https://doi.org/10.1038/ncomms11104 doi: 10.1038/ncomms11104

Liu, Y. (2013). Numerical simulations on megathrust rupture stabilized under strong dilatancy strengthening in slow slip region. *Geophysical Research Letters*, *40*(7), 1311-1316. Retrieved from

https://agupubs.onlinelibrary.wiley.com/doi/abs/10.1002/grl.50298 doi: https://doi.org/10.1002/grl.50298

Liu, Y. (2014). Source scaling relations and along-strike segmentation of slow slip events in a 3-d subduction fault model. *Journal of Geophysical Research: Solid Earth*, *119*(8), 6512-6533. Retrieved from https://agupubs.onlinelibrary.wiley.com/doi/abs/10.1002/2014JB011144 doi: https://doi.org/10.1002/2014JB011144

Liu, Y., & Rice, J. R. (2005). Aseismic slip transients emerge spontaneously in three-dimensional rate and state modeling of subduction earthquake sequences. *Journal of Geophysical Research: Solid Earth*, *110*(B8). Retrieved from https://agupubs.onlinelibrary.wiley.com/doi/abs/10.1029/2004JB003424 doi: https://doi.org/10.1029/2004JB003424

Liu, Y., & Rice, J. R. (2007). Spontaneous and triggered aseismic deformation transients in a subduction fault model. *Journal of Geophysical Research: Solid Earth*, *112*(B9). Retrieved from https://agupubs.onlinelibrary.wiley.com/doi/abs/10.1029/2007JB004930 doi: https://doi.org/10.1029/2007JB004930

Liu, Y., & Rubin, A. M. (2010). Role of fault gouge dilatancy on aseismic deformation transients. *Journal of Geophysical Research: Solid Earth*, *115*(B10). Retrieved from https://agupubs.onlinelibrary.wiley.com/doi/abs/10.1029/2010JB007522 doi: https://doi.org/10.1029/2010JB007522

Love, A. E. H. (1911). *Some problems of geodynamics: Being an essay to which the adams prize in the university of cambridge was adjudged in 1911* (Vol. 911). University Press.

Luo, Y., & Ampuero, J.-P. (2018). Stability of faults with heterogeneous friction properties and effective normal stress. *Tectonophysics*, *733*, 257-272. Retrieved from https://www.sciencedirect.com/science/article/pii/S0040195117304596 (Physics of Earthquake Rupture Propagation) doi: https://doi.org/10.1016/j.tecto.2017.11.006

Luo, Y., & Liu, Z. (2021, Mar 30). Fault zone heterogeneities explain depth-dependent pattern and evolution of slow earthquakes in cascadia. *Nature Communications*, *12*(1), 1959. Retrieved from https://doi.org/10.1038/s41467-021-22232-x doi: 10.1038/s41467-021-22232-x

Mallet, R. (1862). *Great neapolitan earthquake of 1857: The first principles of observational seismology as developed in the report to the royal society of london of the expedition made by command of the society into the interior of the kingdom of naples, to investigate the circumstances of the great earthquake of demember 1857* (No. v. 2). Chapman and Hall. Retrieved from https://books.google.com/books?id=BbgQAAAAIAAJ

Maruyama, T. (1963, sep). On the force equivalents of dynamical elastic dislocations with reference to the earthquake mechanism. *Bull. Earthq. Res. Inst.*,

41(3), 467-486. Retrieved from https://ci.nii.ac.jp/naid/120000866527/en/ doi: info:doi/10.15083/0000033709

Masuda, K., Ide, S., Ohta, K., & Matsuzawa, T. (2020, Apr 07). Bridging the gap between low-frequency and very-low-frequency earthquakes. *Earth, Planets and Space*, *72*(1), 47. Retrieved from https://doi.org/10.1186/s40623-020-01172-8 doi: 10.1186/s40623-020-01172-8

Michel, S., Gualandi, A., & Avouac, J.-P. (2019, Oct 01). Similar scaling laws for earthquakes and cascadia slow-slip events. *Nature*, *574*(7779), 522-526. Retrieved from https://doi.org/10.1038/s41586-019-1673-6 doi: 10.1038/s41586-019-1673-6

Michell, J. (1760). Lv. conjectures concerning the cause, and observations upon the phænomena of earthquakes; particularly of that great earthquake of the first november, 1755, which proved so fatal to the city of lisbon, and whose effects were felt as far as africa and more or less throughout almost all europe; by the reverend john michell, m. a. fellow of queen's college, cambridge. *Philosophical Transactions of the Royal Society of London*, *51*, 566-634. Retrieved from https://royalsocietypublishing.org/doi/abs/10.1098/rstl.1759.0057 doi: 10.1098/rstl.1759.0057

Nakamura, S. (1922). On the direction of the first movement of the earthquake. *Journal of the Meteorological Society of Japan. Ser. I*, *41*(2), en1–en10.

Nakano, H. (1923). Note on the nature of forces which give rise to the earthquake motions. *Seismol Bull Centr Meteorol Obs, Tokyo*, *1*, 92–120. Retrieved from https://ci.nii.ac.jp/naid/10012507183/en/

Nakata, R., Ando, R., Hori, T., & Ide, S. (2011). Generation mechanism of slow earthquakes: Numerical analysis based on a dynamic model with brittle-ductile mixed fault heterogeneity. *Journal of Geophysical Research: Solid Earth*, *116*(B8). Retrieved from https://agupubs.onlinelibrary.wiley.com/doi/abs/10.1029/2010JB008188 doi: https://doi.org/10.1029/2010JB008188

National Academies of Sciences, E., & Medicine. (2020). *A vision for nsf earth sciences 2020-2030: Earth in time*. Washington, DC: The National Academies Press. Retrieved from https://www.nap.edu/catalog/25761/a-vision-for-nsf-earth-sciences-2020-2030-earth-in doi: 10.17226/25761

Nishikawa, T., Matsuzawa, T., Ohta, K., Uchida, N., Nishimura, T., & Ide, S. (2019). The slow earthquake spectrum in the japan trench illuminated by the s-net seafloor observatories. *Science*, *365*(6455), 808–813. Retrieved from https://science.sciencemag.org/content/365/6455/808 doi: 10.1126/science.aax5618

Obara, K. (2002). Nonvolcanic deep tremor associated with subduction in southwest japan. *Science*, *296*(5573), 1679-1681. doi: 10.1126/science.1070378

Obara, K. (2020). Characteristic activities of slow earthquakes in japan. *Proceedings of the Japan Academy, Series B*, *96*(7), 297-315. doi: 10.2183/pjab.96.022

Obara, K., & Kato, A. (2016). Connecting slow earthquakes to huge earthquakes. *Science*, *353*(6296), 253–257.

Obara, K., Matsuzawa, T., Tanaka, S., & Maeda, T. (2012). Depth-dependent mode of tremor migration beneath kii peninsula, nankai subduction zone. *Geophysical Research Letters*, *39*(10). Retrieved from `https://agupubs.onlinelibrary.wiley.com/doi/abs/10.1029/2012GL051420` doi: https://doi.org/10.1029/2012GL051420

Okada, Y. (1992, 04). Internal deformation due to shear and tensile faults in a half-space. *Bulletin of the Seismological Society of America*, *82*(2), 1018-1040.

Peng, Z., & Gomberg, J. (2010, Sep 01). An integrated perspective of the continuum between earthquakes and slow-slip phenomena. *Nature Geoscience*, *3*(9), 599-607. Retrieved from `https://doi.org/10.1038/ngeo940` doi: 10.1038/ngeo940

Perfettini, H., & Ampuero, J.-P. (2008). Dynamics of a velocity strengthening fault region: Implications for slow earthquakes and postseismic slip. *Journal of Geophysical Research: Solid Earth*, *113*(B9). Retrieved from `https://agupubs.onlinelibrary.wiley.com/doi/abs/10.1029/2007JB005398` doi: https://doi.org/10.1029/2007JB005398

Perfettini, H., & Avouac, J.-P. (2004). Postseismic relaxation driven by brittle creep: A possible mechanism to reconcile geodetic measurements and the decay rate of aftershocks, application to the chi-chi earthquake, taiwan. *Journal of Geophysical Research: Solid Earth*, *109*(B2). Retrieved from `https://agupubs.onlinelibrary.wiley.com/doi/abs/10.1029/2003JB002488` doi: https://doi.org/10.1029/2003JB002488

Phillips, N. J., Motohashi, G., Ujiie, K., & Rowe, C. D. (2020). Evidence of localized failure along altered basaltic blocks in tectonic mélange at the up-dip limit of the seismogenic zone: Implications for the shallow slow earthquake source. *Geochemistry, Geophysics, Geosystems*, *21*(7), e2019GC008839. Retrieved from `https://agupubs.onlinelibrary.wiley.com/doi/abs/10.1029/2019GC008839` (e2019GC008839 2019GC008839) doi: https://doi.org/10.1029/2019GC008839

Platt, J. P., Xia, H., & Schmidt, W. L. (2018, Apr 27). Rheology and stress in subduction zones around the aseismic/seismic transition. *Progress in Earth and Planetary Science*, *5*(1), 24. Retrieved from `https://doi.org/10.1186/s40645-018-0183-8` doi: 10.1186/s40645-018-0183-8

Poiata, N., Vilotte, J.-P., Shapiro, N. M., Supino, M., & Obara, K. (2021). Complexity of deep low-frequency earthquake activity in shikoku (japan) imaged from the analysis of continuous seismic data. *Journal of Geophysical Research: Solid Earth*, *126*(11), e2021JB022138. Retrieved from

https://agupubs.onlinelibrary.wiley.com/doi/abs/10.1029/2021JB022138 (e2021JB022138 2021JB022138) doi: https://doi.org/10.1029/2021JB022138

Reid, H. F. (1910). The mechanics of the earthquake. *The California Earthquake of April 18, 1906, Report of the State Earthquake Investigation Commission*, *2*, 1-192.

Rice, J. R. (1993). Spatio-temporal complexity of slip on a fault. *Journal of Geophysical Research: Solid Earth*, *98*(B6), 9885-9907. Retrieved from https://agupubs.onlinelibrary.wiley.com/doi/abs/10.1029/93JB00191 doi: https://doi.org/10.1029/93JB00191

Rogers, G., & Dragert, H. (2003). Episodic tremor and slip on the cascadia subduction zone: The chatter of silent slip. *Science*, *300*(5627), 1942-1943. doi: 10.1126/science.1084783

Rubin, A. M. (2011). Designer friction laws for bimodal slow slip propagation speeds. *Geochemistry, Geophysics, Geosystems*, *12*(4). Retrieved from https://agupubs.onlinelibrary.wiley.com/doi/abs/10.1029/2010GC003386 doi: https://doi.org/10.1029/2010GC003386

Rubin, A. M., & Ampuero, J.-P. (2005). Earthquake nucleation on (aging) rate and state faults. *Journal of Geophysical Research: Solid Earth*, *110*(B11). Retrieved from https://agupubs.onlinelibrary.wiley.com/doi/abs/10.1029/2005JB003686 doi: https://doi.org/10.1029/2005JB003686

Ruina, A. (1983). Slip instability and state variable friction laws. *Journal of Geophysical Research: Solid Earth*, *88*(B12), 10359-10370. Retrieved from https://agupubs.onlinelibrary.wiley.com/doi/abs/10.1029/JB088iB12p10359 doi: https://doi.org/10.1029/JB088iB12p10359

Schmidt, W. L., & Platt, J. P. (2022). Stress, microstructure, and deformation mechanisms during subduction underplating at the depth of tremor and slow slip, franciscan complex, northern california. *Journal of Structural Geology*, *154*, 104469. Retrieved from https://www.sciencedirect.com/science/article/pii/S0191814121001930 doi: https://doi.org/10.1016/j.jsg.2021.104469

Scholz, C. H. (2019). *The mechanics of earthquakes and faulting* (3rd ed.). Cambridge University Press. doi: 10.1017/9781316681473

Segall, P., Rubin, A. M., Bradley, A. M., & Rice, J. R. (2010). Dilatant strengthening as a mechanism for slow slip events. *Journal of Geophysical Research: Solid Earth*, *115*(B12). Retrieved from https://agupubs.onlinelibrary.wiley.com/doi/abs/10.1029/2010JB007449 doi: https://doi.org/10.1029/2010JB007449

Shapiro, N. M., Campillo, M., Kaminski, E., Vilotte, J.-P., & Jaupart, C. (2018). Low-frequency earthquakes and pore pressure transients in subduction zones. *Geophysical Research Letters*, *45*(20), 11,083-11,094. Retrieved from

https://agupubs.onlinelibrary.wiley.com/doi/abs/10.1029/2018GL079893 doi: https://doi.org/10.1029/2018GL079893

Shearer, P. M. (2019). *Introduction to seismology*. Cambridge university press.

Shelly, D. R., Beroza, G. C., & Ide, S. (2007, Mar 01). Non-volcanic tremor and low-frequency earthquake swarms. *Nature*, *446*(7133), 305-307. Retrieved from https://doi.org/10.1038/nature05666 doi: 10.1038/nature05666

Shibazaki, B., & Iio, Y. (2003). On the physical mechanism of silent slip events along the deeper part of the seismogenic zone. *Geophysical Research Letters*, *30*(9). Retrieved from https://agupubs.onlinelibrary.wiley.com/doi/abs/10.1029/2003GL017047 doi: https://doi.org/10.1029/2003GL017047

Sibson, R. H. (2017, Aug 15). Tensile overpressure compartments on low-angle thrust faults. *Earth, Planets and Space*, *69*(1), 113. Retrieved from https://doi.org/10.1186/s40623-017-0699-y doi: 10.1186/s40623-017-0699-y

Skarbek, R. M., Rempel, A. W., & Schmidt, D. A. (2012). Geologic heterogeneity can produce aseismic slip transients. *Geophysical Research Letters*, *39*(21). Retrieved from https://agupubs.onlinelibrary.wiley.com/doi/abs/10.1029/2012GL053762 doi: https://doi.org/10.1029/2012GL053762

Steketee, J. A. (1958). Some geophysical applications of the elasticity theory of dislocations. *Canadian Journal of Physics*, *36*(9), 1168-1198. Retrieved from https://doi.org/10.1139/p58-123 doi: 10.1139/p58-123

Sweet, J. R., Creager, K. C., & Houston, H. (2014). A family of repeating low-frequency earthquakes at the downdip edge of tremor and slip. *Geochemistry, Geophysics, Geosystems*, *15*(9), 3713-3721. Retrieved from https://agupubs.onlinelibrary.wiley.com/doi/abs/10.1002/2014GC005449 doi: https://doi.org/10.1002/2014GC005449

Sykes, L. R. (1967). Mechanism of earthquakes and nature of faulting on the mid-oceanic ridges. *Journal of Geophysical Research (1896-1977)*, *72*(8), 2131-2153. Retrieved from https://agupubs.onlinelibrary.wiley.com/doi/abs/10.1029/JZ072i008p02131 doi: https://doi.org/10.1029/JZ072i008p02131

Tada, T. (2005, 09). Displacement and stress Green's functions for a constant slip-rate on a quadrantal fault. *Geophysical Journal International*, *162*(3), 1007-1023. Retrieved from https://doi.org/10.1111/j.1365-246X.2005.02681.x doi: 10.1111/j.1365-246X.2005.02681.x

Tada, T. (2006, 03). Stress Green's functions for a constant slip rate on a triangular fault. *Geophysical Journal International*, *164*(3), 653-669. Retrieved from https://doi.org/10.1111/j.1365-246X.2006.02868.x doi: 10.1111/j.1365-246X.2006.02868.x

Tada, T. (2009). Boundary integral equation method for earthquake rupture dynamics. *International Geophysics*, *94*, 217–267.

Tse, S. T., & Rice, J. R. (1986). Crustal earthquake instability in relation to the depth variation of frictional slip properties. *Journal of Geophysical Research: Solid Earth*, *91*(B9), 9452-9472. Retrieved from https://agupubs.onlinelibrary.wiley.com/doi/abs/10.1029/JB091iB09p09452 doi: https://doi.org/10.1029/JB091iB09p09452

Turcotte, D. L., & Schubert, G. (2002). *Geodynamics*. Cambridge university press.

Volterra, V., & Delphenich, T. (1907). On the equilibrium of multiply-connected elastic bodies. *Ann. Sci. Ec. Norm. Super*, *24*, 401–517.

Wallace, L. M., & Beavan, J. (2010). Diverse slow slip behavior at the hikurangi subduction margin, new zealand. *Journal of Geophysical Research: Solid Earth*, *115*(B12). Retrieved from https://agupubs.onlinelibrary.wiley.com/doi/abs/10.1029/2010JB007717 doi: https://doi.org/10.1029/2010JB007717

Wallace, L. M., Beavan, J., Bannister, S., & Williams, C. (2012). Simultaneous long-term and short-term slow slip events at the hikurangi subduction margin, new zealand: Implications for processes that control slow slip event occurrence, duration, and migration. *Journal of Geophysical Research: Solid Earth*, *117*(B11). Retrieved from https://agupubs.onlinelibrary.wiley.com/doi/abs/10.1029/2012JB009489 doi: https://doi.org/10.1029/2012JB009489

Wei, M., Kaneko, Y., Shi, P., & Liu, Y. (2018). Numerical modeling of dynamically triggered shallow slow slip events in new zealand by the 2016 mw 7.8 kaikoura earthquake. *Geophysical Research Letters*, *45*(10), 4764-4772. Retrieved from https://agupubs.onlinelibrary.wiley.com/doi/abs/10.1029/2018GL077879 doi: https://doi.org/10.1029/2018GL077879

Wells, D. L., & Coppersmith, K. J. (1994, 08). New empirical relationships among magnitude, rupture length, rupture width, rupture area, and surface displacement. *Bulletin of the Seismological Society of America*, *84*(4), 974-1002. Retrieved from https://doi.org/10.1785/BSSA0840040974 doi: 10.1785/BSSA0840040974

Whitten, C. A. (1948). Horizontal earth movement, vicinity of san francisco, california. *Eos, Transactions American Geophysical Union*, *29*(3), 318–323.

Wu, B., Oglesby, D. D., Ghosh, A., & Li, B. (2019). A dynamic rupture source model for very low-frequency earthquake signal without detectable nonvolcanic tremors. *Geophysical Research Letters*, *46*(21), 11934-11943. Retrieved from https://agupubs.onlinelibrary.wiley.com/doi/abs/10.1029/2019GL084135 doi: https://doi.org/10.1029/2019GL084135

Yin, A., Xie, Z., & Meng, L. (2018). A viscoplastic shear-zone model for deep (15–50 km) slow-slip events at plate convergent margins. *Earth and Planetary Science Letters*, *491*, 81–94.

Zheng, G., & Rice, J. R. (1998, Dec 01). Conditions under which velocity-weakening friction allows a self-healing versus a cracklike mode of rupture. *Bulletin of the Seismological Society of America*, *88*(6), 1466-1483.